Rea, D.K., Basov, I.A., Janecek, T.R., Palmer-Julson, A., et al., 1993
Proceedings of the Ocean Drilling Program, Initial Reports, Vol. 145

6. SITE 884[1]

Shipboard Scientific Party[2]

HOLE 884A

Date occupied: 20 August 1992

Date departed: 20 August 1992

Time on hole: 9 hr, 15 min

Position: 51°27.026′N, 168°20.228′E

Bottom felt (rig floor; m, drill-pipe measurement): 3837.8

Distance between rig floor and sea level (m): 11.17

Water depth (drill-pipe measurement from sea level, m): 3826.6

Total depth (rig floor; m): 3847.5

Penetration (m): 9.7

Number of cores (including cores with no recovery): 1

Total length of cored section (m): 9.7

Total core recovered (m): 9.72

Core recovery (%): 100

Oldest sediment cored:
Depth (mbsf): 9.7
Nature: silty clay
Age: Quaternary
Measured velocity(km/s): 1.43

Comments: Missed mud line.

HOLE 884B

Date occupied: 20 August 1992

Date departed: 24 August 1992

Time on hole: 3 days, 17 hr, 15 min

Position: 51°27.026′N, 168°20.228′E

Bottom felt (rig floor; m, drill-pipe measurement): 3836.0

Distance between rig floor and sea level (m): 11.17

Water depth (drill-pipe measurement from sea level, m): 3824.8

Total depth (rig floor; m): 4689.9

Penetration (m): 853.9

Number of cores (including cores with no recovery): 91

Total length of cored section (m): 853.9

Total core recovered (m): 791.76

Core recovery (%): 92.7

Oldest sediment cored:
Depth (mbsf): 853.9
Nature: ashy claystone and clayey ash
Age: early Eocene
Measured velocity(km/s): 1.69

[1] Rea, D.K., Basov, I.A., Janecek, T.R., Palmer-Julson, A., et al., 1993. *Proc. ODP, Init. Repts.,* 145: College Station, TX (Ocean Drilling Program).
[2] Shipboard Scientific Party is as given in list of participants preceding the contents.

HOLE 884C

Date occupied: 24 August 1992

Date departed: 25 August 1992

Time on hole: 1 day, 6 hr, 30 min

Position: 51°27.038′N, 168°20.217′E

Bottom felt (rig floor; m, drill-pipe measurement): 3836.1

Distance between rig floor and sea level (m): 11.17

Water depth (drill-pipe measurement from sea level, m): 3824.9

Total depth (rig floor; m): 4193.9

Penetration (m): 357.8

Number of cores (including cores with no recovery): 38

Total length of cored section (m): 357.8

Total core recovered (m): 294.56

Core recovery (%): 82.3

Oldest sediment cored:
Depth (mbsf): 357.8
Nature: diatom clay and clayey diatom ooze
Age: late Miocene
Measured velocity (km/s): 1.53

HOLE 884D

Date occupied: 25 August 1992

Date departed: 26 August 1992

Time on hole: 8 hr

Position: 51°27.038′N, 168°20.196′E

Bottom felt (rig floor; m, drill-pipe measurement): 3837.2

Distance between rig floor and sea level (m): 11.17

Water depth (drill-pipe measurement from sea level, m): 3826.0

Total depth (rig floor; m): 3852.0

Penetration (m): 14.8

Number of cores (including cores with no recovery): 2

Total length of cored section (m): 14.8

Total core recovered (m): 13.92

Core recovery (%): 94.1

Oldest sediment cored:
Depth (mbsf): 14.8
Nature: clay with diatoms
Age: Quaternary

Comments: Cores used for high-resolution paleomagnetic studies.

HOLE 884E

Date occupied: 26 August 1992

Date departed: 31 August 1992

Time on hole: 5 days, 11 hr

Position: 51°27.034′N, 168°20.216′E

Bottom felt (rig floor; m, drill-pipe measurement): 3836.0

Distance between rig floor and sea level (m): 11.17

Water depth (drill-pipe measurement from sea level, m): 3824.8

Total depth (rig floor; m): 4765.8

Penetration (m): 929.8

Number of cores (including cores with no recovery): 10

Total length of cored section (m): 87.0

Total core recovered (m): 66.78

Core recovery (%): 76.6

Oldest sediment cored:
Depth (mbsf): 0.38
Nature: claystone
Age: unknown

Hard rock:
Depth (mbsf): 929.8
Nature: basalt
Measured velocity(km/s): 5.54

Basement:
Depth (mbsf): 929.8
Nature: basalt
Measured velocity (km/s): 5.54

Comments: Washed from 0 to 842.2 mbsf.

Principal results: The survey for proposed site DSM-4 (Site 884; Figs. 1 and 2) began on the morning of 20 August 1992. A beacon was dropped at 0832 hr, and the ship completed the survey and took up station at Site 884 at 1100 hr. The first core missed the mud line and was designated Hole 884A; the ship moved over 20 m and we began Hole 884B with a good mud-line core retrieved at about 1900 hr on 20 August. Coring in Hole 884B continued for 89 hr, raising 91 APC and XCB cores from 0 to 853.9 mbsf with 92.7% overall recovery. Core 145-884B-91X contained basalt in the core catcher. The core recovery from Hole 884B of 791.76 m and percent recovery of 92.7% exceed the previous ODP records for recovery in very long APC/XCB holes: 716.74 m in Hole 807A, and 89.7% recovery in Hole 806B. Thus, Hole 884B stands with Hole 883B as one of the deepest penetrating and most successful XCB drilling operations to date.

Beginning at 0900 hr on 24 August, we pulled up the drill pipe to the seafloor, offset 20 m, and began piston coring in Hole 884C; Core 145-884C-1H was recovered at about noon that day. Hole 884C was continued to a depth of 357.8 mbsf with 82.3% recovery to duplicate the upper portion of the section and to fill in the coring gaps left in Hole 884B. We were largely successful in achieving these objectives. Hole 884D, consisting of two APC cores extending 0 to 14.8 mbsf with 94.1% recovery, was intended for continuous sampling to determine paleointensity variations of Earth's magnetic field. Drilling was completed late in the evening of 25 August. On 26 August, the drill pipe was pulled up and the bit and BHA changed for rotary drilling; Hole 884E was washed down to 842.8 mbsf, and basalt drilling began at 0600 hr on 27 August. The last basalt core, 145-884E-10R, was recovered at about 0300 hr on 29 August; 87 m of basalt had been penetrated in 45 hr with a recovery of 66.78 m (76.8%). Logging operations followed on 29 and 30 August. Logging was hindered by a bridge at about 750 mbsf, presumably a swelling ash layer, but all five tool systems (the geochemical tool, formation microscanner, Quad combo, magnetic susceptibility, and magnetometer tools) made reasonably to completely successful runs above that depth. Logging operations were completed about 0545 hr on 31 August. Both beacons returned to the surface upon command, so for the first time during Leg 145 no unintended metal was left behind at the drill site. The *JOIDES Resolution* started southeast toward proposed Site NW-4A just before 1300 hr later the same day.

Drilling at Site 884 penetrated 854 m of Cenozoic sediment and 87 m of the underlying basalt. The sediment column was divided into two main lithologic units, each with subunits. Lithologic Subunit IA (0–128 mbsf) is a Quaternary to upper Pliocene clay with diatoms. Vitric ash layers, some more than 1 m in thickness, and a few dropstones occur in this unit. Subunit IB (128.2–440.2 mbsf) is an upper Pliocene to upper Miocene clayey diatom ooze. A pure dolomite concretion occurs at 172 mbsf, and a piece of wood approximately 6 cm across is found at 214 mbsf in sediments of early Pliocene age. Lithologic Subunit IC (440.2–546.1 mbsf) is an upper Miocene to middle Miocene claystone with accessory diatoms and some chalk. Bladed and twinned crystals of native copper occur within the gray claystones of Subunit IC. Subunit ID (546.1–604.8 mbsf) is a middle Miocene to lower Miocene diatomite with clay. Unit II is differentiated from the overlying materials by the clear presence of reworked materials. Subunit IIA (604.8–694.7 mbsf) is a lower Miocene to lower Oligocene claystone with minor chalk. This subunit shows evidence of downslope reworking and contains native copper as discrete grains. Subunit IIB (694.7–771 mbsf) is an upper Eocene claystone conglomerate. Diatoms are no longer present in this part of the section, which is dominated by downslope reworking. Ash layers are present in the lower part of this subunit. Subunit IIC (771–854 mbsf) is a middle Eocene to upper Paleocene(?) claystone with ash. Native copper occurs as streaks on slickenside surfaces in the lowest few cores of Hole 884B. Lithologic Unit III (854–941 mbsf) is basalt that occurs as 13 units, 10 of which are massive flows. Much of the basalt has coarse phenocrysts; fresh olivine is found in the lower 50 m of the recovered section.

At Site 884, dropstones occur in lithologic Subunit IA in amounts comparable to those in material of similar age at Site 883, but in lower amounts than at the sites farther south, thus continuing the trend seen in Leg 145 sites of a northward decline in ice-rafted debris. No dropstones older than late Pliocene (the Matuyama/Gauss reversal boundary) occur. Ash layers are common to abundant in sediments younger than 2.6 Ma and occur again in the Eocene portion of the section. Along with the record from Site 883, these Eocene ashes will help to define the period of Eocene volcanism that has been suggested by scattered data from around the Pacific basin.

The Neogene and Quaternary sediments of Site 884 are characterized by moderate fluxes of clay and silica. An increase in the flux of clay from a few tenths of a $g(cm^2 \cdot k.y.)^{-1}$ to about 1 $g(cm^2 \cdot k.y.)^{-1}$ occurs at the time of a possible brief hiatus about 12 Ma (Subunit ID/IC boundary). The Meiji sediment tongue appears to be a North Atlantic type of drift deposit that has been accumulating since the Eocene/Oligocene boundary. It is characterized by both a mineral assemblage and a diatom flora that are derived from the north, relatively high sedimentation rates and few sedimentary structures. These boreal and neritic diatom assemblages occur only in the Meiji Drift site at Detroit Seamount, not in the shallower sites. The flux of opal has remained at about 1.0 to 1.5 $g(cm^2 \cdot k.y.)^{-1}$ for most of the time since 12 Ma and was highest during the latest Miocene and early Pliocene.

A remarkable result at Site 884 is the construction of a continuous magnetic reversal stratigraphy spanning at least the past 12 m.y. Further, a complete sequence of all North Pacific Ocean diatom zones, late Quaternary to late Oligocene, is present at Site 884, although two severely condensed zones occur at 12.0–13.5 and 17.5–20.0 Ma. The reversal stratigraphy will permit direct correlation of North Pacific Ocean siliceous microfossil biostratigraphy with the reversal time scale for the first time in sediments older than 7 Ma and will permit a more precise reconstruction of the sedimentation processes of the North Pacific Ocean drift deposit than would otherwise be possible.

BACKGROUND AND SCIENTIFIC OBJECTIVES

Site 884 (proposed Site DSM-4) is the deepest of a three-site depth transect down the slopes of Detroit Seamount and was the last site to be drilled. We had several primary objectives at this site. One was to obtain a high-resolution record of calcium carbonate, and eventually carbon and oxygen isotopic information, to be able to define the nature

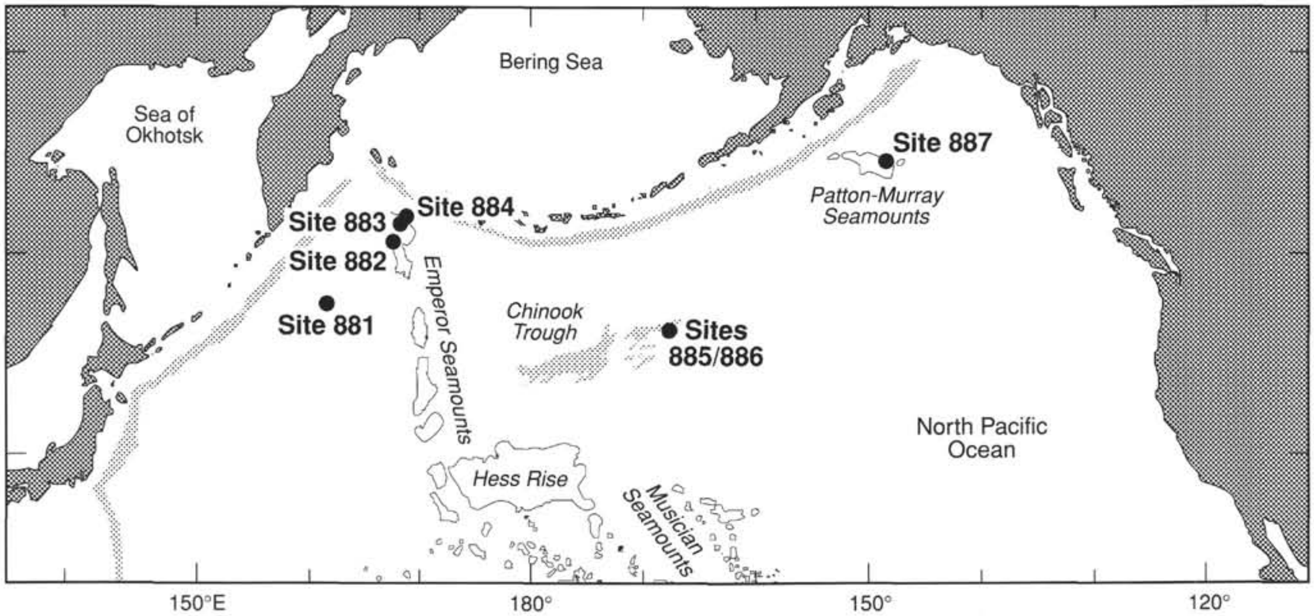

Figure 1. Index map of the North Pacific Ocean showing Leg 145 drill sites.

and variability of North Pacific Ocean deep waters. The carbonate record from Site 884 was to be compared with those from intermediate-depth Site 882 and shallow Site 883 to provide a record of carbonate deposition between 2400 and 3800 m for the northwestern Pacific Ocean. These records then can be compared with records from depth transects in the Atlantic, Indian, and Equatorial Pacific oceans.

A second important objective was to obtain high-resolution middle to late Neogene records of siliceous sedimentation to further our understanding of the timing and amount of the significant silica deposition that began in the North Pacific Ocean in the upper portions of the Miocene. The late Pliocene and Pleistocene history of terrigenous influx, especially ice-rafted debris, and tephrochronology should have been well displayed in the sediments of Site 884. Much of the section should have been of a suitable lithology for the determination of a magnetic reversal stratigraphy.

The unique objective of Site 884 was to define the history of the Meiji Tongue, which may be a drift deposit like those in the North Atlantic Ocean. The Meiji Tongue progrades 2000 km south along the east side of the northern Emperor Seamounts, occasionally spilling over to the west through the deeper passages between the seamounts (Scholl et al., 1977; Damuth et al., 1983; Mammerickx, 1985). The source of the Meiji deposit seems to be the southwestern Bering Sea and Komandordskaya Basin (between the Shirshov Ridge and Kamchatka Peninsula) via a deep passage at the western extreme of the Aleutian Islands between the Komandorskiye Islands and the Kamchatka Peninsula. By analogy with the drift deposits of the North Atlantic Ocean, we anticipated that coring the Meiji Tongue would enable us to document the geologic history of thermohaline circulation in the deep northwestern Pacific Ocean. Before the Leg 145 drilling, this deposit had been sampled only by piston core, so its age, composition, and to a certain degree its thickness, have remained a matter of some speculation and interest.

The lower portion of the section, situated on the lower flanks of Detroit Seamount, may contain Paleogene and Latest Cretaceous carbonates deposited beneath the Northern Hemisphere subtropical gyre. Furthermore, similar settings in the central and South Pacific oceans have been the locus of significant amounts of downslope transport from nearby highs, bringing shallow-water, even reefal debris down to the drill site. Sediments reflecting such a process were expected at Site 884. The timing of the slumping episodes can be compared with that of the presumably erosional unconformities at the shallow Site 883.

To achieve these objectives, three holes were planned. Hole 884A was to be an APC/XCB hole, piston-coring until no longer feasible and then continuing down with XCB-coring. Hole 884B was to be an APC hole to match that portion of Hole 884A with appropriate vertical offsets. After the completion of piston-coring, the bit was to be changed to an RCB assembly. Hole 884C was to be washed down to the depth of the bottom of Hole 884A, where rotary-coring would begin. Rotary-coring was to continue until it was time to start the logging operation. Logging would consist of the standard three-run suite of tools plus two runs for the French magnetometer tools.

OPERATIONS

Transit to Proposed Site DSM-4

The 47-nmi transit to proposed Site DSM-4 began at 0430 hr (local time), 20 August. Seismic gear was deployed throughout the transit. After a beacon was deployed at the proposed site location at 0830 hr, the ship continued the survey until 1030 hr, at which time the seismic gear was retrieved. The ship then returned to the site location, acquired the beacon at 1100 hr, and was positioned on site with thrusters and hydrophones lowered by 1130 hr, 20 August.

Hole 884A

The first piston core was taken at 1745 hr on 20 August at a water depth of 3826.6 mbsl (PDR reading). The core barrel was full with 9.7 m of sediment and therefore could not be used to determine the mud-line depth (see Table 1 for a summary of the coring operations). After Core 145-884A-1H was retrieved, the pipe was pulled above the mud line and the ship was offset to begin a second hole.

Hole 884B

The drill pipe was pulled up 5 m relative to Hole 884A, and the first core from Hole 884B was taken at 1830 hr with 6.47 m of sedimented recovered to establish the mud-line depth at 3836.0 mbrf. Piston coring advanced successfully through Core 145-884B-9H. Core 145-884B-10H (82.596–86.3 mbsf) advanced only 3.8 m and

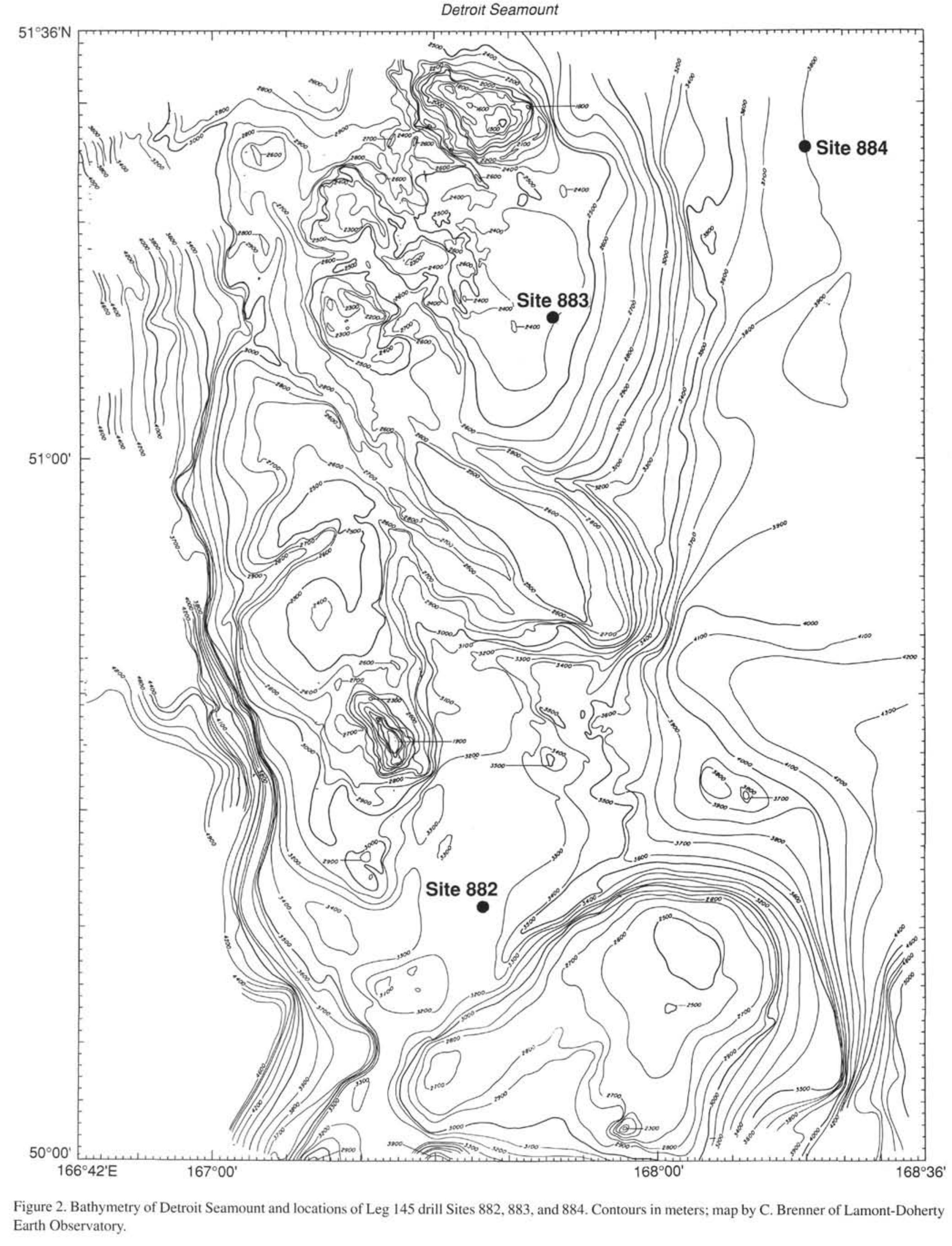

Figure 2. Bathymetry of Detroit Seamount and locations of Leg 145 drill Sites 882, 883, and 884. Contours in meters; map by C. Brenner of Lamont-Doherty Earth Observatory.

Core 145-884B-11H (86.3–87.3 mbsf), the last piston core of this hole, was only able to advance 1 m. APC coring operations ended after Core 145-884B-11H with 87.3 m cored and 89.46 m of sediment recovered (102.5% recovery). Piston cores 145-884B-4H through -11H were oriented.

XCB coring was initiated with Core 145-884B-12X (87.3–93.3 mbsf). Coring advanced routinely to 853.9 mbsf (Core 145-884B-91X). Core 145-884B-91X contained a 40-cm chunk of basalt, confirming that basement had been reached. XCB-coring operations recovered 702.30 m over an interval of 766.6 m (91.6% recovery). The total percentage of recovery from the hole was an impressive 92.7%.

After coring operations ceased, the top drive was set back and the pipe was pulled out of the hole. From 853.9 to 536 mbsf, the hole was sticky, and an overpull of 60,000 lb was required to advance the pipe; above 536 mbsf, resistance disappeared. The bit cleared the mud line at 1100 hr, 24 August, and the vessel was offset 20 m north.

Hole 884C

This hole was spudded at 1130 hr, 24 August, and Core 145-884C-1H contained 2.4 m of sediment, thereby establishing the mud line at 3836.1 mbrf. APC-coring advanced to 78.4 mbsf (Core 145-884C-9H), at which point operations were switched to the XCB-coring system. XCB-coring had advanced to 357.8 mbsf (Core 145-884C-38X) when time expired for this site. Cores 145-884C-4H through -9H were oriented. APC-coring penetrated 78.4 m recovering 74.88 m (95.5%), and XCB-coring recovered 219.68 m over a 279.4-m interval (78.6% recovery). Total recovery was 82.3%.

Hole 884D

After the bit cleared the mud line of Hole 884C at 2000 hr, 25 August, the ship was offset 20 m west, and two cores were taken for high-resolution paleomagnetic studies. A total of 14.8 m of sediment was cored with 13.92 m recovered. At the end of coring operations, the APC/XCB bit and BHA were brought to the drill floor to change to RCB-coring operations.

Hole 884E

An RCB-coring assembly was made up and run to the seafloor. The hole was spudded at 0830 hr, 26 August, and the bit washed ahead to 842.8 mbsf by 0530 hr, 27 August. Wash barrels were retrieved at 300, 600, and 842.8 mbsf. In addition, a wiper trip was made between 842 and 794 mbsf.

RCB-coring began at 0630 hr, 27 August, and the basement-sediment contact was reached with the first core (842.5–852.5 mbsf). Ten RCB cores were taken that penetrated more than 80 m into basement. Coring was terminated at 0300 hr, 29 August, because of time constraints. Overall, 87.0 m of sediment/basement was cored and 66.78 m recovered (76.8% recovery). The rate of penetration (ROP) varied from a low of 1.5 m/hr (Core 145-884E-6R) to a high of 4.5 m/hr (Core 145-884E-1R). The average for the entire cored interval was 2.4 m/hr.

In preparation for logging, a wiper trip was run from total depth (929.8 mbsf) to 111.0 mbsf and back to 912 mbsf, at which point 18 m of hard fill was found. The interval from 912 to 930 mbsf was washed and reamed, followed by a 50-barrel mud sweep.

At 0945 hr, 29 August, the rotary shifting tool was run in the hole with the wireline and released the bit. The top drive then was set back and the pipe was pulled to 82.0 mbsf for logging operations.

Logging in Hole 884E

Five tools were run in Hole 844E: the Schlumberger Quad combination, formation microscanner (FMS), and geochemical tool strings, and the French magnetometer and susceptibility tools. The wireline heave compensator (WHC) was not operational during all logging runs because of electronic failure. A summary of Hole 884E logging operations is shown in Table 2.

Total penetration in Hole 884E was 930 mbsf; however, unstable borehole conditions made logging operations impossible in the lowermost sediment or igneous basement. The first logging run encountered an impenetrable bridge at 760 mbsf, and because of a combination of further bridge formation and sloughing of unconsolidated sediments into the borehole during the course of logging operations, this depth had decreased to 645 mbsf by the final logging run.

The French CEA-LETI/TOTAL/CNRS-ENS magnetometer (NMRT) and susceptibility (SUMT) tools were run first to ensure that both tools would measure a borehole environment unaffected by any electromagnetic induction measurements. Two passes of the NMRT were conducted at 1800 ft/hr over the intervals 760–770 mbsf and 738–770 mbsf, respectively. One main up-going log of the SUMT was recorded at 3600 ft/hr from 682–664 mbsf; a shorter repeat up-going log was recorded from 365–359 mbsf.

The Quad-combo tool (with the new Lamont temperature tool) was run next. During the down-going log run, the sonic tool (SDT) failed at a depth of 614 mbsf, and the tool was pulled out of the hole. After the SDT was replaced, the Quad combo was run back in the hole and set down on a bridge at 693 mbsf. The up-going log was run successfully from 693–652 mbsf.

The fourth logging run consisted of the formation microscanner (FMS) tool string. Three passes were made at 1500 ft/hr over the intervals from 654–52, 654–414, and 428–452 mbsf.

The last logging run consisted of the geochemical tool (GST) with the old Lamont temperature tool. The tool was run from 647 to 652 mbsf at 550 ft/hr. At 310 mbsf, however, the GST calibration failed, and log yields became highly variable.

At 0600 hr, 31 August, the logging equipment was rigged down, and by 0630 hr the pipe was pulled out of the hole. The bit cleared the seafloor at 0645 hr. The drilling equipment was secured by 1230 hr, 31 August, for the transit to proposed Site NW-4A. Concurrent with the pulling of the pipe, both beacons were successfully recalled and on deck by 0900 hr.

LITHOSTRATIGRAPHY

Introduction

Drilling at Site 884 (Figs. 1 and 2) recovered a sedimentary section that is divided into two units, based on sediment lithology and on the presence of structures indicative of reworking and mass movement. The sedimentary section overlies a third lithostratigraphic unit, which is composed of basalt (Figs. 3 and 4). The sedimentary sequence is approximately 850 m thick and ranges in age from Quaternary to early Eocene(?).

Unit I (0–604.8 mbsf) consists mainly of diatoms and clay in varying proportions, which leads to its further division into four subunits. Volcanic ash is present as a minor lithology in Subunits IA and IB (Fig. 3). Except for rare laminations, no primary sedimentary structures are observed in Unit I.

Unit II (604.8–854 mbsf) is composed of a variety of lithologies, including chalk, conglomerate, and claystone; the latter is interpreted as altered ash. The conglomerates are redeposited units consisting of angular clasts of altered ash or claystone dispersed in a matrix of either claystone or chalk. Evidence for both small-scale reworking and significant mass movement is present throughout much of this unit. The boundary between Unit I and Unit II is placed at the first evidence of reworking and visible load structures.

Because approximately 10% of the sedimentary section was not recovered between successive full APC cores, an attempt has been made to quantify the size of these gaps by correlating the GRAPE records between Holes 884B, 884C, and 884D. The coring gaps at these holes average approximately 1.2 m (Table 3; Fig. 5).

Table 1. Summary of coring operations at Site 884.

Core no.	Date (Aug 1992)	Time (UTC)	Depth (mbsf)	Length cored (m)	Length recovered (m)	Recovery (%)
Hole 884A						
1H-	20	0700	0.0–9.7	9.7	9.72	100.0
Coring totals				9.7	9.72	100.0
Hole 884B						
1H-	20	0800	0.0–6.5	6.5	6.47	99.5
2H-	20	0830	6.5–16.0	9.5	9.84	103.0
3H-	20	0915	16.0–25.5	9.5	9.60	101.0
4H-	20	1010	25.5–35.0	9.5	9.83	103.0
5H-	20	1100	35.0–44.5	9.5	9.80	103.0
6H-	20	1140	44.5–54.0	9.5	9.92	104.0
7H-	20	1235	54.0–63.5	9.5	9.75	102.0
8H-	20	1325	63.5–73.0	9.5	9.87	104.0
9H-	20	1415	73.0–82.5	9.5	9.84	103.0
10H-	20	1510	82.5–86.3	3.8	3.48	91.6
11H-	20	1555	86.3–87.3	1.0	1.06	106.0
12X-	20	1700	87.3–83.3	6.0	0.87	14.5
13X-	20	1755	93.3–103.0	9.7	5.21	53.7
14X-	20	1845	103.0–112.6	9.6	9.14	95.2
15X-	20	1940	112.6–122.2	9.6	8.90	92.7
16X-	20	2020	122.2–131.8	9.6	9.54	99.4
17X-	20	2100	131.8–141.5	9.7	9.69	99.9
18X-	20	2230	141.5–151.1	9.6	9.55	99.5
19X-	20	2350	151.1–160.8	9.7	9.65	99.5
20X	21	0040	160.8–170.5	9.7	0.00	0.0
21X	21	0130	170.5–180.1	9.6	9.68	101.0
22X	21	0210	180.1–189.8	9.7	9.53	98.2
23X	21	0250	189.8–199.4	9.6	9.60	100.0
24X	21	0330	199.4–209.1	9.7	9.62	99.2
25X	21	0415	209.1–118.7	9.6	9.69	101.0
26X	21	0500	218.7–228.4	9.7	9.33	96.2
27X	21	0550	228.4–238.0	9.6	9.64	100.0
28X	21	0635	238.0–247.6	9.6	1.29	13.4
29X	21	0715	247.6–257.3	9.7	4.81	49.6
30X	21	0800	257.3–267.0	9.7	9.55	98.4
31X	21	0840	267.0–276.7	9.7	9.81	101.0
32X	21	0920	276.7–286.3	9.6	9.54	99.4
33X	21	1000	286.3–296.0	9.7	7.31	75.3
34X	21	1035	296.0–305.7	9.7	4.06	41.8
35X	21	1130	305.7–315.3	9.6	9.74	101.0
36X	21	1200	315.3–325.0	9.7	9.81	101.0
37X	21	1235	325.0–334.3	9.3	9.63	103.0
38X	21	1330	334.3–343.9	9.6	9.87	103.0
39X	21	1410	343.9–353.6	9.7	9.87	102.0
40X	21	1455	353.6–363.1	9.5	9.79	103.0
41X	21	1550	363.1–372.7	9.6	9.63	100.0
42X	21	1635	372.7–382.4	9.7	9.71	100.0
43X	21	1720	382.4–392.0	9.6	9.60	100.0
44X	21	1815	392.0–401.7	9.7	9.39	96.8
45X	21	1910	401.7–411.3	9.6	9.85	102.0
46X	21	1950	411.3–420.9	9.6	9.20	95.8
47X	21	2030	420.9–430.6	9.7	9.82	101.0
48X	21	2115	430.6–440.2	9.6	8.20	85.4
49X	21	2200	440.2–449.8	9.6	9.85	102.0
50X	21	2250	449.8–459.3	9.5	9.93	104.0
51X	21	2350	459.3–468.9	9.6	9.92	103.0
52X	22	0040	468.9–478.6	9.7	9.86	101.0
53X	22	0130	478.6–488.2	9.6	9.57	99.7
54X	22	0215	488.2–497.8	9.6	9.67	101.0
55X	22	0300	497.8–507.4	9.6	9.80	102.0
56X	22	0340	507.4–517.1	9.7	9.99	103.0
57X	22	0415	517.1–526.7	9.6	9.34	97.3
58X	22	0500	526.7–536.4	9.7	9.89	102.0
59X	22	0550	536.4–546.1	9.7	9.23	95.1
60X	22	0620	546.1–555.6	9.5	9.87	104.0
61X	22	0700	555.6–565.3	9.7	9.51	98.0
62X	22	0740	565.3–574.8	9.5	8.81	92.7
63X	22	0823	574.8–584.4	9.6	9.03	94.0
64X	22	0900	584.4–594.1	9.7	9.96	102.0
65X	22	0945	594.1–603.8	9.7	9.97	103.0
66X	22	1030	603.8–613.3	9.5	8.50	89.5
67X	22	1140	613.3–622.8	9.5	8.54	89.9
68X	22	1240	622.8–632.4	9.6	10.08	105.0
69X	22	1350	632.4–642.0	9.6	9.95	103.0
70X	22	1450	642.0–651.7	9.7	9.69	99.9
71X	22	1545	651.7–661.3	9.6	9.70	101.0
72X	22	1640	661.3–671.0	9.7	9.93	102.0
73X	22	1735	671.0–680.6	9.6	7.02	73.1
74X	22	1845	680.6–690.2	9.6	9.82	102.0
75X	22	1945	690.2–699.8	9.6	9.91	103.0
76X	22	2045	699.8–709.5	9.7	9.99	103.0
77X	22	2145	709.5–719.1	9.6	10.09	105.1
78X	22	2245	719.1–728.8	9.7	8.29	85.4

Table 1 (continued).

Core no.	Date (Aug 1992)	Time (UTC)	Depth (mbsf)	Length cored (m)	Length recovered (m)	Recovery (%)
79X	22	2345	728.8–738.4	9.6	9.04	94.1
80X	23	0040	738.4–748.1	9.7	9.48	97.7
81X	23	0200	748.1–757.7	9.6	6.46	67.3
82X	23	0500	757.7–767.4	9.7	9.86	101.0
83X	23	0645	767.4–777.0	9.6	9.71	101.0
84X	23	0840	777.0–786.7	9.7	9.91	102.0
85X	23	1020	786.7–796.4	9.7	9.72	100.0
86X	23	1200	796.4–806.1	9.7	9.63	99.3
87X	23	1305	806.1–815.6	9.5	8.58	90.3
88X	23	1455	815.6–825.1	9.5	6.05	63.7
89X	23	1650	825.1–834.6	9.5	9.33	98.2
90X	23	1915	834.6–844.3	9.7	4.40	45.3
91X	23	2200	844.3–853.9	9.6	4.23	44.0
Coring totals				853.9	791.69	92.7
Hole 884C						
1H	24	0130	0.0–2.4	2.4	2.40	100.0
2H	24	0205	2.4–11.9	9.5	9.69	102.0
3H	24	0245	11.9–21.4	9.5	8.92	93.9
4H	24	0330	21.4–30.9	9.5	7.98	84.0
5H	24	0420	30.9–40.4	9.5	9.77	103.0
6H	24	0520	40.4–49.9	9.5	9.92	104.0
7H	24	0640	49.9–59.4	9.5	7.87	82.8
8H	24	0730	59.4–68.9	9.5	9.65	101.0
9H	24	0820	68.9–78.4	9.5	8.68	91.3
10X	24	0930	78.4–88.2	9.8	5.24	53.4
11X	24	1025	88.2–97.8	9.6	0.92	9.6
12X	24	1105	97.8–107.4	9.6	5.72	59.6
13X	24	1155	107.4–117.0	9.6	9.15	95.3
14X	24	1235	117.0–126.7	9.7	2.27	23.4
15X	24	1325	126.7–136.3	9.6	9.28	96.6
16X	24	1400	136.3–146.0	9.7	9.47	97.6
17X	24	1435	146.0–155.7	9.7	8.84	91.1
18X	24	1510	155.7–165.3	9.6	9.49	98.8
19X	24	1550	165.3–175.0	9.7	9.66	99.6
20X	24	1625	175.0–184.6	9.6	9.60	100.0
21X	24	1700	184.6–194.3	9.7	9.65	99.5
22X	24	1735	194.3–204.0	9.7	9.65	99.5
23X	24	1830	204.0–213.6	9.6	9.84	102.0
24X	24	1900	213.6–223.3	9.7	9.48	97.7
25X	24	1945	223.3–232.9	9.6	9.79	102.0
26X	24	2030	232.9–242.5	9.6	9.77	102.0
27X	24	2100	242.5–252.2	9.7	9.55	98.4
28X	24	2140	252.2–261.8	9.6	9.93	103.0
29X	24	2215	261.8–271.4	9.6	9.82	102.0
30X	24	2300	271.4–281.1	9.7	0.67	6.9
31X	24	2345	281.1–290.7	9.6	9.57	99.7
32X	25	0020	290.7–300.4	9.7	9.88	102.0
33X	25	0100	300.4–310.1	9.7	0.00	0.0
34X	25	0200	310.1–319.7	9.6	2.14	22.3
35X	25	0300	319.7–329.2	9.5	9.76	103.0
36X	25	0400	329.2–338.7	9.5	9.79	103.0
37X	25	0440	338.7–348.2	9.5	9.73	102.0
38X	25	0520	348.2–357.8	9.6	1.02	10.6
Coring totals				357.8	294.56	82.3
Hole 884D						
1H	25	0750	0.0–5.3	5.3	5.33	100.0
2H	25	0830	5.3–14.8	9.5	8.59	90.4
Coring totals				14.8	13.92	94.1
Hole 884E						
(Washed from 0 to to 842.8 mbsf)						
1R	26	2245	842.8–852.5	9.7	6.08	62.7
2R	27	0310	852.5–862.3	9.8	9.29	92.9
3R	27	0630	862.3–872.1	9.8	9.40	95.9
4R	27	1100	872.1–881.8	9.7	7.63	78.6
5R	27	1640	881.8–891.5	9.7	7.00	72.1
6R	27	2115	891.5–896.1	4.6	4.62	100.0
7R-	28	0045	896.1–901.1	5.0	5.70	114.0
8R	28	0710	901.1–910.7	9.6	0.87	9.1
9R	28	1115	910.7–920.3	9.6	8.30	86.4
10R	28	1535	920.3–929.8	9.5	7.89	83.0
Coring totals				87.0	66.78	76.6
Washed				842.8		
Total				929.8		

Table 2. Summary of logging operations in Hole 884E.

Date (Aug. 1992)	Time (local)	Depth (mbrf)	Comment
29			French magnetometer (NRMT) tool made up, RIH.
30	0345	Surface	Make up Quad tool string with new Lamont temperature tool, RIH.
	0545	3930	Quad out of pipe, begin down-going log at 2500 ft/hr.
	0610	4450	Sonic (SDT) tool failure, POOH.
	0945	Surface	Replace SDT, Quad RIH again
	1050	4529	Quad set down on bridge, begin up-going log at 1800 ft/hr. Pipe raised to 52 mbsf.
	1215	3836	Quad at mud line, end up-going log, POOH.
	1415	Surface	Make up FMS tool string, RIH.
	1645	4490	Begin first up-going log to base of pipe at 1500 ft/hr. Pipe raised to 52 mbsf.
	1740	4490	Begin second up-going log to 4250 mbrf.
	1850	4264	Adjust gains, begin third up-going log to base of pipe.
	1945	3888	FMS at end of pipe, POOH.
	2145	Surface	Make up geochemical tool string with old Lamont temperature tool, RIH.
	2150	50	GST fails to calibrate, continue RIH.
	2338	4483	GST successfully calibrates,, start up-going log at 550 ft/hour.
31	0225	4164	GST calibration fails (RDF>15), BHT ≤7°C. Yield logs become highly variable, continue up-going log. Raise pipe to 52 mbsf.
	0500	3836	End up-going log, POOH.
	0700	Surface	Rig down, end logging operations.

Description of Lithologic Units

Unit I

Intervals: Core 145-884A-1H
Cores 145-884B-1H to -66X
Cores 145-884C-1H to -38X
Cores 145-884D-1H to -2H
Depth: 0–604.8 mbsf
Age: Quaternary to early Miocene

Unit I is composed of clay and claystone, clayey diatom ooze, clayey diatomite and diatomite. Volcanic ash layers and carbonate-rich horizons are present as subordinate lithologies. Dropstones are present in the upper 119 m of the unit.

Evidence of bioturbation is present in the form of burrow fills, burrowed gradational upper surfaces on decimeter-scale volcanic ash horizons, and *Zoophycos* trace fossils below 495 mbsf.

With the exception of the bases of ash layers, boundaries between the different lithologies within Unit I are gradational.

Based on the different proportions of clay to diatoms and on the distribution of ash layers and dropstones, Unit I has been divided into four subunits. Subunit IA (0–128 mbsf) contains predominantly clay and diatom clay; spicule-rich zones form a minor lithology. Vitric ashes are also present. Dropstones are scattered throughout this subunit. Subunit IB (128–440.2 mbsf) is composed of clayey diatom ooze. Volcanic ashes are much less common than in Subunit IA. Subunit IC (440.2–546.1 mbsf) mainly consists of diatom clay with no discrete ash layers present. Subunit ID (546.1–604 mbsf) is composed of diatomite and contains no volcanic ashes. The boundary between Subunits IA and IB is gradational and corresponds to a decrease in grain density and an increase in water content (see "Physical Properties" section, this chapter). The boundary between Subunits IB and IC is set at 440.2 m, at the base of a diatom claystone and diatomite interval. The boundary between Subunits IC and ID is placed at 546.1 mbsf, at the base of a major claystone interval. The positions of these boundaries also are substantiated by XRD data (Figs. 6 and 7).

X-ray diffraction patterns reveal relatively low smectite/quartz and plagioclase/quartz ratios throughout Unit I, suggesting the importance of "continental" sources through eolian and water column transport processes (Fig. 7). A relatively high abundance of the terrigenous component and a relatively low abundance of opal characterize Subunit IA (Fig. 6). Variations in both the terrigenous and the biogenic components show the compositional heterogeneity within this subunit. A distinct change in the relative abundances of the terrigenous and biogenic components separates Subunit IA from Subunit IB. Subunit IB has a relatively high opal content and a relatively low content of terrigenous material, with a large amount of variability in both. The seemingly gradual decrease in the opal/terrigenous component ratio through the subunit is difficult to assess with the data provided. The XRD data for Subunit IC show the well-defined boundaries of this interval and its characteristic increase in the abundance of the terrigenous component and decrease in opal (Fig. 6). Subunit ID is well defined by changes in opal and is characterized by a very high relative opal abundance and a relatively low terrigenous component abundance.

Subunit IA

Intervals: Core 145-884A-1H
Cores 145-884B-1H to -16X
Cores 145-884C-1H to -15X
Cores 145-884D-1H to -2H
Depth: 0–128 mbsf
Age: Quaternary to late Pliocene

Subunit IA contains a variety of sediment types, ranging from clay and diatom clay as major lithologies to diatom ooze with clay as a minor lithology. These lithologies contain abundant spicule-enriched horizons. Dropstones occur at irregular intervals throughout Subunit IA (Fig. 4). Dropstone varieties present in Subunit IA include fine-grained felsic volcanic material, quartzo-feldspathic sandstone, litho-feldspathic sandstone (volcaniclastic), hyaloclastite, and phyllite or semischist.

Fresh vitric ashes constitute a minor lithology in Subunit IA (Fig. 3). Individual ash layers are up to 2.5 m thick (e.g., Interval 884C-6H-4, 8 cm, to -6H-5, 115 cm). Some volcanic ash intervals represent multiple eruptions, as indicated by the presence of a sharp boundary between light- and dark-colored ash (Figs. 8 and 9). Many ash layers have sharp bases and bioturbated upper surfaces. The ashes are more abundant between 40 and 100 mbsf (Fig. 3).

Indurated green and purple layers having thicknesses ranging from 0.5 to 10 cm are common in the upper 80 m of Subunit IA. These color bands, although clearly defined by their colors, appear to be compositionally identical to the adjacent sediment.

Subunit IB

Intervals: Cores 145-884B-17X to -48X
Cores 145-884C-16X to -38X
Depth: 128–440.2 mbsf
Age: late Pliocene to late Miocene

Subunit IB is composed predominantly of clayey diatom ooze and (below 363 mbsf) clayey diatomite. Diatom ooze with clay and clayey diatom mixed sediment are minor variants. Parallel and lenticular laminations in Core 145-884B-43X and Core 145-884B-45X are the only important physical sedimentary structures noted. The relatively few ash layers (compared with Subunit IA) rarely exceed 13 cm in thickness. No ash layers are observed below 344 mbsf. A piece of wood was found in Interval 145-884B-25X-4, 60–64 cm (214.2 mbsf). Carbonate concretions were encountered in Core 145-884B-31X (272 mbsf; Fig. 10) and a dolomite concretion was observed at 172 mbsf in Core 145-884C-19X.

Subunit IC

Intervals: Cores 145-884B-48X to -59X
Depth: 440.2–546.1 mbsf
Age: late Miocene to middle Miocene

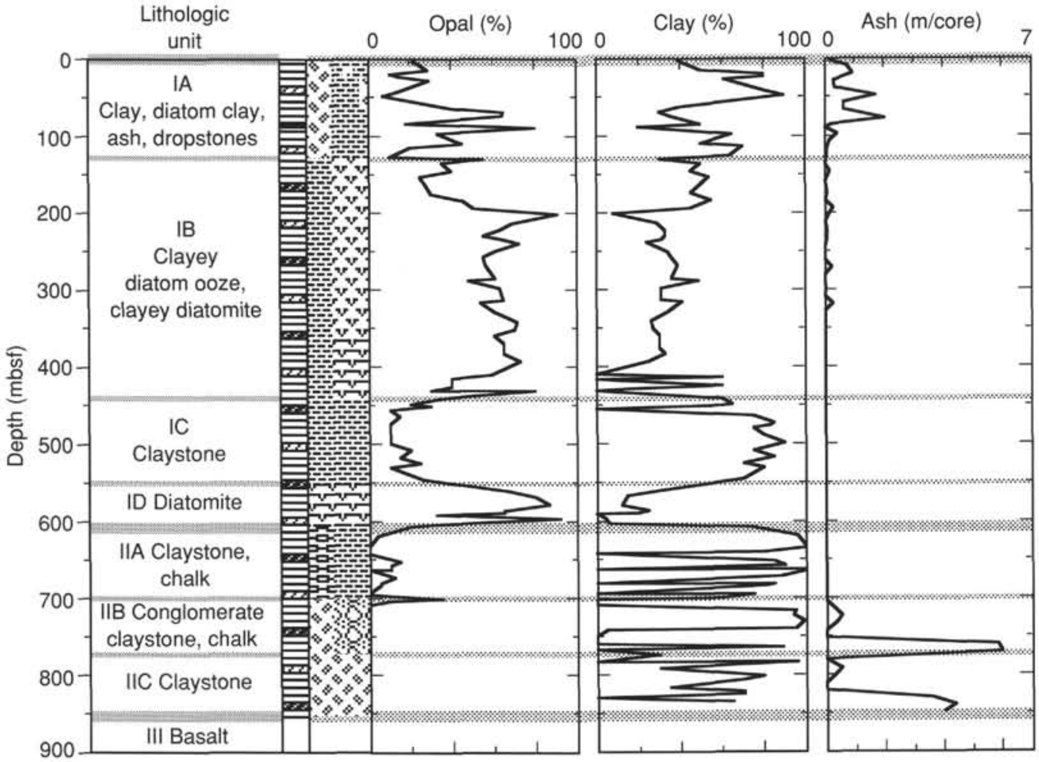

Figure 3. Lithostratigraphic column, with abundances downhole of clay, opal, and ash at Site 884, as determined from smear slides of the dominant lithologies. Lithologic units shown on left.

The main lithology in Subunit IC is dark gray to gray claystone, with greenish gray and reddish black mottles appearing in Cores 145-884B-49X and 145-884B-52X. A sandstone turbidite sequence is present in Core 145-884B-50X at approximately 459.5 mbsf. Metallic copper in the form of bladed and twinned crystals was observed in Sections 145-884B-56X-1 and -4 and 145-884B-57X-2 through -57X-4. *Zoophycos* trace fossils are present downcore from Interval 145-884B-54X-5, 24 cm. No volcanic ash was observed in Subunit IC.

Subunit ID

Intervals: Cores 145-884B-59X to -66X
Depth: 546.1–604.8 mbsf
Age: middle Miocene to early Miocene

Subunit ID consists of diatomite with clay or with spicules as a major lithology, and grades downhole at approximately 590 m (Section 145-884B-64X-4) to diatom chalk and diatomite. *Zoophycos* trace fossils are present in several cores (Fig. 11). No ash layers were observed.

Unit II

Intervals: Cores 145-884B-66X to -91X
Depth: 604.8–854 mbsf
Age: early Miocene to early Eocene(?) late Paleocene(?)

Unit II consists of vitric claystones (some of which are altered vitric ashes), chalks, and conglomerates. The latter are intraformational, being the result of redeposition. A few vitric ashes are also present. The distribution of these sediment types allows the division of Unit II into three subunits.

The upper boundary of Unit II is placed at 604.8 mbsf (Core 145-884B-66X-1) on the basis of the first occurrences of sedimentary structures indicative of scouring and sediment redeposition. Furthermore, micropaleontological data indicate the presence of a hiatus at about this horizon (see "Biostratigraphy" section, this chapter). The contact between Subunits IIA and IIB occurs at 694.7 m (Core 145-884B-75X), at the first appearance of claystone with indication of altered ash.

X-ray diffraction (XRD) data presented in Figure 7 show relatively low opal contents and a declining relative abundance of terrigenous components in Subunit IIA. Both of these components are low in abundance because of the increased abundance of $CaCO_3$ in the sediments. The relative abundance of the terrigenous component remains low in Subunit IIB, but the change in diffractogram background levels increases because of the presence of volcanic ash and slightly altered ash. In Subunit IIC, the change in diffractogram background levels drops, and the relative abundance of terrigenous materials increases slightly because of the importance of clay (including some illite). Low ratios of both smectite and plagioclase (which can be used as an indicator of altered and unaltered volcanic components) relative to quartz (an indicator of silicic "cratonic" components) occur in Subunit IIA (Fig. 6), consistent with the low abun- dances of ash/altered ash observed in the cores during description. Subunits IIB and IIC show increased smectite/quartz and plagioclase/quartz ratios, consistent with the visual description of these more ash-rich units (Fig. 3). The XRD data also may record some grain size dependency, with the maximum plagioclase/quartz ratio in the coarser-grained sediments of Subunit IIB, whereas the maximum smectite/quartz ratio is in Subunit IIC, which is finer grained (clay dominated).

Subunit IIA

Intervals: Cores 145-884B-66X to -75X
Depth: 604.8–694.7 mbsf
Age: early Miocene to late Eocene

Subunit IIA consists predominantly of claystone, with lesser amounts of chalk and nannofossil chalk; the latter two lithologies become more frequent below 662 mbsf. An 85-cm-thick debris flow deposit composed of sand-sized claystone and nannofossil detritus occurs in Sec-

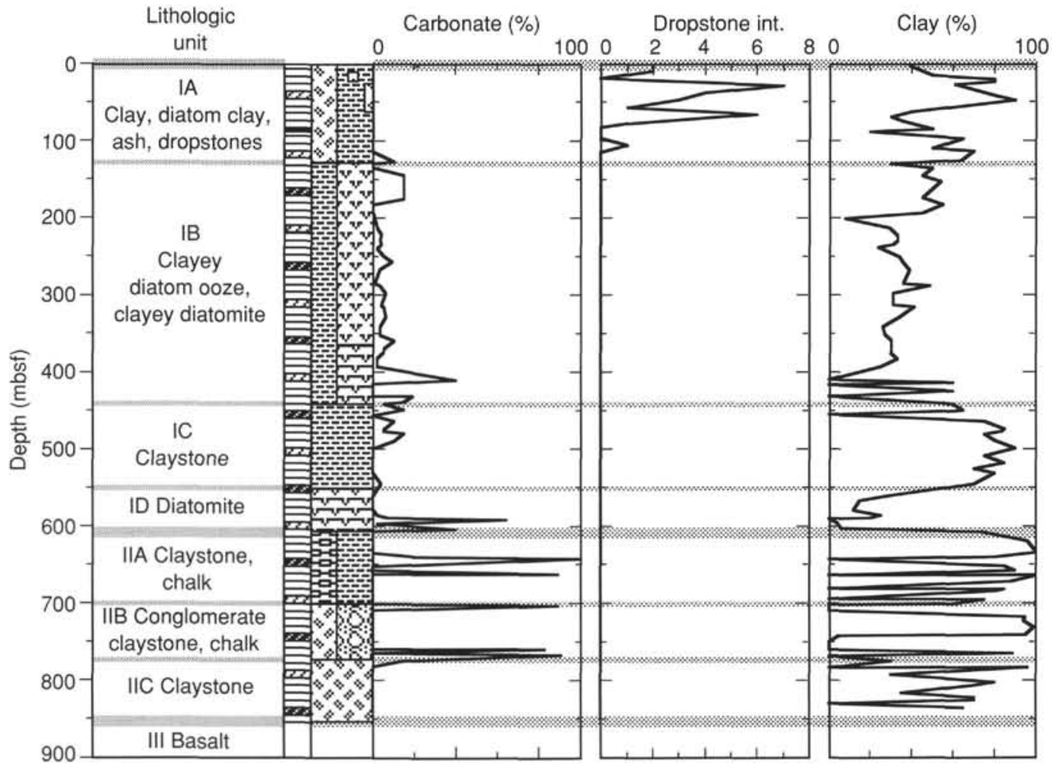

Figure 4. Lithostratigraphic column, with frequency of dropstone intervals and the carbonate and clay abundances, as determined from smear slides of the dominant lithologies downhole at Site 884. Lithologic units shown on left.

Table 3. Recovery gaps between cores as determined from correlation of GRAPE records.

	Between core	and core	Is a gap of (cm)
145-884B-			
	1H	2H	67
	2H	3H	94
	3H	4H	0
	4H	5H	141
	5H	6H	58
	6H	7H	172
	7H	8H	138
	8H	9H	125
145-884C-			
	1H	2H	73
	2H	3H	126
	3H	4H	0
	4H	5H	139
	5H	6H	385
	6H	7H	35
	7H	8H	219
	8H	9H	91
145-884D-			
	1H	2H	162

tion 145-884B-74X-1. Sedimentary structures observed at the top of Subunit IIA (Core 145-884B-66X) include a sandy interval with parallel lamination and micro-loaded base (interval 145-884B-66X-1, 97–101 cm), microfaults (Fig. 12), healed fractures, and several sharp color contacts, interpreted to be surfaces of erosion or nondeposition. At least one of these surfaces may represent an appreciable hiatus (e.g., interval 145-884B-66X-2, 76 cm) (see "Biostratigraphy" section, this chapter). Evidence for reworking and resedimentation includes scour surfaces and thin (<5 cm) turbidite sequences.

Bluish green mottles appear in Core 145-884B-67X and continue in Core 145-884B-68X. Scarce metallic copper grains, seen in Core 145-884B-68X, are found within these bluish green haloes.

Subunit IIB

Intervals: Cores 145-884B-75X to Section 145-884B-83X-3
Depth: 694.7–771 mbsf
Age: late Eocene to early-middle Eocene

Subunit IIB consists of variably colored light to dark chalk, claystone (including altered ash), and minor fresh ash. Diatoms are not found below 710 mbsf. Sedimentary features indicative of soft-sediment deformation and relatively large-scale redeposition are common, and include recumbent folds. At several horizons (e.g., interval 145-884B-81X-1, 90 cm, to -81X-2, 55 cm), slumping has produced diamictic conglomerates composed of plastically deformed, angular, intraformational clasts of claystone, altered ash or chalk dispersed in a matrix composed of either claystone, clayey chalk or chalk. Few intervals within this subunit appear to have remained undisturbed after initial deposition, as indicated by widespread microfaulting and folding (Figs. 13, 14, and 15).

Subunit IIC

Intervals: Section 145-884B-83X-3 to Core 145-884B-91X
Depth: 771–854 mbsf
Age: early–middle Eocene to early Eocene(?) late Paleocene (?)

Subunit IIC consists of claystone, altered clayey ash, and ash. The latter are usually the darker-colored lithologies. Nannofossil chalk occurs throughout Subunit IIC but is a minor lithology. A single vitric ash was noted in Section 145-884B-86X-5. Throughout Subunit IIC, laminated intervals are present to common in abundance, but moderate bioturbation is widespread. The frequent occurrence of sharp contacts between lithologies suggests the presence of scour surfaces and, possibly, diastems. Evidence of redeposition is less widespread in Subunit IIC than it was in Subunit IIB, and diamictic conglomerates

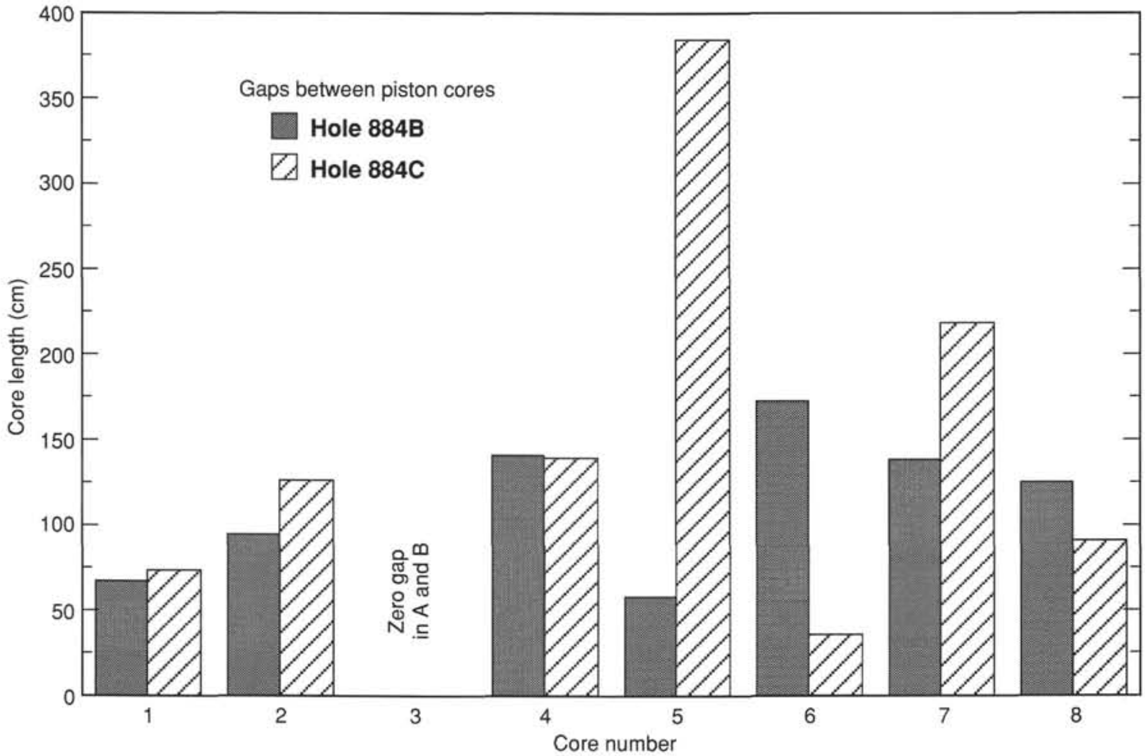

Figure 5. Illustration of recovery gaps between Cores 145-884B-1H to -8H and Cores 145-884C-1H to -8H, as determined from correlation of GRAPE records.

were noted only in Section 145-884B-85X-5 and Core 145-884B-86X. A turbidite interval of silt and fine sand extends from 145-884B-86X-1, 145 cm, to 145-884B-86X-2, 9 cm. Grains of metallic copper occur in Section 145-884B-86X-CC. Small-scale convolute bedding, recumbent folding (Figs. 16 and 17), and microfaulting are distributed throughout Subunit IIC. The trace-element geochemistry of one sample from Subunit IIC was analyzed aboard the ship using X-ray fluorescence (XRF), and those results are presented in Table 4.

Unit III (Basalt)

Unit III is described in detail in the "Igneous Petrology" section of this chapter.

Discussion

The composition of Subunits IIB and IIC, which are Eocene in age, and the redeposition features they display are very similar to those exhibited by Subunit IVB and Unit V at Site 883 (see "Lithostratigraphy" section, Site 883 chapter, this volume), and by Eocene–Campanian sequences described from the Nauru Basin (Moberly and Jenkyns, 1981), the Line Islands (Cook et al., 1976), and Meiji Seamount (Natland, 1973). Moberly and Jenkyns (1981) report metallic copper from the Nauru Basin sequence. Similar occurrence of copper in volcaniclastic sediments is documented at DSDP Site 317 on the Manihiki Plateau (Schlanger, Jackson, et al., 1976).

Two phases of volcanism are clearly indicated by the sediments at Site 884: one of Pleistocene–late Miocene age, the other of Eocene age. The younger phase shows a marked increase in intensity at ca. 2.6 Ma. This is in agreement with the late Pliocene–Pleistocene peak of volcanism identified by Kennett et al. (1977), and also with the data obtained from Sites 881, 882, and 883 (see "Lithostratigraphy" section, "Sites 881, 882, 883" chapters, this volume). The Paleogene ashes at Site 884 are similar in type and stratigraphic position to those recovered at Site 883 (see "Lithostratigraphy" section, "Site 883" chapter, this volume). In marked contrast to the younger pyroclastics, very few fresh vitric ashes occur in the Eocene sequence. Most of the older volcanic material has been altered to clays, and at least some of these volcanics have been redeposited.

The distribution and abundance of dropstones in Subunit IA are similar to those found at Sites 882 and 883. The data from Site 884 yet again substantiate the accepted onset of significant Northern Hemisphere glaciation at ~2.6 Ma, as originally defined by Shackleton et al. (1984) and Rea and Schrader (1985). The dropstone lithologies at Site 884 are more diverse than those at Sites 882 and 883, with the addition of well-sorted quartzose or quartzo-feldspathic sandstones and hyaloclastic source rocks to lithologies represented at Sites 882 and 883.

The onset of the development of the Meiji Drift is not obvious from the lithostratigraphy at Site 884. Subunits IA, IB, and ID are similar to units identified at Sites 882 and 883. A more reliable indicator of the initiation of this enigmatic morphostratigraphic feature may be provided by the first appearance of reworked diatoms in the early Oligiocene, Sample 145-884B-71X-CC (see "Biostratigraphy" section, this chapter).

IGNEOUS PETROLOGY

Two of the holes drilled at Site 884 penetrated basaltic basement. The final core from Hole 884B (Core 145-884B-91X) included approximately 40 cm of moderately altered aphyric basalt (848.2–848.6 mbsf) with a glassy top margin. Coring in Hole 884E penetrated 87 m into basement (842.8–929.8 mbsf) and recovered 66.5 (76% recovery) of basaltic pillows and massive flows.

Cores from Hole 884E were divided into 13 lithologic units based upon changes in crystallinity and the presence of chilled (or occasionally glassy) margins. The three lowest units are highly plagioclase to plagioclase-olivine-phyric pillow basalts with prominent glassy margins. The upper 10 units are massive lava flows that range from 3 to 30 m thick. Three of these 10 units are aphyric basalt, while the other

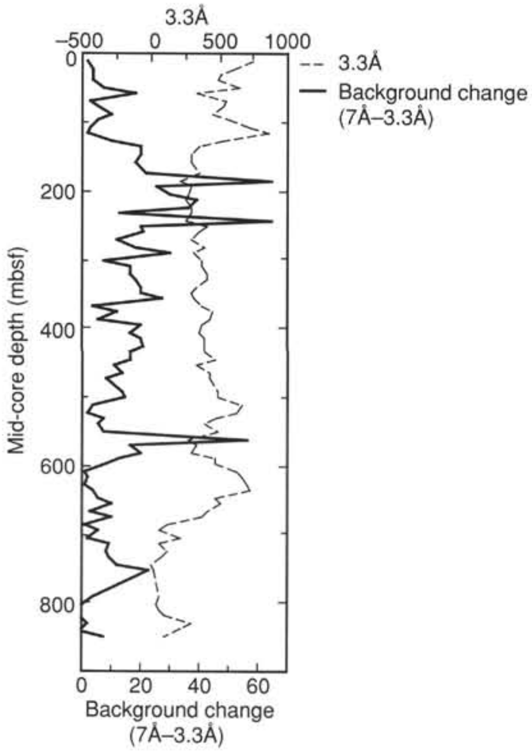

Figure 6. Importance of terrigenous vs. biogenic opal components. 3.3Å peak represents the main quartz and minor illite peaks indicative of a terrigenous (continental or acidic) source. The "background change" is the difference in background values at 7 and 3.3Å, caused by the presence of poorly crystalline SiO_2-rich phases (mostly biogenic opal; some volcanic ash/slightly altered ash in Unit II).

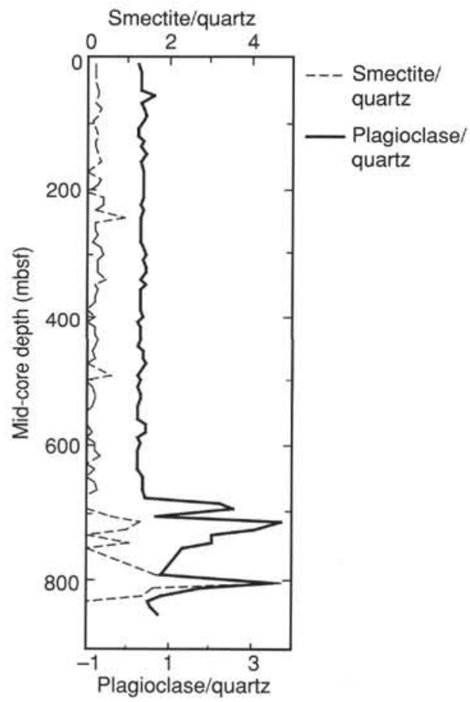

Figure 7. Importance of terrigenous/continental (plagioclase/quartz ratio) vs. volcanic (smectite/quartz ratio) components. "quartz" = 3.3Å quartz + illite peak, represents continental ("acid") components; "plagioclase" = 3.18Å plagioclase peak; "smectite" = 14Å (unglycolated) clay peak, represents altered and unaltered "volcanic" components.

seven are moderately to highly plagioclase phyric to megaphyric basalt. In all of the porphyritic units, plagioclase phenocrysts of up to 25 mm in diameter occur in microcrystalline groundmass (Fig. 18). Olivine phenocrysts never make up more than 1% of the rock, but become more common and less altered with depth. Olivine microphenocrysts are ubiquitous, but have been completely altered to iddingsite. The groundmass of the porphyritic rocks often contains large (<6 mm) clinopyroxene crystals enclosing plagioclase lathes (ophitic texture). Narrow (<5 mm) fractures are fairly common and have been filled in with calcite or calcite with nontronite and/or saponite (XRD analysis). Native copper was reported in one fracture. Vesicles also have often been filled in with clay.

Thirteen samples from Site 884 were analyzed for trace-element concentrations by XRF (Table 5). Data for elements that are present in low concentrations (i.e., Nb) or are susceptible to alteration of olivine (i.e., Ni) and groundmass (i.e., Rb) should be interpreted with extra caution.

Concentrations of the incompatible elements TiO_2, V, Y, and Nb increase linearly with increasing Zr, which suggests that all of the Site 884 basalts are related by fractional crystallization.

Concentrations of most of the incompatible elements are lower than expected for ocean island basalts. Incompatible element concentrations are also significantly lower in the Site 884 basalts than in the Site 883 basalts. This suggests that the Site 884 basalts are either (1) less evolved, (2) from a higher degree of partial melting, (3) from a more depleted source, or (4) some combination of these. The slightly higher Cr concentrations in the Site 884 basalts suggest that they are less evolved than the Site 883 basalts, but this alone cannot account for the low incompatible element concentrations. Zr/Nb and Zr/TiO_2 ratios are similar for the two sites, but Zr/Y ratios are distinctly different (3.8–4.4 for Site 883 and 2.2–2.7 for Site 884). The lower Zr/Y ratios of the Site 884 basalts indicate either a higher degree of partial melting, or a chemically different source. More geochemical data will be necessary to distinguish between these two possibilities.

BIOSTRATIGRAPHY

Drilling at Site 884 recovered an 850 m sequence of upper Paleocene? through Pleistocene sediments. The Neogene–Pleistocene is represented by a 640-m-thick section of diatomites, claystone, and clayey diatom ooze. Calcareous microfossil abundance is highly variable throughout this interval. A limited nannofossil zonation was possible for the Quaternary section. Diatoms are abundant and well-preserved throughout the Miocene to Pleistocene section. Radiolarians are abundant only in the middle Miocene and in three isolated samples from the upper Miocene, upper Pliocene, and lower Pleistocene sequences. Age estimates for the Neogene/Pleistocene sequence have been based primarily on radiolarian and diatom zonations (Fig. 19). Diatom biostratigraphy revealed three hiatuses or condensed sections in the Miocene sequence: one in the lower Miocene (ca. 18.4–19.5 Ma), one in the middle Miocene (ca. 12.0–13.5 Ma), and one in the upper Miocene (ca. 8.9–9.4 Ma).

Preliminary calcareous nannofossil stratigraphy suggests an apparently complete section of upper Paleocene(?) to Oligocene sediments was recovered from Hole 884B (Cores 145-884B-70X to -91X, 640–850 mbsf). Abundances of siliceous microfossils range from rare to barren below Core 145-884B-73X. Age estimates for the Paleogene have been based on calcareous nannofossil zonations (Fig. 20).

Benthic Foraminifers

Of the 111 samples examined, 34 contain benthic foraminifers. The most common occurrences are in upper Pliocene to Pleistocene, upper Miocene, and Eocene-Oligocene sediments (Samples 145-

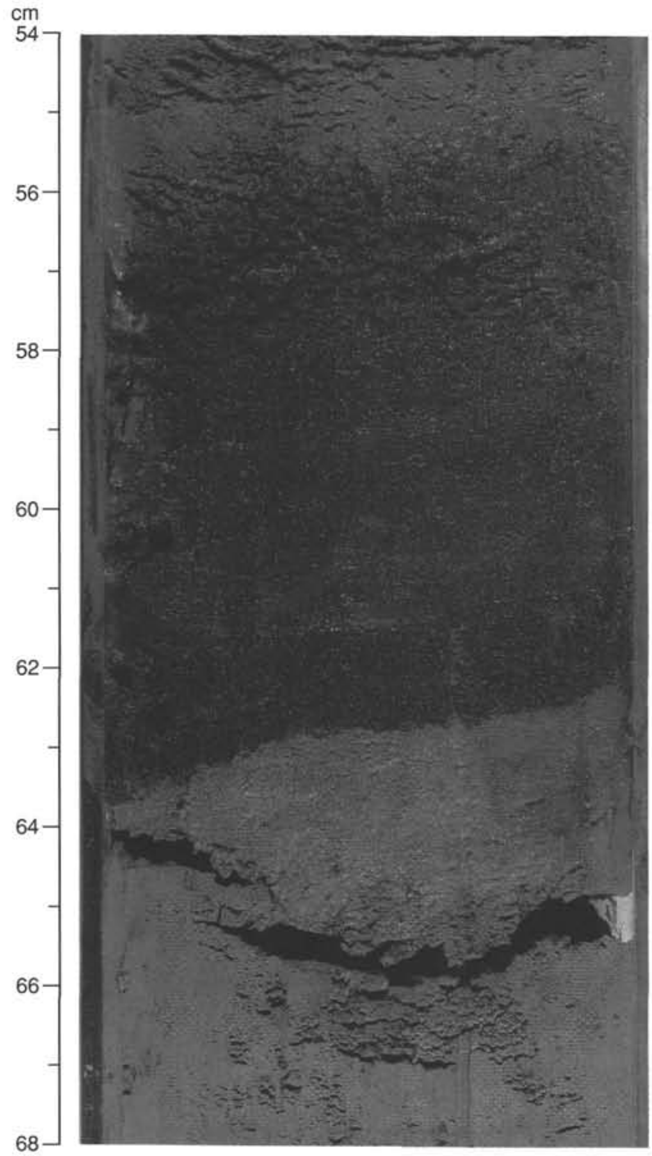

Figure 8. Subunit IA; dark-colored ash layer directly overlying a lighter-colored ash layer (interval 145-884C-9H-2, 54–68 cm).

884C-4H-CC to -21X-CC; Samples 145-884B-30X-CC to -47X-CC; Samples 145-884C-28X-CC to -37X-CC; Samples 145-884B-69X to 145-884B-76X-CC).

Pliocene–Pleistocene

Pliocene-Pleistocene sediments were recovered in Cores 145-884B-1H through -31X and 145-884C-1H through -30X. These samples contain rare-to-common occurrences of a low-diversity calcareous and agglutinated fauna. Dominant species include *Epistominella exigua, Martinottiella communis, Melonis barleeanum, Melonis pompilioides, Oridorsalis umbonatus, Pullenia bulloides, Uvigerina proboscidea,* and *Uvigerina senticosa.* Other common species include *Eggerella bradyi, Nuttallides umbonifera, Planulina rugosa, Planulina wuellerstorfi,* and *Pyrgo murrhina.*

Miocene

Foraminifers are present in upper and lower Miocene sediments (Samples 145-884B-30X-CC to -47X-CC; -64X-CC, -65X-CC, and

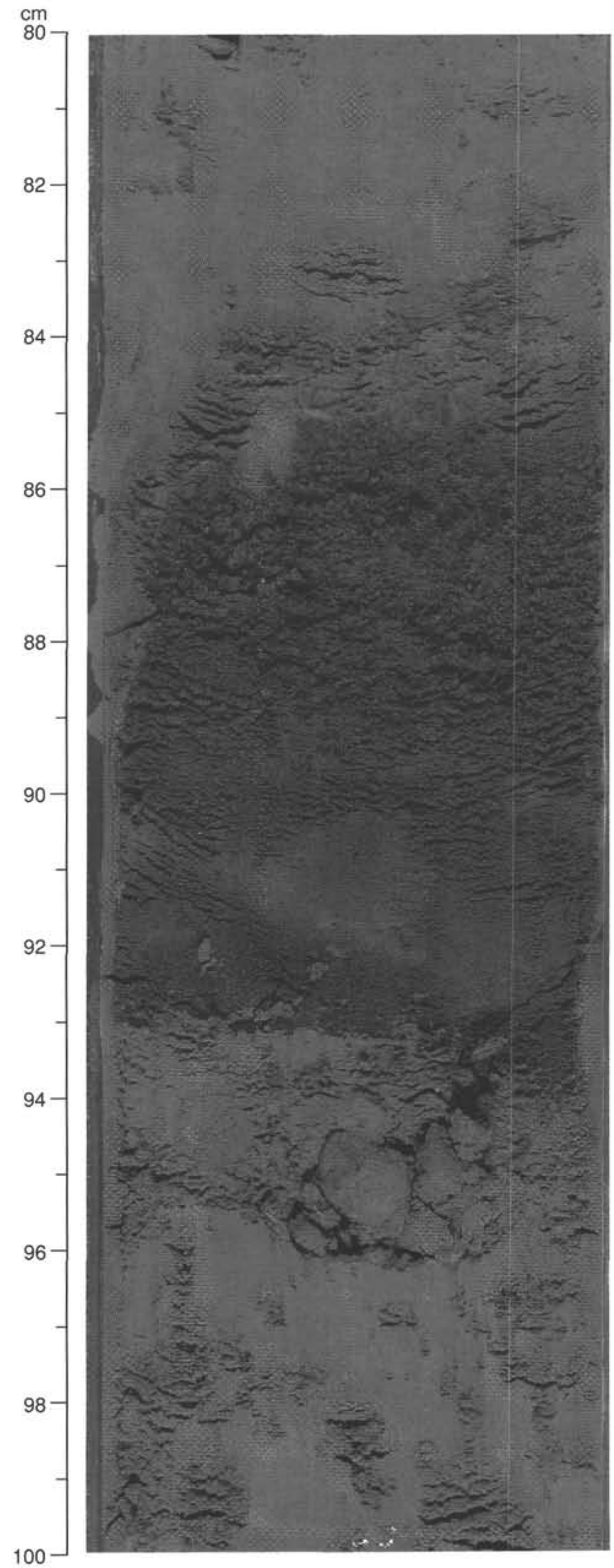

Figure 9. Subunit IA; dark-colored vitric ash layer directly overlying a lighter-colored vitric ash layer. Both ash layers have sharp lower contacts, and the dark one has a (slightly) bioturbated upper contact. Several lone dropstones up to 1 cm in diameter are present at the bottom of the light ash layer (interval 145-884B-8H-5, 80–100 cm).

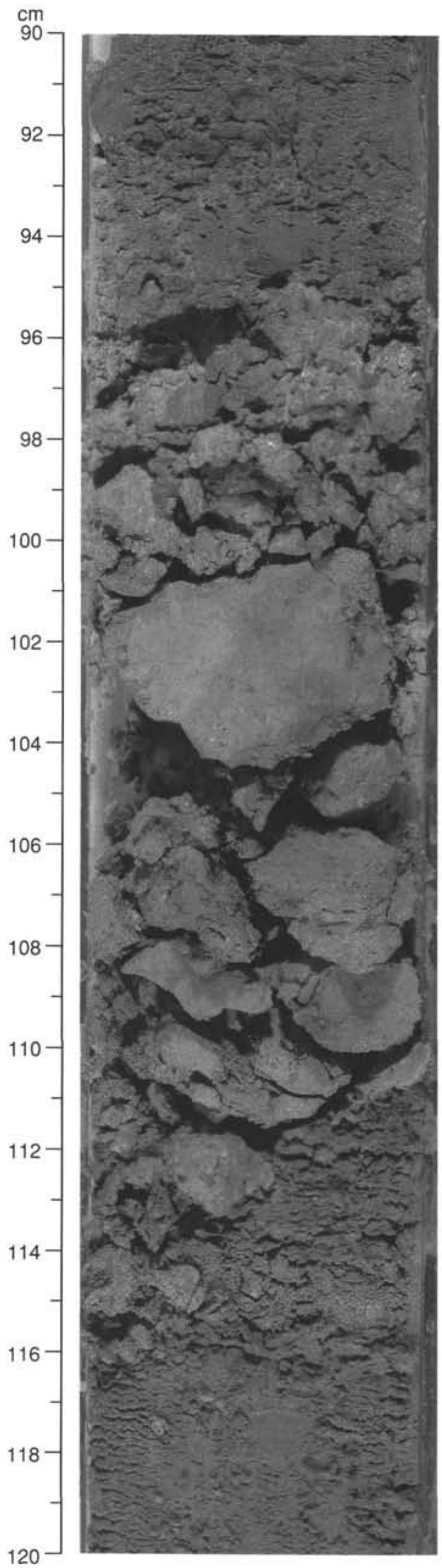

Figure 10. Subunit IB; interval of diagenetic microcrystalline calcite within clayey diatom ooze (interval 145-884C-31X-5, 90–120 cm).

-66X-1, 100–102 cm; Samples 145-884C-28X-CC to -37X-CC). These samples contain a sparse fauna dominated by *Gyroidinoides* spp., *Martinottiella communis, Oridorsalis umbonatus, Pullenia bulloides,* and *Pyrgo murrhina.* In addition, rare occurrences of *Cibicidoides bradyi, C. mundulus, C. robertsonianus* and *Laticarinina pauperata* also are observed.

Evidence of downslope transport is found in one sample from Core 145-884B-66X (Sample 145-884B-66X-1, 100-102 cm), taken from a sandy, laminated interval. This sample contains species not found elsewhere in the Miocene section and its assemblage is dominated by the Paleogene middle-bathyal species *Bolivina tectiformis.*

Eocene–Oligocene

Three samples of Oligocene age (145-884B-69X-CC, -71X-CC, and -73X-CC) contain rare, poorly preserved specimens of *Nuttallides umbonifera* and *Oridorsalis* spp.

Eocene foraminifers are present in three samples (145-884B-75X-CC, -76X-CC, and -82X-CC). Preservation is moderate to poor, with evidence of recrystallization. Assemblages are dominated by *Globocassidulina subglobosa, Nuttallides truempyi, Cibicidoides praemundulus, C. grimsdalei,* and *Oridorsalis umbonatus.* Additional taxa include *Anomalinoides semicribratus, Anomalinoides praeacuta,* and *Bulimina trinitatensis.*

Paleoenvironment

The benthic foraminiferal faunas of Site 884 indicate a lower-bathyal to abyssal paleodepth (>1000 mbsl), based on Tjalsma and Lohmann (1983) and van Morkhoven et al. (1986). A Miocene section deepening from lower bathyal to abyssal depths is supported by the gradual increase in abundance of *Melonis pompilioides, Pyrgo murrhina,* and *Uvigerina senticosa.*

Evidence of downslope transport is found in one sample from the lower Miocene of Site 884 (Sample 145-884B-66X-1, 100–102 cm), which contains a middle bathyal (600–1000 mbsl) fauna.

Calcareous Nannofossils

Calcareous nannofossil assemblages were examined in all core-catcher samples recovered from Site 884. Additional samples from selected intervals also were examined for calcareous nannofossils. Abundances range from barren to abundant, with generally moderate preservation. A limited zonation was possible for the recovered Pleistocene and the Eocene–Oligocene sequences, whereas the Miocene–Pliocene sequence was mostly barren of nannofossils.

Pleistocene

At Site 884, Pleistocene sediments were recovered through Section 145-884B-12X-CC and 145-884C-12X-CC (Fig. 19). Despite low species diversity and the scattered occurrence, one zonal boundary could be recognized within the Pleistocene sequence. The last occurrence (LO) of *Pseudoemiliania lacunosa* (0.49 Ma) can be observed between Samples 145-884B-6H-CC and -9H-1, 80 cm (54.0–73.8 mbsf), and between 145-884C-4H-CC and -5H-CC (30.9–40.4 mbsf), respectively, marking the top of Zone NN19. One additional nannofossil event, the first occurrence (FO) of *Gephyrocapsa oceanica* s.l. (1.67 Ma), can be observed in Hole 884C between Samples 145-884C-9H-CC and -14X-CC (78.4–126.7 mbsf). Because of the total absence of discoasters, the base of Zone NN19 could not be recognized at this site.

Miocene–Pliocene

The Miocene-Pliocene sequence recovered at Site 884 is mostly barren of calcareous nannofossils. The assemblages observed are dominated by species of the genus *Reticulofenestra.* Only one Plio-

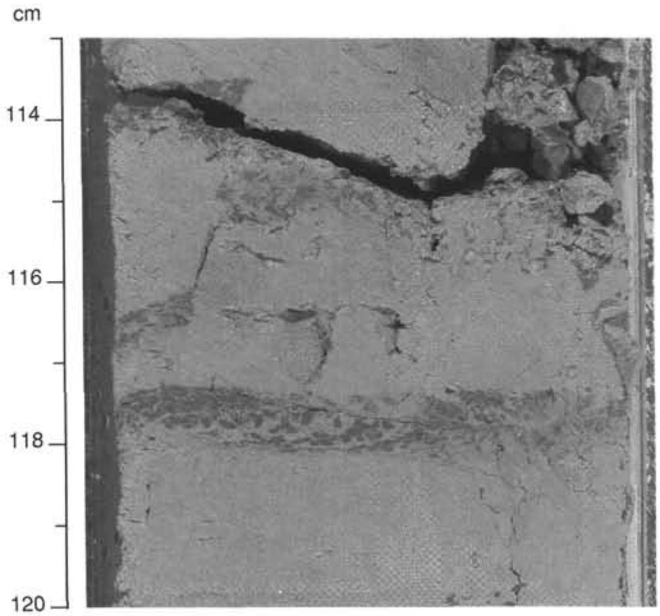

Figure 11. Subunit ID; Horizontal *Zoophycos* burrows in light gray diatom chalk (interval 145-884B-64X-4, 113–120 cm).

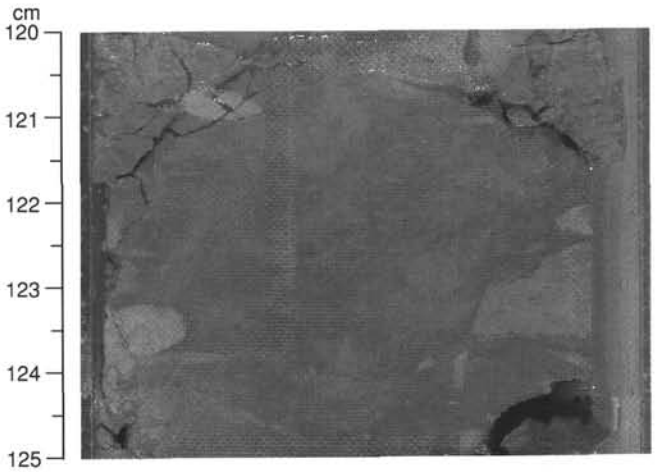

Figure 12. Subunit IIA. Moderately burrowed ashy claystone and chalk with clay. Note microfault in right of center at 124 cm. Several *Zoophycos* burrows traverse the core (interval 145-884B-66X-2, 120–125 cm).

cene calcareous nannofossil event, the LO of *Reticulofenestra pseudoumbilica* (3.71 Ma), can be observed, marking the top of Zone NN15 between Samples 145-884B-19X-CC and -21X-3, 90 cm, and between Samples 145-884C-18X-CC and -19X-CC, respectively, at approximately 167 mbsf (Fig. 19). In the Miocene sequence, calcareous nannofossils are scarce to abundant. The assemblages are dominated by *Reticulofenestra* species with rare *Coccolithus pelagicus*.

Eocene–Oligocene

The Eocene–Oligocene sediments recovered at Site 884 are rich in calcareous nannofossils. Using the LO of *Reticulofenestra bisecta* (top of Zone NP25, 23.81 Ma) as an approximation for the Oligocene/Miocene boundary, the boundary can be placed between Samples 145-884B-69X-CC and -70X-1, 48 cm, at approximately 640 mbsf (Fig. 20).

The LO of *Reticulofenestra umbilica* (14 mm)(31.72 Ma), which marks the top of Zone NP22 of the Oligocene, can be observed between Samples 145-884B-70X-CC and -71X-CC (651.7–661.3 mbsf). The top of Zone NP21, marked by the LO of *Ericsonia formosa* (32.70 Ma), can be seen between Samples 145-884B-73X-CC and -74X-1, 50 cm (~680 mbsf). The latter sample contains rare, probably reworked specimens of *Nannotetrina fulgens* (LO in Zone NP15). The absence of sphenoliths made further subdivision of the Oligocene sequence impossible.

Stratigraphically, the Oligocene/Eocene transition falls between the LO of *E. formosa* and the LO of *Discoaster saipanensis* (top of Zone NP20). In Hole 884B, the latter event can be observed between Samples 145-884B-74X-CC and -75X-2, 132 cm. Therefore, the Oligocene/Eocene transition may be placed between 680.6 and 693.0 mbsf (Fig. 20).

The Eocene calcareous nannofossil assemblages observed at Site 884 show several indications of sediment mixing (see also "Lithostratigraphy" section, this chapter). One sample (Sample 145-884B-81X-CC) contains white nannofossil-bearing clasts of middle Eocene age in a light brown matrix that had a late Eocene age. Another sample (Sample 145-884B-85X-CC), contains both Eocene *Discoaster kuepperi* (NP12-mid NP14) and Paleocene *Discoaster mohleri* (NP7-NP9). *Discoaster multiradiatus* (NP9-NP11) can be observed in only one sample (Sample 145-884B-87X-CC). These observations suggest that sediment mixing took place through the Eocene, making it difficult, at this stage, to establish a zonation for this sequence at Site 884.

In addition to the LO of *D. saipanensis,* the FO of *Isthmolithus recurvus* has been tentatively placed between Samples 145-884B-81X-CC and -82X-CC, marking the top of Zone NP18 of the upper Eocene section (Fig. 19). The last sample holding calcareous nannofossils is Sample 145-884B-87X-CC, which contains specimens of *D. multiradiatus, E. formosa, Reticulofenestra reticulata,* and *Cyclicargolithus floridanus,* again indicating remixing of sediments. Samples 145-884-88X-CC through -91X-CC are barren of calcareous nannofossils. However, the observation of a probably reworked specimen of *D. mohleri* in Sample 145-884B-85X-CC suggests that upper Paleocene sediments may be present at Site 884, although they may not be identifiable at this stage.

Radiolarians

Sediments from core-catcher samples at Site 884 that contain radiolarians ranging in age from late Oligocene/early Miocene through Quaternary. Radiolarian concentrations decrease markedly below the middle part of the Pleistocene, similar to results from Sites 882 and 883. Abundant radiolarians occur in only three isolated samples (in the lower part of the Pleistocene, upper Pliocene, upper Miocene) and a 40-m-long middle Miocene interval. The presence of high concentrations of diatoms within the upper Miocene through the upper Pliocene section may account for these low radiolarian abundances. Pre-Miocene sediments recovered at the site do not contain radiolarians, except for a few samples that may be of early Oligocene age.

Preservation of radiolarians varies from good to poor throughout the sediments, with most middle Pleistocene and younger sediments moderately well to well preserved. Preservation decreases below this level, with an increasing number of poorly preserved samples being encountered with increasing age. The combination of low abundances and only moderately good to poor preservation of radiolarians throughout much of the Miocene and Pliocene sequence make it difficult to determine zonal boundaries for this site. When abundant radiolarians are encountered, a faunal assemblage is present that is usually characteristic of a specific zone. Samples having less than abundant concentrations of radiolarians, however, contain only a few, and in some instances, none of the diagnostic zonal species.

The entire sediment interval from Holes 884A (Core 145-884A-1H) and 884D (Cores 145-884D-1H and -2H) as well as the first two cores from Holes 884B and three cores from Hole 884C contain a

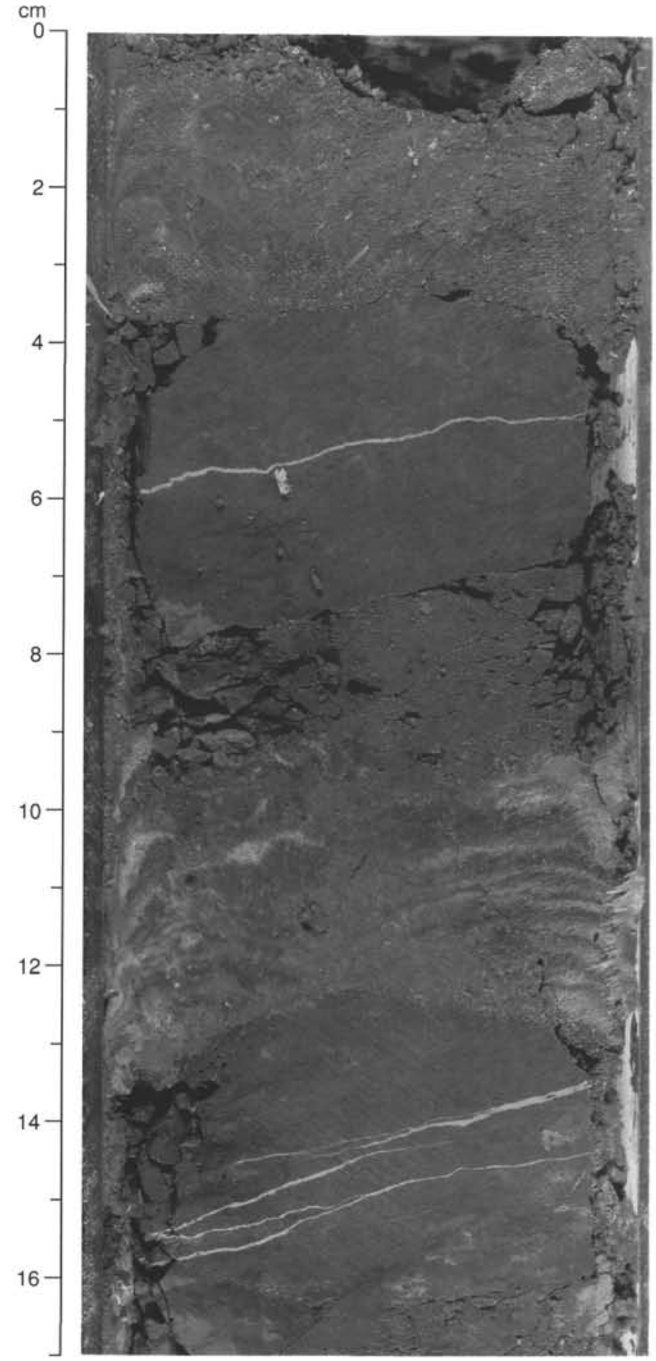

Figure 13. Subunit IIB; fractures filled in by calcite within well-biscuited (by drilling), dark claystone (interval 145-884B-76X-5, 0–17 cm).

moderately well to well preserved faunal assemblage characteristic of the late Quaternary *Botryostrobus aquilonaris* Zone (Hays, 1970). Radiolarians range from abundant to rare in these samples. Although *Lychnocanium grande* is present in the uppermost core-catcher samples from Holes 884A, 884B, and 884D (Samples 145-884A-1H-CC, -884B-1H-CC, -884D-1H-CC), it is not found in Sample 145-884C-1H-CC in Hole 884C, indicating that the sediments from the uppermost 2.4 m of this core are younger than 0.05 Ma. The presence of *Druppatractus acquilonius*, combined with the absence of *Stylatractus universus* in Sample 145-884C-3H-CC, narrows the age range on this sample to between 0.35 and 0.45 Ma (Morley et al., 1982; Hays and Shackleton, 1976; Morley and Shackleton, 1978).

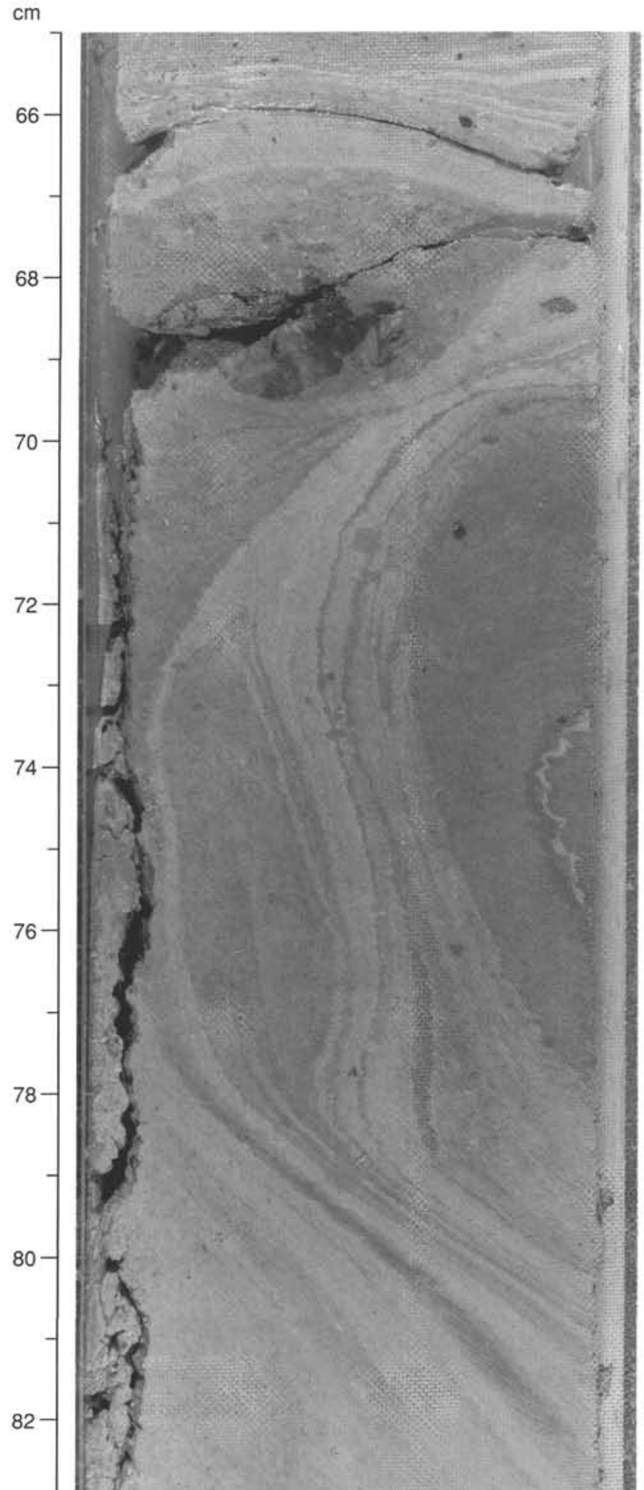

Figure 14. Nose of overturned fold in sediments of Subunit IIB. Note dispersed dark fragments of altered ash, suggesting redeposition before the deformation (interval 145-884B-83X-3, 65–84 cm).

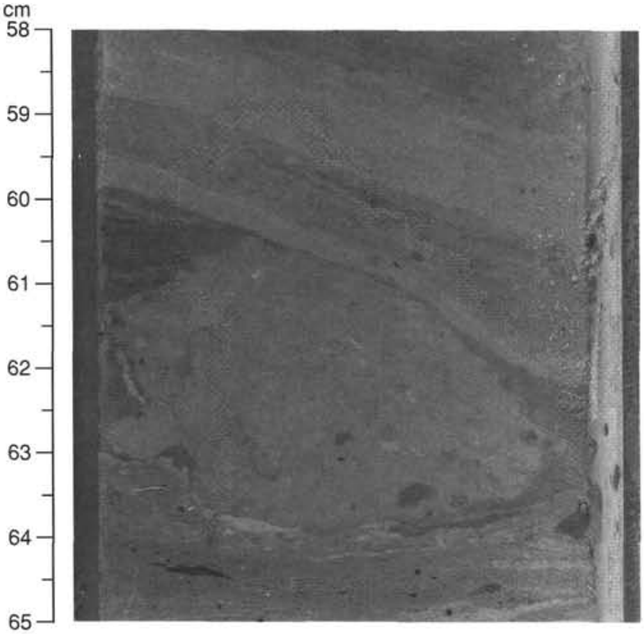

Figure 15. Subunit IIB; intraclast of ashy claystone surrounded by matrix of deformed laminated ashy claystone. Note widespread occurrence of dispersed clasts of dark ash throughout interval, indicative of redeposition (interval 145-884B-83X-3, 58–65 cm).

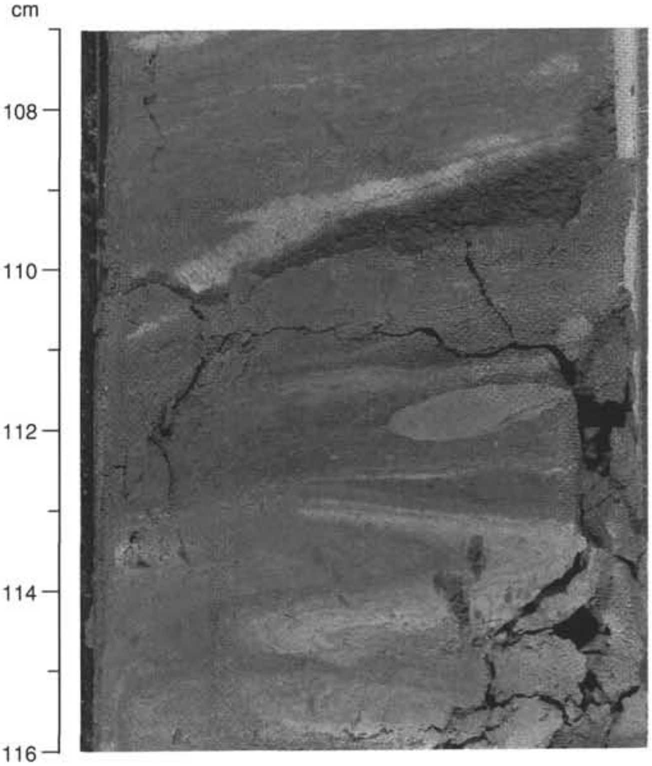

Figure 16. Subunit IIC; recumbent folding within laminated claystone, chalk, and clayey ash. Note the microfault that cuts the lower limb of the fold, and the slightly inclined scour surface that truncates the top of the folded laminae. Uppermost 7 cm exhibit lenticular lamination and possible cross laminations, and have experienced minor deformation (interval 145-884B-84X-5, 107–116 cm).

The sediment interval between Samples 145-884B-3H-CC and -6H-CC in Hole 884B and Samples 145-884C-4H-CC and -7H-CC in Hole 884C has been assigned to the late Quaternary *S. universus* Zone (Hays, 1970), based on the presence of *S. universus, L. grande,* and *D. acquilonius* and the absence of *Eucyrtidium matuyamai.* Radiolarians are abundant in the two core-catcher samples from the uppermost portion of the interval in Hole 884B, but are rare in all other sediments representative of this radiolarian zone in both Holes 884B and 884C. The siliceous fauna is moderately well to well preserved in most samples.

The boundary between the *S. universus* and the *E. matuyamai* (Hays, 1970; Foreman, 1975) zones occurs between Samples 145-884B-6H-CC and -7H-CC in Hole 884B and between Samples 145-884C-7H-CC and -8H-CC in Hole 884C. Except for a single core-catcher sample containing common radiolarians from the middle of the *E. matuyamai* Zone in Hole 884C, radiolarian concentrations are rare, and preservation becomes poorer with increasing age. The base of this zone is marked by the FO of *E. matuyamai,* which coincides with the Olduvai Subchron. This datum level registers in sediments that also contain the Olduvai Subchron in Hole 884B (between Samples 145-884B-11H-CC and -12X-CC). Because of the poor preservation and low abundance of radiolarians, however, this level occurs several meters above the Olduvai in Hole 884C (between Samples 145-884C-9H-CC and -10X-CC).

Directly below the LO of *E. matuyamai* in Hole 884B, abundances of radiolarians increase from common to abundant in two samples before decreasing to rare for the entire remainder of the Pliocene sequence. The occurrence of rare *Stichocorys peregrina* specimens in a single sample (145-884B-23X-CC) permits tentative placement of the boundary between the Pliocene *Lamprocyrtis heteroporos* (Hays, 1970; Foreman, 1975) and *S. langii* (Foreman, 1975) zones (between Samples 145-884B-22X-CC and -23X-CC). Although *L. heteroporos* occurs in samples above and below this interval, this species is not present in the core-catcher samples examined within its named zone (Samples 145-884B-12X-CC through -22X-CC). Therefore, the tentative zonal designation for this interval is based on the absence of both *E. matuyamai* and *S. peregrina* in all samples (with the FO *E. matuyamai* and the LO of *S. peregrina* marking the top and bottom of this zone, respectively) and the presence of *S. langii, Sphaeropyle robusta, D. acquilonius,* and *S. universus* in many of the samples. The recorded LO of *Cycladophora davisiana* var. *davisiana* (with an estimated age of ~3.0 Ma), between Samples 145-884B-15X-CC and -16X-CC provides additional evidence for placement of this radiolarian-bearing sequence within the *L. heteroporos* Zone. It is not possible to identify the boundary between the *L. heteroporos* and *S. langii* zones in Hole 884C because of our inability to locate the LO of *S. peregrina* in comparably-aged sediments. However, the LO of *C. davisiana* var. *davisiana* falls in these sediments between Samples 145-884C-15X-CC and -16X-CC. Radiolarian concentrations in Hole 884C are similar to those in samples found from this interval in Hole 884B.

The boundary between the *S. langii* (Foreman, 1975) and *S. peregrina* (Riedel and Sanfilippo, 1970, 1978) zones apparently is recorded in Hole 884B between Samples 145-884B-31X-CC and -32X-CC. *L. heteroporos* and *S. langii* are present in several of the samples directly above this level and are absent in samples below it. Besides *S. langii,* most samples also include *S. robusta, D. acquilonius,* and *S. universus. L. heteroporos* and *S. peregrina,* however, occur in only a few samples from this interval. The FO of *L. heteroporos* (between Samples 145-884C-30X-CC and -31X-CC) has been used to place tentatively the boundary between these two zones in Hole 884C. Radiolarians are rare in sediments below this boundary, throughout the upper Miocene interval in both Holes 884B and 884C, and preservation is poor in many of the samples. Based on the presence of *S. peregrina* in Samples 145-884C-36X-CC and -37X-CC, along with *D. acquilonius, T. redondoensis, Phormostichoartus fistula,* and *Botryostrobus bramlettei* in most of the remaining sam-

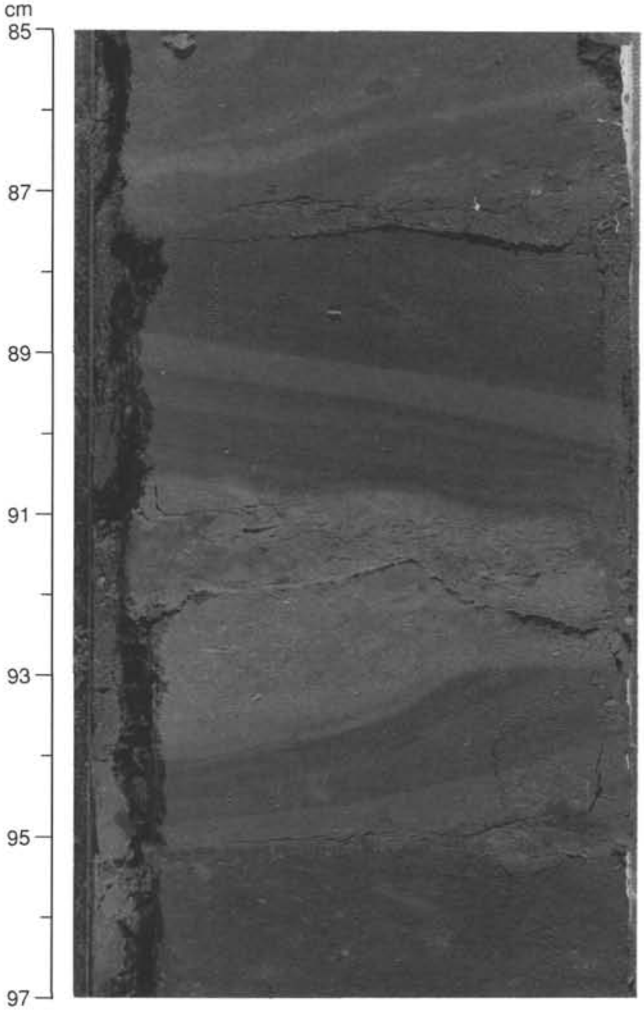

Figure 17. Subunit IIC. Recumbent fold in altered ash and ashy claystone (interval 145-884B-89X-2, 85–97 cm).

ples and the absence of *S. langii* and *L. heteroporos* in all the remaining samples (Samples 145-884C-31X-CC through -38X-CC) from Hole 884C, the radiolarian fauna in this sequence is assigned to the *S. peregrina* Zone. The first common occurrence of *S. peregrina*, marking the base of the *S. peregrina* Zone, is recorded in Hole 884B (between Samples 145-884B-39X-CC and -40X-CC). The FO of *D. acquilonius* registers in sediments between Samples 145-884B-40X-CC and -41X-CC. The close proximity of the FOs of these two species also is found in sediments from Site 883.

With the exception of core-catcher Sample 145-884B-40X-CC, radiolarians are rare and preservation is only moderate in the eight core-catcher samples (145-884B-40X-CC through -47X-CC) below the base of the *S. peregrina* Zone in Hole 884B. Although diagnostic species of Miocene radiolarian zonations evidently are absent in sediments from these samples, this interval is most likely of late Miocene age, based on the presence of *P. fistula, Botryostrobus auritus/australis, T. redondoensis,* and *S. robusta* in some of these samples and the absence of *D. acquilonius* and *Lychnocanoma nipponica magnacornuta.*

Samples 145-884B-48X-CC through -57X-CC contain a radiolarian fauna of middle to late Miocene age dominated by *L. nipponica nipponica* and *L. nipponica magnacornuta.* Sakai (1980) gave the range of *L. nipponica magnacornuta* as extending from the upper part of the *Dorcadospyris alata* Zone (Riedel and Sanfilippo, 1970; 1971) into the lower half of the *Didymocyrtis antepenultima* Zone (Riedel and Sanfilippo, 1970, 1978). Radiolarians are common to abundant and moderately well to well preserved in most of the samples from the upper portion of this interval. Abundances, however, decrease rapidly, with only rare radiolarians present in sediments from Samples 145-884B-53X-CC through -57X-CC.

The succeeding six core-catcher samples (Samples 145-884B-58X-CC through -63X-CC) contain rare to abundant radiolarians of varying degrees of preservation. The presence of *Eucyrtidium inflatum* in a typical Miocene assemblage (i.e., *Cyrtocapsella tetrapera, Cyrtocapsella cornuta, Cyrtocapsella japonica, S. robusta,* and *Amphymenium* sp. [Ling, 1973]) in Samples 145-884B-58X-CC through -61X-CC indicates that this interval is most likely middle Miocene in age. The other two core-catcher samples, which contain abundant radiolarians (145-884B-62X-CC and -63X-CC), are possibly of late early Miocene to early middle Miocene age, based on the presence of *S. robusta, T. redondoensis,* and *Acanthodesmid* sp. (Ling, 1973) in both samples, along with *C. tetrapera, C. cornuta, C. japonica, Amphymenium* sp., and *Stichocorys delmontensis,* which occur in only a single sample.

Radiolarian concentrations decrease rapidly below this interval, with only core-catcher Sample 145-884B-64X-CC containing more than rare radiolarians. The FO of *S. delmontensis* is recorded in Hole 884B (between Sample 145-884B-64X-CC and -65X-CC), indicating that this sample is of early Miocene age. The presence of *C. tetrapera, C. cornuta*, and *C. japonica* in at least one sample and the absence of *S. robusta, Acanthodesmid* sp., and *S. delmontensis* in Samples 145-884B-65X-CC and -66X-CC indicate that these sediments are of early Miocene age (possibly the *C. tetrapera* Zone [Riedel and Sanfilipo, 1978]).

Only rare radiolarians are present in Samples 145-884B-67X-CC through -78X-CC, with poor preservation in all samples below 145-884B-72X-CC. In most of these samples, it is not possible to identify the few specimens that they contain beyond the genus level. The presence of *Prunopyle titan* in a few of these samples may indicate a late Oligocene to Miocene age for these sediments. Radiolarians were not present in sediment samples below Core 145-884B-78X.

Diatoms

In general, diatoms are abundant to common and well preserved to moderately well preserved throughout the lowermost Miocene through Quaternary section cored above 632.4 mbsf at Site 884. Selected intervals of the Oligocene (Samples 145-884B-70X-CC, -71X-CC and -73X-CC) also contain fairly diverse diatom assemblages. Preservation is generally poor below Sample 145-884B-70X-CC (651.7 mbsf).

A complete sequence of all of the Neogene North Pacific Ocean diatom zones from the late Quaternary *Neodenticula seminae* Zone to the upper part of the early Miocene–latest Oligocene *Rocella gelida* Zone was cored at Site 884 (Figs. 19 and 20). The middle Miocene *Crucidenticula nicobarica* and the early Miocene *Thalassiosira fraga* zones, however, are greatly compressed and may be truncated by hiatuses. Standard diatom datum levels have been used to recognize these zones (Table 6), and little or no displacement of diatom biostratigraphic levels is apparent between Holes 884B and 884C.

At Site 884, sediments correlative to the late middle Miocene *Thalasssiosira yabei* Zone and earliest Miocene *Thalassiosira spinosa* and latest Oligocene *Rocella gelida* zones were recovered, whereas these same intervals were either missing or greatly compressed at Site 883. An added bonus of drilling at Site 884 is the recording of an excellent paleomagnetic stratigraphy for the lower Pliocene through uppermost middle Miocene (see "Paleomagnetism" section, this chapter), making possible for the first time direct correlation of North Pacific Ocean diatom datum levels with paleomagnetic stratigraphy for the older part of the late Miocene (>7 Ma) as well as parts of the middle Miocene.

For example, the LO of *Thalassiosira jacksonii* is documented in the upper reversed event of the Gilbert reversed-polarity Chron

Table 4. Trace-element geochemistry of interval 145-884B-90X-3, 25-30 cm, Subunit IIC.

Interval: 145-884B-90X-3, 25-30 cm	
Element	Abundance*
Nb	6.6
Zr	157.8
Y	109.1
Sr	502.8
Rb	67.8
Zn	284.1
Cu	340.6
Ni	206.2
Cr	42.1
V	254.8
TiO_2	1.06
Ba	15,676.0

*Abundances are in ppm for all elements except TiO_2; TiO_2 abundances in weight %.

(Subchron C2An.3r) at 3.75 Ma, instead of in the middle portion of the Gauss (3.3 Ma), as was proposed by Koizumi (1992). This discrepancy may possibly be explained by dissolution of the relatively delicate valves of *T. jacksonii* in sediments from Site 884. The FO of *Neodenticula koizumii* (ca. 195-199 mbsf) is found at an equivalent horizon to the LO *T. jacksonii* at Site 884 (3.75 Ma), an age equivalent to that suggested by Koizumi and Tanimura (1985) in DSDP Leg 86 sediments to the south, but somewhat younger than the 4.2-Ma (Subchron C3r.1r) age reported by Basilian et al. (1991) in Kamchatka. The age of this datum level is especially important, because it defines the boundary between the *Neodenticula koizumii/N. kamtschatica* Zone and the underlying *Neodenticula kamtschatica* Zone and because it constrains sedimentation rates in the middle part of the Pliocene.

The FO of *Thalassiosira latimarginata* (276.7-281.1 mbsf) falls at the base of the lower normal event (Subchron C3n.4n) of the Gilbert reversed-polarity Chron. This is slightly higher than the FO of *T. oestrupii* (286.3-290.7 mbsf). Koizumi (1992) also reported the FO of *T. latimarginata* as just above the FO of *T. oestrupii* in the Sea of Japan.

The FO of *Thalassiosira praeoestrupii* at Site 884 (320-325 mbsf) coincides with the base of Subchron C3An.1n (5.95 Ma), an age that agrees with the correlations of Bodén (in press) at DSDP Site 578 in the Northwest Pacific. The LO of *Thalassiosira miocenica* in the same interval at Site 884, on the other hand, is slightly older than the 5.7-Ma age estimated by Koizumi and Tanimura (1985) at Site 578. This discrepancy may result from an earlier disappearance of *T. miocenica,* a warm-water species, at the more northern Site 884.

The FO of *Neodenticula kamtschatica,* which marks the boundary between the early Pliocene-latest Miocene *N. kamtschatica* Zone and the late Miocene *Thalassionema schraderi* Zone, has been estimated to be about 7.0 Ma (Koizumi, 1992), based on the paleomagnetic calibration of this event by Burckle and Opdyke (1977) with the lowermost part of reversed polarity Chron C3B (Koizumi, 1992). At Site 884, the FO of *N. kamtschatica* in Sample 145-884B-41X-CC (372.7 mbsf) falls at the top of Chron C4n, at a slightly older age (7.25 Ma). Similarly, the last common occurrence of *Thalassionema schraderi,* which Barron estimated (1992) was about 7.2 Ma, is slightly older at Site 884 (ca. 7.45 Ma), based on its coincidence with the top of Subchron C4n.2n (Table 6, Fig. 20).

Paleomagnetic stratigraphy identifies Subchron C4Ar between about 437 and 451 mbsf (Fig. 20), but this dominantly reversed subchron seems to be reduced in length compared to normally polarized Subchrons C4An and C5n, and it contains only one short normal polarity event, instead of the two that should be present in Subchron 4Ar. (1992)'s Barron correlation of the LO of *Denticulopsis dimorpha* (Sample 145-884B-48X-CC) with the upper part of Subchron C4Ar (9.0 Ma) is in accord with this interpretation. Thus, the possibility exists of a short hiatus in the middle part of the *D. dimorpha* Zone

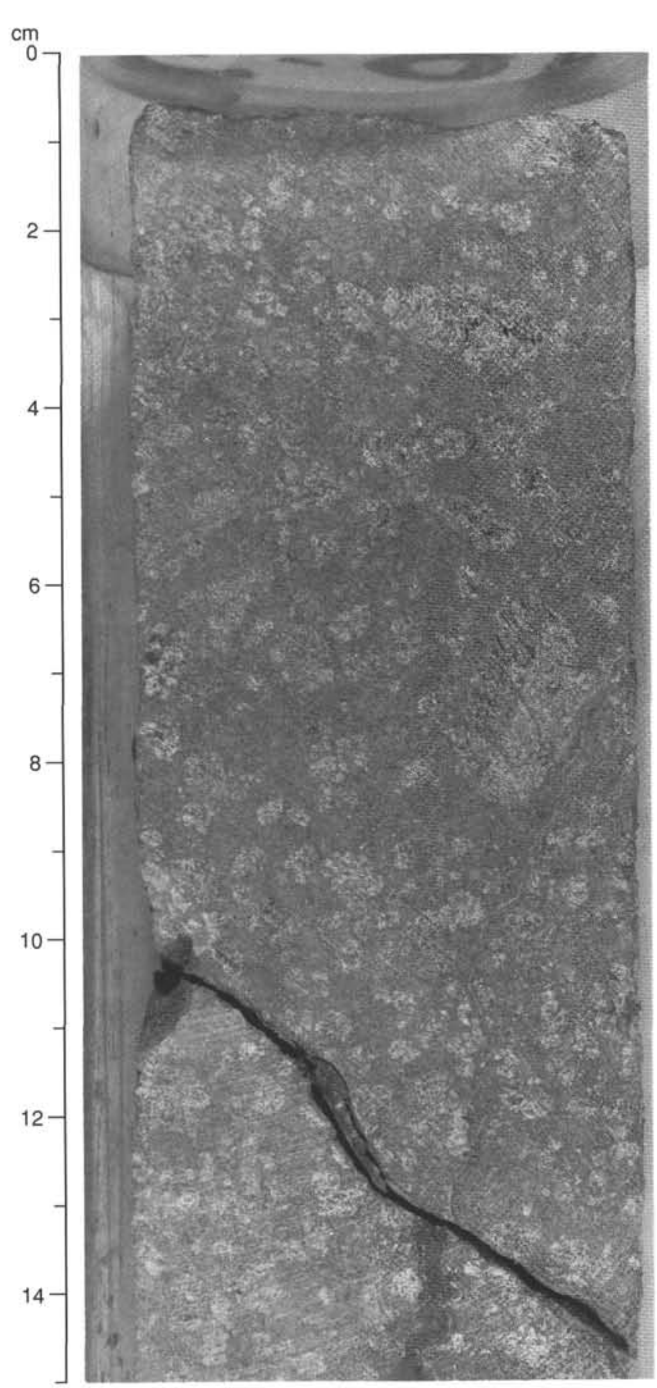

Figure 18. Photograph of interval 145-884E-10R-3, 0–15 cm, showing large plagioclase phenocrysts.

between Samples 145-884B-48X-CC (440.2 mbsf) and -49-1, 25-26 cm (440.45 mbsf). This is supported by the presence of common *Denticulopsis katayamae* in the former sample and the presence of *D. crassa* in the latter sample. According to Yanagisawa and Akiba (1990), these occurrences are restricted to the uppermost and lowermost parts of the *D. dimorpha* Zone, respectively. Lithostratigraphy (see "Lithostratigraphy" section, this chapter) identifies the boundary between lithologic Subunit IB (clayey diatom ooze and diatomite), and lithologic Subunit IC (claystone) at the break between Cores 145-884B-48X and -49X.

The FO of *Denticulopsis dimorpha,* which defines the base of the *D. dimorpha* Zone, is calibrated to paleomagetic stratigraphy for the

Table 5. Results of whole-rock analyses of trace element by XRF.

Core, section, interval (cm)	Unit	Depth (mbsf)	Nb	Zr	Y	Sr	Rb	Zn	Cu	Ni	Cr	V	TiO_2
Hole 884B-													
91X-CC, 8–12	1	848.30	2.2	80	30	135	12	70	143	138	342	269	1.31
Hole 884E-													
1R-1, 121–126	1	844.01	2.0	79	29	127	14	74	139	120	330	301	1.30
2R-2, 36–40	1	854.32	2.0	76	29	120	0	58	125	88	325	280	1.27
4R-4, 27–32	2	876.78	2.0	66	30	109	13	73	124	106	194	306	1.26
4R-4, 118–123	2	877.69	1.0	54	27	112	3	62	134	115	175	276	1.19
5R-4, 19–24	4	886.45	2.0	65	29	108	0	75	157	73	210	327	1.29
5R-6, 20–24	6	888.98	3.0	83	33	141	11	72	134	70	259	351	1.48
6R-2, 4–8	6	892.90	3.0	88	35	129	0	69	138	80	243	340	1.58
6R-3, 25–29	6	894.54	4.0	88	33	122	0	70	142	76	259	357	1.53
9R-2, 134–139	8	913.42	3.0	59	23	134	0	42	113	63	216	240	0.99
10R-4, 0–6	10	924.52	3.0	56	20	145	1	42	101	78	230	208	0.91
10R-5, 76–80	11	926.62	2.0	41	18	161	5	37	89	53	237	182	0.80
10R-6, 132–136	13	928.38	2.2	60	23	152	5	52	119	60	277	245	1.07

Concentrations are in parts per million, except for TiO_2, which is in weight percent. See "Explanatory Notes" chapter (this volume) for machine conditions and replicate standard analyses.

first time at Site 884 and falls in the upper part of Chron C5n (Fig. 20). This event has an extrapolated age of about 9.8 Ma, rather than the age of 9.5 Ma estimated by Barron (1992).

A second hiatus or greatly compressed interval in the middle Miocene occurs during the early part of the *Denticulopsis praedimorpha* Zone and the greater part of the underlying *Crucidenticula nicobarica* Zone in Sample 145-884B-58X-CC. Based on the interpreted absence of Subchrons C5A through C5AB (Fig. 20), the interval between about 12.4 and 13.2 Ma may be removed at an unconformity in the lower part of Core 145-884B-58X. Equivalent hiatuses have been documented at DSDP Sites 438 and 584 off Japan by Akiba (1985) and at DSDP Site 183 in the Gulf of Alaska by Barron (1989). This hiatus also corresponds with the lower part of a major hiatus or compressed interval present between 547.1 and 558.77 mbsf in Hole 883B.

The early Miocene *Thalassiosira fraga* Zone is restricted to the interval from Samples 145-884B-66X-1, 25–26 cm, to -66X-3, 25–26 cm (603.8–607.05 mbsf) (Table 6). This long zone (18.4–20.1 Ma) is either greatly compressed or truncated by a hiatus within this interval. Lithologic evidence for an unconformity in this interval is a sandy, laminated interval that occurs between 97 and 101 cm of Section 145-884B-66X-1 (604.8 mbsf) (see "Lithostratigraphy" section, this chapter). Samples 145-884B-66X-2, 25–26 cm, and -66X-3, 25–26 cm, below this sandy interval contain common *Thalassiosira spinosa* and lack well-developed specimens of *Thalassiosira fraga*, characteristics that indicate the lower part of the *T. fraga* Zone. The underlying *T. spinosa* Zone is recognized below the FO of *T. fraga* in Sample 145-884B-66X-3, 25–26 cm, and above the LO of *Rocella gelida* in Sample 145-884B-68X-CC.

Sample 145-884B-68X-CC contains *Rocella gelida* and *Lisitzinia ornata* and is latest Oligocene or earliest Miocene in age. A diverse assemblage from the middle part of the Oligocene, including *Cavitatus (Synedra) jouseana*, *C. rectus* (n. sp., Akiba et al., in press), *Kisseleviella carina*, and *Cestodiscus trochus*, is present in Sample 145-884B-70X-CC. The presence of few *Pyxilla* spp. and rare *Cavitatus miocenica* suggests a late early Oligocene age for Sample 145-884B-71X-CC, while poorly preserved specimens of *Rouxia* sp. and *Pyxilla* spp. in Sample 145-884B-73X-CC are also probably early Oligocene in age.

In contrast to the diatom assemblages recovered at Sites 882 and 883, those examined from the uppermost Miocene through Quaternary section of Site 884 contain consistent, but typically few, neritic planktonic diatoms from the arcto-boreal region, as well as benthic diatoms displaced from shelf environments. These taxa include *Thalassiosira gravida*, *Porosira glacialis*, *Detonula conferavea*, *Cosmiodiscus insignis*, *Thalassiosira hyalina*, *Pyxidicula zabelinae*, *Delphineis* spp., *Odontella aurita*, *Actinoptychus senarius*, *Paralia sulcata*, *Pseudopyxilla americana*, as well as representatives of the benthic genera *Cocconeis* and *Diploneis*, and are taken as evidence for sediment transport from the Bering Sea or Aleutian shelf. Note that this distinct arcto-boreal assemblage only evolved during the latest Miocene (Barron, 1980), so that such a Bering Sea or Aleutian influence on sedimention may extend farther back in time. In fact, neritic taxa (such as *Actinoptychus senarius*, *Kisseleviella* spp., and *Paralia sulcata*) are scattered down through Sample 145-884B-71X-CC (early Oligocene?), the lowermost sample observed to have relatively common diatoms. This transport must have been contemporaneous, because reworked diatoms are extremely rare in Site 884 sediments. Scattered occurrences of early Pliocene to late Miocene and early Miocene diatoms are present in selected intervals of the Pleistocene and upper Pliocene section.

In selected intervals of the Pliocene and Miocene section at Site 884, rare-to-few, warm-water taxa are recorded. These intervals and their warm-water taxa include Samples 145-884B-22X-CC and -23X-CC (ca. 3.6–3.8 Ma)(*Hemidiscus cuneiformis* and *Nitzschia reinholdii*), Samples 145-884B-29X-CC through -31X-CC (4.7–5.0 Ma) (*Thalassiosira convexa*), Samples 145-884B-36X-CC and -37X-CC (ca. 5.8–-6.3 Ma) (*T. convexa* and *T. miocenica*), Sample 145-884B-61X-CC (ca. 15 Ma) (*Coscinodiscus lewisianus*), and Samples 145-884B-64X-1, 25–26 cm, to -64X-CC (ca. 16.2–17 Ma) (*Azpeitia* spp. and common *Crucidenticula* spp.). These intervals probably record the proximity to Site 884 of warm surface waters. Quantitative study will be necessary to constrain these and other possible warm intervals further.

PALEOMAGNETISM

At Site 884, pass-through measurements of magnetic susceptibility and remanence were performed on APC and XCB cores from Holes 884B (Cores 145-884B-1H to -83X) and 884C (Cores 145-884-1H to -38X). Readings were taken at 10-cm spacings. Measurements of natural remanent magnetization (NRM) after 15 mT demagnetization were performed on all sections of all cores; the undemagnetized NRM of one section per core was measured also. Two or three 7-cm^3 samples were taken from all sections of Hole 884B that contained soft sediment (Cores 145-884B-1H to -40X). A single sample per section was taken between Cores 145-884B-41X and -66X. Measurements were performed using both the Molspin and the Japanese spinner magnetometers. Samples were demagnetized in five steps up to 25 or 35 mT. In addition to the NRM demagnetization, the Japanese instrument provided anhysteretic remanent magnetization (ARM) data. The multishot orientation devices were deployed in the upper parts of Holes 884B and 884C, and orientations obtained for Cores 145-884B-4H to -11H and Cores 145-884C-4H to -9H. Where both the multishot and tensor tools were used, orientations from the two devices agree to within 8°. Automated susceptibility (K) was measured at 5-cm intervals for all cores from Holes 884A, 884B, 884C, and 884D, in conjunction with other measurements performed using the multisensor track.

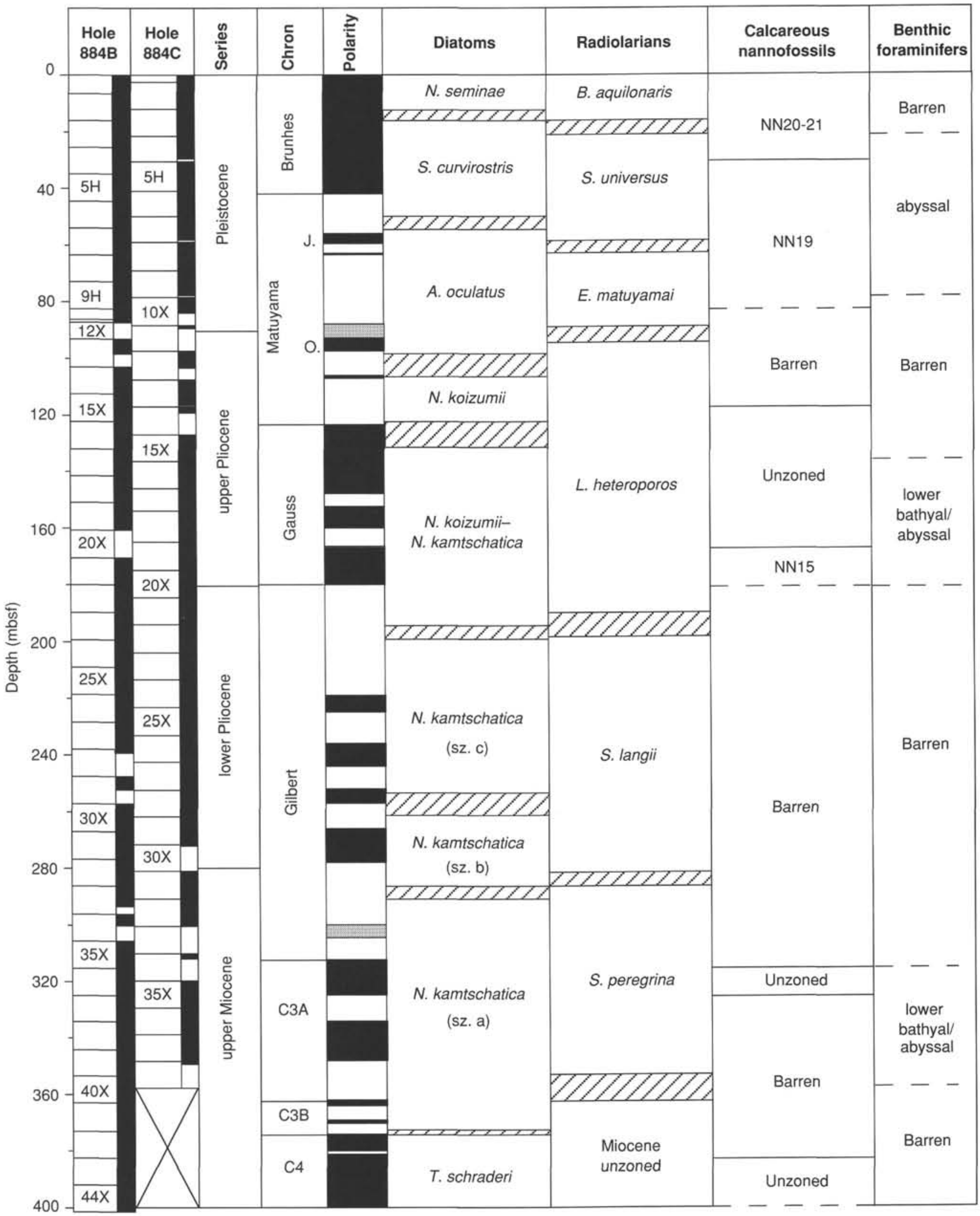

Figure 19. Stratigraphic position of cores, recovery (black), ages, placement of magnetostratigraphic chrons and subchrons, polarity log, and placement of diatom, radiolarian, calcareous nannofossil zones and the bathymetric range of benthic foraminifers in Holes 884B and 884C. Intervals filled by slanted lines indicate uncertainty in the placement of biostratigraphic boundaries.

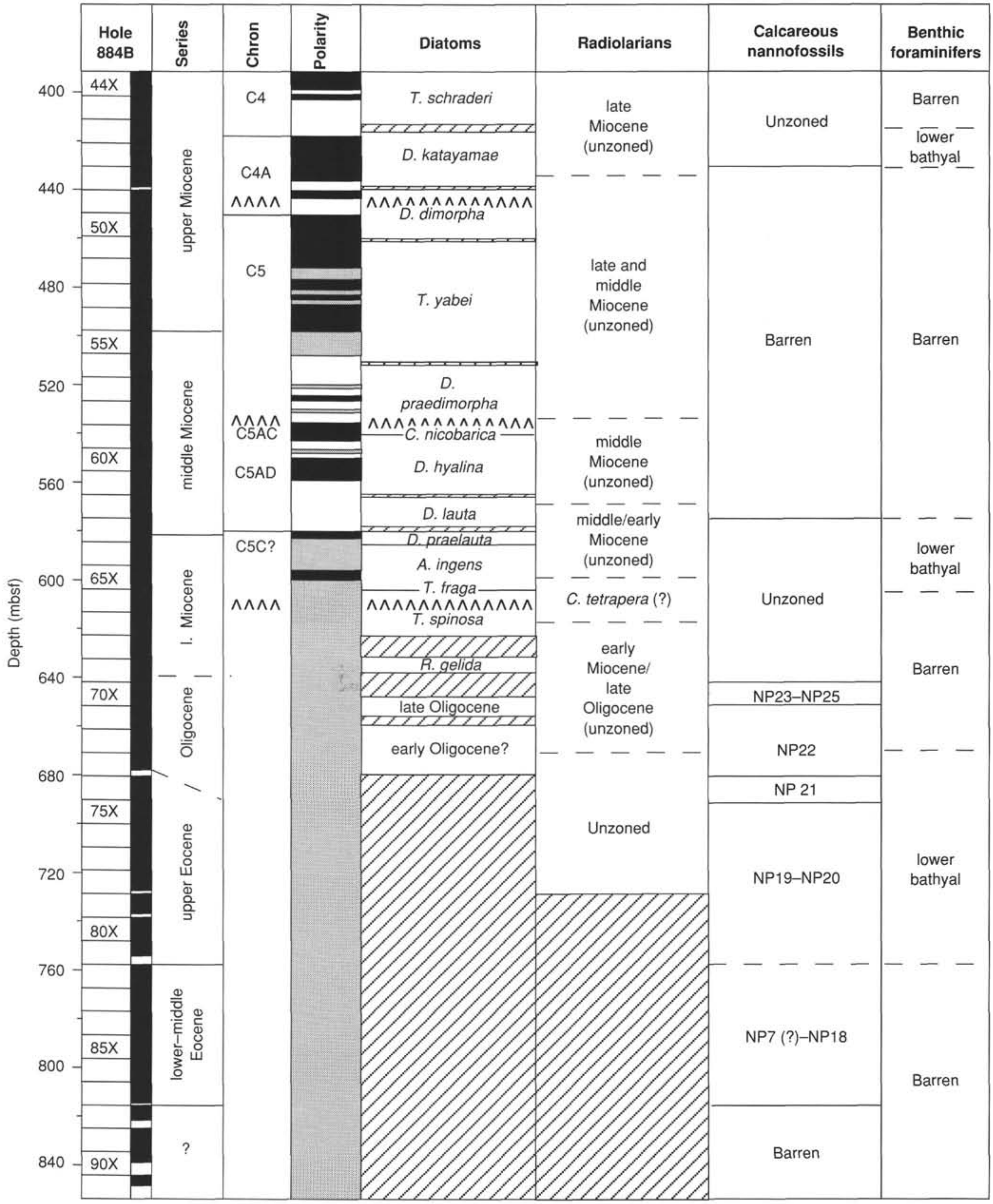

Figure 20. Stratigraphic position of cores; recovery (black); ages; placement of diatom, radiolarian, and calcareous nannofossil zones; and the bathymetric range of benthic foraminifers in Holes 884B. Intervals filled by slanted lines indicate uncertainty in the placement of biostratigraphic boundaries.

Table 6. Age and stratigraphic position of radiolarian (R), diatom (D) and calcareous nannofossil (N) datum levels in Holes 884B and 884C.

Sample no.		Datum	CK 92 (Ma)	Interval 145-884B-	Depth (mbsf) 145-884B-	Interval 145-884C-	Depth (mbsf) 145-884C-
R1	LO	*Lychnocanoma grande*	0.05	/1H-CC	/6.5	1H-CC/2H-CC	2.4/11.9
D2	LO	*Simonseniella curvirostris*	0.3	1H-CC/2H-CC	6.5/16.0	2H-CC/3H-CC	11.9/21.4
R2	LO	*Druppatractus acquilonius*	0.35	2H-CC/3H-CC	16.0/25.5	2H-CC/3H-CC	11.9/21.2
R3	LO	*Stylatractus universus*	0.45	2H-CC/3H-CC	16.0/25.5	3H-CC/4H-CC	21.4/30.9
N3	LO	*Pseudoemiliania lacunosa*	0.49	6H-CC/9H-1, 80	54.0/73.8	4H-CC/5H-CC	30.9/40.4
D5	LCO	*Actinocyclus oculatus*	1.00	5H-CC/6H-CC	44.5/54.0	6H-CC/7H-CC	49.9/59.4
R5	LO	*Eucyrtidium matuyamai*	1.05	6H-CC/7H-CC	54.0/63.5	7H-CC/8H-CC	59.4/68.9
D6	FO	*Simonseniella curvirostris*	1.58	11H-CC/12X-CC	87.3/93.3	10X-CC/11X-CC	88.2/97.8
N8	FO	*Gephyrocapsa oceanica* s.l.	1.67			9H-CC/14X-CC	78.4/126.7
D7	LO	*Coscinodiscus pustulatus*	1.8	13X-4, 54/14X-4, 47	98.34/108.97		
R7	FO	*Eucyrtidium matuyamai*	1.9	11H-CC/12X-CC	87.3/93.3	9H-CC/10X-CC	78.4/88.2
D8	LO	*Pyxidicula horridus*	1.8	12X-CC/13X-4, 54	93.3/98.34	12X-CC/13X-CC	107.4/117.0
D9	LO	*Neodenticula koizumii*	2.0	13X-4, 54/144, 47	98.34/108.97	11X-CC/12X-CC	97.8/107.4
D12	LCO	*Neodenticula kamtschatica*	2.63–2.7	15X-CC/16X-CC	122.2/131.8	15X-CC/16X-CC	136.3/146.0
D13	FO	*Neodenticula seminae*	2.7	15X-CC/16X-CC	122.2/131.8	15X-CC/16X-CC	136.3/146.0
R8	FO	*Cycladophora davisiana*	2.8	15X-CC/16X-CC	122.2/131.8	15X-CC/16H-CC	136.3/146.0
R9	LO	*Stichocorys peregrina*	2.9	22X-CC/23X-CC	189.8/199.4		
D14	LO	*Thalassiosira marujamica*	3.2	18X-CC/19X-CC	151.0/160.8	17X-CC/18X-CC	155.7/165.3
D15	LO	*Thalassiosira jacksonii*	3.3	22X-CC/23X-CC	189.8/199.4	21X-CC/22X-CC	194.3/204.0
N15	LO	*Reticulofenestra pseudoumbilica*	3.71	19X-CC/21X-3, 82	160.8/175.7	18X-CC/19X-CC	165.3/175.0
D17	FO	*Neodenticula koizumii*	3.75	22X-CC/23X-CC	189.8/199.4	21X-CC/22X-CC	194.3/204.0
D16	FO	*Actinocyclus oculatus*	3.8	23X-CC/24X-CC	199.4/209.1	22X-CC/23X-CC	204.0/213.7
R11	LO	*Theocorys redondoensis*		35X-CC/36X-CC	315.3/325.0	31X-CC/32X-CC	290.7/300.4
R12	FO	*Lamprocyrtis heteroporos*	4.6	31X-CC/32X-CC	276.7/286.3	30X-CC/31X-CC	281.1/290.7
D18A	LO	[a]*Thalassiosira plicata*	4.6	29X-CC/30X-CC	252.4/267.0	28X-CC/29X-CC	261.8/271.4
D18B	LO	[a]*Cosmiodiscus insignis*	4.6	29X-CC/30X-CC	252.4/267.0		
D19	FO	[a]*Thalassiosira latimarginata*	5.05	30X-CC/31X-CC	276.7/286.3	29X-CC/30X-CC	271.4/281.1
D21	FO	*Thalassiosira oestrupii*	5.4	32X-CC/33X-CC	286.3/296.0	30X-CC/31X-CC	281.1/290.7
D23	LO	*Thalassiosira miocenica*	5.7	35X-CC/36X-CC	315.3/325.0	34X-CC/35X-CC	319.7/329.2
D24	FO	*Thalassiosira praeoestrupii*	5.95	35X-CC/36X-CC	315.3/325.0	34X-CC/35X-CC	319.7/329.2
D24B	FO	*Thalassiosira miocenica*	6.3	37X-CC/38X-CC	334.3/343.9	36X-CC/37X-CC	338.7/348.2
R	FO	*Druppatractus acquilonius*	6.75		40X-CC/41X-CC	363.1/372.7	
R	FCO	*Stichocorys peregrina*	6.75	39X-CC/40X-CC	353.6/363.1		
D25	FO	[a]*Neodenticula kamtschatica*	7.25	41X-CC/42X-2, 26	372.7/374.46		
D26	LCO	[a]*Thalassionema schraderi*	7.45	42X-5, 25/42X-CC	378.95/382.4		
D30	LCO	[a]*Denticulopsis hustedtii*	8.4	46X-2, 25/46X-4, 25	413.05/416.05		
R	LO	*Lychnocanoma nipponica magnacornuta*	8.5	47X-CC/48X-CC	430.6/440.2		
D32	LO	*Denticulopsis dimorpha*	9.0	48X-6, 25/48X-CC	438.35/440.2		
D33	FO	*Denticulopsis katayamae*	9.3	48X-CC/49X-1, 25	440.2/440.45		
D32A	FO	*Thalassionema schraderi*		48X-CC/49X-CC	440.2/449.8		
D34	FO	[a]*Denticulopsis dimorpha*	9.8	50X-CC/51X-2, 27	459.3/461.07		
D36	LCO	*Denticulopsis praedimorpha*	10.8	56X-2, 25/56X-4, 25	509.15/512.15		
R	LO	*Cyrtocapsella tetrapera*	12.1	55X-CC/56X-CC	507.4/517.1		
R	[b]FO	*Lychnocanoma nipponica magnacornuta*	12.15	57X-CC/58X-CC	526.7/536.4		
R	[b]LO	*Eucyrtidium inflatum*	12.2	57X-CC/58X-CC	526.7/536.4		
D38	FO	*Simonseniella barboi*	11.5	57X-CC/58X-2, 25	526.7/528.45		
D41	LO	*Crucidenticula nicobarica*	12.4	58X-5, 25/58X-6, 25	532.75/534.25		
D42	FO	*Denticulopsis praedimorpha*	12.8	58X-5, 25/58X-6, 25	532.75/534.25		
D44	FCO	[a]*Denticulopsis hustedtii*	13.3	58X-7, 25/58X-CC	535.75/536.4		
D46	FO	*Denticulopsis hustedtii*	14.2	60X-CC/61X-CC	555.6/565.3		
R	FO	*Eucyrtidium inflatum*	14.8	61X-CC/62X-CC	565.3/574.8		
D49	FO	*Denticulopsis hyalina*	14.9	61X-CC/62X-2, 25	565.3/567.05		
D50	FO	*Actinocyclys ingens nodus*	15.1	62X-4, 25/62X-CC	570.05/574.8		
D52	FO	*Denticulopsis lauta*	15.9	63X-2, 25/63X-5, 25	576.55/581.05		
D53	FO	*Denticulopsis praelauta*	16.2	63X-CC/64X-1, 25	584.4/584.65		
R	FO	*Stichocorys delmontensis*	20.6	64X-CC/65X-CC	594.1/603.8		
D54	FO	*Crucidenticula sawamurae*	18.4	65X-CC/66X-1, 25	603.8/604.05		
D55	FO	*Actinocyclus ingens*	18.4	65X-CC/66X-1, 25	603.8/604.05		
D57	FO	*Thalassiosira fraga*	20.1	66X-3, 25/66X-5, 25	607.05/610.05		
R	FO	*Cryptocapsella tetrapera*	22.6	66X-CC/67X-CC	613.3/622.8		
D58	LO	*Rocella gelida*	21.8	67X-CC/68X-CC	622.8/632.4		
D60	FO	*Thalassiosira spinosa*	24.1	67X-CC/68X-CC	622.8/632.4		
D61	LO	*Lisitzinia ornata*	24.1	67X-CC/68X-CC	622.8/632.4		
N54	LO	*Reticulofenestra bisecta*	23.8	69X-CC/70X-1, 48	642.0/642.48		
N62	LO	*Reticulofenestra umbilica*	31.7	70X-CC/71X-CC	651.7/661.3		
N63	LO	*Ericsonia formosa*	32.7	73X-CC/74X-1, 50	680.6/681.1		
N64	LO	*Discoaster saipanensis*	35.0	74X-CC/75X-CC	690.2/699.8		
N66	FO	*Isthmolithus recurvus*	35.1	81X-CC/82X-CC	757.7/767.4		

[a] New age based on paleomagnetic stratigraphy of this site.
[b] First or last occurrence truncated by hiatus.

Notes: Samples constraining each datum level are separated by a slash (/) as is the meters sub-bottom depths (mbsf) of these samples. LO = last occurrence; LCO = last common occurrence; FO = first occurrence; FCO = first common occurrence. CK92 refers to the Cande and Kent (1992) geomagnetic polarity time scale.

In addition to the above measurements on the sediments from Site 884, whole-core measurements were performed on the basaltic basement recovered in Hole 884E. With the exception of parts of Cores 145-884E-5R and -9R, recovery was continuous enough to make this a meaningful measurement. Discrete paleomagnetic core samples were drilled and extracted from basaltic basement in Cores 145-884E-1R to -10R. Two to four samples per core were subjected to either AF alternating field or thermal demagnetization. In addition to these samples, the 7-cm^3 samples, cut for physical property measurements, were alternating field (AF) demagnetized and measured before the physical property experiments were performed. This represents an additional two to six samples per core.

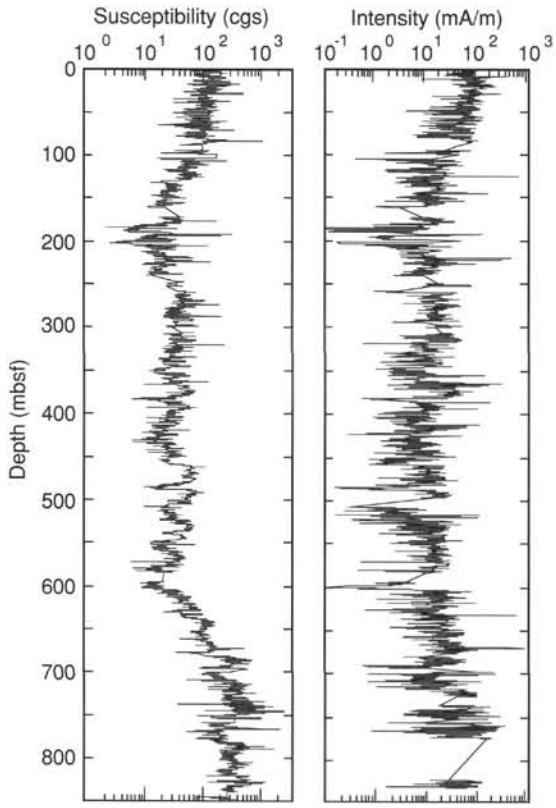

Figure 21. Magnetic susceptibilities and NRM intensities, after demagnetization at 15 mT, from Hole 884B compared with whole-core susceptibility (both on log scales).

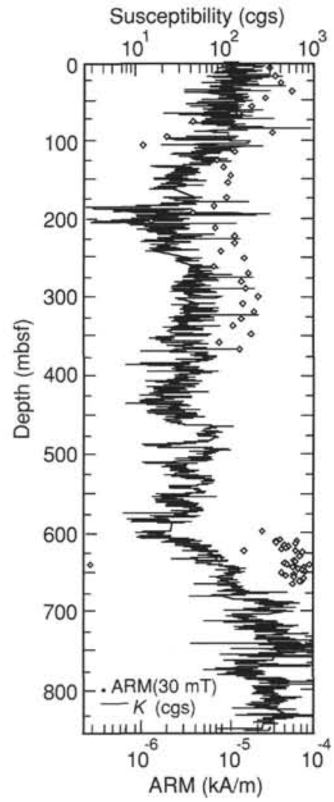

Figure 22. Comparison of results from whole-core measurements of susceptibility (solid line) with ARM, demagnetized to 30 mT, from discrete samples (open triangles) for Hole 884B. Both are plotted on log scales spanning an equal number of orders of magnitude to preserve the relative magnitudes of the ARM and *K*. Variation in the separation of the two curves indicates a change in the ARM/*K* ratio.

Results

Pass-through measurements of NRM 15 mT demagnetization, and whole-core susceptibility are shown in Figure 21 for Hole 884B. Site 884 is characterized, at all depths, by higher remanence and susceptibility values than those at Sites 882 and 883. This difference is particularly marked in the intermediate depth regions (e.g., Site 883, 87–600 mbsf), which have weaker intensities at all sites because of the dilution by diatoms. Between 200 and 600 mbsf, the intensity is about an order of magnitude higher than at equivalent intermediate depths at Site 883. This result is in keeping with the generally higher clay contents found at all depths at Site 884. An additional contrast to the other sites is that no abrupt decrease in intensity with depth marks the top of the high diatom zone, but rather a gradual decrease is seen between about 100 and 150 mbsf. At Site 884, the remanence intensity curve follows the susceptibility curve. The zone of low intensity and *K* between 200 and 600 mbsf is followed, with depth, by a gradual increase, between 600 and 700 mbsf, to values comparable to those found in the top 100 m of the sediment column. Mean intensities after demagnetization are about 100 mA/m from 0 to 100 mbsf (varying between 20 and 300 mA/m), about 30 mA/m from 150 to 600 mbsf (varying between 1 and 100 mA/m), and about 200 mA/m from 600 to 850 mbsf. These changes in *K* and intensity coincide with lithologic Subunits IA (initial high *K* and intensity), Subunits IB to ID (all at fairly low *K* and intensity) and Unit II (high *K* and intensity), respectively.

Measurements of ARM, demagnetized at 30 mT on the Japanese spinner magnetometer, are shown in comparison to susceptibility in Figure 22. The ratio of ARM to susceptibility (seen qualitatively in the separation between the two curves) is an indicator of magnetic grain size. This is because the ARM is mostly held in the finer grained fraction, whereas the susceptibility (*K*) is controlled by the coarse fraction. Between 150 and 370 mbsf, the two curves parallel each other, indicating a constant ARM/*K* ratio (Fig. 22). In this region, the various troughs and peaks of the two curves reflect only dilution changes of a magnetic faction whose basic properties are constant. However, between about 50 and 130 mbsf the ratio changes significantly. The two curves cross each other at about 75 mbsf and again near 100 mbsf. This indicates either a significant coarsening of the magnetic grain size or a change in magnetic mineralogy. The phenomenon cannot be explained by dilution effects. This zone is close to the Olduvai Chron reversal, where serious core recovery problems occurred in both Holes 884B and 884C. Another zone of interest lies between about 30 and 70 mbsf, where an apparent gradual coarsening of the magnetic grain size with depth may reflect the zone of iron oxide reduction predicted by the geochemistry. The finer grains are the first to be affected by alteration.

As at earlier sites, a reversed drilling overprint was observed in cores from Site 884. Discrete sample demagnetizations show that this overprint is removed by 5 to 10 mT demagnetization fields. However, in contrast to earlier sites, the discrete samples held a measurable and, apparently, stable remanence throughout most of Hole 884B. Examples of sample demagnetizations are shown in Figure 23, and a comparison of the whole-core measured inclinations (after 15 mT demagnetization), with the discrete sample results (after 25 mT demagnetization), is shown in Figure 24. With the exception of disturbed parts of the cores, the sediments appear to record stable normal and reversed field directions between 0 and at least 600 mbsf in Hole 884B (the axial dipole field inclination is about ±68° at a latitude of 51°33′N).

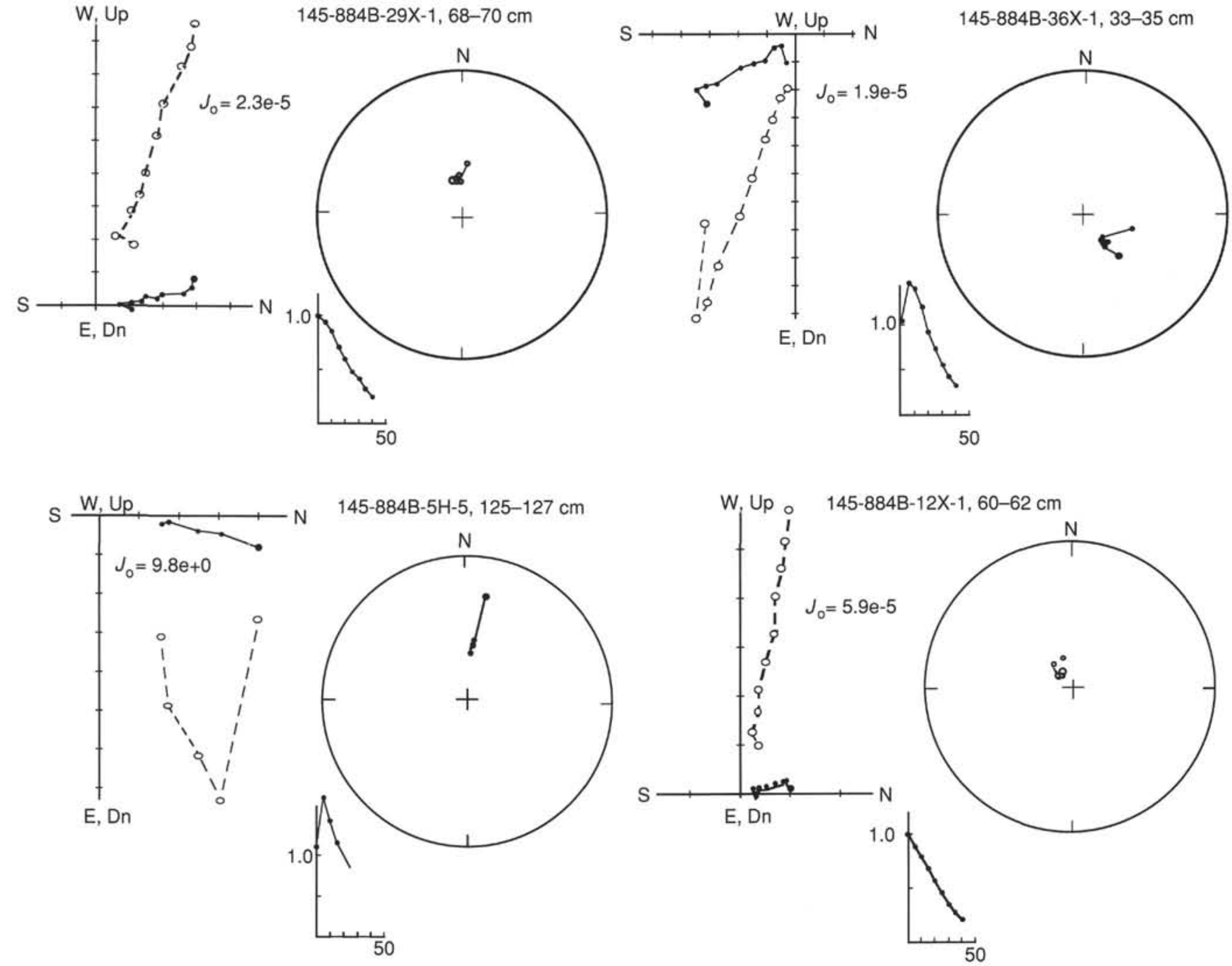

Figure 23. Examples of discrete sample demagnetizations from Hole 884B. For the Zijderfeld plots the open circles joined by dotted lines indicate the vertical component plotted against the *x* (north-south) component. In the equal area projections, open/filled circles indicate an upward/downward pointing vector.

In whole-core measurement, the directional results from XCB-coring contain more noise than results from APC-coring. The record from Section 145-884C-24X-3 (Fig. 25) illustrates particularly well some of the nature of the noise introduced by XCB coring. The periodic signal in inclination, declination, and intensity delineates zones of twisting, separated by breaks (failure). Both inclination and declination have been significantly modified by this deformation process. However, the polarity of the magnetization in the sediment seems to have remained largely intact. Support for this conclusion is found in results from Hole 884C, which agree remarkably well with those from Hole 884B and show little depth offset. With the exception of poor recovery near the termination of the Olduvai Chron, the recovery in Hole 884C completed zones of poor recovery in Hole 884B, so that a continuous depth coverage was obtained down to 350 mbsf.

Core 145-884B-40X marks the transition from soft sediment to more lithified sediment in Hole 884B. Below this level, the sediment was broken into drilling biscuits by XCB-coring. Despite this deformation, the cores again appear to have retained a coherent magnetostratigraphy, at least as far down as Core 145-884B-65X. This indicates that, on average, the drilling biscuits must have retained their vertical orientation.

Whole cores were measured from the basaltic basement recovered in Hole 884E (Cores 145-884E-1R to -10R). The NRM was strong enough to exceed the dynamic range of the 2G magnetometer. However, a small amount of AF demagnetization was sufficient to reduce the magnetization into a measurable range. The results, after 15 mT demagnetization, are shown in Figure 26. Individual samples, taken in pairs, were subjected to AF and thermal demagnetization. Examples of the results also are shown in Figure 26. Thermal demagnetization gave comparable results to AF demagnetization but was much more noisy. The results appear to show a two-step demagnetization: a large component was removed between 400° and 450°C, and a second component became unblocked between 550° and 600°C. Both components appear to carry roughly the same direction of magnetization.

Conclusions

The results from Holes 884B and 884C provide at least 600 m of coherent magnetostratigraphy. In the first 350 mbsf, the two holes provide an almost continuous record, because zones of poor recovery and coring gaps in one hole are completed by results from the other. Figure 27 illustrates the complete magnetostratigraphy, how it was constructed from the two holes, and its correlation to the polarity time scale of Cande and Kent (1992). A clear interpretation is possible from 0 Ma to as far back as the top of Chron 5Ar-1n (12.618 Ma) at about 580 mbsf. Although the magnetic results appear to provide a continu-

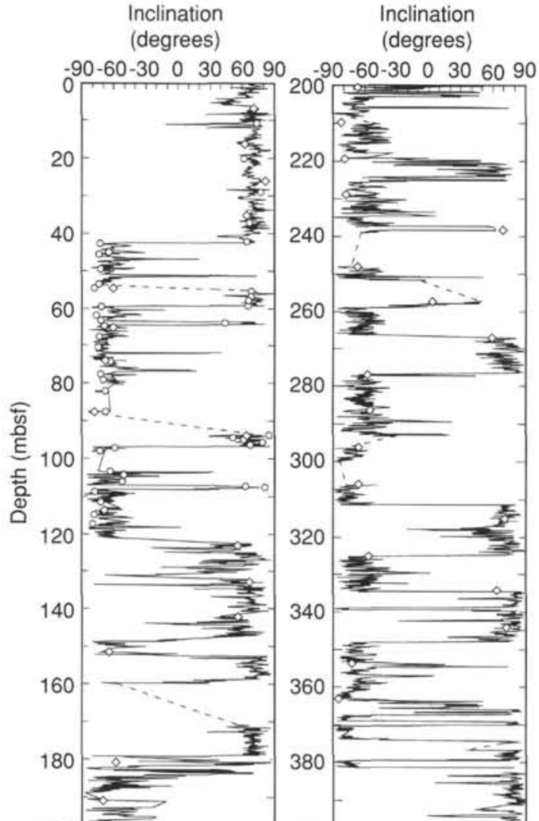

Figure 24. Whole-core measurements of inclination, after 15 mT demagnetization, from Hole 884B compared with inclinations from discrete samples demagnetized at 25 mT (open diamonds).

ous record over this interval, and do provide a coherent picture of sedimentation rate variation (Fig. 28), the biostratigraphy suggests that a hiatus or compressed zone occurs below the base of Chron 5n. The duration of the hiatus and its location are uncertain, and better definition should be achieved with further and more-detailed biostratigraphic work within this zone. However, a second possible interpretation of the magnetostratigraphy (shown in Fig. 28, and given in Table 7) has been made to include a compressed zone at the base of Chron 5n.

An age vs. depth curve, based on the magnetostratigraphy, is shown in Figure 28. A significant low value in sedimentation rate occurs at the level of the apparent and large change in rock magnetic indicators of grain size (70–120 mbsf). The middle of this region is the zone of poor recovery at the top of the Olduvai.

We attempted to obtain a mean inclination from the lava units recovered in Hole 884E. Results are summarized in Table 8. Two approaches were followed: first, the whole-core inclinations were averaged within each of the lava units; then a mean of the 13 units was calculated (the last three pillow basalts were treated as one unit); second, linear regressions were performed on the individual sample AF demagnetizations between 10 and 45 mT. Again averages within the units were calculated, followed by the mean of the units. The whole-core results give a mean inclination of 54.3°, and the individual sample results give a mean of 51.6°. However, these results correspond to a paleolatitude of 34.8° and 32.2°, respectively. However results must be treated with caution, because nothing is yet known of the age range represented by the lava units recovered. Also, we do not know if the magnetization of the lavas is primary, and results from 10 lava units are unlikely to provide an unbiased estimate of the mean paleofield.

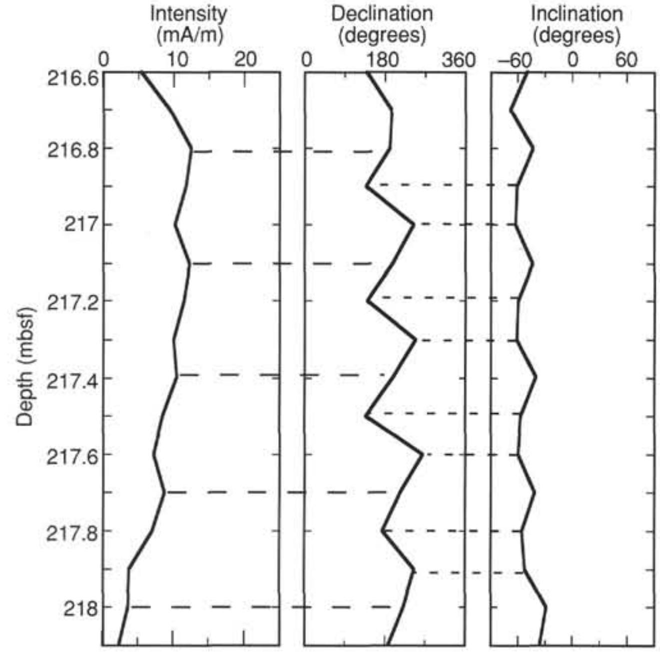

Figure 25. Inclination, declination, and intensity from Section 145-884C-24X-3. The directional and intensity results show a periodic variation produced by drilling deformation. The core apparently broke into 20- to 30-cm sections, which were deformed by twisting before failure as the drill penetrated the sediment.

SEDIMENTATION RATES AND FLUXES

To calculate sedimentation rates and sediment fluxes (mass accumulation rates), we considered the sedimentary section at Site 884 to consist of five time-stratigraphic intervals. The limits of these intervals were chosen on the basis of changes in sedimentation rate and dry-bulk density, as well as changes in sediment composition. Thus, these should represent intervals of relatively constant flux, but do not necessarily coincide with lithologic units defined for this site. As shown in Figure 29, three of these intervals correspond directly to lithologic units, whereas the two intervals between ~120 and 530 mbsf are equivalent to parts or combinations of lithologic units.

Sedimentation Rates

Linear rates of sedimentation were calculated using magnetostratigraphy for the upper three intervals and biostratigraphy for the deepest two intervals. In general, rates decrease down the core, but as at other Detroit Seamount locations (Sites 882 and 883), maximum rates occurred during early Pliocene and late Miocene time, where we find an average rate of ~60 m/m.y. (Fig. 29 and Table 9). For our lowermost interval, which is identical to lithologic Subunit IIA, the biostratigraphy is uncertain and datum levels only approximate a straight line. The sedimentation rate for that unit (6.2 m/m.y.) is probably a minimum estimate because of the likelihood of undetected hiatuses. It is important to stress that our estimated rates of sedimentation reflect averages for intervals of time millions of years long. It is likely that significant variability exists within these intervals, which might cause large changes in mass accumulation rate on shorter time scales.

Sediment Fluxes

Sediment fluxes were determined in the conventional way, taking the product of the sedimentation rate, the dry-bulk density, and the

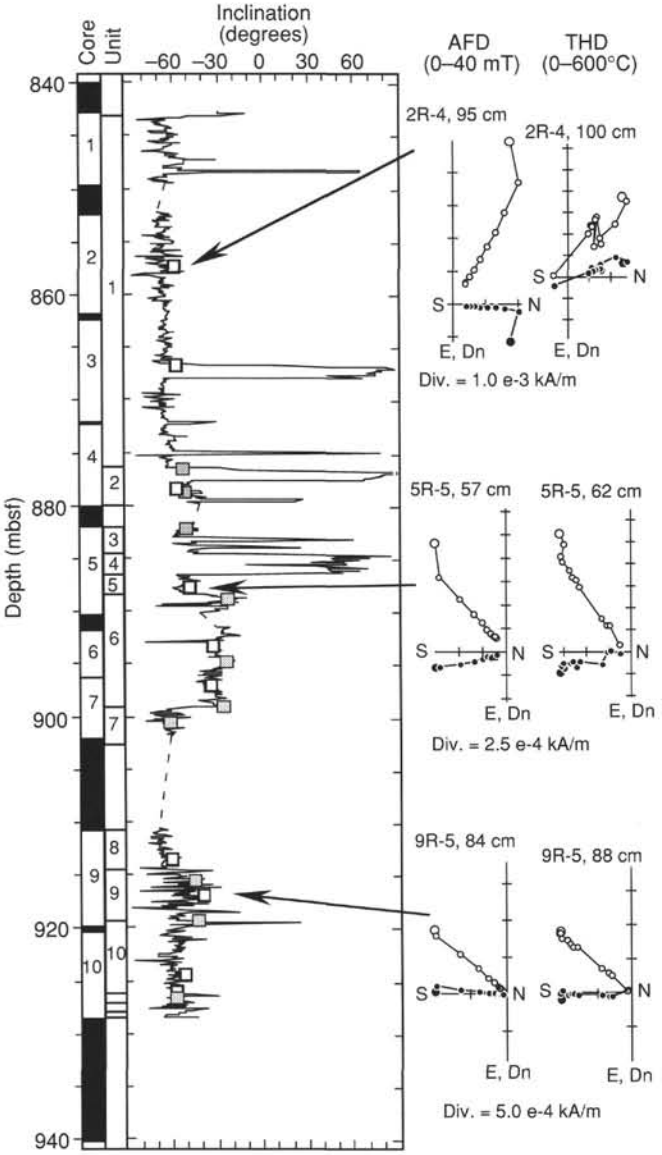

Figure 26. Results from lava basement recovered in Hole 884E, Cores 145-884E-1R to -10R. The solid line shows the whole-core inclination after demagnetization at 15 mT, and the squares illustrate the directions obtained from linear regressions on single sample AF demagnetizations. Some examples of AF and thermal demagnetizations of single samples are shown on the right. Core number and basalt unit are indicated on the left.

concentration of the sediment component. Average fluxes were calculated for the five time-stratigraphic intervals, results of which are shown as histograms in Figure 29 and keyed to the depth intervals with dashed lines. Raw data for each of these intervals in Hole 884B were averaged and are presented in Table 9. Dry-bulk density values were taken from pycnometer measurements, and sedimentary component data come from smear slide estimates, with the exception of percentages of carbonate and total organic carbon (TOC), which were measured analytically. Flux results (in g[$cm^2 \cdot$ k.y.]$^{-1}$) for diatoms, clay, glass, quartz, and carbonate are listed in Table 9 and are shown in the histograms (TOC fluxes are too near zero to be visible in the histograms). These results are only semiquantitative, because of the nature of estimates of smear slide abundances as well as possible errors when calculating deposition rates. For example, Thiede and Rea (1981) noted previously that smear slide results tended to overestimate coarse-grained sedimentary components that were subsequently measured analytically in shore-based studies. Additional errors may stem from the assumption that abundance estimates are directly proportional to the weight percentage of each sedimentary component. Thus, taking the 0- to 2.6-Ma, interval gram for example, we assume that an average of 30% diatoms translates directly to 0.30 g diatoms per g of bulk sediment.

Average sediment fluxes for the five time-stratigraphic intervals reveal distinctive changes with time (Fig. 29). As at Sites 881 through 883, the base of the uppermost interval at Site 884 is time equivalent with the onset of Northern Hemisphere glaciation, and the sediment is dominated by clay and diatom fluxes. Quartz is a minor component of the upper interval, whereas it is virtually absent below.

During the second interval, roughly equivalent to latest Miocene through the middle Pliocene time, the sediment is still dominated by diatom and clay fluxes, but diatoms are relatively more important than above. At Site 884, this interval contrasts with that at the shallower Detroit Seamount sites (882 and 883) by its significant clay flux and relatively reduced diatom flux. The late Miocene through middle Pliocene aged sections at those sites are marked by both higher rates of sedimentation and higher diatom percentages, resulting in diatom fluxes that are higher than those at Site 884 by at least a factor of two. At the deeper Site 884, on Meiji Drift, clay fluxes in the Pliocene and late Miocene sections are as high as is in the Pleistocene at the other sites. This attests to the significance of clay transport and focusing by bottom currents at depths greater than 3300 m (the depth of Site 882).

Between 6.2 and 11.9 Ma, clay and diatom fluxes are of equal, but reduced, importance; fluxes are reduced even further in the next interval (12.8–17.5 Ma; Fig. 29). By Oligocene to earliest Miocene time (20.1–34.8 Ma), opal flux had become insignificant, and the clay flux remained relatively unchanged. Meiji Drift sedimentation appears to have begun as early as 34.8 Ma, with the change in clay character from authigenic (>34.8 Ma) to terrigenous. Unlike at the shallower Detroit Seamount sites, carbonate flux is never significant at Site 884.

In summary, as with the long record at Site 883, the evolution of flux patterns at Site 884 reflects plate migration of this site northward since the Paleogene, coupled with changing oceanographic and climatic conditions. Because carbonate flux at this site was never significant, whereas it was significant during the Paleogene at Site 883, we infer that Site 884 must have been beneath the CCD at least since the early Oligocene. As we have seen at Site 883, beginning during the middle Miocene, silica deposition became important at Site 884. This probably reflects evolving deep-ocean circulation patterns at that time (Keller and Barron, 1987), which may also account for increased clay flux. Thus, the origin of Meiji Drift can be traced by its terrigenous clay flux, beginning at ~35 Ma, increasing at ~12 Ma, and culminating at ~2.6 Ma in response to increased supply owing to high-latitude climate changes and increased transport activity by deep currents.

INORGANIC GEOCHEMISTRY

Thirty-seven interstitial water samples were collected at Site 884 at depths ranging from 2.95 to 831 mbsf. Three closely spaced samples were taken from Hole 884A between 3.65 and 5.15 mbsf, and 34 broadly spaced samples were collected from Hole 884B at depths ranging from 2.95 mbsf to near the bottom of the hole at 831 mbsf. The trio of samples from Hole 884A was assigned to the depth scale for Hole 884B by correlating the magnetic susceptibility profiles for the two holes. Analytical results are listed in Table 10 and have been plotted separately for the two sample sets in all graphs in this section.

The pore-water samples span all of Subunits IA (0–128 mbsf), IB (128–440.2 mbsf), and IC (440.2–546.1 mbsf), which are composed of clay and ash, calcareous diatom ooze, clayey diatomite, and claystone; and Subunits IIA (604.8–694.7 mbsf), IIB (694.7–771 mbsf), and IIC (771–854 mbsf), which are composed of diatomite, claystone,

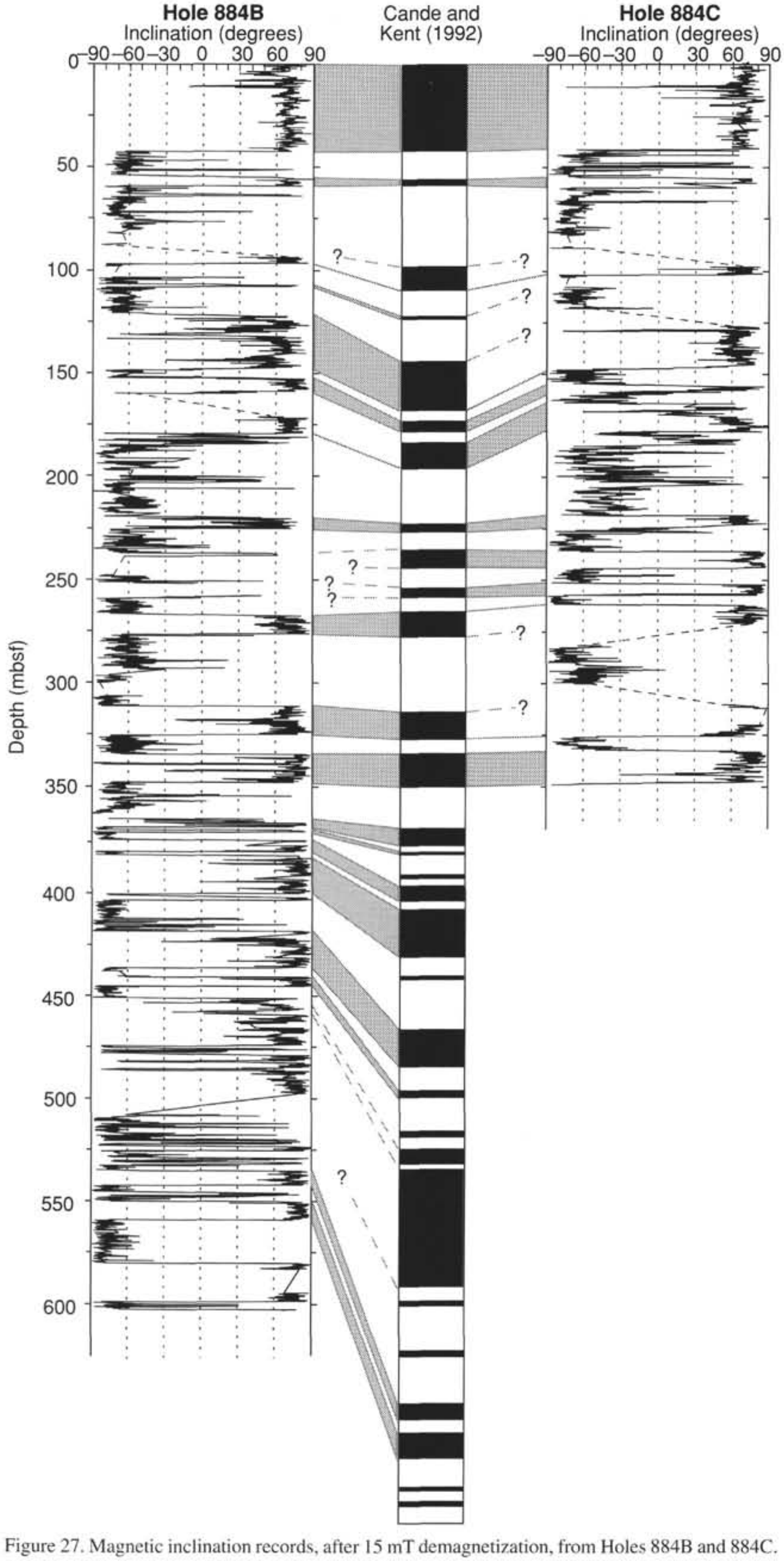

Figure 27. Magnetic inclination records, after 15 mT demagnetization, from Holes 884B and 884C. The magnetostratigraphic interpretation is shown in the center where the gray zones connect normal periods to their location on Cande and Kent's (1992) time scale. Changes in the slope of the gray zones indicate changes in sedimentation rate with respect to the linear time scale.

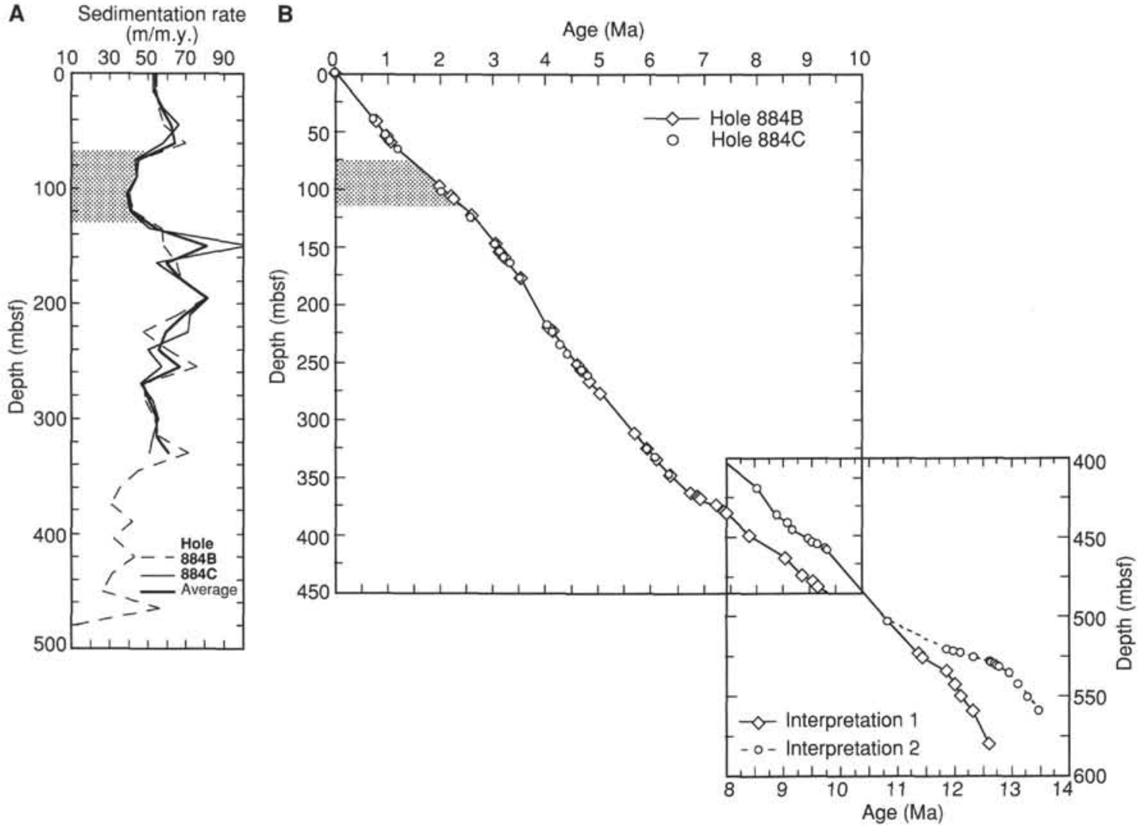

Figure 28. **A.** Plot of sedimentation rate vs. depth. **B.** Plot of depth vs. age for Site 884. Plots were calculated for both Holes 884B and 884C. The mean of the two holes is shown as the solid black line.

nannofossil chalk, conglomerates, and altered ash (see "Lithostratigraphy" section, this chapter).

Chloride concentrations in interstitial waters at Site 884 range from the value of North Pacific Ocean Deep Water (554 mM) in the shallowest samples (2.95–6.95 mbsf; Fig. 30A) to a maximum of ~565 mM between about 31 and 41 mbsf. As at Sites 881 through 883, the Cl^- maximum probably reflects the ongoing diffusive adjustment of the pore-water Cl^- distribution to the increased mean salinity of seawater during the glacially dominated Pleistocene age, and the fresher seawater of the Holocene (McDuff, 1985). The depth of the Cl^- maximum in Hole 884B is similar to that normally encountered in pelagic sections (McDuff, 1985), but is about 10 to 15 m deeper than was observed at Site 883 (see "Inorganic Geochemistry" section, "Site 883" chapter, this volume). This contrast probably reflects a greater degree of upward advection at Site 883, which is attributable to underconsolidation of the thick high-porosity diatomaceous ooze at that location. Below 41 mbsf in Hole 884B, the chloride content remains relatively constant to about 715 mbsf, with concentrations ranging between 559 and 563 mM (Fig. 30B). A slight but measurable decline in Cl^- occurs between 715 and 802 mbsf, in an interval dominated by claystone, calcareous chalk, and altered ash (Subunit IIB). This depletion may represent uptake of chloride by the alteration of volcanic ash and underlying basalt that was intersected at ~854 mbsf. Chloride concentrations in Cores 145-884B-74X (~687 mbsf) and -89X (831 mbsf) were unusually low (524 and 527 mM, respectively). Both whole-round samples from these cores yielded small amounts of interstitial water (3–6 mL, as opposed to the normal 30–40 mL), and we suspect that these low Cl^- concentrations are either an artifact of squeezing at very high pressure for long periods (3 hr) in the case of Core 145-884B-89X, or a reflection of contamination by traces of fresh water in the squeezing apparatus.

Nitrite is present at 5.10 and 6.95 mbsf in Hole 884A; NO_2^- concentrations were undetectable in the sample above these locations at 3.65 mbsf in Hole 884A and in the four uppermost samples taken from Hole 884B (2.95 and 12.45–31.45 mbsf; Fig. 30C; Table 10). These data suggest that nitrate reduction is occurring between about 5 and 7 mbsf, which is consistent with the distributions of manganese, alkalinity, and sulfate (see below).

The concentration of dissolved manganese in the shallowest sample at Site 884 (61 µM at 2.95 mbsf) is sharply higher than in the overlying bottom water (<100 nM in seawater; Landing and Bruland, 1980). Concentrations continue to increase to a shallow subsurface maximum of 145 µM at ~22 mbsf. The upward concavity in the profile above this maximum is approximately coincident with the occurrence of dissolved nitrite, implying that the zones of denitrification and MnO_2 reduction overlap (Fig. 30C). The first-order decline in the dissolved manganese content between a depth of about 30 and 180 mbsf suggests that precipitation of a manganese carbonate phase is occurring in this interval, which is characterized by green gray clayey diatom ooze. A pronounced, deep maximum in dissolved manganese occurs between 610 and 720 mbsf at Site 884, relatively near the bottom of the drilled section (Fig. 30D). A disconformity representing a 1.5-m.y. hiatus can be defined by diatom biostratigraphy between 604 and 610 mbsf (see "Biostratigraphy" section, this chapter) and separates overlying diatom-rich sediments of Subunit ID from the underlying section, which consists of the claystone and chalk of Subunit IIA. These deposits were frequently noted as being reworked and bioturbated and grayish-brown to dark reddish-brown (see "Lithostratigraphy" section, this chapter). This set of characteristics implies that the sediment column remained oxic during the deposition of these facies in the Eocene to early Miocene time. In contrast, the overlying diatom ooze, diatomites, and diatom-bearing claystones are

Table 7. Depths of polarity chron boundaries in Holes 884B and 884C.

Chron	Age (Ma)	Hole 884B Depth (mbsf)	Hole 884B Notes	Hole 884C Depth (mbsf)	Hole 884C Notes	Interpretation 2 Depth (mbsf)
	0.780	42.50		41.10		
C1r.1n	0.984	54.00–55.10		55.00		
	1.049	59.40		59.70		
C1r.2r-1n	1.201			66.15		
	1.212			66.60		
C2n	1.757					
	1.983	96.90	cb	101.90		
C2r.1n	2.197	107.10				
	2.229	108.20				
C2An.1n	2.600	121.30–122.50	cb	118.50–127.00	cb	
	3.054	148.10		147.00–147.80		
C2An.2n	3.127	152.35		154.50–156.00	cb	
	3.221	159.50–159.70		158.50–159.50		
C2An.3n	3.325			164.4		
	3.553	179.20		178.0		
C3n.1n	4.033	219.65		218.45		
	4.134	224.20		224.50		
C3n.2n	4.265		g	235.90		
	4.432		g	244.25		
C3n.3n	4.611	252.10(?)	cb+g	251.50–252.40	cb	
	4.694	258.40(?)	cb+g	256.90		
C3n.4n	4.812	266.30–267.20	cb	261.80–261.90	cb	
	5.046	276.50–276.90	cb		g	
C3An.1n	5.705	311.55			g	
	5.946	324.80–325.20	cb	325.70		
C3An.2n	6.078	334.50	cb	332.40		
	6.376	348.00		348.20	cb	
C3Bn	6.744	364.00–364.60				
	6.901	367.60				
C3Br.1n	6.946	369.10				
	6.981	370.25				
C3Br.2n	7.153					
	7.187					
C4n.1n	7.245	374.20				
	7.376	379.65				
C4n.2n	7.464	381.50				
	7.892	400.20				
C4r.1n	8.047					
	8.079					
C4An	8.529	418.45				
	8.861	436.15				
C4Ar.1n	9.069	440.65				
	9.149	445.20				
C4Ar.2n	9.428	451.10(?)				
	9.491	453.10(?)				
C5n.1n	9.592	453.50(?)				
	9.735	457.30(?)				
C5n.2n	9.777	458.00–459.50(?)				458.00
	10.065	478.00				
	10.330	481.00				
	10.595	485.00				
	10.834	498.00–507.00				
C5r.1n	10.940					
	10.989					
C5r.2n	11.378	523.00				
	11.434	526.00				
C5An.1n	11.852	534.50				520.70
	12.000	542.50				522.10
C5An.2n	12.108	550.00				523.00
	12.333	559.00				525.50
C5Ar.1n	12.618	580.00				528.50
	12.649					530.00
C5Ar.2n	12.718					531.00
	12.764					532.50
C5AAn	12.941					535.00
	13.094					542.30
C5ABn	13.263					550.00
	13.476					559.00
C5ACn	13.674					
	14.059					

Note: The annotation "cb" indicates that a reversal occurred in a core break; "g" indicates a core gap. Below Chron 5n, a second possible interpretation is given for Hole 884B magnetostratigraphy.

moderately bioturbated and gray to greenish-gray or occasionally brown, suggesting that the sediments immediately above the disconformity were less oxidizing and perhaps mildly reducing at shallow depths during deposition. This paleodepositional scenario is supported by the present dissolved manganese profile in the pore fluids, which indicates that the formerly oxic deposits below the hiatus are now suboxic. Progressive dissolution of manganese oxides within the zone of a downward-migrating reduction front can account for the observed release of manganese to solution in the interval immediately below the disconformity. The dissolved sulfate profile supports this hypothesis, as discussed below. At the base of the section (~740–831 mbsf), the pore-water samples show a dramatic decline in dissolved manganese concentrations (from 145 µM at 715 mbsf to 20 µM at 773 mbsf; Fig. 30D). Black coatings on lithic clasts and black laminae

Table 8. The calculation of mean inclinations from basaltic basement recovered in Hole 884E.

Hard rock unit	Whole-core average inclination (deg.)		Sample results S_1 (deg.)	S_2 (deg.)	S_3 (deg.)	S_4 (deg.)	S_5 (deg.)	Sample absolute average inclination (deg.)
1	−64.66	64.66	−59.4	−57.7				58.55
2	−48.49	48.49	−57.4	−52.8	−49.7			53.30
3	−48.84	48.84	−48.4					48.40
4	49.63	49.63	50.7					50.70
5	−52.74	52.74	−48.8					48.80
6	−32.06	32.06	−32.5	−35.5	−15.4	−24.5	−25.9	26.76
7	−63.58	63.58	−63.1					63.10
8	−67.18	67.18	−60.7					60.70
9	−54.11	54.11	−40.9	−44.5	−43.6			43.00
10	−59.62	59.62	−53.4	−58.1				55.75
11	−56.18		−58.0					58.00
12	−54.40	56.35						
13	−58.48							

Whole core-average		Sample absolute average	
Inclination	54.30°	Inclination	51.55°
Paleolatitude	34.83°	Paleolatitude	32.20°

in this interval, although not yet positively identified, may be ferromanganese oxides (see "Lithostratigraphy" section, this chapter) and their presence, coupled with the low dissolved manganese levels, suggests that the consolidated sediments in this zone are not yet (and may never become) suboxic or anoxic; the original oxic nature of these deposits may have been preserved for about 50 m.y.

Titration alkalinity increases sharply with depth in the upper section at Site 884, from 4.03 mM at 2.95 mbsf to ~8.6 mM at 50 mbsf (Fig. 31A). A broad maximum with values up to 8.67 mM characterizes the interval between 50 and 263 mbsf; values progressively decrease below this depth, reaching ~0.73 mM at 802.30 mbsf (Fig. 31A). Downward diffusion of alkalinity from the base of the broad maximum toward the basement is implied by the concentration gradient. A low alkalinity would have prevailed during the deposition of Eocene calcareous facies were those deposits oxic; thus, the measured profile supports an interpretation derived from the dissolved manganese distribution. The precipitation of carbonate vein-fillings in the underlying basalts must also have contributed to the low alkalinity values measured in the lowermost three pore-water samples.

The concentration of sulfate at 2.95 mbsf at Site 884 (~28.6 mM; Table 10) is almost identical to that in North Pacific Deep Water (Fig. 31A), indicating that sulfate reduction is not occurring in the top 3 m at this location. Progressive reduction of SO_4^{2-} has produced a first-order decline between 3 and ~250 mbsf, where a minimum of about 20 mM is reached. Below this horizon, a gradual, approximately linear increase to 25.4 mM at 802 mbsf indicates that sulfate is diffusing upward from near the base of the section. Reduction of SO_4^{2-} is unlikely to be occurring at depths greater than about 320 mbsf; which is consistent with the relatively low organic carbon concentrations and organic carbon accumulation rates observed in the lower half of the drilled section, implying a low oxidant demand (see "Organic Geochemistry" and "Sedimentation Rates and Fluxes" sections, this chapter). In addition, sulfate reduction would effectively be prohibited by the (presumed) presence of the manganese and iron oxyhydroxides in this interval; these phases would act as the thermodynamically preferred electron acceptors.

Dissolved ammonium in pore waters at Site 884 increases with depth from 96 µM at 2.95 mbsf to about 689 µM at 176 mbsf (Fig. 31B). Concentrations are essentially constant between ~176 and 321 mbsf and decrease approximately linearly below this interval to a value of 29 µM at 831 mbsf (Fig. 31B). The upward convexity in the interval between the uppermost sample and ~290 mbsf indicates that this is the principal zone of NH_3 release. This is consistent with the sulfate distribution, which indicates that the highest rate of anerobic decomposition occurs over roughly the same depth range. The generally linear decline of the ammonium content below 321 mbsf is a reflection of downward diffusion from the zone of production in the more organic-rich upper portion of the section toward the organic-lean sediments overlying the basement. The profile implies that a sink for ammonium may lie near the base of the hole. Illite, for example, is a common constituent of the clay-rich deposits below the hiatus at ~600 mbsf and is known to take up ammonium through isomorphous substitution of NH_4^+ for K^+.

The concentration of magnesium in the uppermost sample (2.95 mbsf) is slightly lower than that of North Pacific Deep Water (52.1 mM, compared with 53.5 mM) and decreases gradually to a minimum of about 47 mM at 321 mbsf (Fig. 31C). Between 321 and 629 mbsf, the magnesium content rises slightly, before increasing sharply between 802 and 831 mbsf. This increase should be viewed with caution, however, as the basal pore water sample at 831 mbsf consisted of only 3 mL, and squeezing artifacts may have influenced the measured concentration. The decline in the dissolved magnesium contents in the upper ~200 m may reflect dolomitization in the sulfate reduction zone. Indeed, a concretion sampled from Core 145-884C-19X of Hole 884C (Interval 145-884C-19X, 66–68 cm, ~172 mbsf) was determined by XRD to consist of essentially pure dolomite.

The concentration of calcium in the uppermost sample is about the same as that in North Pacific Deep Water (10.5 mM) and remains constant to a depth of about 176 mbsf (Fig. 31C). Below this horizon, concentrations increase steadily, reaching a maximum value of 31.3 mM at 715 mbsf. A pronounced decline to 26.5 mM occurs in the interval between 715 and 831 mbsf. A steady increase between ~300 and 700 mbsf is not matched by a commensurate depletion in magnesium, suggesting that alteration reactions in the basalts are not controlling the overall distribution of calcium. Instead, alteration of calcic feldspars in ash, plus dissolution of calcite (pressure dissolution?) in the calcareous ash-bearing chalks and claystones below ~600 mbsf, can potentially account for addition of Ca^{2+} to pore waters. The dissolved strontium profile is generally similar to that of calcium (as discussed below) and offers some support for the dissolution hypothesis. The slight progressive decline in calcium toward the basement in the lower 100 m of the sampled section indicates consumption at greater depths, which is consistent with the presence of well-crystallized calcite fracture-fillings in the underlying basalt and observed alteration of olivine to iddingsite (see "Igneous Petrology" section, this chapter). Iddingsitization releases magnesium (Deer et al., 1966), which may account for the increased (but suspect) Mg^{2+} content in the deepest pore-water sample. The apparent lack of reactivity, evinced by the largely invariant magnesium profile below 300 mbsf, particularly in the 600- to 700-mbsf interval, implies that the ubiquitous authigenic smectite in the latter zone is not magnesian. Instead, the high iron content, typified by the common reddish-brown color of the clay and ashstones in this horizon, implies that nontronite may be the dominant smectite phase.

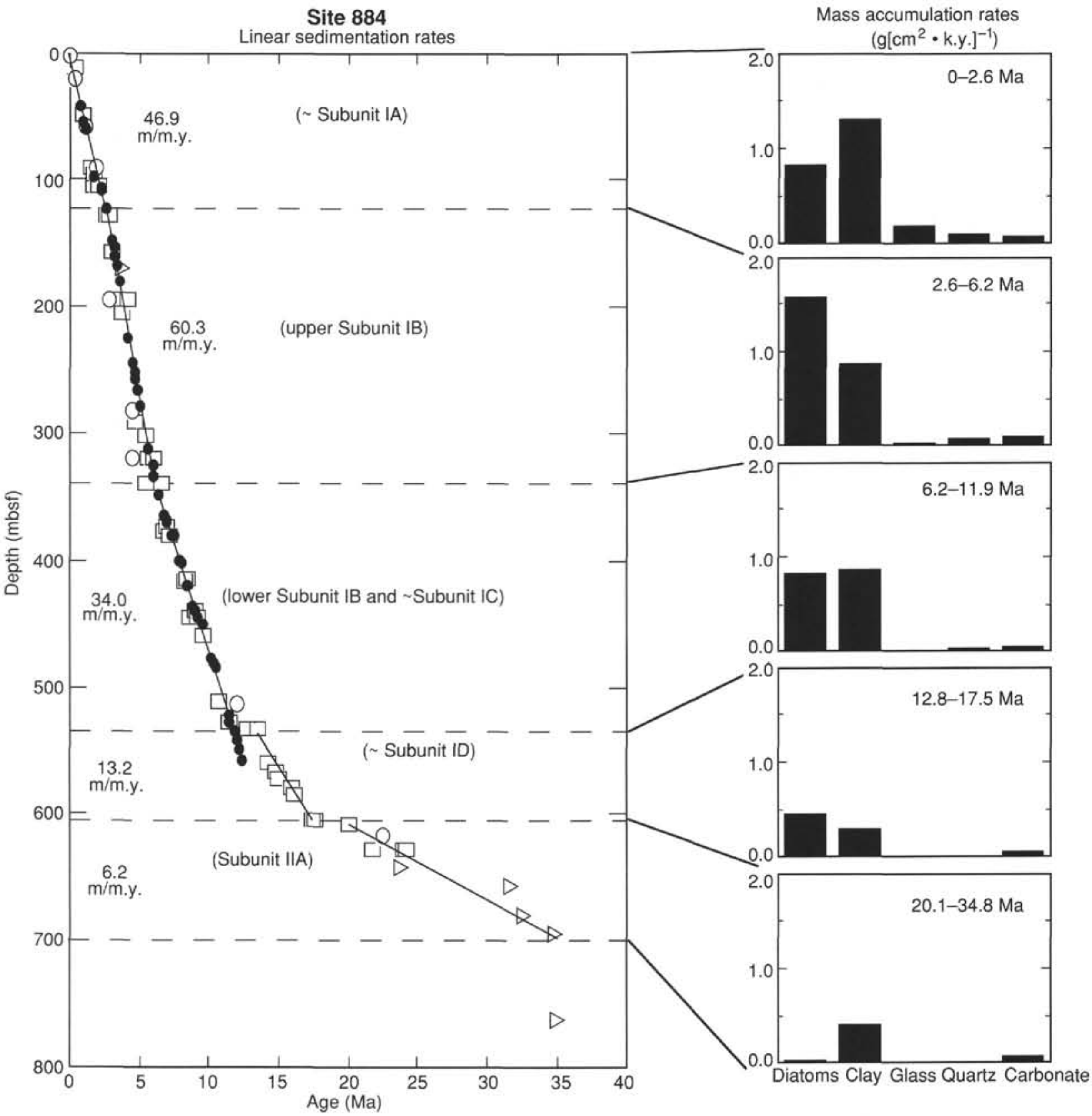

Figure 29. Sedimentation rate plot (left) for Site 884 using magnetostratigraphy from Holes 884A and 884B (solid symbols) and biostratigraphy from Hole 884B (open symbols; squares, circles, and triangles = diatoms, radiolarians, and nannofossils, respectively). For flux (mass accumulation rate) calculations, the section was divided into five intervals where rates of sedimentation, dry-bulk density, and sediment composition are relatively constant. These intervals are identified by dashed lines tie the stratigraphic column to the flux results (histograms at right). The flux results quantify the origin of late Paleogene Meiji Drift sedimentation, Neogene siliceous and hemipelagic sedimentation, and late Neogene and Quaternary terrigenous sedimentation associated with glaciation.

The concentration of dissolved silicate in the uppermost pore-water sample at Site 884 (~962 µM) is sharply higher than that in the overlying North Pacific Bottom Water (~160 µM), reflecting pronounced dissolution of opaline diatom frustules within the uppermost sediment column (Fig. 31D), as observed previously at Sites 881 through 883. The average concentration of silicate generally increases with depth to a maximum of ~1300 µM at ~600 mbsf, then decreasing between this level and 715 mbsf to about 1100 µM. The dissolved silicate maximum between 550 and 600 mbsf is coincident with a pronounced increase in diatom abundance, which occurred during the middle Miocene cooling event (at about 15 Ma; see "Biostratigraphy" section for a comprehensive discussion). Between 744 and 831 mbsf, the concentration of silicate decreases dramatically to about 180 µM, coincident with the total disappearance of diatoms below about 700 mbsf (see "Biostratigraphy" section, this chapter). The lowest values occur in the nannofossil chalk and clayey ash interval just above the basalt basement, probably reflecting uptake during smectite authigenesis, which is ubiquitous in this zone (see "Lithostratigraphy" section, this chapter). The extreme sharpness of the discontinuity in the silicate profile at about 725 mbsf can be attributed to three factors: (1) immediately above the discontinuity, the pore fluids are kept in a state of saturation with respect to opal by continuing dissolution of

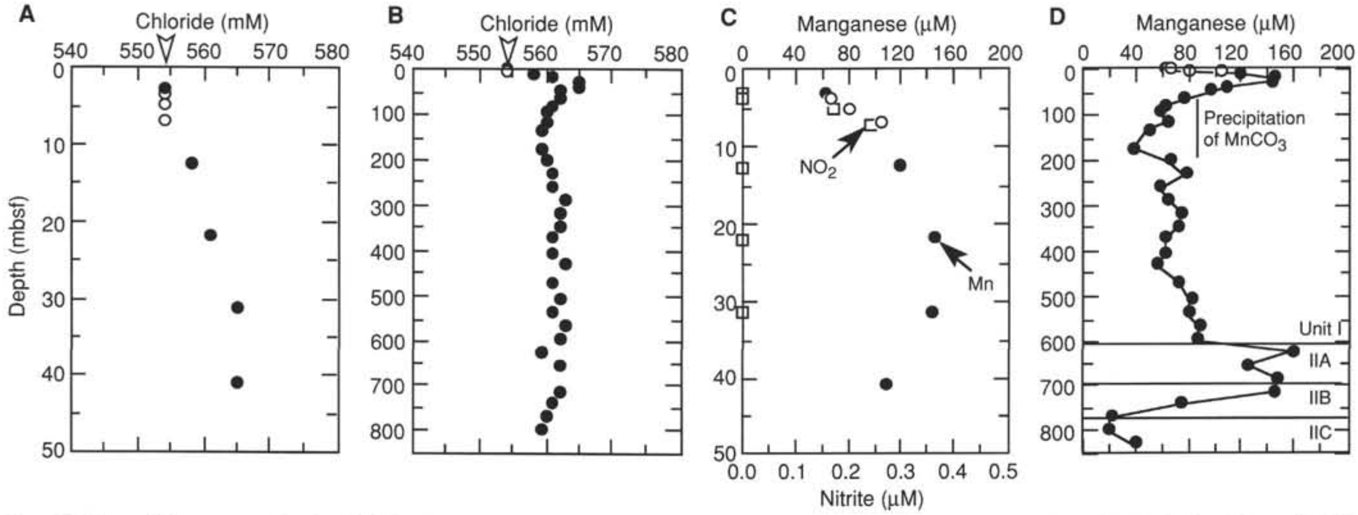

Figure 30. Interstitial-water profiles for Site 884. **A.** Chloride in the top 50 m of Holes 884A and 884B. **B.** Chloride composite profile for Holes 884A and 884B. **C.** Manganese in the top 50 m of Holes 884A and 884B (circles), with nitrite plotted for comparison (squares). **D.** Manganese composite profile for Holes 884A and 884B. Horizontal line at 604 mbsf represents a hiatus in Hole 884B. Open and closed circles indicate data from Holes 884A and 884B, respectively. Open arrowhead indicates the chloride concentration in modern North Pacific Deep Water.

diatoms; (2) the complete absence of diatoms, coupled with clay formation immediately below the discontinuity, renders this zone a pronounced sink for dissolved silicate; and (3) porosity and permeability decrease abruptly at ~740 mbsf (see "Physical Properties" section, this chapter), a few meters above the silicate-depleted pore-water sample at ~744 mbsf, and this would inhibit downward diffusive transport of silicate to the zone of uptake.

The concentration of strontium in the uppermost pore-water sample (87 µM) is about the same as that in modern North Pacific Deep Water (86.3 µM; Fig. 32A). This concentration is constant with depth until ~140 mbsf, below which it begins to increase gradually and nonlinearly to the base of the section, reaching a maximum concentration of 236 µM at 831 mbsf. The steady increase in Sr^{2+} with depth reflects upward diffusion of Sr^{2+} from the base of the section, probably as a result of dissolution/recrystallization of calcite. The slight upward concavity evident in the profile above 600 mbsf may reflect co-recipitation in authigenic carbonates, particularly above 400 m depth.

The lithium content (26.5 µM) in the shallowest sample at Site 884 matches that of North Pacific Deep Water (26.8 µM; Fig. 32A). The profile shows a concentration maximum of 91.8 µM, centered at 600 mbsf, with a pronounced decrease below this depth. The maximum is approximately coincident with the abundance maximum of biogenic opal. Previous workers (see for example, Gieskes, 1981) speculated that a positive genetic relationship exists between the lithium content in pore waters and the abundance of biogenic silica in the associated solid phases; however, it is not clear from the present data whether opal dissolution can be invoked as the principal source of dissolved lithium in the section. Both upward diffusive and downward flux, having a sink near the basement are implicit in the profile. The lithium depletion at the base of the section may reflect consumption during the formation of authigenic clays.

Sodium (calculated by charge balance at this site) shows little variation in the pore waters down the core, with concentration in the uppermost sample being equal to that of seawater (480 mM; Fig. 32B). A slight enrichment in sodium, similar to the chloride maximum, occurs between 30 and 40 mbsf (Table 10), reflecting the Quaternary salinity effect discussed earlier. The calculated Na^+ concentration gradually decreases from top to bottom in the section, suggesting that the element is being removed during alteration of the underlying basalts at this location, perhaps by albitization.

The concentration of potassium in the surface sample (10.17 mM) is slightly below that of North Pacific Deep Water (10.35 mM) and remains at approximately this value until about 377 mbsf, below which the average K^+ concentration decreases linearly to 1.78 mM at the base of the section (831 mbsf). The potassium data show significant scatter, which may result from the temperature-of-squeezing effect (see "Inorganic Geochemistry" section, "Site 883" chapter, this volume). The linear decline below 300 mbsf indicates downward diffusion toward a sink or sinks at depth, where either alteration of the underlying basalts and/or the formation of illite in the overlying clay-rich deposits may be consuming potassium.

A small quantity of native copper occurred in veinlets up to 1 mm wide and as rare disseminated grains in three cores in Hole 884B (Cores 145-884B-56X, -57X, and -68X), as smears on slickenside surfaces in the core-catcher sample of Core 145-884B-86X, and as veinlets and smeared blebs on a single fracture surface in the basalt cored in Hole 884E. The grains ranged up to about 1 mm in longest dimension and in habit from twinned crystals to irregular, discrete masses. Bluish "haloes" were observed around some of the occurrences of the metal. The element was positively identified by XRD of a small, clean isolate that was collected from Core 145-884B-57X of Hole 884B by repeated agitation and settling of a composite sediment sample and by pipetting off the diatomaceous clay fraction. In the sedimentary section, the copper apparently occurred only in clay-rich units, including the claystone of lithologic Subunit IC, the claystone and calcareous chalk of Subunit IIA, and the altered ash of Subunit IIC.

Elemental copper precipitates syngenetically in sediments only under extreme reducing conditions where sulfide is absent. This is a rare circumstance in marine sediments, given the abundance of sulfate in seawater and the ready incorporation of copper in precipitating pyrite. However, the metal has been reported to occur in sulfate-depleted settings, such as swamp sediments (Krauskopf, 1979), where ionic copper is apparently reduced by organic matter. In marine deposits having significant activity of dissolved sulfide, various highly insoluble copper sulfide phases (e.g., chalcopyrite or covellite) will precipitate readily should dissolved copper be introduced; in contrast, the formation of native copper is strongly thermodynamically disfavored under such conditions. Sediments in the upper half of the drilled section at Site 884 are clearly reducing, as discussed above, but the oxidant demand is insufficient to quantitatively deplete the sulfate inventory. The lower half of the section, where organic matter is present only in low concentrations (see "Organic Geochemistry" section, this chapter) and where the copper occurs, appears to be suboxic, but not anoxic. Therefore, the presence of elemental copper

Table 9. Listing of average sediment data and flux ($g/cm^2 \cdot k.y.$) results for five time-stratigraphic intervals at Site 884.

Depth int. (mbsf)	Age int. (m.y.)	Dry-bulk density (g/cm^3)	Linear sed. rate (cm/k.y.)	Diatoms (%)	Diatoms ($g[cm^2 \cdot k.y.]^{-1}$)	Clay (%)	Clay ($g[cm^2 \cdot k.y.^{-1}$)	Glass (%)	Glass ($g[cm^2 \cdot k.y.]^{-1}$)	Quartz (%)	Quartz ($g[cm^2 \cdot k.y.]^{-1}$)
0–122	0–2.6	0.60	4.69	29.6	0.833	46.9	1.320	6.6	0.186	3.50	0.097
122–339.1	2.6–6.2	0.53	6.03	49.3	1.580	27.2	0.869	0.5	0.016	2.10	0.067
339.1–530	6.2–11.9	0.62	3.40	39.1	0.824	40.9	0.862	0.0	0.000	0.63	0.013
530–604.5	12.8–17.5	0.66	1.32	50.6	0.441	32.1	0.280	0.0	0.000	0.25	0.002
604.5–700	20.1–34.8	0.90	0.62	4.5	0.025	70.8	0.395	0.0	0.000	1.90	0.011

in the section is enigmatic. Deductions previously done about the redox state of the sediments during deposition imply that this copper could not have been precipitated syngenetically; therefore, it must be of later-stage diagenetic origin. The source of the copper is unknown, but modern nontronitic clays are known to host substantial quantities of the metal in interlayer sites (>1000 mg/kg; see Pedersen et al., 1986). It may be that remobilization of copper has occurred during progressive alteration of the (presumed) nontronites in the lower reaches of the section at this site, but such a supposition is highly speculative.

Native copper has been recorded at previous drilling sites, including Site 105, Leg 11, in the western Atlantic Ocean (Hollister, Ewing, et al., 1972) where the metal occurred some 20 m above basalt, and on the Manihiki Plateau at Site 317 of Leg 33, where strands, wires, and blebs up to 1 mm in longest dimension were recovered from volcaniclastic sediments up to 150 m above basalts (Jenkyns, 1976). The metal occurs at Site 884 up to 350 m above the basement volcanics. Jenkyns suggested that the Manihiki Plateau occurrence can be attributed to deposition from acidic iron and copper-bearing hydrothermal fluids, with copper possibly being transported as a chloride complex. Upon reaction with carbonates and zeolites, neutralization of such solutions induces precipitation of native copper and ferric oxyhydroxides. In this model, the bluish haloes around some of the occurrences at Site 884 would be explained as having been caused by alteration products produced by reaction of the circulating fluids with the walls of conduit fractures.

ORGANIC GEOCHEMISTRY

Volatile Hydrocarbons

The shipboard safety and pollution considerations require real-time monitoring of the volatile hydrocarbon content in the sediments drilled. For this reason, 114 samples were collected using the headspace technique (see "Organic Geochemistry" section, "Explanatory Notes" chapter, this volume). The released gas was measured in a Carle gas chromatograph, and the results are presented in Table 11. As at the previous sites, no considerable amounts of C_1 (ethane), C_2 (methane), or C_3 (propane) were detected in the sediments of Site 884. The low gas contents can be ascribed to the low organic carbon contents measured in the sediments (see below) and indicated no methanogenesis in the sediment column that could dangerously affect drilling.

Carbonate Carbon

Te calcium carbonate ($CaCO_3$) content of 258 samples gathered from Site 884 was calculated by multiplying the inorganic carbon (IC) content (measured using a Coulometrics carbon dioxide coulometer) by 8.334. The results of $CaCO_3$ and IC are reported in weight percent in Table 12 and plotted vs. depth in Figure 33.

Generally, the $CaCO_3$ pattern is similar compared with that of Site 883, although the values are lower throughout the entire sequence. This fact has been interpreted as an effect of dissolution, because Site 884 is positioned at a water depth of 3826 m and, thus, about 1440 m deeper than Site 883.

In lithologic Subunits IA and IB (0–128 mbsf and 128–440.2 mbsf, respectively; see "Lithostratigraphy" section, this chapter), the values of $CaCO_3$ do not exceed 20 wt%, as indicated by the vertical line in Figure 33. Calcium carbonate was undetectable in most of the samples, and the carbonate concentrations measured in the remainder probably reflect the abundance of calcareous nannofossils in some intervals (see "Biostratigraphy" section, this chapter).

In lithologic Unit II (604.8–854 mbsf) carbonate abundance is highly variable, having values ranging from 0 to 85 wt%. Because of strong reworking, the overall distribution of the calcareous nannofossil ooze and chalk does not permit the three subunits of lithologic Unit II to be distinguished in the $CaCO_3$ record.

Organic Carbon

Total carbon (TC) was measured using a Carlo Erba NCS analyzer on 101 samples collected from Hole 884B. Total organic carbon (TOC) was calculated by the difference between TC and IC. Detailed procedures are outlined in the "Organic Geochemistry" section of the "Explanatory Notes" chapter (this volume). Total nitrogen values were near or below the detection threshold of the NCS analyzer and were not used for further interpretations. Results of TC, TN, and TOC are presented in weight percent in Table 12.

The organic carbon concentration of Site 884 sediments is low throughout the lower two-thirds and low in the upper one-third of the sequence. The increasing upward trend is clear (indicated by an arrow in Fig. 34). Values range between zero in the lower interval and 0.75 wt% in sediments of the uppermost section from Hole 884B. According to the distribution of sulfate in pore waters (see "Inorganic Geochemistry" section, this chapter), sulfate reduction principally occurs within the upper 250 mbsf. Unusually high sulfate concentrations in the interstitial water of sediments below 250 mbsf, however, indicate that little or no sulfate reduction by organic carbon decay has occurred in this interval. This distribution can be explained as reflecting a low oxidant demand owing to a depleted accumulation rate of organic carbon (Fig. 34; see "Inorganic Geochemistry" section, this chapter).

In the first section of Hole 884B (Section 145-884B-1H-1) a distinct zonation in color is visible. Brownish to brownish-green sediments occur between about 0 and 35 cm, followed by about 40 cm of olive-greenish diatom ooze. Below about 75 cm, the clayey sediments with ash and dropstones display the light gray color typical of the upper few hundred meters of the sediment column. In the greenish layer, organic carbon values range up to 0.75 wt% and show a distinct peak that corresponds with high calcium carbonate values, but is deeper than the $CaCO_3$ concentration peak (Fig. 35). This feature also was seen by Keigwin et al. (1992) in other Detroit Seamount and Meiji Seamount cores. Based on radiocarbon ages, these green sediments represent the last deglaciation, and Keigwin et al. (1992) interpreted the organic carbon peak (which also corresponds with an opal peak in their cores) as a deglacial productivity maximum. If this peak is controlled by orbital forcing, it should also appear in previous deglaciations, which can be tested by high-resolution analysis of deeper intervals at sites such as Site 884.

PHYSICAL PROPERTIES

Introduction

Index property (densities, porosities, water contents, and void ratios), digital sediment velocimeter (DSV), and shear strength meas-

Table 9 (continued).

Carbonate		TOC	
(%)	(g[cm^2·k.y.]$^{-1}$)	(%)	(g[cm^2·k.y.]$^{-1}$)
2.7	0.076	0.41	0.012
2.9	0.093	0.24	0.076
2.4	0.051	0.13	0.003
5.9	0.051	0.17	0.001
10.6	0.059	0.08	0.000

urements were taken at 1.5-m intervals in cores from Holes 884A and 884B. In cores from Hole 884C, index properties were measured at 1.5-m intervals and shear strength and DSV measurements were taken at approximately 3-m intervals. A summary of all measurements taken is shown in Table 13. Continuous measurements of GRAPE bulk density, P-wave velocities, and magnetic susceptibility were taken in all five holes using the multisensor track (MST). Tables containing the compressional wave velocity (from DSV and Hamilton Frame) and shear strength data from Holes 884B, 884C, and 884E are included, as are tables of index property data from Holes 884A, 884B, 884C, and 884E (Tables 14 through 17). GRAPE and the P-wave logger data have been smoothed and culled in the same manner as those from Sites 881, 882, and 883 (see "Physical Properties" section, "Site 881" chapter, this volume). Thermal conductivity measurements were conducted on the core of Holes 884B and 884C.

Index Properties and Vane Shear Strength

Profiles of sediment wet-bulk density, dry-bulk density, dry water content, and porosity values for Holes 884B and 884C (see Figs. 36 and 37) show good correspondence. The shear strength profiles correlate well in the top 85 mbsf, which was cored using the APC, but this correlation does not continue to such an extent in the XCB-cored section (see Fig. 38). Shear strength values increase along trends consistent with increasing overburden pressure downhole.

In lithologic Subunit IA (see "Lithostratigraphy" section, this chapter), the wet-bulk density, dry-bulk density, dry water content, and wet porosity values in the upper 128 mbsf remain fairly constant, averaging 1.38 g/cm^3, 0.60 g/cm^3, 136%, and 76%, respectively. Based upon the physical properties data from Holes 884B and 884C, Subunit IB (128–440 mbsf) is characterized by a distinct decrease in both wet-bulk density (to an average of 1.33 g/cm^3), and dry-bulk density (to an average of 0.55 g/cm^3) and a corresponding increase in wet porosity and dry water content to averages of 77% and 145%, respectively (see Figs. 37 through 39). These slope breaks at approximately 128 mbsf correspond to a change in sediment type from a clay with diatoms above 128 mbsf to a clayey diatom ooze below (see "Lithostratigraphy" section, this chapter). The changes observed in index properties are most likely the result of a relative increase in biogenic silica in Subunit IB. A second, less marked change in the baseline value of wet-bulk density occurs at approximately 440 mbsf, marking the top of Subunit IC. At this point, the wet-bulk and dry-bulk density values increase (to an average of 1.41 and 0.67 g/cm^3, respectively), which corresponds to a slight decrease in the dry water content (averaging 114%) and wet porosity (to an average of 73%). This boundary is more pronounced in the grain density profiles (Fig. 39). The top of Subunit IC is coincident with a slight decrease in the percentage diatom component that was observed from smear slide analysis, and may explain the changes in index-property data (see "Lithostratigraphy" section, this chapter). In lithologic Subunit ID,

Table 10. Interstitial-water data for Site 884.

Core, section, interval (cm)	Depth (mbsf)[a]	pH	Alk. (mM)	S (g/kg)	C (mM)	Mg (mM)	Ca (mM)	SO_4 (mM)	NH_4 (µM)	NO_2 (µM)	H_4SiO_4 (µM)	K (mM)	Li (µM)	Na (mM)	Sr (µM)	Mn (µM)	Mg/Ca (mol ratio)
145-884A-																	
1H-1, 145–150	3.65	7.79	4.63	35.0	554	52.2	10.6	27.5	74	0	859	10.54	25.5	477	86	66	4.94
1H-2, 145–150	5.10	7.77	4.84	35.0	554	52.9	10.8	27.5	110	0.17	747	10.42	24.9	476	87	80	4.88
1H-4, 145–150	6.95	7.67	5.15	35.0	554	53.2	11.0	27.6	393	0.24	768	9.95	24.3	475	88	105	4.82
145-884B-																	
1H-2, 145–150	2.95	7.63	4.03	35.0	554	52.1	10.5	28.6	96	0	962	10.17	26.5	480	87	61	4.96
2H-4, 145–150	12.45	7.73	5.98	35.0	558	53.4	11.1	26.7	209	0	732	9.90	23.8	478	89	118	4.80
3H-4, 145–150	21.95	7.72	6.66	35.0	561	52.4	10.9	25.6	408	0	950	10.17	24.0	482	88	145	4.83
4H-4, 145–150	31.45	7.77	7.58	35.0	565	51.8	11.2	25.0	372	0	833	9.91	23.6	486	87	143	4.64
5H-4, 145–150	40.95	7.80	7.91	35.0	565	51.4	11.1	24.7	576	n.m.	828	10.06	23.8	486	89	109	4.63
6H-4, 145–150	50.45	7.85	8.58	35.0	562	51.8	11.2	24.0	452	n.m.	823	10.77	24.2	481	88	96	4.62
8H-4, 145–150	69.45	7.81	8.50	35.0	562	50.3	10.8	23.5	603	n.m.	921	10.04	25.0	485	85	76	4.66
10H-1, 115–120	83.65	7.77	8.67	35.0	561	49.9	11.0	22.9	567	n.m.	881	9.76	26.6	483	88	62	4.55
13X-3, 145–150	97.75	7.69	8.54	35.0	560	49.3	10.9	22.4	546	n.m.	830	9.95	26.0	482	87	58	4.51
15X-4, 145–150	118.55	7.85	8.50	35.0	560	48.8	10.6	21.9	569	n.m.	1165	9.78	27.9	483	86	64	4.61
17X-4, 145–150	137.75	7.75	8.23	34.5	559	48.4	10.7	21.9	623	n.m.	909	10.80	28.2	481	88	49	4.52
21X-4, 145–150	176.45	7.91	8.02	34.5	559	48.4	10.6	21.4	689	n.m.	1012	9.84	31.8	481	89	38	4.55
24X-4, 145–150	205.35	7.64	8.23	34.5	560	48.5	11.3	21.4	678	n.m.	1039	8.57	33.8	482	93	65	4.29
27X-4, 145–150	234.35	7.63	8.20	35.0	561	48.5	12.0	20.8	668	n.m.	1058	9.48	36.6	480	96	77	4.05
30X-4, 145–150	263.25	7.75	8.13	35.0	561	47.3	12.2	20.9	668	n.m.	1060	8.82	40.8	482	96	58	3.89
33X-3, 145–150	290.75	7.57	7.65	34.5	563	47.7	12.9	21.2	695	n.m.	1094	8.89	44.9	482	100	64	3.68
36X-4, 145–150	321.25	7.56	6.63	35.0	562	46.9	13.4	20.9	661	n.m.	1115	9.72	52.0	479	101	74	3.49
39X-4, 145–150	349.85	7.58	7.65	35.0	562	47.1	15.4	21.5	560	n.m.	1180	10.64	56.2	476	110	72	3.07
42X-3, 145–150	377.15	7.60	7.17	35.0	561	47.1	16.1	21.8	574	n.m.	1086	10.38	61.7	474	113	62	2.93
45X-5, 145–150	407.65	7.67	6.94	35.0	561	48.0	17.3	21.6	519	n.m.	1084	8.25	67.6	472	123	62	2.78
48X-5, 145–150	436.55	7.77	6.12	35.0	563	47.8	18.2	22.5	488	n.m.	1163	8.79	75.9	472	123	56	2.63
52X-4, 145–150	474.85	7.46	6.13	35.0	561	48.3	19.9	22.7	662	n.m.	n.m.	8.85	78.8	466	131	72	2.42
56X-4, 145–150	513.35	7.67	6.40	35.0	562	48.8	22.2	22.5	400	n.m.	1213	6.92	85.9	464	143	81	2.20
59X-4, 145–150	542.35	7.16	5.05	35.0	561	48.5	22.8	23.4	379	n.m.	1173	8.35	85.9	461	151	79	2.12
62X-4, 145–150	571.25	7.31	6.00	35.0	563	48.8	24.8	24.0	395	n.m.	1194	6.99	87.9	462	168	88	1.97
65X-4, 145–150	600.05	7.57	4.56	35.0	562	48.5	24.6	23.2	472	n.m.	1331	6.76	91.8	459	175	85	1.97
68X-4, 145–150	628.75	7.26	4.54	35.0	559	48.9	27.4	23.9	225	n.m.	1225	6.12	86.4	452	168	158	1.78
71X-4, 145–150	657.65	7.35	3.92	35.0	562	48.8	29.0	24.8	194	n.m.	1209	7.07	73.6	452	174	125	1.68
74X-4, 145–150	686.55	n.m.	n.m.	n.m.	524	48.7	29.3	23.0	144	n.m.	1086	5.11	65.4	n.m.	184	147	1.66
77X-4, 145–150	715.40	7.43	1.95	35.0	562	48.4	31.3	25.2	162	n.m.	1108	3.37	39.5	451	204	145	1.55
80X-4, 145–150	744.30	7.89	0.71	35.0	561	47.2	31.3	24.2	103	n.m.	179	2.06	32.4	451	215	73	1.51
83X-4, 145–150	773.30	8.09	1.17	35.0	560	47.1	30.0	25.0	79	n.m.	206	2.82	31.1	454	216	21	1.57
86X-4, 145–150	802.30	8.12	0.73	35.0	559	48.4	29.7	25.4	83	n.m.	198	1.86	34.6	452	236	20	1.63
89X-4, 145–150	831.00	n.m.	n.m.	n.m.	527	53.7	26.4	23.2	29	n.m.	131	1.78	32.7	n.m.	236	39	2.04

[a] Depth of Hole 883A cores is based on correlation of Holes 883A and 883B using magnetic susceptibility data. n.m. = not measured.

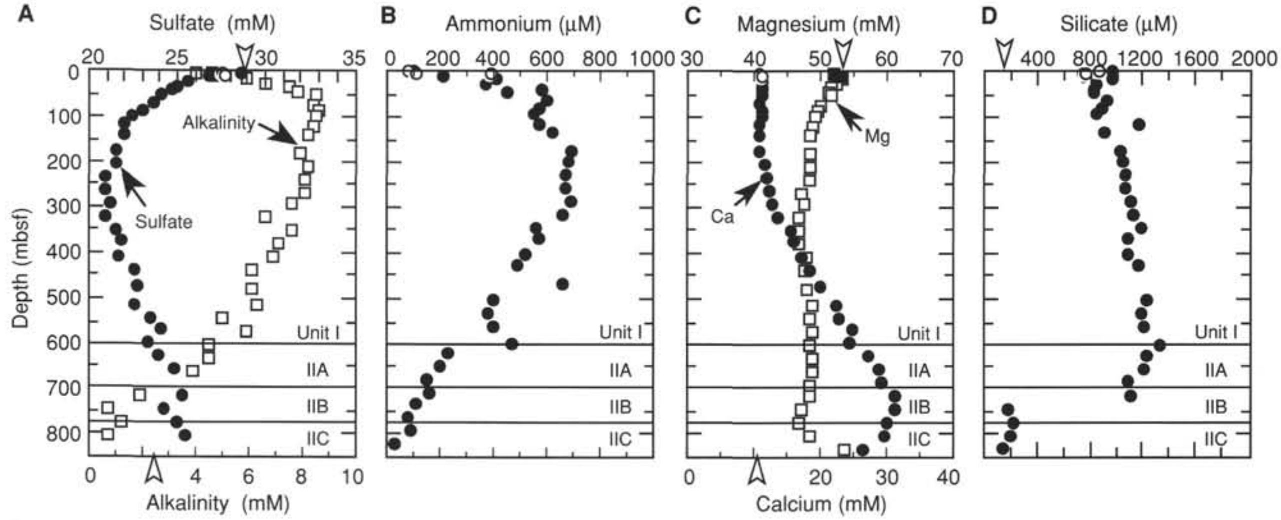

Figure 31. Interstitial-water profiles for Site 884. **A.** Sulfate and alkalinity composite profile for Holes 884A and 884B. **B.** Ammonium composite profile for Holes 884A and 884B. **C.** Magnesium and calcium composite profiles for Holes 884A and 884B. **D.** Silicate composite profile for Holes 884A and 884B, open circles and closed squares represent data from Hole 884A, while closed circles and open squares mark data from Hole 884B. Open arrowhead indicates the concentration in modern North Pacific Deep Water.

which begins at 550 mbsf, the values of wet-bulk density, dry-bulk density, dry water content, and wet porosity remain similar to those in Subunit IC. However, the break of slope seen in the profiles of wet and dry-bulk densities, dry water content, and wet porosity, which occurs a little higher at approximately 535 mbsf, does not correspond to the boundary of Subunits IC and ID.

The top of Subunit IIA (at 604 mbsf), is marked by a distinct increase in the values of wet-bulk (to 1.57 g/cm^3) and dry-bulk (to 0.89 g/cm^3) densities, and by decreases in both dry water content and wet porosity, to averages of 81% and 66%, respectively. This coincides with the lithologic change to claystones and chalks and is probably the result of diagenesis and cementation of the clays. In Subunit IIB, index-property data do not display any distinct slope breaks, and the average values are almost identical to those seen in Subunit IIA. However, the onset of lithologic Subunit IIC is clearly shown as an increase in the wet-bulk and dry-bulk density data and a decrease in values for dry water content and wet porosity (to averages of 1.82 g/cm^3, 1.27 g/cm^3, 45% and 54% respectively). These variations can be accounted for by the presence of altered ashes, because of their higher grain densities (see "Lithostratigraphy" section, this chapter). Basalt (Unit III), was cored in the base of Holes 884B and 884E, 843 to 930 mbsf (see "Igneous Petrology" section, this chapter); the bulk densities within Unit III range from 2.64 to 2.95 g/cm^3.

The grain density profiles (Fig. 39) display trends similar to those seen in the wet-bulk density profiles. Within lithologic Subunit IA, the grain density is fairly constant at 2.56 g/cm^3, while in Subunit IB, below 128 mbsf, grain density decreases to approximately 2.38 g/cm^3. This decrease is probably the result of the relative decrease in terrigenous clay and increase in biogenic opal content. The grain density values then increase to values of approximately 2.53 g/cm^3 in Subunit IC (due to the appearance of claystone), at 440 mbsf, then decrease in Subunit ID at 550 mbsf to an average of 2.46 g/cm^3, most likely the results of the relative increase in diatom content. The boundary between Units IC and ID is much more evident in the grain density profiles, which contrasts with other index-properties data, whose values do not change significantly (see Fig. 36).

Within Subunit IIA, grain densities increase to an average of 2.66 g/cm^3 and then increase again in Subunit IIB to approximately 2.68 g/cm^3, this lithostratigraphic boundary is not as clearly delineated by the profile of grain density, as it is by the profiles of other index properties (see Fig. 36). In Subunit IIC, a further increase in values can be seen, to an average of 2.76 g/cm^3, perhaps because of the presence

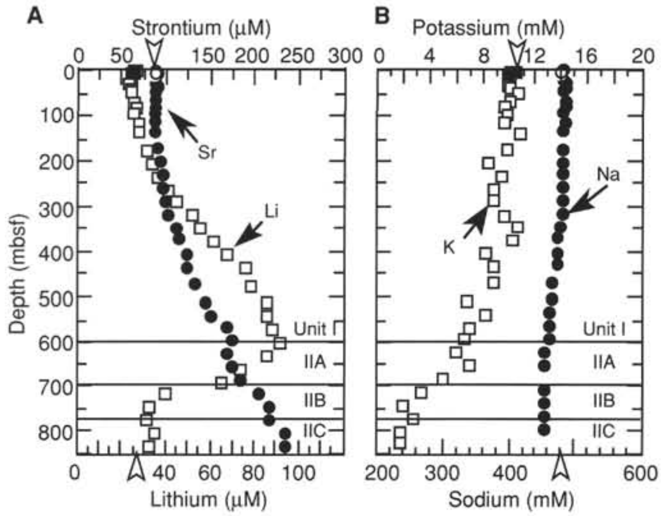

Figure 32. Interstitial-water profiles for Site 884. **A.** Strontium and lithium composite profiles for Holes 884A and 884B. **B.** Potassium and sodium composite profiles for Holes 884A and 884B. Open circles and closed squares represent data from Hole 884A, while closed circles and open squares mark data from Hole 884B. Open arrowhead indicates the concentration in modern North Pacific Deep Water.

of altered ashes found in this subunit. Within the basalts (Unit III) at the base of Hole 884E, grain densities range from 2.79 to 3.02 g/cm^3.

GRAPE Density

Figure 40 shows a profile of the GRAPE bulk density for each of Holes 884A, 884B, and 884C. Although in all three cases GRAPE bulk density profiles parallel the trends of those obtained with the pycnometer, GRAPE data were consistently higher in value than those data produced by pycnometer analysis by approximately 0.1 g/cm^3 (see "Physical Properties" section, Site 881 chapter, this volume); however data from the two methods converge in the bottom 250 m of Hole 884B, in lithologic Unit II (a similar phenomenon is seen in the logging data; see "Downhole Measurements" section, this chapter). The convergence of the two data sets may result from the cores being

Table 11. Results of headspace gas analyses from Holes 884A, 884B, and 884C.

Core, section, interval (cm)	Depth (mbsf)	C_1 (ppm)	C_2 (ppm)	C_3 (ppm)
145-884A-				
1H-5, 0–3	6.00	7	3	1
145-884B-				
1H-3, 0–3	3.00	4	4	2
2H-5, 0–3	12.50	3	3	1
3H-5, 0–3	22.00	3	3	1
4H-5, 0–3	31.50	2	2	1
5H-5, 0–3	41.00	8	6	1
6H-5, 0–3	50.50	8	9	1
7H-5, 0–3	60.00	8	6	1
8H-5, 0–3	69.50	7	8	1
9H-5, 0–3	79.00	8	11	1
10H-2, 0–3	83.70	5	7	1
12X-1, 0–3	87.30	11	1	11
13X-4, 0–3	97.80	2		
15X-4, 0–3	117.10	9	14	1
16X-5, 0–3	128.20	14	6	1
17X-5, 0–3	137.80	10	11	1
18X-5, 0–3	147.50	15	3	1
19X-5, 0–3	157.10	11		
21X-5, 0–3	176.50	9	3	3
22X-5, 0–3	186.10	17	5	1
23X-4, 0–3	194.30	10	4	1
24X-5, 0–3	205.40	5	6	1
25X-5, 0–3	215.10	6	5	1
26X-5, 0–3	224.70	11	5	2
27X-5, 0–3	234.40	13	6	1
29X-2, 0–3	249.10	3	4	1
30X-5, 0–3	263.30	5	8	1
31X-5, 0–3	273.00	3	2	1
32X-5, 0–3	282.70	4	5	2
33X-4, 0–3	290.80	2	2	1
34X-2, 0–3	297.50	4	10	2
35X-5, 0–3	311.70	7	10	2
36X-5, 0–3	321.30	4	2	2
37X-5, 0–3	331.00	10	7	2
38X-5, 0–3	340.30	3	4	1
39X-5, 0–3	349.90	9	10	1
40X-5, 0–3	359.60	7	6	1
41X-5, 0–3	369.10	8	1	8
42X-4, 0–3	377.20	3		
43X-5, 0–3	388.40	6	1	6
44X-5, 0–3	398.00	11	8	1
45X-5, 0–3	407.70	15	2	8
46X-5, 0–3	417.30	9	3	3
47X-5, 0–3	426.90	13	4	3
48X-5, 0–3	436.60	11	1	11
49X-5, 0–3	446.20	8	1	8
50X-5, 0–3	455.80	8		
51X-5, 0–3	465.30	12	1	12
52X-5, 0–3	474.90	14	1	1
53X-5, 0–3	484.60	11		
56X-5, 0–3	513.40	7		
57X-5, 0–3	523.10	9	1	9
58X-5, 0–3	532.70	4		
59X-5, 0–3	542.40	7		
60X-5, 0–3	552.10	8		
61X-5, 0–3	561.60	3		
62X-5, 0–3	571.30	8		
63X-5, 0–3	580.80	2		
65X-5, 0–3	600.10	5		
66X-5, 0–3	609.80	6		
67X-5, 0–3	619.30	5		
68X-5, 0–3	628.80	6		
69X-5, 0–3	638.40	4		
70X-5, 0–3	648.00	4		
71X-5, 0–3	657.70	2		
72X-5, 0–3	667.30	4		
73X-4, 0–3	675.50	3		
74X-5, 0–3	686.60	2		
75X-5, 0–3	696.20	2		
76X-5, 0–3	705.80	3		
77X-5, 0–3	715.50	2		
78X-5, 0–3	725.10	3		
79X-5, 0–3	734.80	3		
83X-5, 0–3	773.40	3		
84X-4, 0–3	781.50	2		
85X-4, 0–3	791.20	3		
86X-4, 137–140	802.27	3		
87X-5, 0–3	812.10	2		
88X-3, 0–3	818.60	2		
89X-4, 137–140	830.97	2		
90X-2, 0–3	836.10	2		
91X-2, 0–3	845.80	2		

Table 11 (continued).

Core, section, interval (cm)	Depth (mbsf)	C_1 (ppm)	C_2 (ppm)	C_3 (ppm)
145-884C-				
2H-5, 0–3	8.40	2	2	
3H-5, 0–3	17.90	6	2	3
4H-4, 0–3	25.90	7	2	1
5H-4, 0–3	35.40	8	1	8
6H-6, 0–3	47.90	9	1	9
7H-4, 0–3	54.40	8	1	8
8H-5, 0–3	65.40	7		
9H-5, 0–3	74.90	12		
10X-3, 0–3	81.40	8		
12X-3, 0–3	100.80	10		
13X-4, 0–3	111.90	6		
14X-2, 0–3	118.50	6		
15X-5, 0–3	132.70	10		
16X-5, 0–3	142.30	11		
17X-4, 0–3	150.50	11		
18X-5, 0–3	161.70	11		
19X-5, 0–3	171.30	11		
20X-5, 0–3	181.00	11		
21X-5, 0–3	190.60	10		
22X-5, 0–3	200.30	12		
23X-5, 0–3	210.00	12		
24X-5, 0–3	219.60	10		
25X-5, 0–3	229.30	11		
26X-5, 0–3	238.90	7		
27X-5, 0–3	248.50	5		
28X-5, 0–3	258.20	6		
29X-5, 0–3	267.80	6		
31X-5, 0–3	287.10	3		
32X-5, 0–3	296.70	3		
35X-5, 0–3	325.70	7		
36X-5, 0–3	335.20	9		
37X-5, 0–3	344.70	7		

C_1 = methane, C_2 = ethane, C_3 = propane.
Note: all samples analyzed were headspace samples.

held in their liners, under some pressure, during GRAPE testing and because when they are split, expansion takes place and any water between the liner and the sediment may be soaked up, thus yielding lower bulk density values. Discrete 2-min count measurements were used when testing the selected samples of basalt from Hole 884E.

Compressional Wave Velocities

Figure 41 shows profiles of compressional wave velocity data. The P-wave profiles include data from the P-wave logger (PWL), Hamilton Frame, and the DSV. Below 85 mbsf, PWL data are not available due to the nature of the XCB cores. Compressional wave velocities obtained from the PWL average 1480 m/s (1451 m/s in Hole 884B, 1508 m/s in Hole 884C) throughout the section logged, but increase down the hole (Fig. 41A), as do the velocities measured with the DSV and Hamilton Frame. The spiky nature of the PWL data may be attributed to the presence of ash layers and coarse ice-rafted debris (IRD) (see "Lithostratigraphy" section, this chapter). The DSV and Hamilton Frame measurements are less sensitive to the presence of the ash layers and IRD because of the bias inherent in the discontinuous nature of DSV and Hamilton Frame sampling. Figure 41B shows data from the DSV, and the Hamilton Frame and the predicted velocity curve for a diatomaceous silty clay (Hamilton, 1979). Data from Site 884 have lower values, which may be attributable to high concentrations of diatoms and clay, which have lower compressional wave velocities, as reported by Tucholke et al. (1976; e.g., clayey diatom ooze: 1580 m/s and diatom-rich clay: 1520 m/s), or more likely, second a rebound effect whereby the sediments experience gas expansion during recovery causing velocities to decrease. This effect also can be seen when comparing physical properties data with sonic log data (see "Downhole Measurements" section, this chapter).

The compressional wave velocity, obtained from DSV and Hamilton Frame measurements of cores from Hole 884B, range from 1416

Table 12. Results of geochemical analyses from Hole 884B.

Core, section, interval (cm)	Depth (mbsf)	TC (wt%)	IC (wt%)	TOC (wt%)	$CaCO_3$ (wt%)	TN (wt%)
145-884B-						
1H-1, 14–15	0.14	1.49	1.30	0.19	10.8	0
1H-1, 32–33	0.32	1.44	1.20	0.24	10.0	0.05
1H-1, 41–42	0.41	2.16	1.66	0.50	13.8	0.08
1H-1, 46–47	0.46	1.85	1.21	0.64	10.1	0.08
1H-1, 53–54	0.53	1.95	1.21	0.74	10.1	0.10
1H-1, 60–61	0.60	1.35	0.60	0.75	5.0	0.11
1H-1, 68–69	0.68	0.89	0.15	0.74	1.2	0.10
1H-1, 72–73	0.72	0.81	0.08	0.73	0.7	0.10
1H-1, 76–77	0.76	0.40	0	0.40	0	0.06
2H-1, 74–75	7.24	0.35	0.20	0.15	1.7	0.04
2H-3, 77–78	10.27	0.51	0.05	0.46	0.4	0.08
2H-6, 76–77	14.76	0.49	0	0.49	0	0.06
3H-1, 77–78	16.77	0.34	0	0.34	0	0.06
3H-3, 70–71	19.70	0.48	0.06	0.42	0.5	0.07
3H-6, 61–62	24.11	0.53	0.14	0.39	1.2	0.06
4H-1, 111–112	26.61	0.45	0	0.45	0	0.07
4H-3, 111–112	29.61	0.37	0	0.37	0	0.06
4H-5, 76–77	32.26	0.32	0	0.32	0	0.05
5H-1, 78–79	35.78	0	0			
5H-3, 77–78	38.77	1.21	0.86	0.35	7.2	0.05
5H-6, 77–78	43.27	0	0			
6H-1, 77–78	45.27	0	0			
6H-3, 76–77	48.26	0.49	0	0.49	0	0.07
6H-6, 76–77	52.76	0	0			
7H-1, 76–77	54.76	0	0			
7H-3, 75–76	57.75	0.40	0	0.40	0	0.08
7H-6, 76–77	62.26	0	0			
8H-1, 76–77	64.26	0	0			
8H-3, 76–77	67.26	0.47	0	0.47	0	0.08
8H-6, 66–67	71.66	0	0			
9H-1, 76–77	73.76	0	0			
9H-3, 76–77	76.76	0.29	0	0.29	0	0.06
9H-7, 31–32	82.31	0	0			
12X-1, 35–36	87.65	0.30	0	0.30	0	0.07
13X-1, 76–77	94.06	0	0			
13X-3, 77–78	97.07	0.18	0	0.18	0	0.05
14X-1, 77–78	103.77	0	0			
14X-3, 77–78	106.77	0.13	0	0.13	0	0.05
14X-6, 77–78	111.27	0	0			
15X-1, 76–77	113.36	0	0			
15X-3, 76–77	116.36	0.20	0	0.20	0	0.06
15X-6, 77–78	120.87	0	0			
16X-1, 76–77	122.96	0	0			
16X-3, 76–77	125.96	0.22	0	0.22	0	0.06
16X-6, 76–77	130.46	0	0			
17X-1, 77–78	132.57	0	0			
17X-3, 77–78	135.57	0.21	0	0.21	0	0.06
17X-6, 77–78	140.07	0	0			
18X-1, 77–78	142.27	1.53	1.33	0.2	11.1	0.05
18X-3, 77–78	145.27	1.32	1.00	0.32	8.3	0.07
18X-6, 77–78	149.77	0	0			
19X-1, 78–79	151.88	1.39	1.18	0.21	9.8	0.05
19X-3, 78–79	154.88	0	0			
19X-6, 78–79	159.38	0.49	0.3	0.19	2.5	0.05
21X-1, 76–77	171.26	0	0			
21X-3, 76–77	174.26	2.03	1.85	0.18	15.4	0.07
21X-6, 76–77	178.76	0	0			
22X-1, 77–78	180.87	0	0			
22X-3, 77–78	183.87	0.34	0	0.34	0	0.06
22X-6, 77–78	188.37	0	0			
23X-1, 77–78	190.57	0	0			
23X-3, 77–78	193.57	0.29	0	0.29	0	0.06
23X-6, 77–78	198.07	0	0			
24X-1, 77–78	200.17	0	0			
24X-3, 76–77	203.16	0.27	0	0.27	0	0.06
24X-6, 76–77	207.66	0	0			
25X-1, 77–78	209.87	0	0			
25X-3, 77–78	212.87	0.24	0	0.24	0	0.06
25X-6, 76–77	217.36	0	0			
26X-1, 77–78	219.47	0	0			
26X-3, 76–77	222.46	0.45	0	0.45	0	0.07
26X-6, 76–77	226.96	0	0			
27X-1, 76–77	229.16	0	0			
27X-3, 76–77	232.16	0.21	0	0.21	0	0.07
27X-6, 75–76	236.65	0	0			
28X-1, 38–39	238.38	0	0			
29X-1, 76–77	248.36	0	0			
29X-3, 76–77	251.36	0.28	0	0.28	0	0.05
30X-1, 77–78	258.07	0.26	2.2			
30X-3, 77–78	261.07	0.19	0	0.19	0	0.05
30X-6, 77–78	265.57	1.54	12.8			
31X-1, 77–78	267.77	0	0			
31X-3, 77–78	270.77	2.03	1.84	0.19	15.3	0.05
31X-6, 77–78	275.27	0	0			
32X-1, 77–78	277.47	0	0			
32X-3, 77–78	280.47	0.19	0	0.19	0	0.05
32X-6, 77–78	284.97	0	0			
33X-1, 77–78	287.07	0.20	1.7			
33X-2, 77–78	288.57	0.25	0	0.25	0	0.05
33X-5, 77–78	293.07	0	0			
34X-1, 77–78	296.77	0	0			
34X-3, 76–77	299.76	0.19	0	0.19	0	0.05
35X-1, 77–78	306.47	0.28	2.3			
35X-3, 77–78	309.47	0.22	0	0.22	0	0.05
35X-6, 77–78	313.97	0	0			
36X-1, 78–79	316.08	0	0			
36X-3, 77–78	319.07	0.26	0	0.26	0	0.05
36X-6, 77–78	323.57	0.35	2.9			
37X-1, 76–77	325.76	0	0			
37X-3, 77–78	328.77	0.28	0.15	0.13	1.2	0.01
37X-6, 75–76	333.25	0.45	3.7			
38X-1, 76–77	335.06	0.36	3			
38X-3, 76–77	338.06	0.71	0.48	0.23	4	0.05
38X-4, 76–77	339.56	0.13	1.1			
39X-1, 78–79	344.68	0	0			
39X-3, 78–79	347.68	0.17	0	0.17	0	0.04
39X-6, 76–77	352.16	0	0			
40X-1, 76–77	354.36	0	0			
40X-3, 76–77	357.36	0.15	0	0.15	0	0.04
40X-6, 76–77	361.86	0	0			
41X-1, 76–77	363.86	0	0			
41X-3, 66–67	366.76	0.15	0	0.15	0	0.01
41X-6, 82–83	371.42	0	0			
42X-1, 77–78	373.47	0	0			
42X-3, 77–78	376.47	0.11	0	0.11	0	0.03
42X-6, 74–75	380.94	0	0			
43X-1, 61–62	383.01	0	0			
43X-3, 61–62	386.01	0.10	0	0.10	0	0.01
43X-6, 56–57	390.46	0	0			
44X-1, 83–84	392.83	0	0			
44X-3, 74–75	395.74	0.01	0	0.01	0	0.01
45X-1, 79–80	400.29	0	0			
45X-3, 88–89	402.58	1.80	15.0			
45X-6, 78–79	405.48	0.86	0.74	0.12	6.2	0.01
46X-1, 55–56	409.75	0.25	2.1			
46X-3, 83–84	412.13	0.53	4.4			
46X-6, 82–83	415.12	2.30	2.11	0.19	17.6	0.04
47X-1, 77–78	419.57	0.90	7.5			
47X-3, 126–127	422.16	0	0			
47X-6, 88–89	424.78	0.1	0	0.1	0	0.03
48X-1, 84–85	429.24	1.36	11.3			
48X-3, 60–61	431.20	0.52	4.3			
48X-6, 60–61	434.20	2.43	2.34	0.09	19.5	0.01
49X-1, 20–21	438.30	0.14	1.2			
49X-3, 84–85	441.04	0	0			
49X-6, 98–99	444.18	0.15	0	0.15	0	0.03
50X-1, 79–80	448.49	0	0			
50X-3, 36–37	450.16	0	0			
50X-6, 125–126	454.05	2.74	22.8			
51X-1, 93–94	458.23	1.15	9.6			
51X-3, 54–55	459.84	0.24	2.0			
51X-6, 72–73	463.02	0.31	0	0.31	0	0.02
52X-1, 121–122	468.01	0	0			
52X-3, 105–106	469.95	0	0			
52X-6, 80–81	472.70	0.09	0	0.09	0	0.02
53X-1, 142–143	477.82	0	0			
53X-3, 36–37	478.96	0	0			
53X-6, 91–92	482.51	0.24	0.15	0.09	1.2	0.02
54X-1, 33–34	486.43	0	0			
54X-3, 44–45	488.64	0.11	0.9			
54X-6, 90–91	492.10	0.10	0	0.1	0	0.03
55X-1, 90–91	496.60	0	0			
55X-3, 24–25	498.04	0	0			
55X-6, 67–68	501.47	0.25	0.09	0.16	0.7	0.03
56X-1, 23–24	505.23	0	0			
56X-3, 79–80	508.19	0	0			
56X-6, 103–104	511.43	0.12	0	0.12	0	0.02
57X-1, 77–78	515.67	0	0			
57X-3, 57–58	517.67	0	0			
57X-6, 57–58	520.67	0.12	0	0.12	0	0.03
58X-1, 57–58	525.17	0	0			
58X-3, 82–83	527.52	0	0			
58X-6, 91–92	530.61	0.08	0	0.08	0	0.03
59X-1, 79–80	534.99	0	0			
59X-3, 86–87	537.26	1.94	16.2			
59X-6, 80–81	540.20	0.29	0.15	0.14	1.2	0.03
60X-1, 81–82	544.71	0	0			
60X-3, 78–79	546.88	0	0			

Table 12 (continued).

Core, section, interval (cm)	Depth (mbsf)	TC (wt%)	IC (wt%)	TOC (wt%)	$CaCO_3$ (wt%)	TN (wt%)
60X-6, 64–65	549.74	0.1	0	0.1	0	0.02
61X-1, 93–94	554.53	0.53	4.4			
61X-3, 75–76	556.35	0	0			
61X-6, 62–63	559.22	0.07	0	0.07	0	0.02
62X-1, 69–70	563.79	0	0			
62X-3, 76–77	566.06	0	0			
62X-6, 78–79	569.08	0.09	0	0.09	0	0.03
63X-1, 65–66	573.45	0	0			
63X-3, 20–21	575.00	0	0			
63X-6, 57–58	578.37	0.27	0	0.27	0	0
64X-1, 57–58	582.87	0	0			
64X-3, 56–57	584.96	0	0			
64X-6, 68–69	588.08	0.62	0.13	0.49	1.1	0.03
65X-1, 94–95	592.14	4.68	39			
65X-3, 83–84	594.93	5.73	47.7			
65X-6, 89–90	597.99	4.77	4.72	0.04	39.3	0.02
66X-1, 50–51	602.10	3.27	27.2			
66X-3, 76–77	604.56	2.33	19.4			
66X-6, 75–76	607.55	0.08	0	0.08	0	0
67X-1, 73–74	612.03	0	0			
67X-3, 76–77	614.06	0	0			
67X-5, 81–82	617.11	0.08	0	0.08	0	0
68X-1, 81–82	620.11	0	0			
68X-3, 77–78	623.57	0	0			
68X-6, 70–71	626.50	0.14	0	0.14	0	0.03
69X-1, 81–82	631.11	0	0			
69X-3, 77–78	633.17	0	0			
69X-6, 77–78	636.17	0.06	0	0.06	0	0.04
70X-1, 77–78	640.67	0	0			
70X-3, 133–134	643.33	0	0			
70X-6, 52–53	645.52	0.06	0	0.06	0	0
71X-1, 80–81	650.30	0	0			
71X-3, 92–93	652.62	0	0			
71X-6, 44–45	655.14	0.14	0	0.14	0	0
72X-1, 76–77	659.96	1.46	12.2			
72X-3, 113–114	662.43	3.44	28.7			
72X-6, 106–107	665.36	0.06	0	0.06	0	0
73X-1, 78–79	669.58	0	0			
73X-3, 59–60	671.59	0	0			
74X-1, 65–66	674.65	2.91	2.84	0.07	23.7	0.01
74X-3, 42–43	681.02	3.91	32.6			
74X-6, 82–83	684.42	0.08	0	0.08	0	0.01
75X-1, 63–64	688.73	0	0			
75X-3, 105–106	691.25	0	0			
75X-6, 89–90	694.09	9.90	9.83	0.07	81.9	0
76X-1, 53–54	698.23	1.44	12			
76X-3, 72–73	700.52	3.96	33			

Table 12 (continued).

Core, section, interval (cm)	Depth (mbsf)	TC (wt%)	IC (wt%)	TOC (wt%)	$CaCO_3$ (wt%)	TN (wt%)
76X-6, 67–68	703.47	2.98	2.97	0.01	24.7	0.01
77X-1, 24–25	707.54	0	0			
77X-3, 47–48	709.97	9.34	77.8			
77X-6, 99–100	713.49	1.46	1.40	0.06	11.7	0
78X-1, 75–76	717.75	0	0			
78X-3, 77–78	719.87	0	0			
78X-5, 76–77	722.86	0.01	0	0.01	0	0
79X-1, 77–78	725.87	0	0			
79X-3, 77–78	729.57	0	0			
80X-1, 69–70	732.49	3.10	3.02	0.08	25.2	0
80X-3, 78–79	739.18	1.25	10.4			
80X-6, 63–64	742.03	0.04	0	0.04	0	0
81X-1, 47–48	746.37	0	0			
81X-3, 71–72	748.81	2.3	19.2			
82X-1, 82–83	751.92	5.30	5.23	0.07	43.6	0
82X-3, 91–92	758.61	2.1	17.5			
83X-1, 70–71	761.40	7.27	7.28	0	60.6	0
83X-2, 76–77	768.16	6.63	55.2			
83X-6, 72–73	769.62	6.01	5.63	0.38	46.9	0
84X-1, 51–52	775.41	5.12	42.6			
84X-3, 79–80	777.79	2.89	24.1			
84X-6, 77–78	780.77	0.39	0.24	0.15	2.0	0
85X-1, 65–66	785.15	0.45	3.7			
85X-3, 86–87	787.56	4.26	35.5			
85X-6, 60–61	790.30	7.38	7.24	0.14	60.3	0
86X-1, 57–58	794.77	1.54	12.8			
86X-3, 79–80	797.19	4.67	38.9			
86X-6, 67–68	800.07	5.25	5.07	0.18	42.2	0
87X-1, 56–57	804.46	0	0			
87X-3, 68–69	806.78	0	0			
87X-6, 98–99	810.08	0.02	0	0.02	0	0
88X-1, 77–78	814.37	0.2	1.7			
88X-3, 72–73	816.32	0	0			
89X-1, 60–61	819.20	2.92	2.78	0.14	23.2	0.01
89X-3, 29–30	825.39	0	0			
89X-6, 88–89	828.98	0.02	0	0.02	0	0.01
89X-7, 64–65	833.24	0	0			
90X-1, 10–11	834.20	0	0			
90X-3, 93–94	835.53	0	0			
90X-3, 84–85	838.44	0.02	0	0.02	0	0.01
91X-1, 25–26	844.55	0	0			

TC = total carbon, IC = inorganic carbon, TOC = total organic carbon, and TN = total nitrogen. All results are given in weight percent of bulk dry sediment.

to 2247 m/s and average 1572 m/s. In the upper part of Hole 884B (Unit I), velocities range from 1416 to 1683 m/s, increasing down the hole. These data reflect a fluid-dominated system of relatively unconsolidated sediment; this is illustrated in Figure 42, showing compressional wave velocity vs. dry water content; the higher water contents are characteristic of velocities ranging from 1400 to 1600 m/s (mostly data from Unit I). In the lower portion of Hole 884B (within lithologic Unit II), velocities exhibit the greatest variation (1554–2247 m/s) and the highest values, with an average of 1744 m/s. This is probably a response to the variation in the degree of lithification of the sediments, which have typically increasing compressional wave velocity with decreasing dry water content (Fig. 42). The general trend of velocities increasing down the hole can be explained by the sediments consolidating and forming grain-to-grain contacts while increasing bulk modulus and rigidity. Compressional wave velocities of the basalt cored in Hole 884E were measured using the Hamilton Frame, revealing values that range from 4774 to 6135 m/s and average 5763 m/s.

Thermal Conductivity

The thermal conductivity profiles of Holes 884B and 884C (Fig. 43) show three distinct divisions. Within lithologic Unit I (0–604 mbsf), thermal conductivity averages 0.99 W/(m ·°C) and then increases at 604 mbsf (the boundary of Units I and II) to an average of 1.24 W/(m ·°C). At approximately 770 mbsf, the top of Subunit IIC, a further increase to 1.38 W/(m ·°C) is seen, but the range of values is much greater than in Hole 884B (0.55–2.06 W/(m ·°C). The thermal conductivity data are inversely related to the porosity data (Fig. 44). Within Units I and II, little scatter can be seen, indicating that porosity (and water content, because the sediments are saturated) is controlling thermal conductivity. The theoretical thermal conductivity of a mix of fused silica and seawater also is shown in Figure 44, calculated from the following equation relating the conductivities of two phases via porosity.

$$K = K_f \varnothing K_s (1 - \varnothing),$$

where K is thermal conductivity, K_f is fluid conductivity (1.46 W/[m ·°C] for seawater), K_s is the solid conductivity is the solid (3.25 W/[m ·°C] for fused silica), and ϕ is porosity expressed as a fraction (from Wilkens and Handyside, 1985). The data from Hole 884B fall below this line, which may result from the domination of clays and opaline ilica.

DOWNHOLE MEASUREMENTS

Logging Operations and Quality of Logs

Five tools were run in Hole 884E: the Schlumberger Quad combination, formation microscanner (FMS), and geochemical tool strings, and the French magnetometer and susceptibility tools. The wireline heave compensator (WHC) was not operational during any of the logging runs because of failed electronics. Sea-state conditions were mild throughout the logging operations (1–2 m wave amplitude), but inspection of the individual gamma-ray logs from the three separate

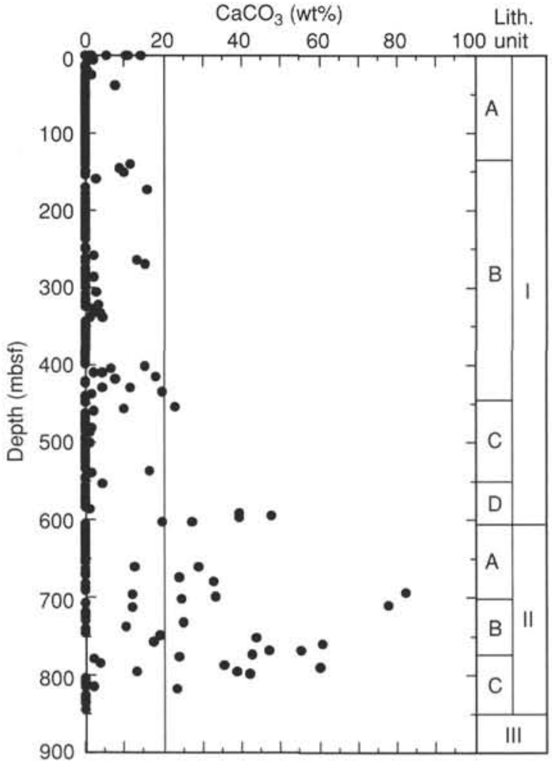

Figure 33. Plot of calcium carbonate contents vs. depth at Hole 884B. Lithostratigraphic units are shown on the right.

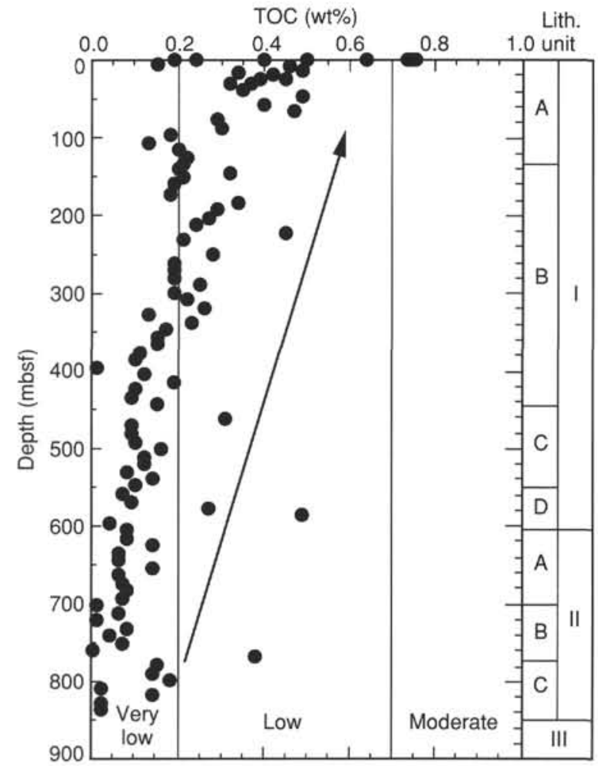

Figure 34. Total organic carbon contents vs. depth at Hole 884B. Arrow indicates increasing upward trend. Lithostratigraphic units are shown on the right.

tool strings demonstrates that ship heave (~1 m) did compromise the resolution of fine-scale lithologic variations. This is particularly true for the slowest logging speed logs (i.e., log data collected from the geochemical tool string). The base of the drill pipe was set at 82 mbsf. A summary of the logging tool strings used on Leg 145, the basis of their measurement principles, and logging operations is provided in the "Explanatory Notes" chapter (this volume).

Total penetration in Hole 884E was 930 mbsf; however, unstable borehole conditions, primarily within lithostratigraphic Subunit IIA, precluded logging operations in the lowermost sediment and igneous basement units. The first logging run was restricted by a bridge at 760 mbsf; continued sloughing of unconsolidated sediments into the borehole during the course of logging operations decreased the total loggable depth to 645 mbsf by the final logging run.

The French CEA-LETI/TOTAL/CNRS-ENS magnetometer (NMRT) and susceptibility (SUMT) tools were run first to ensure that both tools would measure a borehole environment unaffected by any electromagnetic induction measurements. Two passes of the NMRT were conducted uphole at 1800 ft/hour (550 m/hr) over the intervals 760–58.5 and 737.5–62.2 mbsf, respectively. The total field measurements of the NMRT were highly reproducible between the two runs, although the data were degraded by the ship's heave because of the inoperative WHC. In addition, there was a variable depth offset between the two passes. To conserve time, one main up-going log of the SUMT was recorded at the fastest speed of 3600 ft (1100 m/hr) from 682–64 mbsf, and only a shorter repeat up-going log was recorded from 365–59 mbsf.

The Quad combination tool string using the Lamont temperature tool was run third, recording a down-going log from the end of pipe until the failure of the sonic tool (SDT) at 614 mbsf. After a defective SDT sonde was replaced the tool string was deployed a second time, and a main up-going log was recorded from 693 mbsf to the mud line. The quality of the logs recorded durin the Quad run is good; virtually no cycle skipping is apparent in the sonic velocity log despite the rugose nature of the borehole in the uppermost and lowermost sections of the hole.

The formation microscanner (FMS) tool string was run into the hole and set down on a bridge at 654 mbsf, 39 m shallower than on the previous quad run. The main up-going log was recorded at 1500 ft/hr (455 m/hr) from this depth to the base of the pipe, which had been raised from 82 to 52 mbsf. Two repeat up-going logs were recorded over the intervals 654–414 mbsf and, after a slight gain recalibration, 428–52 mbsf. FMS data quality commonly are compromised by ship's heave when the WHC is not used, but the preliminary processed images are of good quality and show little heave-induced "streaking."

The geochemical tool string, consisting of natural gamma ray (NGT), aluminum activation (AACT) and gamma-ray spectrometry (GST) tools, along with the Lamont temperature tool, was the final string run into Hole 884E. As in Hole 883F, problems were encountered when calibrating the GST tool because of the cold borehole temperatures. After several attempts, the GST did calibrate successfully in the warmer, but still distinctly chilly, 13.2°C temperature at total depth (Fig. 45). One complete up-going log of the hole was recorded at a logging speed of 500 ft (150 m) from 647 mbsf to the mud line. However, because of the decreasing borehole temperature during the upgoing log, the GST tool failed calibration tolerance levels at about 328 mbsf, at a borehole temperature of about 7°C. As a result, the elemental yield logs are of uncertain quality in the upper part of the hole, and the yield data are not presented here. Post-cruise processing will determine whether these data contain any valid information. The Al yield from the AACT and K, Th, and U yields from the NGT were not similarly affected and are reliable and of excellent quality.

In all of the logs, signals are either absent or strongly attenuated by the drill pipe in the uppermost section of the hole. The low values in the natural gamma-ray data (Fig. 46) from 69 to 76 mbsf are a result of the NGT entering the end of the drill pipe just before it was pulled

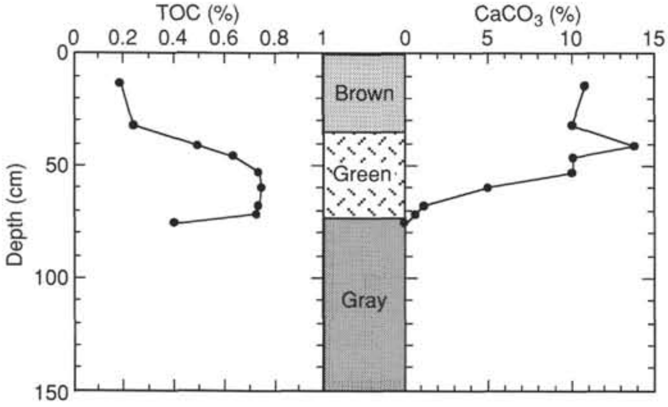

Figure 35. Total organic carbon and calcium carbonate contents vs. depth of Section 145-884B-1H-1. Sediment color is shown in the center of plot.

up 30 m, which caused an attenuation of the signal over this short interval. The neutron porosity log (Fig. 47) appears noisy throughout the entire logged interval and is not a reliable indicator of true formation porosity. This is a result of the high formation porosities encountered in Hole 884E, which are outside the limits for which the tool is calibrated.

Results

Borehole Temperature

Borehole temperatures measured by the Lamont temperature tool (TLT) reflect the temperature of the seawater in the borehole rather than the true formation temperature. The formation cools during drilling operations because of circulation of cold seawater, and only after drilling operations have ceased can the temperatures begin to rebound. The first deployment of the TLT, on the Quad tool string, about 24 hr after the end of drilling operations, yielded a bottom-hole temperature of 10.5°C (Fig. 45). The second deployment of the TLT, on the geochemical tool string, yielded a bottom-hole temperature of 13.2°C; an increase of 2.7°C over the intervening 12 hr.

Lithology

Variations in the log data reflect changes in the physical and chemical properties of the formation. The geochemical and geophysical log data recorded at Hole 884E are presented in Figures 46, 47, and 48. These data are shown adjacent to the major lithology variations, as determined primarily from visual and smear-slide analyses of sediments from Hole 884B (see "Lithostratigraphy" section, this chapter). Good general agreement exists between the lithologic classification of core and the various log responses.

Although the NGT is run on each of the Schlumberger tool strings, the data presented in Figure 46 are taken from the geochemical tool string, which is run at a much lower logging speed and, hence, provides much better counting statistics.

The 850-m-thick sedimentary column at Site 884 is divided into two units based on sediment lithology and on the presence of structures indicative of reworking. Unit I is further divided into four subunits, the uppermost of which, Subunit IA, is rich in clay, IRD, and ash layers. The boundary between Subunits IA and IB at 128 mbsf is well defined in the natural gamma-ray logs (Fig. 46) by a sharp decline in the total gamma-ray flux from the formation, indicative of the change from clay-rich Subunit IA to the clayey diatom ooze of Subunit IB, which contains considerably less clay and, therefore, has a lower K, Th, and U content. This compositional change also is reflected in the Al log (Fig. 47), which shows a sharp decrease across the transition to Subunit IB. The bulk density and resistivity logs

Table 13. Summary of physical properties measurements, Site 884.

Physical properties measurements	Hole 884A	Hole 884B	Hole 884C	Hole 884D	Hole 884E
Index properties	X	X	X		X
Vane shear strength	X	X	X		
DSV or Hamilton Frame	X	X	X		X
GRAPE	X	X	X	X	X
P-wave logger	X	X	X	X	
Thermal conductivity		X	X		

(Fig. 48) decrease across the boundary from Subunit IA to IB; the variability in the logs decreases as well across this boundary. This reflects the change from the higher density and more variable lithology of clay-rich Subunit IA into the more uniform lower density and higher porosity of Subunit IB; this is confirmed by physical property measurements on core samples (see "Physical Properties" section, this chapter). The sonic velocity increases slightly into Subunit IB despite both the decrease in bulk density and increase in porosity. This increase in sonic velocity is caused by the increased matrix rigidity of the diatomaceous material in comparison to the more clay-rich Subunit IA above. Borehole diameter (Fig. 48) also decreases from greater than 18 in. just below the base of the drill pipe in Subunit IA to between 11 and 13 in. in most of Subunit IA. The small inflections in the caliper log at 10-m intervals apparent in Subunit IB were caused by overwashing at the addition of each pipe joint during drilling.

Lithologic Subunits IB, IC, and ID exhibit less variability in all of the logs compared with the overlying Subunit IA. The logs in the lower three subunits reflect the variation of clay and diatomaceous content with little IRD, and with fewer and thinner volcanic ash layers. The natural gamma-ray and Al logs (Figs. 46 and 47) indicate that the lowest clay contents are found from the top of Subunit IB to about 240 mbsf and again in Subunit ID, the less clay-rich diatomite. The positive spike in the gamma-ray log at 275 mbsf, also exhibited in the Al, resistivity, and sonic velocity logs, probably is caused by a volcanic ash layer, although this is not recorded in the cores. Carbonate concretions were encountered in Core 145-884B-31X (~272 mbsf), but these would not produce an increase in the Al log. The bulk density and sonic velocity logs (Fig. 48) indicate a classical compaction trend throughout Subunits IA, IB, and IC, with gradual increase in values with depth. The gradual and normal compaction profile is not evident in the resistivity log, as resistivity actually decreases slowly downhole. The expected increase in resistivity is obscured by the effect of a gradual downward increase in borehole temperatures, which decreases fluid resistivity (compare Figs. 45 and 48).

Within Subunit IC, a pronounced increase in resistivity is centered at about 520 mbsf (Fig. 48). This increase in resistivity is accompanied by a slight increase in both sonic velocity and bulk density logs, but the change is most apparent in the resistivity log, indicating a decrease in porosity. This resistivity anomaly is unusually symmetric and smooth, and little evidence suggests it is entirely related to a lithology change based on core description and information from the other logs. However, native (metallic) copper particles were observed in the depth range of this resistivity anomaly in Cores 145-884B-56X and -57X. The presence of copper implicates probable hydrothermal fluid circulation through this zone, and, therefore, the resistivity increase may result from a decrease of porosity caused by the deposition of secondary minerals from solution. Physical property measurements on discrete core samples confirm a decrease in porosity over this zone (see "Physical Properties" section, this chapter).

Lithologic Subunit IIA consists predominantly of claystone, with lesser amounts of nannofossil chalk, and is the lowermost unit that was logged in Hole 884E. The natural gamma-ray logs (Fig. 46) cover only the uppermost 30 m of this subunit but show a marked increase in total gamma ray, and the Th and K logs indicate higher clay content

Table 14. Index properties, compressional wave velocity, and shear strength data, Hole 884A.

Core, section, interval (cm)	Depth (mbsf)	Wet-bulk density (g/cm^3)	Dry-bulk density (g/cm^3)	Grain density (g/cm^3)	Wet porosity (%)	Dry water content (%)	Void ratio	Shear strength (kPa)	Compressional wave velocity (m/s)
145-884A-									
1H-1, 60	0.60								1487.2
1H-1, 74	0.74	1.31	0.48	2.53	80.7	172.4	4.18		
1H-1, 110	1.10							23.26	
1H-2, 60	2.10								1556.0
1H-2, 74	2.24	1.42	0.65	2.69	75.6	119.6	3.09		
1H-2, 75	2.25								1488.7
1H-2, 115	2.65							24.77	
1H-3, 60	3.60								1504.6
1H-3, 74	3.74	1.29	0.45	2.55	81.8	184.4	4.49		
1H-3, 110	4.10							19.48	
1H-4, 30	4.80								1525.7
1H-4, 59	5.09	1.35	0.55	2.54	78.1	145.9	3.56		
1H-4, 60	5.10								1503.0
1H-4, 110	5.60							33.39	
1H-5, 53	6.53								1453.5
1H-5, 74	6.74	1.37	0.58	2.51	76.5	134.5	3.25		
1H-5, 110	7.10							16.70	
1H-6, 45	7.95								1479.4
1H-6, 74	8.24	1.47	0.74	2.64	71.7	99.4	2.53		
1H-6, 110	8.60							20.87	
1H-7, 29	9.29	1.48	0.73	2.73	72.9	102.5	2.70		

compared with the overlying Subunit ID. The Th/K ratio in this subunit is higher than in the clay-rich lithology of Subunit IA. This may be a reflection of clay type; turbidite deposits are evident in Subunit IIA, and these tend to have higher Th/K ratios than pelagic clays (Fertl, 1979).

There is an increase in baseline values and in the variance of bulk density, resistivity, and sonic velocity on the downward transition into Subunit IIA, which is a reflection of the more varied and rapidly changing lithology within this unit. The borehole diameter (Fig. 47) increases markedly from 11.5 to 16 in. at 620 mbsf, just below the top of Subunit, then rises rapidly from this depth to the base of the logged section at 680 mbsf. These variations in hole size are indicative of the unstable borehole conditions that led to bridge formation and hole fill, and prevented the logging of the lowermost section of this hole.

Comparison of Logs with Core-based Physical Property Measurements

The log and core-based bulk density measurements are displayed in Figure 49. The log bulk density measurements are taken from the high-temperature lithodensity tool (HLDT) and have been smoothed by a linear five-point (0.76 m) moving average filter. The core bulk density measurements have been performed on discrete samples (see "Physical Properties" section, this chapter). Overall correlation between the two types of measurements is good, although on average the discrete core samples are 0.1 g/cm^3 less dense than the log measurements. The origin of this error is uncertain; the core bulk density measurements were back-calculated from dry volumes to account for expansion of samples caused by the rebound effect, but the error may be related to water adsorption by the samples during recovery or while at the surface. The largest discrepancies in correlation between the core and log values occur in the upper and lower portions of the hole in the more variable lithologies of Subunits IA and IIA, where core recovery was poorer and the borehole diameter larger. The poorer recovery in these zones limits information from the core-based studies, and the larger borehole diameter will decrease the statistics of the log-based bulk density measurements.

The comparison of sonic velocity from core- and log-based measurements is shown in Figure 50. The log measurements have been taken from the digital sonic tool (SDT) and are an average of the long- and short-spacing measurements. The core measurements on discrete samples were performed by using the digital sediment velocimeter (DSV) in the upper 350 m of the hole and by using the Hamilton Frame apparatus in the lower portion of the hole (see "Physical Properties" section, this chapter). The correlation between the log and core measurements is much better in the upper part of the hole than in the lower portion because of the greater reliability of the core measurements performed with the DSV in comparison with those from the Hamilton Frame apparatus. The log and core measurements both show an increasing divergence with depth, with the logs indicating higher velocities than those determined from the core. This is a result of the decompression of sediments brought to the surface, known as the "rebound" effect, which is primarily a function of sediment type and depth of burial. The log data presented in Figure 50 fit well with the rebound-corrected empirical velocity/depth trend of Hamilton (1979) for siliceous sediments.

Porosity can be determined from the resistivity logs by using Archie's equation (Archie, 1942):

$$Swa = aRw/fmRt,$$

where Sw is water saturation, equal to 1 for these virtually hydrocarbon-free sediments, Rw is resistivity of the formation water, f is the fractional porosity, Rt is the measured formation resistivity, and both a and m are constants, depending on lithology and pore geometry. In this case, we calculated porosity using the medium phasor induction resistivity log (IMPH) from the dual induction tool (DITE) with set values of $a = 1$ and $m = 2$. Rw is calculated based on its known relationships to temperature and salinity (Keller, 1982); temperature data were provided by the Lamont temperature tool (TLT) (Fig. 45), and interstitial salinities from core measurements (see "Inorganic Geochemistry" section, this chapter). Rw is calculated as a variable downhole; the variation of Rw downhole with increasing temperature is significant. Although the TLT measures the borehole fluid temperature, we assumed for the purpose of this calculation that formation adjacent to the borehole is of similar temperature.

The calculated porosities have an excellent overall correlation with those determined from discrete core samples, although there is a linear offset between the two (Fig. 51). The log-derived porosities are slightly lower than the core-derived values, probably because the values of a and m are not correct for these sediments. The average offset between the two measurements is lowest in Subunits IA (0–128 mbsf) and IIA (604.8–694.7 mbsf), where the actual correlation between the core and log values is poorest. These zones are higher in clay content, which may result in increased surface conduction of clay minerals, giving an anomalously lower resistivity and, therefore, slightly higher apparent porosities.

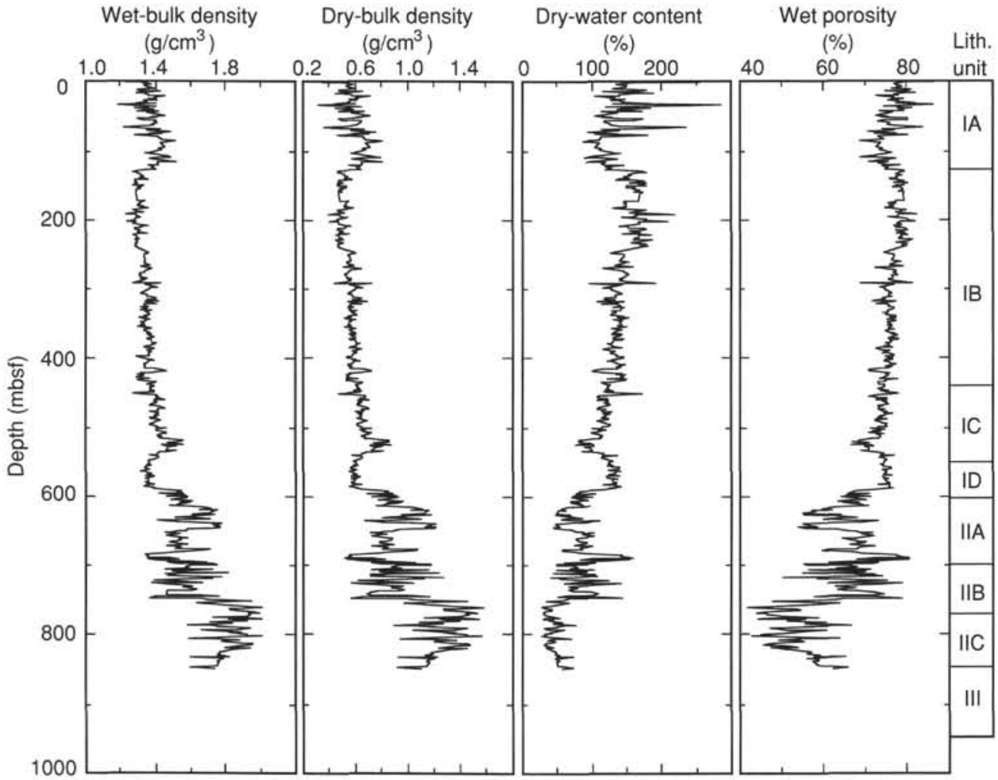

Figure 36. Index property data vs. depth for Hole 884B. Lithologic units are shown at right.

Magnetic Induction and Magnetic Susceptibility Log Results

Hole 884E was logged with two passes each of the two French magnetic logging tools (total induction and susceptibility). The repeat logs will permit analysis of the different components that affect the measurement of the surrounding formation magnetization. For the magnetometer and the susceptibility tools, several components were measured together and must be separated before isolating total induction or susceptibility data that accurately reflect the sedimentary formations surrounding the borehole.

Total Induction

The magnetometer measures the total induction $B = \mu_0[H + (J_i + J_r)]$ (SI units), which is commonly and incorrectly referred to as "Earth's magnetic field." B (Earth's total induction) is expressed in nannoteslas (nT) and is the induction resulting either from a magnetic field H (Earth's field in that case) and/or from an induced magnetization J_i or remanent magnetization J_r, both expressed in amperes per meter (A/m), with μ_0 being the permeability of vacuum. To avoid confusion between the mathematically defined total induction B and the induced magnetization J_i, here we refer to induction as the "B field," which will be expressed in nannoteslas.

In a borehole, B is the sum of several components:

$$B(z, t) = Br(z) + Ba(z) + Bf(z) + Bt(z, t)$$

with Br being the inner regular induction, Ba the induction caused by nearby highly magnetized rocks (anomaly field), Bf the induction produced by the geological formations surrounding the hole (what we finally want to measure), and Bt the induction caused by transient variations of Earth's field H. To isolate Bf, the desired component, we must first evaluate and remove Br, Ba, and Bt.

To a first approximation (see "Explanatory Notes" chapter, this volume), Br can be estimated by assuming it is dipolar, axial, and centered. Thus, we easily can remove its contribution to the field B, measured by the magnetometer using the local value (48,715 nT) and its gradient as a linear function of depth (~22 nT/km). Figure 52 shows the remaining "local" field $B_L(z)$ for the two runs that only contain local effects, i.e.: $B_{L1}(z) = Bf(z) + Ba(z) + Bt_1(z, t)$ and, $B_{L2}(z) = Bf(z) + Ba(z) + Bt_2(z, t)$.

Three different magnetic signatures can be recognized throughout the logged sequence (Fig. 52). In the uppermost part, the remaining "local" B_L field shows large variations, with values exceeding 1000 nT followed by a sharp decrease at about 68–69 mbsf. Down to about 85 mbsf, B_L increases downward from a value of about –1600 nT at 70 mbsf to an average value of –600 nT, a result of the highly magnetic drill pipe set at 70 mbsf. A broad zone, free of any large magnetic variations apart from sharp negative peaks, occurs between 90 and 720 mbsf and corresponds to the sediments of Site 884. Below about 700 mbsf, the remaining B_L signal becomes constant with "anomalies" within 0.4 nT peak to peak (Figs. 52 and 53).

The average value of the "local" fields B_{L1} and B_{L2} in the central sedimentary section is significantly lower than zero. To get the true value of Bf, the signal attributable to the close surrounding rocks, which should be the same for the two runs, one must evaluate the anomaly field Ba and the transient fields Bt_1 and Bt_2.

Analysis of the Components of the Magnetic Induction

Figure 53 shows the "local" B_L field for the two runs between 150 and 750 mbsf. At this scale, the two runs are similar, indicating that no major disturbance of Earth's field occurred during logging.

Figure 54 shows, in detail, the two runs between 150 and 600 mbsf. Again, agreement is good between the two runs, but with a variable depth offset between them. This depth offset is more significant in the lower part of the hole than in the upper part. Thus, it seems that a varying depth discrepancy occurred between and/or during the two logs. The WHC was not used during logging operations at Hole 884E because of an electronics failure. Although some of the depth errors

Table 15. Index properties, compressional wave velocity, and shear strength data, Hole 884B.

Core, section interval (cm)	Depth (mbsf)	Wet bulk density (g/cm^3)	Dry bulk density (g/cm^3)	Grain density (g/cm^3)	Wet porosity (%)	Dry water content (%)	Shear strength (kPa)	Compressional wave vel. (m/s)
145-884B-								
1H-1, 44	0.44	1.23	0.35	2.56	86.1	253.7		
1H-1, 45	0.45							1506.2
1H-1, 109	1.09	1.32	0.51	2.52	79.4	159.4		
1H-1, 110	1.10						16.70	
1H-2, 45	1.95							1490.3
1H-2, 74	2.24	1.37	0.58	2.55	76.9	135.8		
1H-2, 105	2.55						20.41	
1H-3, 53	3.53							1493.5
1H-3, 74	3.74	1.38	0.59	2.68	77.8	135.7		
1H-3, 105	4.05						21.33	
1H-4, 45	4.95							1517.5
1H-4, 79	5.29	1.33	0.53	2.42	77.5	148.5		
1H-4, 11	5.60						21.33	
2H-1, 40	6.90							1504.6
2H-1, 71	7.21	1.35	0.54	2.57	78.6	148.7		
2H-1, 10	7.55						21.12	
2H-2, 40	8.40							1462.5
2H-2, 81	8.81	1.39	0.60	2.68	77.1	130.7		
2H-2, 110	9.10						33.86	
2H-3, 40	9.90							1504.6
2H-3, 74	10.24	1.38	0.60	2.56	76.2	129.7		
2H-3, 110	10.60						42.20	
2H-4, 42	11.42							1415.7
2H-4, 74	11.74	1.30	0.47	2.50	80.9	177.4		
2H-4, 10	12.05						54.73	
2H-5, 40	12.90							1596.4
2H-5, 74	13.24	1.32	0.50	2.51	79.7	163.4		
2H-5, 110	13.60						65.29	
2H-6, 35	14.35							1504.6
2H-6, 74	14.74	1.43	0.66	2.67	74.7	115.2		
2H-6, 110	15.10						56.29	
2H-7, 49	15.99	1.29	0.45	2.54	82.0	188.3		
3H-1, 40	16.40							1504.6
3H-1, 74	16.74	1.33	0.51	2.57	79.7	160.1		
3H-1, 110	17.10						48.78	
3H-2, 74	18.24	1.35	0.56	2.49	77.0	139.9		
3H-2, 90	18.40							1517.5
3H-2, 110	18.60						50.28	
3H-3, 40	19.40							1493.5
3H-3, 70	19.70	1.37	0.58	2.64	77.9	138.4		
3H-3, 105	20.05						42.03	
3H-4, 40	20.90							1504.6
3H-4, 70	21.20	1.45	0.71	2.62	72.7	105.4		
3H-4, 11	21.62						44.28	
3H-5, 40	22.40							1496.6
3H-5, 74	22.74	1.39	0.60	2.62	76.9	131.7		
3H-5, 110	23.10						48.78	
3H-6, 40	23.90							1498.2
3H-6, 59	24.09	1.40	0.62	2.63	76.1	125.6		
3H-6, 110	24.60						55.54	
3H-7, 39	25.39	1.36	0.55	2.69	79.2	148.1		
4H-1, 75	26.25							1498.2
4H-1, 10	26.55						60.79	
4H-1, 105	26.59	1.41	0.61	2.74	77.2	128.6		
4H-2, 40	27.40							1499.8
4H-2, 104	28.04	1.33	0.56	2.32	75.6	138.4		
4H-2, 110	28.10						45.78	
4H-3, 40	28.90							1493.5
4H-3, 109	29.59	1.35	0.55	2.59	78.5	146.3		
4H-3, 110	29.60						50.28	
4H-4, 40	30.40							1509.4
4H-4, 109	31.09	1.29	0.45	2.53	81.8	185.0		
4H-4, 110	31.10						59.29	
4H-5, 50	32.00							1488.7
4H-5, 74	32.24	1.40	0.60	2.70	77.3	131.1		
4H-5, 11	32.60						60.04	
4H-6, 40	33.40							1501.4
4H-6, 74	33.74	1.19	0.31	2.31	86.2	285.3		
4H-6, 11	34.10						42.03	
4H-7, 39	34.89	1.40	0.64	2.54	74.5	119.2		
5H-1, 40	35.40							1488.7
5H-1, 74	35.74	1.33	0.53	2.51	78.6	152.5		
5H-1, 110	36.10						60.79	
5H-2, 40	36.90							1511
5H-2, 74	37.24	1.36	0.56	2.57	77.7	140.9		
5H-2, 11	37.60						49.53	
5H-3, 50	38.50							1512.7
5H-3, 74	38.74	1.28	0.45	2.47	81.4	184.7		
5H-3, 110	39.10						51.03	
5H-4, 40	39.90							1498.2
5H-4, 74	40.24	1.39	0.59	2.72	78.0	136.1		
5H-4, 10	40.55						49.53	
5H-5, 35	41.35							1501.4

Table 15 (continued).

Core, section interval (cm)	Depth (mbsf)	Wet bulk density (g/cm^3)	Dry bulk density (g/cm^3)	Grain density (g/cm^3)	Wet porosity (%)	Dry water content (%)	Shear strength (kPa)	Compressional wave vel. (m/s)
5H-5, 74	41.74	1.30	0.48	2.40	79.6	170.1		
5H-5, 11	42.15						50.28	
5H-6, 40	42.90							1499.8
5H-6, 74	43.24	1.42	0.67	2.55	73.6	113.1		
5H-6, 11	43.60						56.29	
5H-7, 39	44.39	1.36	0.57	2.49	76.6	136.5		
6H-1, 55	45.05							1506.2
6H-1, 74	45.24	1.35	0.57	2.46	76.5	137.3		
6H-1, 110	45.60						57.04	
6H-3, 40	47.90							1501.4
6H-3, 74	48.24	1.45	0.71	2.63	72.7	104.9		
6H-3, 110	48.60						57.04	
6H-4, 74	49.74	1.38	0.61	2.54	75.7	127.4		
6H-4, 75	49.75							1503.0
6H-4, 115	50.15						56.29	
6H-5, 40	50.90							1504.6
6H-5, 74	51.24	1.41	0.65	2.51	73.8	116.5		
6H-5, 110	51.60						59.29	
6H-6, 40	52.40							1511.0
6H-6, 74	52.74	1.36	0.57	2.55	77.4	140.2		
6H-6, 110	53.10						60.79	
6H-7, 39	53.89	1.30	0.48	2.43	80.1	172.8		
7H-1, 40	54.40							1471.7
7H-1, 74	54.74	1.33	0.51	2.60	80.0	160.5		
7H-1, 110	55.15						60.79	
7H-2, 40	55.90							1525.7
7H-2, 64	56.14	1.40	0.64	2.54	74.5	119.5		
7H-2, 12	56.72						48.03	
7H-3, 40	57.40							1504.6
7H-3, 74	57.74	1.39	0.64	2.43	73.2	117.0		
7H-3, 10	58.05						55.54	
7H-4, 40	58.90							1520.8
7H-4, 74	59.24	1.41	0.63	2.63	75.8	123.4		
7H-4, 11	59.60						84.05	
7H-5, 40	60.40							1509.4
7H-5, 80	60.80	1.38	0.61	2.54	75.7	127.6		
7H-5, 110	61.10						71.30	
7H-6, 40	61.90							1504.6
7H-6, 74	62.24	1.39	0.61	2.52	75.3	125.5		
7H-6, 11	62.65						65.29	
7H-7, 29	63.29	1.37	0.57	2.57	77.4	138.3		
8H-1, 40	63.90							1511.0
8H-1, 74	64.24	1.34	0.55	2.49	77.5	144.4		
8H-1, 115	64.65						58.54	
8H-2, 40	65.40							1535.7
8H-2, 74	65.74	1.22	0.36	2.28	83.7	235.5		
8H-2, 110	66.10						49.53	
8H-3, 40	66.90							1507.8
8H-3, 74	67.24	1.41	0.63	2.72	76.6	125.2		
8H-3, 110	67.60						59.29	
8H-4, 40	68.40							1514.3
8H-4, 74	68.74	1.43	0.67	2.62	74.2	114.4		
8H-4, 110	69.10						98.31	
8H-5, 40	69.90							1515.9
8H-5, 74	70.24	1.35	0.57	2.49	76.8	138.8		
8H-5, 110	70.60						68.29	
8H-6, 40	71.40							1507.8
8H-6, 64	71.64	1.48	0.73	2.71	72.6	101.3		
8H-6, 110	72.10						64.54	
8H-7, 29	72.79	1.49	0.76	2.61	70.4	94.4		
9H-1, 40	73.40							1493.5
9H-1, 74	73.74	1.37	0.58	2.56	77.2	137.3		
9H-1, 110	74.10						59.29	
9H-2, 40	74.90							1509.4
9H-2, 74	75.24	1.44	0.70	2.55	72.2	105.6		
9H-2, 110	75.60						66.79	
9H-3, 40	76.40							1532.3
9H-3, 74	76.74	1.28	0.46	2.32	80.0	179.5		
9H-3, 110	77.10						66.79	
9H-4, 40	77.90							1501.4
9H-4, 74	78.24	1.40	0.65	2.47	73.4	115.7		
9H-4, 110	78.60						57.04	
9H-5, 40	79.40							1499.8
9H-5, 74	79.74	1.41	0.66	2.5	73.2	113.3		
9H-5, 110	80.10						48.78	
9H-7, 39	82.39	1.44	0.68	2.69	74.4	111.9		
10H-2, 40	84.10							1527.4
10H-2, 74	84.44	1.51	0.80	2.59	68.7	87.8		
10H-2, 120	84.90						42.03	
12X-1, 39	87.69	1.43	0.68	2.62	73.8	111.5		
13X-1, 40	93.70							1499.8
13X-1, 74	94.04	1.45	0.71	2.63	72.7	105.3		
13X-1, 110	94.40						36.77	
13X-2, 40	95.20							1509.4

Table 15 (continued).

Core, section interval (cm)	Depth (mbsf)	Wet bulk density (g/cm^3)	Dry bulk density (g/cm^3)	Grain density (g/cm^3)	Wet porosity (%)	Dry water content (%)	Shear strength (kPa)	Compressional wave vel. (m/s)
13X-2, 74	95.54	1.42	0.66	2.59	74.0	114.2		
13X-2, 110	95.90						39.02	
13X-3, 40	96.70							1504.6
13X-3, 74	97.04	1.43	0.67	2.60	73.7	112.0		
13X-3, 110	97.40						42.78	
13X-4, 39	98.19	1.44	0.68	2.61	73.6	110.6		
14X-1, 40	103.40							1511.0
14X-1, 74	103.74	1.37	0.59	2.54	76.3	131.8		
14X-1, 74	103.74	1.34	0.56	2.39	76.4	140.8		
14X-1, 110	104.10						55.54	
14X-2, 30	104.80							1504.6
14X-2, 110	105.60						63.04	
14X-3, 40	106.40							1509.4
14X-3, 74	106.74	1.47	0.73	2.62	71.8	100.7		
14X-3, 110	107.10						59.29	
14X-4, 40	107.90							1532.3
14X-4, 74	108.24	1.49	0.79	2.54	68.7	89.3		
14X-4, 110	108.60						66.04	
14X-5, 40	109.40							1512.7
14X-5, 74	109.74	1.43	0.69	2.53	72.5	108.4		
14X-5, 110	110.10						70.54	
14X-6, 45	110.95							1511
14X-6, 74	111.24	1.37	0.58	2.59	77.3	136.5		
14X-6, 110	111.60						55.54	
15X-1, 53	113.13							1509.4
15X-1, 110	113.70						50.28	
15X-2, 53	114.63							1476.3
15X-2, 74	114.84	1.52	0.80	2.79	71.1	91.5		
15X-2, 110	115.20						48.78	
15X-3, 25	115.85							1482.5
15X-3, 74	116.34	1.42	0.65	2.70	75.7	120.2		
15X-3, 110	116.70						42.03	
15X-4, 53	117.63							1507.8
15X-4, 74	117.84	1.41	0.66	2.48	73.1	113.8		
15X-4, 110	118.20						60.04	
15X-5, 53	119.13							1514.3
15X-5, 74	119.34	1.42	0.65	2.66	75.3	119.1		
15X-5, 110	119.70						54.78	
15X-5, 39	120.49							1496.6
15X-6, 74	120.84	1.36	0.55	2.59	78.3	144.7		
15X-6, 95	121.05						44.28	
16X-1, 53	122.73							1509.4
16X-1, 74	122.94	1.39	0.63	2.49	74.3	120.5		
16X-1, 110	123.30						47.28	
16X-2, 53	124.23							1515.9
16X-2, 74	124.44	1.38	0.61	2.53	75.7	128.2		
16X-2, 110	124.8						47.28	
16X-3, 53	125.73							1509.4
16X-3, 74	125.94	1.40	0.64	2.56	74.7	119.9		
16X-3, 110	126.30						62.29	
16X-4, 53	127.23							1519.2
16X-6, 74	127.44	1.36	0.58	2.48	76.3	135.4		
16X-4, 110	127.80						50.28	
16X-4, 53	128.73							1527.4
16X-5, 74	128.94	1.30	0.48	2.39	79.5	169.6		
16X-5, 110	129.30						41.28	
16X-5, 53	130.23							1544.1
16X-6, 74	130.44	1.27	0.46	2.29	79.6	178.1		
16X-6, 110	130.80						27.77	
16X-6, 19	131.39	1.29	0.48	2.27	78.4	165.8		
17X-1, 53	132.33							1529.0
17X-1, 74	132.54	1.31	0.52	2.35	77.7	154.5		
17X-1, 110	132.90						45.78	
17X-2, 53	133.83							1530.7
17X-2, 74	134.04	1.32	0.52	2.36	77.5	152.2		
17X-2, 110	134.40						39.02	
17X-3, 53	135.33							1539.0
17X-3, 74	135.54	1.32	0.52	2.47	78.6	155.5		
17X-3, 110	135.90						52.53	
17X-4, 53	136.83							1529.0
17X-4, 74	137.04	1.33	0.54	2.43	77.3	146.2		
17X-4, 110	137.40						41.28	
17X-5, 53	138.33							1529.0
17X-5, 74	138.54	1.31	0.52	2.36	77.7	153.3		
17X-5, 110	138.90						40.53	
17X-6, 53	139.83							1539.0
17X-6, 74	140.04	1.33	0.55	2.33	76.0	141.5		
17X-6, 110	140.40						30.02	
17X-7, 19	140.99	1.36	0.58	2.46	76.2	135.1		
18X-1, 53	142.03							1530.7
18X-1, 74	142.24	1.28	0.49	2.15	76.9	160.9		
18X-1, 110	142.60						27.77	
18X-2, 53	143.53							
18X-2, 74	143.74	1.28	0.47	2.30	79.4	174.9		

Table 15 (continued).

Core, section interval (cm)	Depth (mbsf)	Wet bulk density (g/cm³)	Dry bulk density (g/cm³)	Grain density (g/cm³)	Wet porosity (%)	Dry water content (%)	Shear strength (kPa)	Compressional wave vel. (m/s)
18X-2, 110	144.10						27.02	
18X-3, 53	145.03							1530.7
18X-3, 74	145.24	1.30	0.51	2.26	77.1	155.0		
18X-3, 110	145.60						28.52	
18X-4, 53	146.53							1529.0
18X-4, 53	146.53							1539.0
18X-4, 74	146.74	1.28	0.46	2.34	80.0	177.9		
18X-4, 110	147.10						30.02	
18X-5, 15	147.65							1582.1
18X-5, 53	148.03							1532.3
18X-5, 74	148.24	1.30	0.49	2.36	79.0	166.8		
18X-5, 110	148.60						31.52	
18X-6, 53	149.53							1530.7
18X-6, 74	149.74	1.27	0.46	2.27	79.5	177.5		
18X-6, 110	150.10						18.01	
18X-7, 19	150.69	1.33	0.53	2.42	77.7	150.0		
19X-1, 53	151.63							1547.4
19X-1, 74	151.84	1.31	0.53	2.29	76.6	149.3		
19X-1, 110	152.20						38.27	
19X-2, 53	153.13							1544.1
19X-2, 74	153.34	1.30	0.49	2.35	78.6	162.9		
19X-2, 110	153.70						26.27	
19X-3, 53	154.63							1529.0
19X-3, 74	154.84	1.32	0.51	2.45	78.8	158.2		
19X-3, 110	155.20						32.27	
19X-4, 53	156.13							1535.7
19X-4, 74	156.34	1.29	0.48	2.32	79.0	169.2		
19X-4, 110	156.70						30.02	
19X-5, 53	157.63							1532.3
19X-5, 74	157.84	1.29	0.50	2.29	78.0	161.2		
19X-5, 110	158.20						33.77	
19X-6, 53	159.13							1545.8
19X-6, 74	159.34	1.29	0.47	2.35	79.6	173.0		
19X-6, 110	159.70						42.03	
19X-7, 19	160.29	1.29	0.48	2.34	79.2	169.0		
21X-1, 53	171.03							1534.0
21X-1, 74	171.24	1.30	0.49	2.42	79.5	166.8		
21X-1, 110	171.60						51.78	
21X-2, 53	172.53							1493.5
21X-2, 74	172.74	1.34	0.55	2.43	77.2	144.5		
21X-2, 110	173.10						45.78	
21X-3, 53	174.03							1530.7
21X-3, 74	174.24	1.32	0.53	2.35	77.2	149.9		
21X-3, 110	174.60						68.29	
21X-4, 53	175.53							1542.4
21X-4, 74	175.74	1.31	0.53	2.23	75.7	145.1		
21X-4, 110	176.10						74.3	
21X-5, 53	177.03							1509.4
21X-5, 74	177.24	1.32	0.53	2.38	77.3	148.9		
21X-5, 110	177.60						71.3	
21X-6, 74	178.74	1.30	0.52	2.18	75.9	150.0		
21X-6, 110	179.10						52.53	
21X-7, 19	179.69	1.33	0.54	2.37	76.7	144.6		
22X-1, 53	180.63							1544.1
22X-1, 74	180.84	1.31	0.52	2.30	76.8	150.1		
22X-1, 110	181.20						35.27	
22X-2, 53	182.13							1499.8
22X-2, 74	182.34	1.36	0.59	2.37	74.8	130.2		
22X-2, 110	182.70						34.52	
22X-3, 53	183.63							1549.1
22X-3, 74	183.84	1.27	0.46	2.22	78.9	175.2		
22X-3, 110	184.20						36.02	
22X-4, 53	185.13							1535.7
22X-4, 74	185.34	1.28	0.46	2.32	79.9	178.5		
22X-4, 110	185.70						36.02	
22X-5, 53	186.63							1545.8
22X-5, 74	186.84	1.29	0.49	2.31	78.5	164.7		
22X-5, 110	187.20						45.03	
22X-6, 53	188.13							1544.1
22X-6, 74	188.34	1.33	0.52	2.48	78.5	153.4		
22X-6, 110	188.70						53.28	
22X-7, 19	189.29	1.30	0.51	2.29	77.3	154.9		
23X-1, 35	190.15							1459.5
23X-1, 57	190.37						11.26	
23X-1, 74	190.54	1.23	0.39	2.22	82.3	218.8		
23X-2, 53	191.83							1552.5
23X-2, 74	192.04	1.29	0.49	2.3	78.2	162.3		
23X-2, 110	192.40						43.53	
23X-3, 53	193.33							1545.8
23X-3, 74	193.54	1.29	0.49	2.27	78.2	164.7		
23X-3, 110	193.90						44.28	
23X-4, 53	194.83							1545.8
23X-4, 74	195.04	1.31	0.51	2.32	77.6	155.9		
23X-4, 110	195.40						40.53	

Table 15 (continued).

Core, section interval (cm)	Depth (mbsf)	Wet bulk density (g/cm^3)	Dry bulk density (g/cm^3)	Grain density (g/cm^3)	Wet porosity (%)	Dry water content (%)	Shear strength (kPa)	Compressional wave vel. (m/s)
23X-5, 53	196.33							1537.3
23X-5, 74	196.54	1.32	0.54	2.26	75.7	143.6		
23X-5, 110	196.90						36.77	
23X-6, 53	197.83							1554.3
23X-6, 74	198.04	1.28	0.46	2.36	80.0	176.9		
23X-6, 110	198.40						53.28	
23X-7, 19	198.99	1.28	0.46	2.35	80.3	180.6		
24X-1, 53	199.93							1539.0
24X-1, 74	200.14	1.28	0.47	2.36	80.0	176.1		
24X-1, 110	200.50						48.03	
24X-2, 53	201.43							1545.8
24X-2, 74	201.64	1.24	0.40	2.26	81.9	208.8		
24X-2, 110	202.00						50.28	
24X-3, 53	202.93							1544.1
24X-3, 74	203.14	1.29	0.48	2.32	78.8	167.2		
24X-3, 110	203.50						77.3	
24X-4, 53	204.43							1545.8
24X-4, 74	204.64	1.27	0.47	2.15	77.7	168.8		
24X-4, 110	205.00						65.29	
24X-5, 53	205.93							1539.0
24X-5, 74	206.14	1.31	0.51	2.41	78.6	159.0		
24X-5, 110	206.50						92.31	
24X-6, 53	207.43							1547.4
24X-6, 74	207.64	1.36	0.57	2.50	76.9	138.5		
24X-6, 110	208.00						76.55	
24X-7, 19	208.59	1.33	0.53	2.47	78.3	151.6		
25X-1, 53	209.63							1547.4
25X-1, 74	209.84	1.31	0.52	2.34	77.4	152.0		
25X-1, 110	210.20						36.02	
25X-2, 53	211.13							1535.7
25X-2, 74	211.34	1.28	0.47	2.28	79.0	172.4		
25X-2, 110	211.70						41.28	
25X-3, 53	212.63							1542.4
25X-3, 74	212.84	1.28	0.46	2.33	79.8	177.0		
25X-3, 110	213.20						37.52	
25X-4, 53	214.13							1540.7
25X-4, 74	214.34	1.32	0.50	2.54	80.0	164.1		
25X-4, 110	214.70						30.02	
25X-5, 53	215.63							1547.4
25X-5, 74	215.84	1.31	0.51	2.29	77.2	153.6		
25X-5, 110	216.20						58.54	
25X-6, 53	217.13							1545.8
25X-6, 74	217.34	1.30	0.48	2.41	79.6	168.5		
25X-6, 110	217.70						75.8	
25X-0, 19	218.68	1.35	0.55	2.47	77.2	142.7		
26X-1, 53	219.23							1512.7
26X-1, 74	219.44	1.31	0.50	2.44	79.1	162.0		
26X-1, 110	219.80						29.27	
26X-2, 53	220.73							1504.6
26X-2, 74	220.94	1.27	0.45	2.31	80.3	184.0		
26X-2, 110	221.30						53.28	
26X-3, 53	222.23							1499.8
26X-3, 74	222.44	1.28	0.48	2.25	78.3	166.9		
26X-3, 110	222.80						43.53	
26X-4, 53	223.73							1540.7
26X-4, 74	223.94	1.29	0.48	2.32	78.9	167.4		
26X-4, 110	224.30						75.8	
26X-5, 53	225.23							1545.8
26X-5, 74	225.44	1.30	0.50	2.31	78.1	160.5		
26X-5, 112	225.82						85.55	
26X-6, 53	226.73							1520.8
26X-6, 74	226.94	1.29	0.48	2.29	78.6	167.6		
26X-6, 90	227.10						65.29	
26X-7, 19	227.39	1.31	0.51	2.38	78.2	157.5		
26X-1, 53	228.93							1532.3
27X-1, 74	229.14	1.28	0.45	2.46	81.4	186.1		
27X-1, 110	229.50						45.78	
27X-2, 53	230.43							1540.7
27X-2, 74	230.64	1.30	0.48	2.47	80.1	169.8		
27X-2, 110	231.00						45.03	
27X-3, 53	231.93							1547.4
27X-3, 74	232.14	1.30	0.51	2.25	77.2	156.1		
27X-3, 110	232.50						39.78	
27X-4, 53	233.43							1544.1
27X-4, 74	233.64	1.28	0.46	2.37	80.2	177.9		
27X-4, 110	234.00						57.04	
27X-5, 53	234.93							1549.1
27X-5, 69	235.09	1.29	0.48	2.33	79.1	169.8		
27X-5, 110	235.50						54.03	
27X-6, 53	236.43							1540.7
27X-6, 74	236.64	1.29	0.48	2.31	78.9	168.9		
27X-6, 110	237 .00						63.04	
27X-7, 19	237.59	1.28	0.46	2.31	79.9	179.1		
27X-1, 39	238.39	1.29	0.48	2.32	78.9	167.8		

Table 15 (continued).

Core, section interval (cm)	Depth (mbsf)	Wet bulk density (g/cm^3)	Dry bulk density (g/cm^3)	Grain density (g/cm^3)	Wet porosity (%)	Dry water content (%)	Shear strength (kPa)	Compressional wave vel. (m/s)
28X-1, 70	238.70							1545.8
28X-1, 105	239.05						25.52	
28X-1, 53	248.13							1545.8
29X-1, 74	248.34	1.36	0.60	2.38	74.4	126.8		
29X-1, 110	248.70						74.30	
29X-2, 53	249.63							1539.0
29X-2, 74	249.84	1.33	0.54	2.41	77.1	0.6		
29X-2, 110	250.20						78.05	
29X-3, 53	251.13							1532.3
29X-3, 74	251.34	1.33	0.55	2.41	77.0	144.6		
29X-3, 110	251.70						81.80	
29X-1, 40	257.70							1549.1
30X-1, 74	258.04	1.34	0.56	2.41	76.4	139.1		
30X-1, 110	258.40						67.54	
30X-2, 40	259.20							1534.0
30X-2, 74	259.54	1.34	0.53	2.52	78.5	151.2		
30X-2, 110	259.90						50.28	
30X-3, 40	260.70							1539.0
30X-3, 74	261.04	1.33	0.53	2.43	77.9	150.8		
30X-3, 110	261.40						60.79	
30X-4, 40	262.20							1545.8
30X-4, 74	262.54	1.34	0.55	2.43	77.1	144.0		
30X-4, 110	262.90						72.80	
30X-5, 40	263.70							1539.0
30X-5, 74	264.04	1.37	0.59	2.47	75.9	132.1		
30X-5, 110	264.40						84.05	
30X-6, 40	265.20							1527.4
30X-6, 74	265.54	1.37	0.59	2.52	76.4	133.3		
30X-6, 110	265.90						79.55	
30X-1, 40	267.40							1519.2
30X-1, 74	267.74	1.32	0.51	2.47	79.0	159.0		
31X-1, 110	268.10						69.04	
31X-2, 40	268.90							1524.1
31X-2, 74	269.24	1.38	0.64	2.34	72.2	115.0		
31X-2, 110	269.60						65.29	
31X-3, 40	270.40							1527.4
31X-3, 74	270.74	1.36	0.58	2.48	76.4	135.8		
31X-3, 110	271.10						57.04	
31X-4, 40	271.90							1537.3
31X-4, 74	272.24	1.36	0.57	2.51	76.7	136.7		
31X-4, 110	272.60						57.04	
31X-5, 40	273.40							1545.8
31X-5, 74	273.74	1.34	0.55	2.48	77.5	144.8		
31X-5, 110	274.10						57.04	
31X-6, 40	274.90							1509.4
31X-6, 74	275.24	1.33	0.54	2.42	77.3	146.0		
31X-6, 110	275.60						75.80	
31X-7, 39	276.39	1.32	0.53	2.31	76.6	147.2		
31X-1, 40	277.10							1529.0
31X-1, 74	277.44	1.31	0.52	2.32	77.2	151.9		
32X-1, 110	277.80						59.29	
32X-2, 40	278.60							1534.0
32X-2, 74	278.94	1.32	0.53	2.39	77.6	150.7		
32X-2, 110	279.30						62.29	
32X-3, 40	280.10							1539.0
32X-3, 74	280.44	1.31	0.53	2.28	76.4	147.2		
32X-3, 110	280.80						66.04	
32X-4, 40	281.60							1540.7
32X-4, 74	281.94	1.32	0.53	2.33	76.7	146.9		
32X-4, 110	282.30						58.54	
32X-5, 40	283.10							1537.3
32X-5, 74	283.44	1.35	0.56	2.45	76.6	139.2		
32X-5, 110	283.80						61.54	
32X-5, 40	284.60							1562.9
32X-6, 74	284.94	1.32	0.54	2.28	76.0	144.1		
32X-6, 110	285.30						78.80	
32X-7, 19	285.89	1.34	0.56	2.33	75.7	138.4		
32X-1, 40	286.70							1544.1
32X-1, 74	287.04	1.33	0.56	2.33	75.7	138.8		
32X-1, 110	287.40						51.03	
33X-2, 40	288.20							1519.2
33X-2, 74	288.54	1.32	0.54	2.36	77.0	147.2		
33X-2, 110	288.90						54.03	
33X-3, 40	289.70							1532.3
33X-3, 74	290.04	1.27	0.44	2.41	81.4	190.6		
33X-3, 110	290.40						49.53	
33X-4, 40	291.20							1535.7
33X-4, 74	291.54	1.43	0.73	2.34	68.7	96.7		
33X-4, 110	291.90						54.78	
33X-5, 40	292.70							1550.8
33X-5, 74	293.04	1.34	0.55	2.41	76.8	142.6		
33X-1, 40	296.40							1517.5
33X-1, 74	296.74	1.41	0.66	2.52	73.6	114.9		
33X-1, 110	297.10						78.05	

Table 15 (continued).

Core, section interval (cm)	Depth (mbsf)	Wet bulk density (g/cm^3)	Dry bulk density (g/cm^3)	Grain density (g/cm^3)	Wet porosity (%)	Dry water content (%)	Shear strength (kPa)	Compressional wave vel. (m/s)
34X-2, 74	298.24	1.37	0.60	2.42	74.8	127.4		
34X-2, 110	298.60						72.05	
34X-3, 74	299.74	1.37	0.60	2.40	74.6	126.9		
34X-1, 74	306.44	1.32	0.54	2.30	76.1	143.7		
34X-1, 110	306.80						104.32	
35X-2, 74	307.94	1.35	0.58	2.38	75.4	133.6		
35X-2, 110	308.30						80.30	
35X-3, 40	309.10							1535.7
35X-3, 74	309.44	1.35	0.58	2.41	75.6	133.5		
35X-3, 110	309.80						85.55	
35X-4, 40	310.60							1509.4
35X-4, 74	310.94	1.37	0.58	2.50	76.4	134.1		
35X-4, 110	311.30						81.80	
35X-5, 74	312.44	1.40	0.64	2.51	74.1	118.6		
35X-5, 120	312.90						87.06	
35X-6, 74	313.94	1.39	0.62	2.47	74.4	122.1		
35X-7, 19	314.89	1.35	0.58	2.35	74.9	131.8		
35X-1, 74	316.04	1.42	0.69	2.47	71.8	107.2		
35X-1, 110	316.40						60.79	
35X-2, 40	317.20							1491.9
36X-2, 74	317.54	1.34	0.54	2.43	77.3	145.8		
36X-2, 110	317.90						81.80	
36X-3, 40	318.70							1550.8
36X-3, 74	319.04	1.36	0.59	2.41	75.1	129.6		
36X-3, 110	319.40						81.80	
36X-4, 74	320.54	1.40	0.65	2.41	72.7	114.4		
36X-4, 110	320.90						75.80	
36X-5, 40	321.70							1519.2
36X-5, 74	322.04	1.33	0.56	2.28	75.0	137		
36X-5, 110	322.40						89.31	
36X-6, 48	323.28							1542.4
36X-6, 74	323.54	1.33	0.55	2.33	76.0	141.5		
36X-6, 105	323.85						83.30	
36X-7, 29	324.59	1.36	0.59	2.44	75.4	130.7		
36X-1, 40	325.40							1545.8
36X-1, 74	325.74	1.32	0.54	2.32	76.5	145.5		
36X-1, 110	326.10						74.30	
37X-2, 40	326.90							1550.8
37X-2, 74	327.24	1.35	0.56	2.45	76.9	141.4		
37X-2, 110	327.60						90.81	
37X-3, 74	328.74	1.32	0.55	2.29	75.8	141.7		
37X-3, 110	329.10						69.04	
37X-4, 40	329.90							1530.7
37X-4, 74	330.24	1.38	0.61	2.53	75.6	127.8		
37X-4, 110	330.60						78.05	
37X-5, 40	331.40							1537.3
37X-5, 74	331.74	1.34	0.57	2.33	75.1	134.1		
37X-5, 110	332.10						94.56	
37X-6, 40	332.90							1568.1
37X-6, 74	333.24	1.36	0.59	2.46	75.7	131.9		
37X-6, 110	333.61						14.82	
37X-7, 39	334.39	1.35	0.58	2.30	74.3	130.5		
37X-1, 74	335.04	1.36	0.59	2.40	75.2	131.3		
37X-1, 110	335.40						71.30	
37X-2, 74	336.54	1.37	0.61	2.43	74.8	126.5		
38X-2, 110	336.90						80.30	
38X-3, 74	338.04	1.33	0.54	2.42	77.2	146.0		
38X-4, 74	339.54	1.35	0.57	2.41	76.0	136.6		
38X-4, 110	339.90						74.30	
38X-5, 74	341.04	1.31	0.52	2.32	77.3	152.9		
38X-5, 110	341.40						72.05	
38X-6, 74	342.54	1.34	0.56	2.38	76.1	139.2		
38X-6, 110	342.90						80.30	
38X-7, 39	343.69	1.37	0.60	2.44	75.2	129.5		
38X-1, 40	344.30							1535.7
38X-1, 74	344.64	1.34	0.55	2.47	77.4	143.8		
38X-1, 110	345.00						57.04	
39X-2, 74	346.14	1.34	0.56	2.41	76.3	139.3		
39X-2, 110	346.50						66.04	
39X-3, 40	347.30							1568.1
39X-3, 74	347.64	1.32	0.55	2.26	75.2	139.6		
39X-3, 110	348.00						69.04	
39X-4, 40	348.80							1554.3
39X-4, 74	349.14	1.33	0.55	2.33	75.9	140.2		
39X-4, 110	349.50						63.04	
39X-5, 40	350.30							1573.3
39X-5, 74	350.64	1.32	0.54	2.32	76.2	143.9		
39X-5, 110	351.00						82.55	
39X-6, 74	352.14	1.33	0.56	2.30	75.2	137.1		
39X-6, 110	352.50						96.81	
39X-0, 9	353.59	1.34	0.56	2.39	76.3	140.3		
39X-1, 50	354.10							1557.7
39X-1, 74	354.34	1.30	0.52	2.21	76.1	149.8		
39X-1, 110	354.70						69.04	

Table 15 (continued).

Core, section interval (cm)	Depth (mbsf)	Wet bulk density (g/cm^3)	Dry bulk density (g/cm^3)	Grain density (g/cm^3)	Wet porosity (%)	Dry water content (%)	Shear strength (kPa)	Compressional wave vel. (m/s)
40X-2, 74	355.84	1.38	0.60	2.50	75.6	128.6		
40X-2, 110	356.20						87.06	
40X-3, 74	357.34	1.34	0.55	2.43	76.9	142.6		
40X-3, 110	357.70						95.31	
40X-4, 74	358.84	1.33	0.55	2.33	76.1	142. 0		
40X-4, 110	359.20						70.54	
40X-5, 74	360.34	1.33	0.57	2.27	74.7	135.1		
40X-5, 110	360.70						120.83	
40X-6, 74	361.84	1.37	0.60	2.52	76.0	130.4		
40X-6, 110	362.20						127.58	
40X-7, 39	362.99	1.35	0.58	2.41	75.8	134.7		
40X-1, 74	363.84	1.35	0.55	2.48	77.3	142.8		
40X-1, 115	364.25						120.08	
40X-2, 74	365.34	1.38	0.60	2.57	76.1	129.1		
41X-3, 60	366.70	1.36	0.57	2.57	77.6	140.6		
41X-4, 54	368.14	1.39	0.60	2.59	76.3	129.6		
41X-5, 74	369.84	1.36	0.59	2.44	75.5	131.7		
41X-6, 79	371.39	1.35	0.55	2.55	78.0	144.9		
41X-7, 29	372.39	1.36	0.56	2.55	77.6	141.1		
41X-1, 74	373.44	1.38	0.60	2.52	75.9	130.0		
41X-2, 59	374.79	1.38	0.60	2.58	76.4	130.3		
41X-3, 74	376.44	1.38	0.61	2.56	75.9	128.2		
42X-3, 108	376.78							1539. 0
42X-4, 45	377.65							1484.3
42X-4, 74	377.94	1.40	0.63	2.55	74.9	122.0		
42X-5, 37	379.07							1570.8
42X-5, 59	379.29	1.39	0.61	2.53	75.4	125.8		
42X-6, 74	380.94	1.37	0.60	2.5	75.8	129.8		
42X-7, 39	382.09	1.35	0.59	2.33	74.4	129.9		
42X-1, 59	382.99	1.33	0.55	2.38	76.6	143.4		
42X-2, 59	384.49	1.34	0.58	2.25	73.8	129.9		
42X-3, 59	385.99	1.39	0.65	2.41	72.8	115.0		
43X-4, 74	387.64	1.35	0.59	2.35	74.5	129.0		
43X-5, 74	389.14	1.36	0.58	2.45	75.8	132.8		
43X-6, 54	390.44	1.38	0.61	2.48	75.0	125.8		
43X-7, 49	391.89	1.36	0.60	2.36	74.3	127.2		
43X-1, 80	392.80							1563.2
43X-1, 81	392.81	1.36	0.59	2.44	75.5	130.7		
43X-2, 69	394.19	1.37	0.58	2.55	76.9	136.4		
44X-3, 72	395.72	1.36	0.58	2.47	76.1	134.2		
44X-4, 73	397.23	1.29	0.53	2.12	74.8	145.5		
44X-5, 77	398.77	1.32	0.54	2.32	76.6	146.1		
44X-6, 77	400.27	1.36	0.60	2.4	74.9	128.9		
44X-7, 3	401.03	1.37	0.58	2.53	76.7	135.0		
44X-1, 87	402.57	1.39	0.63	2.5	74.7	122.4		
44X-2, 67	403.87	1.36	0.59	2.36	74.6	129.3		
44X-2, 67	403.87							1542.8
45X-3, 76	405.46	1.36	0.59	2.46	75.7	131.9		
45X-4, 81	407.01	1.34	0.56	2.37	76.1	139.3		
45X-5, 89	408.59	1.33	0.54	2.39	77.2	147.2		
45X-6, 53	409.73	1.34	0.55	2.38	76.4	141.2		
45X-7, 31	411.01	1.34	0.58	2.34	75.0	133.7		
45X-1, 81	412.11	1.33	0.55	2.34	76.1	141.8		
45X-2, 81	413.61	1.34	0.57	2.35	75.2	134.0		
45X-3, 82	415.12	1.39	0.64	2.44	73.4	117.2		
46X-4, 82	416.62	1.43	0.70	2.43	70.9	103.9		
46X-4, 100	416.80							1549.3
46X-5, 68	417.98							1558.5
46X-5, 85	418.15	1.46	0.73	2.56	71.1	99.6		
46X-6, 75	419.55	1.37	0.59	2.46	75.6	130.9		
46X-7, 39	420.19	1.32	0.55	2.31	76.0	142.3		
46X-1, 123	422.13	1.33	0.57	2.28	74.8	135.3		
46X-2, 79	423.19	1.30	0.53	2.17	75.5	147.2		
46X-3, 86	424.76	1.33	0.55	2.30	75.7	140.8		
47X-4, 81	426.21	1.29	0.53	2.09	74.5	145.2		
47X-5, 79	427.69	1.30	0.53	2.13	74.8	144.6		
47X-6, 82	429.22	1.37	0.62	2.35	73.4	121.5		
47X-7, 19	430.09	1.33	0.53	2.44	77.8	149.6		
47X-1, 59	431.19	1.30	0.53	2.17	75.3	146.5		
47X-2, 67	432.77	1.37	0.61	2.41	74.5	126.0		
47X-2, 67	432.77							1574.6
48X-3, 55	434.15	1.40	0.66	2.45	72.9	113.5		
48X-3, 57	434.17							1545.3
48X-4, 81	435.91	1.39	0.64	2.41	73.2	117.6		
48X-5, 125	437.85	1.35	0.60	2.29	73.3	124.6		
48X-5, 126	437.86	1548.8						
48X-6, 19	438.29	1.36	0.60	2.38	74.5	127.2		
48X-1, 88	441.08	1.39	0.62	2.50	74.7	122.5		
48X-1, 89	441.09							1563.9
48X-2, 79	442.49	1.37	0.61	2.41	74.1	123.7		
49X-3, 100	444.20	1.38	0.63	2.35	73.0	119		
49X-3, 101	444.21							1557.6
49X-4, 83	445.53	1.37	0.59	2.46	75.6	131.3		
49X-5, 8	446.28	1.39	0.64	2.46	73.7	118.5		

Table 15 (continued).

Core, section interval (cm)	Depth (mbsf)	Wet bulk density (g/cm^3)	Dry bulk density (g/cm^3)	Grain density (g/cm^3)	Wet porosity (%)	Dry water content (%)	Shear strength (kPa)	Compressional wave vel. (m/s)
49X-5, 9	446.29							1545.9
49X-6, 76	448.46	1.39	0.62	2.54	75.1	123.6		
49X-7, 40	449.60	1.39	0.61	2.56	75.7	126.7		
49X-1, 35	450.15	1.27	0.47	2.17	78.2	171.8		
49X-2, 78	452.08	1.41	0.67	2.43	72.3	111.3		
49X-3, 126	454.06	1.40	0.68	2.36	71.0	107.4		
50X-3, 27	454.07							1534.5
50X-4, 106	455.36	1.41	0.67	2.39	71.5	108.5		
50X-5, 71	456.51	1.42	0.67	2.5	73	112.1		
50X-6, 94	458.24	1.40	0.63	2.56	75.1	122.3		
50X-7, 55	459.35	1.45	0.70	2.6	72.7	106.2		
50X-1, 51	459.81	1.39	0.62	2.55	75.2	124.0		
50X-2, 24	461.04	1.40	0.64	2.5	74.2	119.4		
50X-3, 70	463.00	1.39	0.62	2.55	75.2	123.4		
51X-4, 79	464.59	1.41	0.65	2.6	74.8	118.6		
51X-4, 80	464.60							1565.1
51X-5, 87	466.17	1.38	0.61	2.5	75.4	127.1		
51X-6, 118	467.98	1.37	0.63	2.34	72.9	118.8		
51X-6, 119	467.99							1544.8
51X-7, 28	468.58	1.39	0.63	2.47	74.0	119.4		
51X-1, 103	469.93	1.43	0.68	2.58	73.4	110.7		
51X-2, 97	471.37	1.45	0.70	2.61	72.9	106.8		
51X-3, 78	472.68	1.41	0.64	2.59	74.9	119.8		
52X-4, 114	474.54	1.42	0.67	2.53	73.3	112.6		
52X-5, 127	476.17	1.41	0.65	2.57	74.5	117.7		
52X-6, 141	477.81	1.37	0.6	2.43	75.1	128.7		
52X-7, 33	478.23	1.42	0.66	2.62	74.5	115.4		
52X-1, 32	478.92	1.40	0.62	2.67	76.5	126.7		
52X-2, 136	481.46	1.40	0.64	2.56	74.9	120.7		
52X-3, 89	482.49	1.42	0.65	2.62	74.8	117.5		
53X-4, 71	483.81	1.39	0.63	2.46	73.9	119.7		
53X-5, 89	485.49	1.40	0.65	2.45	73.0	114.4		
53X-6, 30	486.40	1.37	0.61	2.4	74.2	124.1		
53X-7, 40	488.00	1.38	0.64	2.38	72.8	116.9		
53X-1, 42	488.62	1.40	0.63	2.56	75.2	123.1		
53X-2, 71	490.41	1.43	0.69	2.53	72.2	106.6		
53X-3, 88	492.08	1.39	0.64	2.45	73.7	118.6		
54X-3, 141	492.61							1527.2
54X-4, 76	493.46	1.39	0.62	2.48	74.5	122.7		
54X-5, 67	494.87	1.38	0.61	2.47	75.1	127		
54X-6, 88	496.58	1.37	0.61	2.44	74.7	125.8		
54X-7, 28	497.48	1.41	0.64	2.61	75.3	121.4		
54X-1, 23	498.03	1.40	0.65	2.43	72.9	115.2		
54X-1, 58	498.38						1549.90	
54X-2, 63	499.93	1.42	0.66	2.54	73.5	113.7		
55X-3, 68	501.48	1.46	0.73	2.56	71.3	100.7		
55X-4, 54	502.84						1596.00	
55X-4, 74	503.04	1.40	0.63	2.54	74.7	120.8		
55X-5, 70	504.5	1.41	0.68	2.42	71.8	108.9		
55X-5, 114	504.94						1601.50	
55X-6, 22	505.22	1.42	0.66	2.57	73.9	114.4		
55X-7, 20	506.70	1.46	0.73	2.53	70.8	99.4		
55X-1, 77	508.17	1.46	0.69	2.75	74.4	109.7		
55X-2, 58	509.48	1.44	0.70	2.59	72.7	107.1		
55X-3, 104	511.44	1.41	0.65	2.51	73.7	115.9		
56X-4, 75	512.65	1.44	0.68	2.63	73.7	110.6		
56X-5, 72	514.12	1.42	0.67	2.56	73.6	113.3		
56X-6, 73	515.63	1.43	0.67	2.58	73.6	112.1		
56X-7, 25	516.65	1.43	0.70	2.51	71.9	105.8		
56X-1, 57	517.67	1.56	0.86	2.74	68.3	81.2		
56X-1, 118	518.28						1582.10	
56X-2, 31	518.91						1573.40	
57X-2, 45	519.05	1.53	0.83	2.67	68.7	85.1		
57X-3, 53	520.63	1.55	0.86	2.64	67.2	80.4		
57X-4, 63	522.23	1.47	0.74	2.58	70.9	98.2		
57X-5, 67	523.77	1.56	0.87	2.63	66.5	78.0		
57X-5, 138	524.48						1569.40	
57X-6, 50	525.10						1567.40	
57X-6, 57	525.17	1.44	0.71	2.51	71.4	103.3		
57X-7, 19	525.79	1.46	0.72	2.6	72.0	102.8		
57X-1, 79	527.49	1.52	0.80	2.69	70.0	89.8		
57X-1, 97	527.67						1535.90	
57X-2, 64	528.84	1.47	0.75	2.57	70.5	96.2		
58X-3, 89	530.59	1.47	0.74	2.59	71.1	98.2		
58X-4, 74	531.94	1.46	0.73	2.53	70.9	99.5		
58X-5, 84	533.54	1.52	0.82	2.66	69.0	86.6		
58X-6, 77	534.97	1.46	0.72	2.61	72.3	103.4		
58X-7, 39	536.09	1.43	0.69	2.49	71.9	106.4		
58X-1, 84	537.24	1.41	0.64	2.58	74.6	118.6		
58X-2, 98	538.88	1.41	0.65	2.54	73.9	115.8		
58X-3, 79	540.19	1.37	0.58	2.58	77.1	136.1		
59X-4, 71	541.61	1.42	0.66	2.57	74.1	115.4		
59X-5, 89	543.29	1.42	0.66	2.53	73.4	113.5		
59X-6, 79	544.69	1.41	0.65	2.57	74.2	116.2		

Table 15 (continued).

Core, section interval (cm)	Depth (mbsf)	Wet bulk density (g/cm^3)	Dry bulk density (g/cm^3)	Grain density (g/cm^3)	Wet porosity (%)	Dry water content (%)	Shear strength (kPa)	Compressional wave vel. (m/s)
59X-1, 76	546.86	1.39	0.62	2.54	75.1	123.6		
59X-2, 81	548.41	1.36	0.59	2.37	74.8	130.3		
59X-3, 59	549.69	1.37	0.61	2.42	74.4	125.0		
60X-4, 84	551.44	1.37	0.61	2.42	74.5	125.3		
60X-5, 67	552.77	1.37	0.61	2.37	73.9	124.1		
60X-6, 91	554.51	1.35	0.59	2.33	74.5	130.0		
60X-7, 44	555.54	1.38	0.62	2.42	74.0	122.4		
60X-1, 74	556.34	1.34	0.57	2.27	74.4	132.9		
60X-2, 69	557.79	1.34	0.56	2.37	76.0	138.7		
60X-3, 59	559.19	1.34	0.56	2.41	76.4	139.7		
61X-4, 69	560.79	1.37	0.61	2.39	74.2	124.5		
61X-5, 81	562.41	1.32	0.55	2.25	75.3	140.5		
61X-6, 69	563.79	1.34	0.58	2.34	75.1	133.8		
61X-1, 74	566.04	1.35	0.58	2.33	74.8	131.8		
61X-2, 79	567.59	1.38	0.61	2.43	74.4	124.2		
61X-3, 75	569.05	1.34	0.56	2.38	76.1	139.0		
62X-4, 81	570.61	1.39	0.63	2.47	74.1	120.2		
62X-5, 77	572.07	1.38	0.62	2.45	74.3	122.9		
62X-6, 63	573.43	1.34	0.56	2.34	75.7	137.8		
62X-1, 23	575.03	1.36	0.60	2.36	74.4	127.5		
62X-2, 104	577.34	1.36	0.59	2.42	75.3	131.2		
62X-3, 55	578.35	1.34	0.57	2.35	75.3	135.3		
63X-4, 84	580.14	1.35	0.58	2.42	75.8	134.6		
63X-5, 94	581.74	1.39	0.64	2.42	73.0	116.2		
63X-6, 55	582.85	1.37	0.60	2.52	76.0	130.8		
63X-1, 54	584.94	1.33	0.55	2.32	75.9	141.4		
63X-1, 92	585.32							1531.4
63X-2, 65	586.55	1.39	0.62	2.57	75.5	124.9		
64X-2, 103	586.93							1530.3
64X-3, 66	588.06	1.38	0.60	2.58	76.6	131.6		
64X-4, 79	589.69	1.40	0.64	2.47	73.7	117.8		
64X-5, 29	590.69	1.53	0.84	2.61	67.3	81.8		
64X-6, 92	592.12	1.55	0.85	2.65	67.5	81.1		
64X-7, 79	593.49	1.52	0.83	2.54	67.0	82.6		
64X-1, 81	594.91	1.56	0.88	2.61	66.0	76.8		
64X-2, 54	596.14	1.42	0.69	2.4	70.9	105.2		
64X-3, 87	597.97	1.57	0.91	2.62	65.1	73.5		
65X-4, 73	599.33	1.46	0.73	2.56	71.2	99.9		
65X-5, 51	600.61	1.58	0.93	2.61	64.2	70.9		
65X-6, 48	602.08	1.57	0.88	2.72	67.5	78.9		
65X-6, 82	602.42							1538.4
65X-7, 56	603.66	1.49	0.77	2.6	70.1	93.2		
65X-1, 74	604.54	1.51	0.82	2.55	67.6	84.8		
65X-2, 6	605.36							1564.0
65X-2, 74	606.04	1.61	0.96	2.63	63.4	67.9		
66X-3, 79	607.59	1.54	0.84	2.7	68.4	83.1		
66X-4, 74	609.04	1.60	0.94	2.67	64.6	70.7		
66X-4, 120	609.50							1582.9
66X-5, 59	610.39	1.53	0.83	2.69	69.0	85.5		
66X-6, 14	611.44							1581.3
66X-6, 74	612.04	1.52	0.81	2.69	69.4	87.5		
66X-1, 74	614.04	1.48	0.76	2.6	70.5	95.2		
66X-1, 115	614.45							1583.1
66X-2, 64	615.44	1.66	1.02	2.76	62.8	63.2		
67X-3, 79	617.09	1.72	1.11	2.76	59.6	55.2		
67X-4, 74	618.54	1.65	1.02	2.69	61.9	62.4		
67X-4, 84	618.64							1621.9
67X-5, 79	620.09	1.75	1.16	2.73	57.2	50.5		
67X-6, 49	621.29	1.73	1.14	2.74	58.1	52.3		
67X-1, 79	623.59	1.71	1.14	2.55	55.0	49.4		
67X-2, 89	625.19	1.61	0.95	2.67	64.0	68.7		
67X-3, 69	626.49	1.74	1.18	2.64	55.2	48.1		
68X-4, 74	628.04	1.65	1.00	2.73	63.2	64.8		
68X-5, 105	629.85	1.51	0.81	2.56	68.0	85.8		
68X-5, 146	630.26							1555.2
68X-6, 79	631.09	1.62	0.96	2.75	64.8	69.1		
68X-7, 49	632.29	1.71	1.10	2.74	59.8	55.9		
68X-1, 134	633.74	1.50	0.81	2.50	67.4	85.5		
68X-1, 146	633.86							1585.7
68X-2, 133	635.23	1.41	0.67	2.49	72.9	112		
69X-3, 132	636.72	1.54	0.83	2.74	69.3	85.3		
69X-3, 139	636.79							1584.0
69X-4, 66	637.56	1.59	0.92	2.72	65.9	73.5		
69X-5, 74	639.14	1.78	1.22	2.71	54.9	46.2		
69X-5, 123	639.63							1641.0
69X-6, 88	640.78	1.73	1.16	2.67	56.4	50		
69X-7, 51	641.91	1.76	1.18	2.71	56.0	48.5		
69X-1, 131	643.31	1.74	1.14	2.78	58.6	52.5		
69X-2, 44	643.94	1.77	1.22	2.65	53.9	45.4		
69X-2, 52	644.02							1587.5
70X-3, 50	645.50	1.76	1.20	2.7	55.5	47.6		
70X-4, 91	647.41	1.58	0.93	2.56	63.4	69.8		
70X-5, 101	649.01	1.57	0.89	2.66	66.2	76.1		
70X-5, 107	649.07							1550.1

Table 15 (continued).

Core, section interval (cm)	Depth (mbsf)	Wet bulk density (g/cm^3)	Dry bulk density (g/cm^3)	Grain density (g/cm^3)	Wet porosity (%)	Dry water content (%)	Shear strength (kPa)	Compressional wave vel. (m/s)
70X-6, 68	650.18							1576.1
70X-6, 77	650.27	1.53	0.83	2.61	67.8	83.3		
70X-7, 42	651.42	1.49	0.78	2.55	68.9	90.0		
70X-1, 89	652.59	1.45	0.71	2.54	71.6	102.9		
70X-1, 101	652.71							1582.7
70X-2, 61	653.81	1.52	0.81	2.69	69.6	88.0		
71X-3, 36	655.06							1571.2
71X-3, 41	655.11	1.54	0.84	2.73	69.1	84.6		
71X-4, 42	656.62	1.46	0.72	2.61	72.1	102.8		
71X-5, 42	658.12	1.51	0.79	2.67	70.0	90.5		
71X-5, 83	658.53							1569.6
71X-6, 74	659.94	1.58	0.89	2.74	67.4	78.0		
71X-7, 20	660.9	1.53	0.87	2.48	64.6	76.0		
71X-1, 111	662.41	1.55	0.87	2.66	67.2	79.4		
71X-2, 106	663.86	1.52	0.82	2.63	68.6	85.8		
71X-2, 117	663.97							1584.8
72X-3, 106	665.36	1.50	0.78	2.66	70.3	92.2		
72X-4, 86	666.66							1606.0
72X-4, 99	666.79	1.48	0.78	2.48	68.2	89.5		
72X-5, 33	667.63							1582.1
72X-5, 47	667.77	1.49	0.78	2.61	70.0	92.4		
72X-6, 77	669.57	1.58	0.90	2.69	66.2	75.1		
72X-7, 43	670.73	1.46	0.73	2.62	71.9	101.4		
72X-1, 57	671.57	1.47	0.74	2.67	72.2	100.6		
72X-1, 65	671.65							1577.0
72X-2, 78	673.28	1.55	0.85	2.71	68.4	82.8		
73X-3, 59	674.59							1575.1
73X-3, 65	674.65	1.51	0.81	2.57	68.1	85.7		
73X-4, 63	676.13	1.71	1.08	2.82	61.5	58.5		
73X-4, 69	676.19							1631.2
73X-5, 39	677.39	1.67	1.06	2.63	59.6	57.8		
73X-1, 40	681.00	1.56	0.88	2.67	66.8	78.0		
73X-2, 45	682.55	1.44	0.72	2.44	70.0	99.0		
73X-3, 81	684.41	1.34	0.55	2.47	77.2	143.0		
74X-4, 35	685.45	1.36	0.57	2.59	77.8	140.5		
74X-5, 70	687.30							1589.9
74X-5, 102	687.62	1.35	0.52	2.75	80.6	158		
74X-6, 62	688.72	1.47	0.73	2.70	72.7	102.4		
74X-7, 31	689.91	1.53	0.83	2.63	68.2	84.2		
74X-1, 72	690.92							1612.2
74X-1, 103	691.23	1.36	0.54	2.79	80.4	153.2		
74X-2, 55	692.25	1.41	0.65	2.60	74.7	117.8		
75X-3, 86	694.06	1.69	1.06	2.75	61.2	59.1		
75X-4, 58	695.28							1604.8
75X-4, 111	695.81	1.47	0.72	2.71	73.1	104.3		
75X-5, 70	696.90	1.52	0.79	2.79	71.3	92.4		
75X-5, 78	696.98							1683.0
75X-6, 52	698.22	1.73	1.17	2.62	55.2	48.5		
75X-7, 24	698.94	1.75	1.18	2.72	56.5	49.2		
75X-1, 70	700.50	1.61	0.93	2.77	66.0	72.4		
75X-1, 89	700.69							1592.8
75X-2, 74	702.04	1.57	0.87	2.75	68.0	79.9		
76X-3, 68	703.48	1.59	0.95	2.58	63.0	68.0		
76X-3, 120	704.00							1610.7
76X-4, 58	704.88	1.45	0.72	2.53	71.4	101.9		
76X-5, 75	706.55	1.73	1.16	2.66	56.3	49.9		
76X-5, 82	706.62							1880.2
76X-6, 17	707.47							1664.3
76X-6, 23	707.53	1.50	0.78	2.66	70.2	91.7		
76X-6, 23	707.53	1.50	0.78	2.66	70.2	91.7		
76X-7, 45	709.25	1.57	0.88	2.77	68.0	79.4		
76X-1, 45	709.95	1.81	1.24	2.77	54.8	45.1		
76X-2, 63	711.63	1.45	0.71	2.61	72.5	104.4		
76X-3, 96	713.46	1.52	0.83	2.57	67.3	82.9		
77X-3, 103	713.53							1666.4
77X-4, 77	714.77	1.47	0.71	2.78	74.1	106.6		
77X-5, 84	716.34	1.78	1.27	2.55	50.2	40.6		
77X-5, 115	716.65							1653.7
77X-6, 74	717.74	1.68	1.05	2.73	61.1	59.5		
77X-7, 37	718.87	1.73	1.13	2.75	58.4	52.7		
77X-0, 21	719.32	1.66	1.06	2.58	58.6	56.4		
77X-1, 74	719.84	1.71	1.11	2.71	58.6	53.9		
77X-2, 43	721.03							1598.9
77X-2, 74	721.34	1.39	0.62	2.52	75.1	124.4		
78X-3, 39	722.49							1587.3
78X-3, 74	722.84	1.57	0.88	2.70	67.2	78.3		
78X-4, 74	724.34	1.67	1.05	2.70	61.0	59.6		
78X-5, 15	725.25							1722.0
78X-5, 74	725.84	1.38	0.57	2.72	78.7	141.6		
78X-1, 74	729.54	1.61	0.96	2.62	62.9	66.9		
78X-2, 16	730.46							1618.5
78X-2, 79	731.09	1.56	0.88	2.63	66.2	77.0		
79X-3, 67	732.47	1.57	0.87	2.72	67.6	79.3		
79X-4, 84	734.14	1.63	0.98	2.71	63.6	66.6		

Table 15 (continued).

Core, section interval (cm)	Depth (mbsf)	Wet bulk density (g/cm³)	Dry bulk density (g/cm³)	Grain density (g/cm³)	Wet porosity (%)	Dry water content (%)	Shear strength (kPa)	Compressional wave vel. (m/s)
79X-4, 143	734.73							1953.4
79X-5, 49	735.29	1.60	0.93	2.76	66.0	72.9		
79X-6, 34	736.64							1780.4
79X-6, 74	737.04	1.47	0.77	2.44	68.1	90.3		
79X-1, 74	739.14	1.46	0.73	2.59	71.6	100.9		
79X-1, 88	739.28							1584.3
79X-2, 74	740.64	1.46	0.69	2.74	74.4	109.8		
80X-2, 141	741.31							2246.7
80X-3, 14	741.54							2154.3
80X-3, 59	741.99	1.47	0.73	2.62	71.7	100.0		
80X-4, 59	743.49	1.65	1.00	2.75	63.2	64.6		
80X-4, 104	743.94							1603.8
80X-4, 109	743.99	1.76	1.17	2.79	57.7	50.4		
80X-5, 134	745.74	1.40	0.66	2.44	72.6	112.5		
80X-6, 22	746.12							1554.5
80X-6, 44	746.34	1.37	0.56	2.68	78.8	144.3		
80X-0, 20	747.71	1.66	1.00	2.87	64.9	66.6		
80X-1, 68	748.78	1.70	1.06	2.86	62.7	60.6		
80X-2, 69	750.29	1.95	1.46	2.81	48.0	33.8		
80X-2, 103	750.63							1714.9
81X-3, 21	751.31							1706.0
81X-3, 25	751.35	1.84	1.30	2.77	52.8	41.5		
81X-3, 79	751.89	1.90	1.41	2.71	47.9	34.9		
81X-4, 30	752.90	1.63	0.98	2.71	63.7	66.9		
81X-1, 89	758.59	1.83	1.29	2.74	52.5	41.5		
81X-1, 108	758.78							1664.4
81X-2, 84	760.04	2.01	1.58	2.73	41.9	27.2		
82X-3, 59	761.29	1.87	1.35	2.76	51.0	38.8		
82X-3, 78	761.48							1775.7
82X-4, 63	762.83	1.82	1.27	2.75	53.6	43.3		
82X-4, 116	763.36							1657.7
82X-5, 74	764.44	1.83	1.28	2.82	54.4	43.6		
82X-5, 83	764.53							1651.5
82X-6, 74	765.94	1.96	1.49	2.76	45.8	31.5		
82X-1, 79	768.19	1.99	1.54	2.75	43.8	29.2		
82X-2, 54	769.44	1.93	1.45	2.72	46.3	32.7		
82X-2, 92	769.82							1980.0
83X-3, 58	770.98							1848.7
83X-3, 74	771.14	1.94	1.47	2.75	46.4	32.5		
83X-4, 74	772.64	1.92	1.39	2.88	51.5	38.0		
83X-4, 129	773.19							1697.4
83X-5, 73	774.13							1772.5
83X-5, 79	774.19	1.73	1.12	2.74	58.7	53.6		
83X-6, 79	775.69	1.91	1.42	2.75	48.4	35.0		
83X-7, 69	776.44	2.01	1.55	2.8	44.3	29.2		
83X-7, 80	776.55							1838.4
83X-1, 74	777.74	1.81	1.25	2.81	55.5	45.6		
83X-2, 79	779.29	1.92	1.40	2.88	51.4	37.7		
83X-2, 85	779.35							1633.1
84X-3, 75	780.75	1.71	1.09	2.8	60.6	56.7		
84X-4, 88	782.38	1.79	1.21	2.82	56.8	48.1		
84X-4, 97	782.47							1673.2
84X-5, 64	783.64	1.84	1.27	2.86	55.5	44.8		
84X-6, 56	785.06							1625.3
84X-6, 62	785.12	1.58	0.90	2.72	66.7	76.0		
84X-7, 32	786.32	1.71	1.06	2.88	62.9	60.7		
84X-1, 83	787.53	1.79	1.22	2.75	55.4	46.6		
84X-1, 94	787.64							1664.4
84X-2, 63	788.83	1.75	1.16	2.74	57.4	50.8		
85X-2, 65	788.85							2163.0
85X-3, 59	790.29	1.94	1.46	2.77	47.2	33.1		
85X-4, 77	791.97	1.86	1.34	2.77	51.5	39.5		
85X-5, 65	793.35	1.66	1.04	2.66	60.7	59.8		
85X-5, 71	793.41							1994.3
85X-6, 56	794.76	1.77	1.20	2.72	55.7	47.6		
85X-7, 7	795.77							1742.0
85X-7, 17	795.87	1.89	1.36	2.82	51.7	39.0		
85X-1, 78	797.18	1.82	1.28	2.74	53.1	42.6		
85X-1, 83	797.23							1684.5
85X-2, 7	797.97	1.92	1.46	2.66	44.9	31.5		
86X-3, 65	800.05	1.92	1.44	2.75	47.4	33.8		
86X-3, 106	800.46							1879.6
86X-4, 23	801.13	2.01	1.57	2.76	42.8	28.0		
86X-5, 104	803.44							1716.2
86X-5, 108	803.48	1.83	1.27	2.81	54.6	44.2		
86X-6, 45	804.35							2138.6
86X-6, 54	804.44	1.59	0.94	2.6	63.7	69.6		
86X-7, 20	805.10	1.73	1.17	2.61	54.9	48.0		
86X-1, 68	806.78	1.88	1.38	2.73	49.3	36.8		
86X-2, 62	808.22	1.82	1.27	2.77	54.1	43.8		
86X-2, 68	808.28							1688.8
87X-3, 99	810.09	1.78	1.21	2.73	55.4	46.9		
87X-4, 23	810.83	1.91	1.40	2.77	49.0	35.8		
87X-4, 29	810.89							1762.3

Table 15 (continued).

Core, section interval (cm)	Depth (mbsf)	Wet bulk density (g/cm^3)	Dry bulk density (g/cm^3)	Grain density (g/cm^3)	Wet porosity (%)	Dry water content (%)	Shear strength (kPa)	Compressional wave vel. (m/s)
87X-5, 74	812.84	1.96	1.46	2.85	48.6	34.1		
87X-6, 66	814.26							1742.0
87X-6, 76	814.36	1.95	1.48	2.74	45.8	31.7		
87X-1, 67	816.27							1705.9
87X-1, 70	816.30	1.88	1.35	2.8	51.6	39.2		
87X-2, 54	817.64	1.80	1.24	2.72	54.0	44.5		
88X-3, 60	819.20	1.94	1.46	2.78	47.3	33.3		
88X-3, 103	819.63							1783.9
88X-4, 53	820.55	1.85	1.32	2.75	51.8	40.2		
88X-4, 64	820.66							1615.1
88X-1, 27	825.37	1.76	1.18	2.75	57.0	49.6		
88X-2, 80	827.40	1.77	1.19	2.73	56.0	48.1		
88X-2, 86	827.46							1648.2
89X-3, 86	828.96	1.75	1.14	2.81	59.1	52.9		
89X-4, 63	830.23							1633. 0
89X-4, 83	830.43	1.82	1.23	2.94	57.9	48.4		
89X-5, 104	832.14	1.60	0.93	2.70	65.4	72.20		
89X-6, 48	833.08							1662.9
89X-6, 62	833.22	1.78	1.21	2.76	55.9	47.3		
89X-7, 12	834.22	1.79	1.20	2.86	57.9	49.6		
89X-1, 87	835.47							1590.4
89X-1, 90	835.50	1.77	1.16	2.85	59.0	51.9		
89X-2, 81	836.91	1.75	1.15	2.81	58.8	52.5		
90X-3, 81	838.41	1.76	1.17	2.77	57.4	50.1		
90X-1, 22	844.52	1.75	1.15	2.81	58.7	52.1		
90X-2, 71	846.51	1.60	0.92	2.74	66.1	73.6		
90X-2, 146	847.26							1689.1
91X-3, 34	847.64	1.74	1.10	2.97	62.5	57.9		

can be attributed to variable ship's heave, some depth offsets exceeded 4 m between the two logging runs.

The remaining "local" fields B_{L1} and B_{L2} decrease overall with depth for both runs (Figs. 53 and 54). This decrease changes as a function of depth. Down to about 250–280 mbsf, the decrease is masked by the effect of the pipe located in the upper part of the hole and, as a result, an apparent increase occurs. Below this level, the average values of B_L remain more or less constant and then decrease systematically with increasing depth (Fig. 53). This overall negative gradient is consistent with the overall negative value of the "local" remaining B_L field. Indeed, if the average value of *Bf*, the field arising from the sediments, must be slightly positive when assuming an average Koenigsberger ratio of 1, a 600- to 900-nT value would imply rock magnetizations [Bf (nT) = $\mu_0(J_i + J_r)$ (A/m)] in excess of 1 A/m. These magnetizations would be equivalent to susceptibilities of about 2.5 10^{-2} SI, which are much higher than the values measured in the sediments (see "Paleomagnetism" section, this chapter). Thus, one must consider that Site 884 is located in a negative anomaly field (*Ba*, >500 nT). However, one must also be aware that the changes of gradient may arise partially from an increase in susceptibility, as observed below 600 mbsf in the susceptibility log (see below). A precise estimate of *Ba* requires further analysis.

To evaluate the true *Bf* field arising from the sedimentary formation, the last component of the "local fields" B_{L1} and B_{L2} to consider is any variation in the local time-dependent (transient) field. Because the measurements were performed below more than 2000 m of conductive salt water, only low frequency variations ($\leq 10^{-2}$ Hz: ≥ 16 m in the logs) might affect the recorded values (skin effect). During a magnetic storm, the difference between the two logs should show uncorrelated variations on the 10-m scale or more. This variation was not observed, and any variations are mostly because of depth discrepancies among the logs. Figure 55 shows $B_{L1} - B_{L2}$, the variation of the difference between the "local fields" obtained from the two runs with respect to depth and to B_{L1}, the local field obtained from Run 1. On the whole, the greatest differences between the two runs are related to the highest variations of the local B_L field and thus are related to depth errors. However, the average difference is significant and cannot arise from local depth errors only. In Figure 55, and for three selected shorter depth intervals, the two runs have been plotted together. A decreasing systematic depth shift is evident between the two passes. By adjusting the depth, one may correct most of the difference for any one segment, but a unique adjustment cannot be made to correct the whole log. Moreover, if the same general variation can be seen on both runs on such an expanded scale, small differences are seen in the internal shape of the peaks and lows. Indeed, the WHC was engaged before the first run, but it failed immediately, and the logs were recorded without it. As a consequence, the wavelength of the ship's heave, based on the tension log, appears to be roughly 1 m. Thus, variations smaller than 1 m may be attributable to variable ship's heave. The tension logs indicate no abrupt changes in wireline tension that correspond to a release of the WHC arm, and depth shift evolution appears more or less continuous. Depth offsets between the main and repeat logs show a difference ranging from about 3.3 m at 690 mbsf to only 0.6 m at 155 mbsf, which, according to determination uncertainties, can be modeled either as a linear or polynomial (z^2) function of time or depth.

Susceptibility Results

The susceptibility tool measurement is based on two coils that are in equilibrium (tuned) in the absence of magnetically susceptible material. During logging, the variation of a secondary flux induced by the surrounding rocks between the two coils is measured in parts per million (ppm) of the main flux, 1 ppm being roughly equivalent to 10^{-6} SI. One of the problems is the absence of a true zero; hence, the baseline must be estimated from the logs and, when available, from adjacent core measurements. The possible errors can be estimated by comparisons between the main log and the repeat section. These can be measurement errors, depth errors, or discrepancies resulting from thermal drift of the measurement coils.

Main Susceptibility Zones

Figure 56 shows both the main susceptibility log and the repeat section, expressed in parts per million. The second pass is only a partial repeat section that starts at 365 mbsf and ends within the drill pipe. We were unable to log below 680 mbsf because of deteriorating hole conditions. Most of the values are negative because the susceptibility tool has no fixed zero reference. Six different zones can be deduced

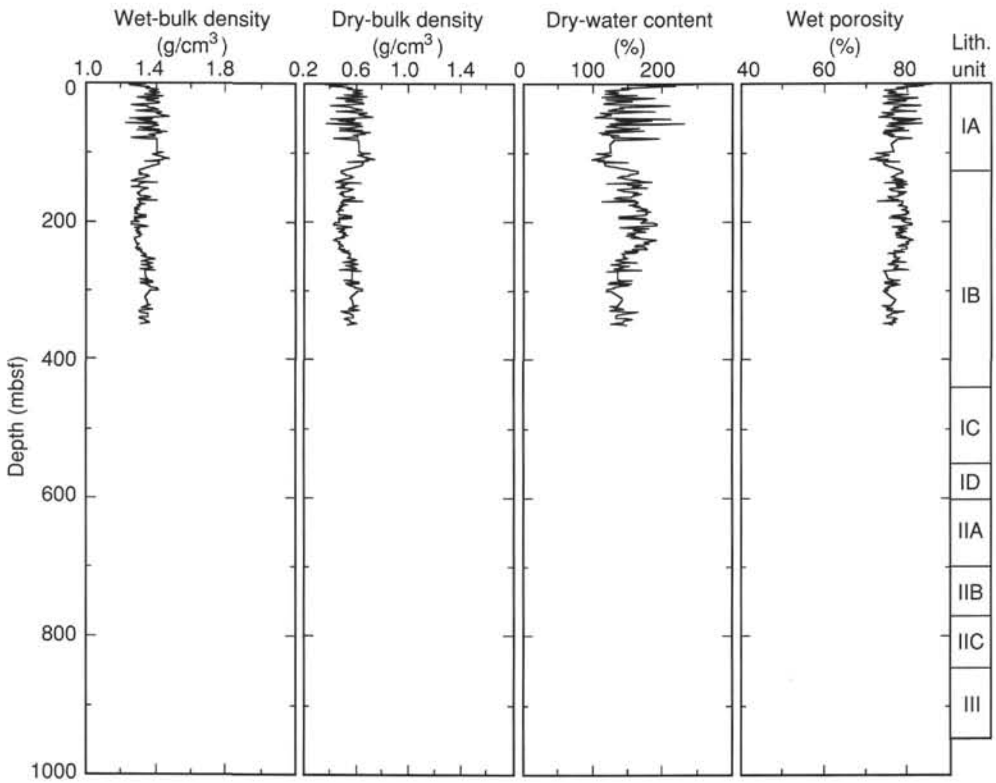

Figure 37. Index property data vs. depth for Hole 884C. Lithologic units are shown at right.

from these logs. From 60 to about 120 mbsf, average susceptibility values are high and have numerous narrow peaks. Between 120 and about 245 mbsf, the average susceptibility is low and contains a few local anomalies. Note that the apparent minimum values, which seem to correspond to a flat line, are not the result of a zero susceptibility but are the result of the lower cutoff from the channel used for that representation. Because of the limited discrete possible values for digitization, two channels are available for susceptibility. One of them, represented here, has a high resolution of 1 ppm/step but a limited dynamic range, whereas the other one has a 5 ppm/step resolution but a broader range. When checking the lower resolution channel, values lower than the apparent limit of Figure 56 were obtained for that zone. From 245 to about 360 mbsf, the average susceptibility gently increases until it reaches a constant level. The data show that susceptibility changes occur within narrow zones. Below 360 and down to about 460 mbsf, the average susceptibility remains the same, but the signal shows broader anomalies than in the overlying zone. Between 460 and 630 mbsf, the average susceptibility is slightly higher and has broad and smooth variations. Below 630 mbsf to the bottom of the log, susceptibility increases markedly with depth.

Analysis of the Susceptibility Records

Figure 57 shows a close-up of the susceptibility records, corrected for a –2750 offset of the zero value, for the 60 to 360 mbsf interval of the repeat section. The correlation between the main log (Run 1) and the repeat section is good in terms of their general shape and variability. No broad discrepancies exist between the two runs, indicating few large measurement errors or thermal drift. However, fine-scale differences do occur.

In Figure 58, a plot is presented for the first run between 60 and 360 mbsf as well as the difference in susceptibility between the two runs ($k_2 - k_1$). In some zones, the difference is small and more or less constant at about 20 ppm. Thermal drift is a function of two temperatures: the external temperature measured at the receiving coil and the difference in temperature between the excited coil and the receiving coil. The temperature of the tool decreased during logging operations, but temperature differences between the two runs remained within 2°C, and the observed discrepancy, in the zone where few susceptibility discrepancies exist between the two logs, is consistent with the known thermal drift of the tool. Most of the highest peaks on the difference plot are related to zones of high susceptibility variations and thus to depth discrepancy. When compared with the log from Hole 883F, the differences are much larger and are not related to local depth discrepancies only. Figure 58 also presents a detailed plot of the two runs at the same scale for three zones. As for the total induction (*B* field) logs, a systematic depth shift was observed between the two susceptibility runs, which indicates an overall decrease with decreasing depth (Fig. 58). However, the evolution of that depth shift is not regular; it begins at about a 2.2-m offset at 350 mbsf and declines to about 0.4 m at 60 mbsf, with an intermediate minimum of 0.9 m at 290 mbsf and a local maximum of 1.6 at 225 mbsf. As for the tension logs, the ship's heave during the susceptibility runs was more significant and more variable than during the total field logging, which induced small-scale errors. This can explain why the detailed comparisons are more difficult on the expanded scale susceptibility plots.

The analysis of the total induction (*B* field) and susceptibility logs reveals that two common problems compromise data quality. The first problem is that the WHC was not operational. Indeed, if repeatability is good above the 2-m scale, it becomes poorer for smaller intervals. One must use caution when interpreting small-scale variations in these magnetic logs. Had sea-state conditions been calmer during logging, we may have been able to isolate the cause of the second problem: the larger-valued depth errors. As the hole was collapsing, the bottom of the hole was unexpectedly reached twice: before Run 2 of the magnetometer and before Run 1 of the susceptibility tool. Both cases seem to have been related to the problem of depth shift. Indeed, the data show that the apparent depth of anomalies that can be correlated between the two runs is higher when the bottom of the hole is reached just before the beginning of a log.

Table 16. Index properties, compressional wave velocity, and shear strength data, Hole 884C.

Core, section, interval (cm)	Depth (mbsf)	Wet-bulk density (g/cm^3)	Dry-bulk density (g/cm^3)	Grain density (g/cm^3)	Wet porosity (%)	Dry water content (%)	Shear strength (kPa)	Compressional wave velocity (m/s)
145-884C-								
1H-1, 39	0.39	1.24	0.36	2.55	85.5	242.8		
1H-1, 53	0.53							1502.5
1H-1, 95	0.95							1494.60
1H-1, 99	0.99	1.34	0.53	2.59	79.1	152.0		
1H-1, 15	1.15						10.507	
1H-1, 23	1.23						6.029	
1H-2, 19	1.69	1.34	0.53	2.56	79.0	153.6		
2H-1, 53	2.93							1483.6
2H-1, 45	3.14	1.25	0.39	2.50	83.8	218.0		
2H-1, 10	3.50						10.203	
2H-2, 74	4.64	1.36	0.56	2.53	77.4	140.7		
2H-3, 45	5.85							1512.1
2H-3, 74	6.14	1.34	0.53	2.59	79.3	153.8		
2H-3, 110	6.50						19.479	
2H-4, 74	7.64	1.34	0.53	2.51	78.4	150.1		
2H-5, 45	8.85							1500.9
2H-5, 74	9.14	1.41	0.65	2.58	74.4	116.9		
2H-5, 100	9.40						19.942	
2H-6, 74	10.64	1.41	0.65	2.57	74.5	117.9		
2H-7, 39	11.79	1.36	0.58	2.55	77.0	137.2		
3H-1, 53	12.43							1504.1
3H-1, 74	12.64	1.36	0.58	2.51	76.7	136.3		
3H-1, 110	13.00						12.058	
3H-2, 74	14.14	1.42	0.65	2.65	75.1	118.3		
3H-3, 34	15.24							1505.7
3H-3, 74	15.64	1.37	0.56	2.69	78.8	143.7		
3H-3, 90	15.80						18.087	
3H-4, 74	17.14	1.33	0.51	2.62	80.3	162.9		
3H-5, 45	18.35							1505.7
3H-5, 74	18.64	1.44	0.68	2.66	74.3	112.5		
3H-5, 110	19.00						21.334	
3H-6, 74	20.14	1.29	0.45	2.58	82.3	188.3		
4H-1, 40	21.80							1504.1
4H-1, 74	22.14	1.36	0.54	2.71	79.6	150.6		
4H-1, 110	22.50						41.740	
4H-2, 79	23.69	1.41	0.64	2.61	75.2	120.4		
4H-3, 40	24.80							1518.6
4H-3, 74	25.14	1.34	0.52	2.58	79.4	155.5		
4H-3, 110	25.50						43.131	
4H-4, 69	26.59	1.41	0.64	2.60	75.1	120.7		
4H-5, 60	28.00							1513.8
4H-5, 74	28.14	1.42	0.66	2.61	74.2	114.5		
4H-5, 110	28.50						25.972	
5H-1, 55	31.45							1496.1
5H-1, 74	31.64	1.26	0.41	2.50	83.2	208.6		
5H-1, 110	32.00						39.421	
5H-2, 74	33.14	1.35	0.56	2.45	76.7	140.1		
5H-3, 40	34.30							1512.1
5H-3, 74	34.64	1.35	0.56	2.54	77.7	143.0		
5H-3, 110	35.00						36.175	
5H-4, 74	36.14	1.37	0.59	2.58	76.9	134.3		
5H-5, 40	37.30							1504.1
5H-5, 74	37.64	1.41	0.64	2.67	75.9	122.3		
5H-5, 110	38.00						40.813	
5H-6, 79	39.19	1.29	0.45	2.55	82.1	188.9		
5H-7, 44	40.34	1.28	0.47	2.29	79.0	171.6		
6H-1, 40	40.80							1505.7
6H-1, 74	41.14	1.39	0.62	2.57	75.6	125.7		
6H-1, 110	41.50						38.494	
6H-2, 40	42.30							1485.1
6H-2, 74	42.64	1.43	0.68	2.63	73.9	111.9		
6H-3, 74	44.14	1.40	0.62	2.67	76.5	126.8		
6H-3, 110	44.50						41.276	
6H-6, 40	48.30							1499.3
6H-6, 74	48.64	1.47	0.72	2.72	73.1	103.7		
6H-6, 110	49.00						42.668	
6H-7, 39	49.79	1.25	0.40	2.43	83.0	211.1		
7H-1, 40	50.30							1499.3
7H-1, 74	50.64	1.38	0.59	2.55	76.4	131.8		
7H-1, 110	51.00						35.711	
7H-2, 74	52.14	1.37	0.58	2.63	77.7	138.0		
7H-3, 60	53.50							1510.5
7H-3, 74	53.64	1.29	0.46	2.55	81.7	182.9		
7H-3, 110	54.00						43.595	
7H-4, 74	55.14	1.34	0.53	2.55	79.0	153.7		
7H-5, 40	56.30							1504.1
7H-5, 70	56.60						56.581	
7H-5, 74	56.64	1.40	0.63	2.61	75.6	123.7		
7H-6, 49	57.39	1.22	0.37	2.26	83.3	231.6		
8H-1, 40	59.80							1499.3
8H-1, 89	60.29	1.38	0.59	2.62	77.2	134.7		
8H-1, 110	60.50						45.914	

Table 16 continued.

Core, section, interval (cm)	Depth (mbsf)	Wet-bulk density (g/cm^3)	Dry-bulk density (g/cm^3)	Grain density (g/cm^3)	Wet porosity (%)	Dry water content (%)	Shear strength (kPa)	Compressional wave velocity (m/s)
8H-2, 74	61.64	1.41	0.64	2.58	74.8	119.1		
8H-3, 40	62.80							1507.3
8H-3, 74	63.14	1.35	0.54	2.59	78.8	149.7		
8H-3, 110	63.50						44.987	
8H-4, 74	64.64	1.30	0.48	2.38	79.2	167.5		
8H-5, 40	65.80							1499.3
8H-5, 74	66.14	1.36	0.56	2.61	78.2	142.7		
8H-5, 110	66.50						52.871	
8H-6, 74	67.64	1.42	0.65	2.60	74.5	116.9		
8H-7, 29	68.69	1.29	0.47	2.44	80.2	173.6		
9H-1, 40	69.30							1512.1
9H-1, 74	69.64	1.46	0.7	2.74	74.2	109.1		
9H-1, 110	70.00						65.292	
9H-2, 74	71.14	1.40	0.63	2.63	75.8	123.9		
9H-3, 40	72.30							1507.3
9H-3, 74	72.64	1.43	0.67	2.61	74.1	114.1		
9H-4, 74	74.14	1.36	0.58	2.51	76.7	136.5		
9H-4, 110	74.50						63.791	
9H-5, 50	75.40							1518.6
9H-5, 74	75.64	1.38	0.61	2.50	75.2	125.8		
9H-5, 110	76.00						84.053	
9H-6, 49	76.89	1.39	0.61	2.60	76.4	128.9		
10X-1 40	78.80							1508.9
10X-1, 74	79.14	1.26	0.43	2.29	81.0	193.9		
10X-1, 110	79.50						44.278	
10X-2, 74	80.64	1.35	0.56	2.49	77.2	142.0		
10X-3, 40	81.80							1513.8
10X-3, 74	82.14	1.40	0.61	2.72	77.2	129.6		
10X-3, 110	82.50						50.282	
11X-1, 29	88.49	1.40	0.62	2.61	75.8	124.4		
12X-1, 40	98.20							1504.1
12X-1, 74	98.54	1.40	0.62	2.67	76.6	127.0		
12X-1, 110	98.90						58.537	
12X-2, 74	100.04	1.40	0.65	2.50	73.6	116.0		
12X-3, 40	101.20							1507.3
12X-3, 74	101.54	1.44	0.7	2.57	72.3	105.3		
12X-3, 110	101.90						63.791	
12X-4, 74	103.04	1.38	0.61	2.52	75.4	126.2		
13X-1, 40	107.80							1512.1
13X-1, 74	108.14	1.47	0.74	2.60	71.0	97.6		
13X-1, 110	108.50						56.286	
13X-2, 74	109.64	1.44	0.67	2.71	75.1	115.6		
13X-3, 40	110.80							1517.0
13X-3, 74	111.14	1.44	0.69	2.57	72.7	107.2		
13X-3, 110	111.50						68.293	
13X-4, 74	112.64	1.33	0.53	2.46	78.0	150.5		
13X-5, 40	113.80							1543.5
13X-5, 74	114.14	1.42	0.66	2.57	74.1	115.4		
13X-5, 110	114.50						65.292	
13X-6, 74	115.64	1.41	0.65	2.56	74.3	117.5		
14X-1, 74	117.74	1.42	0.65	2.65	75.0	117.7		
14X-1, 110	118.10						59.288	
14X-2, 19	118.69	1.40	0.64	2.54	74.6	119.6		
15X-1, 40	127.10							1543.5
15X-1, 74	127.44	1.30	0.49	2.33	78.6	164.0		
15X-1, 110	127.80						38.274	
15X-2, 74	128.94	1.30	0.49	2.33	78.6	163.9		
15X-3, 40	130.10							1541.8
15X-3, 74	130.44	1.32	0.52	2.36	77.4	151.2		
15X-3, 110	130.80						54.034	
15X-4, 74	131.94	1.30	0.52	2.27	77.0	152.9		
15X-5, 40	133.10							1548.6
15X-5, 74	133.44	1.34	0.55	2.44	77.1	143.5		
15X-5, 110	133.80						71.295	
15X-6, 74	134.94	1.36	0.58	2.43	75.8	134.2		
15X-7, 39	135.59	1.34	0.56	2.41	76.5	140.6		
16X-1, 40	136.70							1528.5
16X-1, 74	137.04	1.33	0.54	2.37	76.9	146.6		
16X-1, 110	137.40						44.278	
16X-2, 74	138.54	1.29	0.49	2.33	78.8	166.4		
16X-3, 40	139.70							1538.5
16X-3, 74	140.04	1.29	0.5	2.17	76.4	155.2		
16X-3, 110	140.40						43.528	
16X-4, 74	141.54	1.26	0.44	2.20	79.5	183.0		
16X-5, 40	142.70							1531.8
16X-5, 74	143.04	1.40	0.63	2.52	74.4	120.1		
16X-5, 110	143.40						51.032	
16X-6, 74	144.54	1.33	0.53	2.50	78.6	153.2		
16X-7, 19	145.49	1.31	0.52	2.30	76.9	150.2		
17X-1, 40	146.40							1528.5
17X-1, 74	146.74	1.30	0.49	2.44	79.8	168.4		
17X-1, 110	147.10						39.025	
17X-2, 74	148.24	1.30	0.51	2.29	77.4	155.3		
17X-3, 40	149.40							1515.4

Table 16 continued.

Core, section, interval (cm)	Depth (mbsf)	Wet-bulk density (g/cm^3)	Dry-bulk density (g/cm^3)	Grain density (g/cm^3)	Wet porosity (%)	Dry water content (%)	Shear strength (kPa)	Compressional wave velocity (m/s)
17X-3, 74	149.74	1.26	0.45	2.20	79.0	178.0		
17X-3, 110	150.10						45.779	
17X-4, 74	151.24	1.29	0.48	2.32	78.9	167.9		
17X-5, 40	152.40							1533.5
17X-5, 74	152.74	1.35	0.58	2.38	75.4	133.7		
17X-5, 110	153.10						57.036	
17X-6, 74	154.24	1.32	0.54	2.31	76.4	0.5		
18X-1, 40	156.10							1530.2
18X-1, 74	156.44	1.31	0.49	2.44	79.4	165.0		
18X-1, 110	156.80						51.783	
18X-2, 74	157.94	1.30	0.50	2.30	77.8	158.9		
18X-3, 40	159.10							1548.6
18X-3, 74	159.44	1.29	0.48	2.33	79.1	169.2		
18X-3, 110	159.80						43.528	
18X-4, 74	160.94	1.30	0.50	2.33	78.1	159.1		
18X-5, 40	162.10							1555.4
18X-5, 74	162.44	1.31	0.51	2.31	77.4	154.2		
18X-5, 110	162.80						46.530	
18X-6, 74	163.94	1.33	0.56	2.28	75.3	138.5		
19X-1, 40	165.70							1505.7
19X-1, 74	166.04	1.37	0.59	2.47	75.7	130.9		
19X-1, 110	166.40						53.284	
19X-2, 74	167.54	1.29	0.50	2.25	77.6	160.1		
19X-3, 40	168.70							1531.8
19X-3, 74	169.04	1.40	0.65	2.41	72.6	113.8		
19X-3, 110	169.40						45.779	
19X-4, 74	170.54	1.30	0.50	2.36	78.6	162.1		
19X-5, 30	171.60							1500.9
19X-5, 74	172.04	1.30	0.49	2.37	78.9	164.8		
19X-5, 110	172.40						50.282	
19X-6, 74	173.54	1.32	0.51	2.41	78.4	156.3		
19X-7, 39	174.69	1.33	0.53	2.43	78.0	151.5		
20X-1, 50	175.50							1525.2
20X-1, 74	175.74	1.29	0.48	2.27	78.4	166.9		
20X-1, 110	176.10						31.520	
20X-2, 74	177.24	1.30	0.50	2.29	77.7	158.6		
20X-3, 53	178.53							1538.5
20X-3, 74	178.74	1.31	0.49	2.47	79.7	166.3		
20X-3, 110	179.10						48.781	
20X-4, 74	180.24	1.27	0.46	2.26	79.3	176.8		
20X-5, 53	181.53							1536.8
20X-5, 74	181.74	1.30	0.50	2.32	78.3	162.0		
20X-5, 110	182.10						35.272	
20X-6, 74	183.24	1.28	0.47	2.30	79.1	171.3		
20X-7, 19	184.19	1.27	0.45	2.32	80.2	181.7		
21X-1, 53	185.13							1545.2
21X-1, 74	185.34	1.28	0.46	2.29	79.5	176.0		
21X-1, 110	185.70						27.768	
21X-2, 74	186.84	1.29	0.46	2.39	80.2	176.9		
21X-3, 53	188.13							1548.6
21X-3, 74	188.34	1.27	0.46	2.24	78.9	174.1		
21X-3, 110	188.70						36.773	
21X-4, 74	189.84	1.28	0.47	2.29	79.3	174.1		
21X-5, 53	191.13							1540.2
21X-5, 74	191.34	1.34	0.57	2.39	75.9	137.1		
21X-5, 110	191.70						35.272	
21X-6, 74	192.84	1.27	0.46	2.28	79.4	176.4		
21X-7, 19	193.79	1.34	0.57	2.36	75.6	136.2		
22X-1, 53	194.83							1525.2
22X-1, 74	195.04	1.29	0.46	2.40	80.4	178.3		
22X-1, 110	195.40						30.770	
22X-2, 74	196.54	1.27	0.46	2.27	79.3	176.7		
22X-3, 53	197.83							1540.2
22X-3, 74	198.04	1.27	0.46	2.18	78.4	173.8		
22X-3, 110	198.40						32.271	
22X-4, 74	199.54	1.30	0.48	2.38	79.4	168.4		
22X-5, 53	200.83							1538.5
22X-5, 74	201.04	1.26	0.44	2.22	79.8	185.6		
22X-5, 110	201.40						31.520	
22X-6, 74	202.54	1.26	0.43	2.30	80.9	192		
22X-7, 29	203.59	1.26	0.43	2.30	80.8	190.5		
23X-1, 53	204.53							1540.2
23X-1, 74	204.74	1.27	0.45	2.37	80.8	185.7		
23X-1, 110	205.10						31.520	
23X-2, 74	206.24	1.35	0.57	2.43	76.4	138.2		
23X-3, 53	207.53							1528.5
23X-3, 74	207.74	1.27	0.45	2.27	79.7	179.7		
23X-3, 110	208.10						27.768	
23X-4, 74	209.24	1.28	0.47	2.35	79.8	175.4		
23X-5, 53	210.53							1531.8
23X-5, 74	210.74	1.30	0.51	2.31	77.7	157.6		
23X-5, 110	211.10						46.530	
23X-6, 74	212.24	1.28	0.46	2.29	79.4	176.0		
23X-7, 29	213.29	1.28	0.47	2.26	79.0	173.4		

Table 16 continued.

Core, section, interval (cm)	Depth (mbsf)	Wet-bulk density (g/cm³)	Dry-bulk density (g/cm³)	Grain density (g/cm³)	Wet porosity (%)	Dry water content (%)	Shear strength (kPa)	Compressional wave velocity (m/s)
24X-1, 53	214.13							1540.2
24X-1, 74	214.34	1.31	0.52	2.32	77.1	150.7		
24X-1, 110	214.70						52.533	
24X-2, 74	215.84	1.31	0.50	2.39	78.7	160.3		
24X-3, 53	217.13							1531.8
24X-3, 74	217.34	1.29	0.50	2.23	77.2	158.3		
24X-3, 110	217.70						59.288	
24X-4, 74	218.84	1.32	0.53	2.37	77.1	147.8		
24X-5, 53	220.13							1538.5
24X-5, 74	220.34	1.31	0.51	2.34	78.0	158.0		
24X-5, 110	220.70						66.792	
24X-6, 74	221.84	1.30	0.49	2.39	79.3	167.1		
24X-7, 39	222.49	1.31	0.51	2.30	77.3	153.8		
25X-1, 53	223.83							1531.8
25X-1, 74	224.04	1.27	0.45	2.31	80.0	180.6		
25X-1, 110	224.40						33.021	
25X-2, 74	225.54	1.27	0.43	2.35	81.2	191.3		
25X-3, 53	226.83							1538.5
25X-3, 74	227.04	1.28	0.47	2.33	79.6	174.0		
25X-3, 110	227.40						43.528	
25X-5, 53	229.83							1546.9
25X-5, 74	230.04	1.28	0.46	2.33	80.0	179.8		
25X-5, 110	230.40						40.526	
25X-6, 74	231.54	1.29	0.48	2.39	79.7	171.9		
25X-7, 29	232.59	1.30	0.49	2.35	78.6	163.6		
26X-1, 53	233.43							1541.8
26X-1, 74	233.64	1.29	0.50	2.26	77.6	159.5		
26X-1, 110	234.00						47.280	
26X-2, 74	235.14	1.29	0.47	2.35	79.6	173.5		
26X-3, 53	236.43							1538.5
26X-3, 74	236.64	1.29	0.47	2.38	79.9	174.5		
26X-3, 110	237.00						38.274	
26X-4, 74	238.14	1.28	0.46	2.32	79.8	177.5		
26X-5, 53	239.43							1543.5
26X-5, 74	239.64	1.31	0.51	2.40	78.3	156.4		
26X-5, 110	240.00						60.789	
26X-6, 74	241.14	1.29	0.49	2.29	78.3	163.8		
26X-7, 29	242.09	1.32	0.54	2.33	76.6	146.2		
27X-1, 53	243.03							1468.2
27X-1, 74	243.24	1.31	0.50	2.44	79.1	162		
27X-1, 110	243.60						46.530	
27X-2, 84	244.84	1.32	0.55	2.24	75.2	140.4		
27X-3, 53	246.03							1533.5
27X-3, 69	246.19	1.32	0.54	2.32	76.4	144.9		
27X-3, 110	246.60						75.798	
27X-4, 74	247.74	1.34	0.55	2.41	76.9	143.7		
27X-5, 53	249.03							1510.5
27X-5, 74	249.24	1.34	0.55	2.42	76.9	143.1		
27X-5, 110	249.60						72.046	
27X-6, 79	250.79	1.32	0.54	2.34	76.6	0.6		
27X-7, 14	251.64	1.33	0.54	2.39	77.1	146.7		
28X-1, 53	252.73							1536.8
28X-1, 74	252.94	1.33	0.53	2.45	77.9	149.7		
28X-1, 110	253.30						64.541	
28X-2, 74	254.44	1.39	0.60	2.67	77.3	132.6		
28X-3, 43	255.63							1538.5
28X-3, 74	255.94	1.34	0.56	2.41	76.4	140.2		
28X-3, 110	256.30						76.549	
28X-4, 74	257.44	1.32	0.50	2.49	79.5	162.6		
28X-5, 53	258.73							1525.2
28X-5, 74	258.94	1.33	0.54	2.37	77.0	147.0		
28X-5, 110	259.30						78.800	
28X-6, 69	260.39	1.38	0.61	2.51	75.2	125.2		
28X-7, 54	261.74	1.33	0.54	2.42	77.3	146.2		
29X-1, 63	262.43							1536.8
29X-1, 74	262.54	1.32	0.52	2.38	77.6	151.5		
29X-1, 119	262.99						66.042	
29X-2, 74	264.04	1.36	0.57	2.53	77.3	140.0		
29X-3, 53	265.33							1533.5
29X-3, 74	265.54	1.35	0.56	2.48	77.3	142.5		
29X-3, 110	265.90						56.286	
29X-4, 74	267.04	1.38	0.60	2.59	76.6	131.3		
29X-5, 53	268.33							1510.5
29X-5, 74	268.54	1.31	0.48	2.49	80.2	169.7		
29X-5, 110	268.90						51.032	
29X-6, 79	270.09	1.32	0.52	2.37	77.7	153.2		
29X-7, 29	271.09	1.39	0.63	2.47	74.1	120.0		
30X-1, 24	271.64	1.33	0.57	2.24	74.4	134.8		
31X-1, 53	281.63							1540.2
31X-1, 74	281.84	1.34	0.57	2.34	75.3	135.4		
31X-1, 100	282.10						21.764	
31X-2, 74	283.34	1.35	0.56	2.46	76.7	139.2		
31X-3, 53	284.63							1546.9
31X-3, 74	284.84	1.31	0.51	2.39	78.2	156.9		

Table 16 continued.

Core, section, interval (cm)	Depth (mbsf)	Wet-bulk density (g/cm^3)	Dry-bulk density (g/cm^3)	Grain density (g/cm^3)	Wet porosity (%)	Dry water content (%)	Shear strength (kPa)	Compressional wave velocity (m/s)
31X-3, 110	285.20						67.543	
31X-4, 74	286.34	1.38	0.62	2.44	74.4	123.3		
31X-5, 65	287.75							1541.8
31X-5, 74	287.84	1.31	0.52	2.32	77.5	154.0		
31X-5, 125	288.35						66.042	
31X-6, 69	289.29	1.38	0.62	2.46	74.5	122.9		
31X-7, 19	290.29	1.32	0.53	2.33	76.7	147.0		
32X-1, 53	291.23							1535.1
32X-1, 74	291.44	1.33	0.53	2.45	78.2	152.2		
32X-1, 110	291.80						60.038	
32X-2, 74	292.94	1.36	0.58	2.41	75.4	132.0		
32X-3, 53	294.23							1550.3
32X-3, 74	294.44	1.36	0.60	2.39	74.7	127.9		
32X-3, 110	294.80						89.307	
32X-4, 74	295.94	1.36	0.59	2.43	75.5	131.5		
32X-5, 53	297.23							1555.4
32X-5, 74	297.44	1.40	0.64	2.54	74.5	119.5		
32X-5, 110	297.80						71.295	
32X-6, 69	298.89	1.41	0.64	2.62	75.1	119.5		
32X-7, 54	300.24	1.37	0.61	2.40	74.3	125.4		
34X-1, 50	310.60							1460.6
34X-1, 74	310.84	1.33	0.55	2.35	76.2	141.5		
34X-1, 120	311.30						33.021	
34X-2, 24	311.84	1.34	0.56	2.44	76.8	141.5		
35X-1, 53	320.23							1530.2
35X-1, 74	320.44	1.35	0.58	2.42	75.9	135.0		
35X-1, 110	320.80						60.789	
35X-2, 74	321.94	1.37	0.61	2.36	73.9	124.5		
35X-3, 53	323.23							1546.9
35X-3, 74	323.44	1.34	0.58	2.33	74.9	132.9		
35X-3, 110	323.89						54.785	
35X-4, 74	324.94	1.32	0.54	2.31	76.3	144.3		
35X-5, 53	326.23							1546.9
35X-5, 74	326.44	1.34	0.57	2.30	74.7	133.5		
35X-5, 110	326.80						42.027	
35X-6, 74	327.94	1.38	0.62	2.47	74.7	124.3		
35X-7, 29	328.99	1.32	0.53	2.34	76.9	148.0		
36X-1, 53	329.73							1553.7
36X-1, 74	329.94	1.30	0.49	2.41	79.2	165.0		
36X-1, 110	330.30						87.806	
36X-2, 74	331.44	1.31	0.53	2.28	76.4	147.2		
36X-3, 53	332.73							1557.1
36X-3, 74	332.94	1.31	0.54	2.25	75.8			
36X-3, 110	333.30						54.034	
36X-4, 74	334.44	1.35	0.57	2.41	75.9	135.5		
36X-5, 53	335.73							1555.4
36X-5, 74	335.94	1.35	0.58	2.34	74.9	132.3		
36X-5, 110	336.30						87.806	
36X-6, 74	337.44	1.35	0.58	2.36	75.0	131.6		
36X-7, 29	338.49	1.32	0.54	2.29	76.2	145.3		
37X-1, 53	339.23							1543.5
37X-1, 74	339.44	1.32	0.53	2.31	76.5	146.5		
37X-1, 110	339.80						51.032	
37X-2, 74	340.94	1.3	0.51	2.26	77.2	155.7		
37X-3, 53	342.23							1528.5
37X-3, 74	342.44	1.33	0.55	2.36	76.4	142.4		
37X-3, 110	342.80						84.804	
37X-4, 74	343.94	1.34	0.55	2.41	76.8	143.2		
37X-5, 53	345.23							1517
37X-5, 74	345.44	1.35	0.57	2.48	76.8	138.6		
37X-5, 110	345.80						58.537	
37X-6, 74	346.94	1.36	0.60	2.35	74.1	126.9		
37X-7, 29	347.99	1.35	0.59	2.38	75.1	131.4		
38X-1, 49	348.69	1.31	0.53	2.27	76.4	148.4		

Conclusions About Total Induction and Susceptibility Data

Analysis of the downhole magnetic measurements performed in Hole 884E shows that, on the whole, the data are reliable when taking into account the depth shifts that occurred between repeated sections and the small discrepancies arising from ship's heave. These data will permit comparisons with main lithology and laboratory susceptibility measurements.

Comparison of Magnetic Logs with Core Data

Figure 59 shows the comparison of the "local" *B* field obtained from the first run of the magnetometer (B_{L1}, nT) with the corrected susceptibility (k_1, ppm), and the whole-core susceptibility values measured in cores from Hole 884B and transformed into 10^{-6} SI values. Generally, from 70 to 680 mbsf the anomalies from both logs are negatively correlated. This finding was expected for high latitudes. A nearby layer bearing a magnetization direction of x_1, y_1, z_1 will, in a borehole, produce an induction (or *B* field) with an x_1, y_1, $-2z_1$ direction (Barthes, 1990). Thus, the projection of the *B* field arising from the susceptibility of the surrounding rocks onto the direction of the ambient Earth's field will produce a negative correlation. However, this negative correlation is a geometrical effect and is true only for anomalies arising from the sediments surrounding the borehole, not for regional anomalies. For these simple geometrical

Table 17. Index properties and compressional wave velocity data, Hole 884E.

Core, section, interval (cm)	Depth (mbsf)	Wet-bulk density (g/cm³)	GRAPE bulk density (g/cm³)	Dry-bulk density (g/cm³)	Grain density (g/cm³)	Dry porosity (%)	Dry water content (%)	Void ratio	Compressional wave velocity (m/s)
145-884E-									
1R-1,72	843.52	2.69	2.69	2.57	2.90	11.3	4.5	0.13	4773.7
1R-4,71	847.94	2.81	2.80	2.74	2.93	6.6	2.5	0.07	5312.1
1R-5,59	848.99	2.88	2.81	2.84	2.96	4.1	1.5	0.04	5707.6
2R-1,76	853.26	2.95	2.98	2.91	3.02	3.9	1.4	0.04	5851.5
3R-3,57	865.51	2.91	2.42	2.89	2.96	2.5	0.9	0.03	6023.0
4R-2,71	874.22	2.91	2.79	2.89	2.96	2.2	0.8	0.02	6135.2
4R-4,21	876.72	2.76	2.83	2.71	2.86	5.2	2.0	0.05	6028.9
4R-5,79	878.54	2.81	2.73	2.76	2.90	4.6	1.7	0.05	5807.2
5R-1,75	882.55	2.84	2.33	2.80	2.91	4.0	1.5	0.04	5977.0
5R-4,14	886.4	2.86	2.94	2.83	2.93	3.1	1.1	0.03	6084.5
5R-5,134	888.66	2.71	2.83	2.65	2.81	5.8	2.2	0.06	5796.6
6R-3,61	894.9	2.85	2.90	2.80	2.93	4.2	1.6	0.04	5898.0
7R-2,85	898.42	2.87	2.91	2.83	2.95	4.0	1.4	0.04	5923.2
7R-3,136	900.33	2.64	2.84	2.55	2.8	9.0	3.6	0.10	5517.2
9R-2,98	913.06	2.87	2.94	2.84	2.91	2.5	0.9	0.03	6063.9
9R-4,78	915.47	2.68	2.81	2.61	2.81	7.2	2.8	0.08	5818.4
9R-7,22	919.33	2.83	2.92	2.78	2.92	4.7	1.7	0.05	5468.5
10R-5,62	926.48	2.68	2.78	2.62	2.79	6.0	2.3	0.06	5539.8

reasons, and depending on the magnetic latitude (as well as the tool response and hole diameter), a given susceptibility will have a varying effect on the magnetometer sensor: the transfer coefficient between the two tools will depend on the field inclination. In Figure 59, the relative scales for both tools have been selected for practical representation purposes. Thus, the overall variations in relative amplitude in both logs do not mean that surrounding rocks are more susceptible or remanent. The two logs do not always correlate strongly. In the interval from 60 to 100 mbsf, the total induction log has been dominated by the effect of the pipe located in the upper part of the hole. Furthermore, the relative variation of susceptibility and of the *B* field is not always the same, indicating changes in the relative value of the induced and remanent magnetization, as well as changes in the direction of the remanent magnetization.

Comparison with Core Susceptibility Measurements

Several observations can be made by comparing the downhole and laboratory susceptibility data. More sharp and narrow peaks can be seen in the record obtained from whole-core measurements conducted in the laboratory. These peaks are often correlated to lower amplitude and broader ones in the logs. One reason for this difference is the real resolution of the log and core measurements. Laboratory data are recorded each 5 cm and correspond to the measurement of a small volume of material. In contrast, downhole data represent a much larger volume of material, thus the tool's response tends to broaden the anomalies. And wider and smoother anomalies, which sometimes correspond to very thin ash layers, will be seen in the susceptibility log record. Some peaks that may be seen on the logs do not appear in the laboratory core measurements. This may reflect lateral variation between Holes 884B and 884E, incomplete core recovery, and/or discontinuous sources such as discontinuous ash layers. However, in most cases, the two data sets can be correlated, sometimes peak to peak for intervals of several meters or tens of meters (e.g., within the interval at 450–510 mbsf of Hole 884E). Finally, the correlations between the laboratory and downhole data imply that only a small depth offset between Holes 884B and 884E (Fig. 59), which are 24 m apart.

Comparison with Lithology

In general, overall sediment magnetization should decrease as the biogenic silica content of the sediment increases. An increase in clay and ash content should correspond to an increase of the magnetization. Strictly speaking, the clays themselves are paramagnetic, but often are associated with magnetite. Contents of carbonates and nannofossils either can correspond to an increase of magnetization, if magnetite is associated, or not correspond, if the rocks are pure calcium carbonate.

A first-order comparison between the logs and the average lithology for Site 884 reveals some interesting correlations. Subunit IA is characterized by a high susceptibility, in agreement with its high clay and ash content (Figs. 56 and 59A). The transition between Subunits IB and IC, which corresponds to an increase in downhole clay content that matches well with an increase of average susceptibility below 440 to 460 mbsf (Figs. 56, 59B, and 59C). From a more detailed standpoint, the susceptibility record illustrates that this increase occurs in two steps: first, a lesser increase centered at 450 mbsf and a larger increase below 460 mbsf. This observation agrees well with the lithological data (Fig. 3; see "Lithostratigraphy" section, this chapter). The transition between Unit I and Unit II roughly corresponds to the beginning of an increase in susceptibility at a 610-mbsf composite depth (Figs. 56 and 59E). Subunit IB has a complicated susceptibility structure, but can be matched with the evolution of the clay content in Hole 884B. A relatively high clay content occurs at the top of Subunit IB down to about 190 mbsf, followed by relative low clay contents down to 250 mbsf, then by another higher content with minor variations down to about 390 mbsf (Fig. 3; see "Lithostratigraphy" section, this chapter). In the susceptibility record, this sequence shows a low average value that correlates to the central low clay-content zone (Fig. 56).

Ash levels occur within the upper 300 m of Hole 884B. High and variable susceptibility values can be observed in Subunit IA that can be correlated with ash occurrence. At about 170, 225, 270, and 320 mbsf, several discrete susceptibility peaks are correlated with the presence of ash layers. By using the barrel sheets, better correlations probably will be possible between ash occurrence and the magnetic records.

In conclusion, magnetic downhole data show close relationships with lithology and may help to refine the lithostratigraphy during future higher-resolution work. Because susceptibility also was recorded in cores, the downhole susceptibility log may allow us to make a composite depth for the whole 884 Site.

SEISMIC-LITHOLOGIC CORRELATION

All the Leg 145 drilling locations were surveyed in order to drop a beacon at the correct pre-selected location. In every case, surveys were run in the figure of the number 4 with the long leg duplicating the site-survey trackline used to select the site and the cross-leg being as nearly orthogonal as practical. The shipboard air-gun seismic

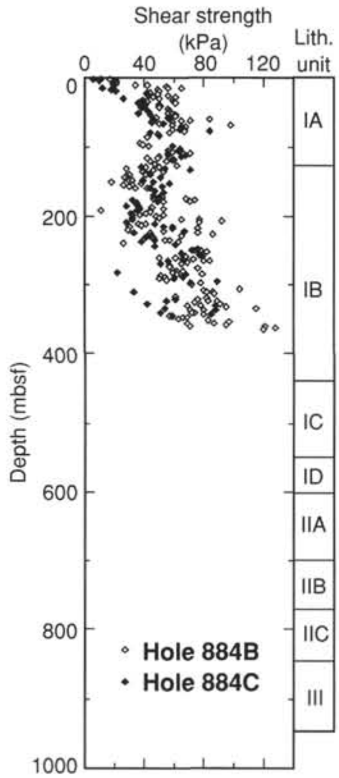

Figure 38. Shear strength data vs. depth for Holes 884B and 884C. Lithologic units are shown at right.

reflection profiling system was used for all the surveys except Site 883 when it was inoperable; the 3.5-kHz profiling system was used to locate that drill site. Details of the survey and seismic processing techniques are given in the Site 881 chapter (see "Seismic-Lithologic Correlation" section, "Site 881" chapter, this volume).

Site 884, located on the Meiji Drift, was selected on the basis of site surveys conducted in 1987 by the *Farnella.* Figure 60 is a seismic profile from the site-survey cruise that has been processed by D. Scholl and S. Dadisman at the U.S. Geological Survey to show depths rather than two-way traveltimes. Basaltic basement is indicated by the change in reflection character at the 4.7-km total depth. Drilling encountered basement at this site within a depth of 10 m of where the USGS-processed record predicted. The carbonates and downslope reworked materials that characterize most of lithologic Unit II make up the strongly reflective acoustic unit overlying basement. Lithologic Subunits ID, IC, and IB are more nearly pure diatom oozes and appear in the profile as a more transparent acoustic unit in the middle portion of the section. The upper, more highly reflective portion of the section corresponds to Subunit IA, which is characterized by significant amounts of clay, ash, and ice-rafted material in the siliceous ooze.

The entire sedimentary accumulation at Site 884 from Subunit IIA up to the seafloor represents the Meiji Drift (Fig. 60). Within this unit, the reflectors show horizontal continuity across the whole deposit. Small channels are evident in the profile. An active one can be seen at the left edge of the figure and buried channels are common. All this present and past small-scale channeling is a strong indication of a long history of bottom-current activity at Site 884, currents associated with the formation of the Meiji Drift deposit.

SUMMARY AND CONCLUSIONS

Geologic Record

Drilling at Site 884 penetrated 854 m of Cenozoic sediments on the lower flank of Detroit Seamount, including the Meiji Drift, and 87 m into the underlying basalt. The sedimentary section can be divided into two major units, each having subunits. Unit I is characterized by clay and diatom ooze in changing relative abundances and Unit II is dominated by chalk and claystone and displays evidence of minor to total downslope redeposition. Lithologic Subunit IA (0–128 mbsf) is a Quaternary to upper Pliocene diatom clay and clay. Dropstones and spicule-enriched horizons occur as minor lithologies, and fresh ash layers up to 2.5 m thick are common. Some of the thicker ash layers record multiple eruptions. Subunit IB (128–440.2 mbsf) is an upper Pliocene to upper Miocene clayey diatom ooze that grades down to a clayey diatomite. This subunit has a few ash layers and rare parallel and lenticular laminae. A dolomite concretion occurs at about 172 mbsf, and a piece of wood was found in lower Pliocene sediments at 214 mbsf. Lithologic Subunit IC (440.2–545.6 mbsf) is an upper to middle Miocene gray clay. *Zoophycos* trace fossils occur in the lower portion of the unit. Native copper in the form of small bladed and twinned crystals and small veinlets was noted at depths of 507 to 526 mbsf. Subunit ID (545.6–604.8 mbsf) is a middle to lower Miocene diatomite with clay or occasionally with spicules. Diatom chalks occur in the lower portion of the unit and *Zoophycos* trace fossils are present.

Lithologic Subunit IIA (604.8–694.7 mbsf) is a lower Miocene to uppermost Eocene claystone with some chalk in the lower portion of the unit. This subunit displays modest evidence for reworking in the form of sharp contacts, parallel laminae, and thin turbidites. Small bluish-green mottles at 623 to 632 mbsf on rare occasions have grains of native copper at their centers. Subunit IIB (694.7–771 mbsf) is an upper to lower-middle Eocene chalk and claystone. Ash is a minor component of this unit; the claystones have been interpreted as altered ashes on the basis of their relatively high smectite content. Little of this unit appears undisturbed. Soft-sediment deformation, including recumbent folding, is common, and large-scale slump features such as conglomerates having angular clasts occur. Subunit IIC (771–854 mbsf) is a middle-lower to lower Eocene (Paleocene nannofossils occur in the reworked materials of Subunit IIB) claystone with clayey ash and ash. These claystones have been interpreted to represent altered ashes on the basis of smectite content. Minor amounts of chalk occur in this subunit. Evidence for redeposition is less widespread than in the overlying subunit, but turbidites and sharp contacts are common. Streaks of native copper were observed at 806 mbsf.

XRD analyses of the minerals in the sediments of Site 884 show a remarkably constant composition of the terrigenous component from the sediment surface down to about 685 mbsf, the time of the Eocene/Oligocene boundary, and near the lower boundary of Subunit IIA. This component is characterized by a relatively low smectite to quartz-plus-illite ratio and a modest plagioclase to quartz-plus-illite ratio. The mineral fraction chlorite-plus-kaolinite, dominated by chlorite in the North Pacific, is of lesser relative abundance in these sediments, but increases gradually in importance up the core, beginning at about 700 mbsf. Below approximately 685 mbsf, both smectite and plagioclase are of much greater relative importance in the clays of Subunits IIB and IIC. These clays, therefore, have been interpreted as altered ashes.

Lithologic Unit III (854–941 mbsf) is basalt that occurs in 13 units. Ten units are flows and three are pillow lavas. These flows are thick—one is 30 m thick—and usually have chilled or baked margins; however, no glassy margins were recovered. Weakly zoned, large (to 25 mm) plagioclase crystals occur in several of the flows, and fresh olivine is common in the lower 50 m; thus, the basalt has been only slightly altered.

A complete sequence of all North Pacific Ocean diatom zones that ranges in age from late Quaternary to late Oligocene occurs at Site 884. The intervals between 12.0 and 13.5 Ma and approximately 17.5 to 20 Ma are characterized by condensed sections or diastems. Nannofossil biostratigraphy permits definition of the Miocene/Oligocene boundary at 640 mbsf and the Oligocene/Eocene boundary between 680 and 693 mbsf, within and at the base of lithologic Subunit IIA.

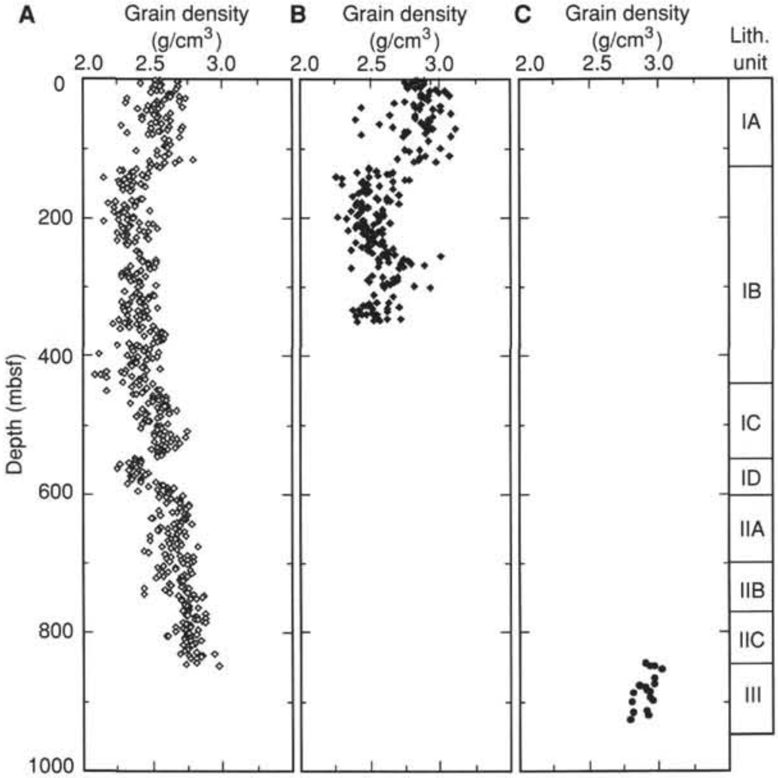

Figure 39. Grain density data vs. depth. **A.** Hole 884B. **B.** Hole 884C. **C.** Hole 884E. Lithologic units are shown at right.

The diatom assemblage at Site 884 includes one component, an arctic-boreal group that has characterized portions of the Bering Sea since it evolved during late Miocene time. In addition, a benthic form that lives only in the shallow waters of the Aleutian-Bering region occurs consistently, although in low abundance, throughout lithologic Unit I and Subunit IIA. These unusual diatom occurrences indicate relatively long-distance, generally southerly transport of the containing sediments.

The rapidly accumulating, clay-rich sediments of Site 884 permitted the development of a magnetic-reversal stratigraphy that is coherent back into the middle Miocene at about 13.5 Ma. This stratigraphy is a singular achievement and, for instance, permits the direct correlation for the first time of the North Pacific Ocean diatom zonations to the magnetic reversal time scale in sediments older than latest Miocene. Further, the depositional history of much of the Meiji Drift can now be constrained with the temporal control provided by the magnetostratigraphy. Initial paleomagnetic results from the basalts of the lower flank of Detroit Seamount indicate that those rocks are reversely magnetized and were erupted at a paleolatitude of approximately 33°N.

Rates of deposition at Site 884 were high during the late Pliocene and Pleistocene, since 2.6 Ma. The linear sedimentation rate (LSR) for that interval is about 47 m/m.y. The clay-plus-quartz flux is 1.4 $g(cm^2 \cdot k.y.)^{-1}$ and diatoms accumulated at 0.8 $g(cm^2 \cdot k.y.)^{-1}$ during the past 2.6 Ma. In the remainder of the Pliocene and uppermost Miocene sequence (2.6–6.2 Ma), the LSR averages 60 m/m.y., while the mass accumulation rate (MAR) of clay-plus-quartz is 0.9 $g(cm^2 \cdot k.y.)^{-1}$ and that of diatoms is 1.6 $g(cm^2 \cdot k.y.)^{-1}$. In the remainder of the upper Miocene and in the upper part of the middle Miocene (between 6.2 and 11.9 Ma), the LSR is 34 m/m.y. and the MAR of clay-plus-quartz is similar to that of the overlying unit, 0.9 $g(cm^2 \cdot k.y.)^{-1}$; however, the diatom flux is somewhat lower, about 0.8 $g(cm^2 \cdot k.y.)^{-1}$. Between 13.5 and 17.5 Ma, LSR values were much reduced, averaging only 13 m/m.y. The MAR of the diatomaceous component is 0.4 $g(cm^2 \cdot k.y.)^{-1}$ and that of the terrigenous component, clay-plus-quartz, is 0.3 $g(cm^2 \cdot k.y.)^{-1}$. In the Oligocene and lower Miocene portion of the section (between 20.1 and 34.8 Ma), LSR values are low, only 6 m/m.y. Diatoms are not a volumetrically important component of the sediment in this unit and clay-plus-quartz fluxes are moderate, about 0.4 $g(cm^2 \cdot k.y.)^{-1}$. Throughout the entire Oligocene to Quaternary interval, the MAR of $CaCO_3$ is low, ranging from about 50 to 90 $mg(cm^2 \cdot k.y.)^{-1}$. Site 884 has not been above the CCD since the end of Eocene time. Meaningful pelagic sedimentation rates could not be calculated for lithologic Subunits IIB and IIC; their total of 159 m of sediment accumulated over a span of about 20 m.y., for a bulk LSR of 8 m/m.y.

Paleoceanography and Paleoclimatology

The basalts of Detroit Seamount were erupted during latest Cretaceous time, based on evidence from Site 883, at the Hawaiian hot spot in the subtropical North Pacific Ocean. Should the estimate for the age of basement be correct, then as much as 20 m.y. passed before any significant accumulation of sediment occurred at Site 884. None of the downslope-transported material of lithologic Unit II, which should be a reliable integrator of upslope lithologies, shows any indication of shallow-water or reefal material. Displaced foraminifers now found in Subunit IIA indicate an original paleodepth of less than 500 m below sea level. This value can be taken as the deeper constraint on seamount depth; the shallower constraint is the 100 to 150 m water depth beyond which no reef growth is possible. We conclude that Detroit Seamount never built up to sea level.

Ash and $CaCO_3$ were deposited on the slopes of Detroit Seamount during early Tertiary time. During the Eocene, and culminating in the middle Eocene, important amounts of sediment reworking and downslope redeposition occurred, resulting in soft sediment deformation, intraformational conglomerates, turbidites, parallel laminae, scour marks, etc. Downslope reworking of this same age has been docu-

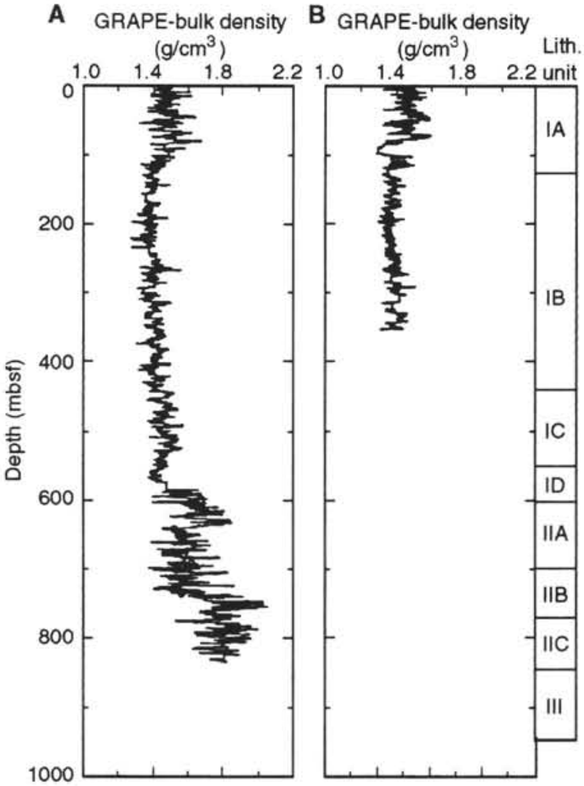

Figure 40. GRAPE bulk density data vs. depth. **A.** Hole 884B. **B.** Hole 884C. Lithologic units are shown at right.

mented elsewhere in the central and northern Pacific Ocean (Schlanger and Premoli Silva, 1981; Rea and Thiede, 1981; Vallier et al., 1983) and the information from Detroit Seamount significantly broadens the known region of that activity. By the end of Eocene time, the early Tertiary ash influx had ended, reworking had essentially ceased, carbonate deposition was reduced to a minor portion of the whole, and the deposition of continentally derived hemipelagic clays and quartz became important.

The flux of the hemipelagic continental component of the Detroit Seamount sediments has increased ever since first becoming important at the time of the Eocene/Oligocene boundary. Oligocene and lower and middle Miocene rates are a few tenths of a $g(cm^2 \cdot k.y.)^{-1}$. Rates increase to 0.9 $g(cm^2 \cdot k.y.)^{-1}$ during the middle Miocene at about 12 Ma, and again to about 1.4 $g(cm^2 \cdot k.y.)^{-1}$ at the time of the onset of Northern Hemisphere glaciation at 2.6 Ma. Diatoms become an important contributor to the sediments above the condensed interval in the lower Miocene with flux rates of 0.4 $g(cm^2 \cdot k.y.)^{-1}$ during the period 17.5 to 13 Ma. During the late middle Miocene the diatom flux doubles to 0.8 $g(cm^2 \cdot k.y.)^{-1}$, and then doubles again to 1.6 $g(cm^2 \cdot k.y.)^{-1}$ in the latest Miocene at 6.2 Ma. This period of maximum diatom flux in the latest Miocene and early and middle portions of the Pliocene has been seen in all the Leg 145 drill sites and corresponds to a relatively warm period in the Northwest Pacific Ocean. During the late Pliocene and Quaternary age, diatom fluxes returned to their previously moderate level of 0.8 $g(cm^2 \cdot k.y.)^{-1}$.

At Site 884, dropstones occur in Subunit IA in similar amounts to those in nearby Site 883, in slightly lower abundances than those encountered at Site 882, 110 km to the south, and in much lower abundances than those at Site 881, about 475 km to the south, again emphasizing the northward decline in IRD. Taken together, the Leg 145 and Leg 86 drill sites (Krissek et al., 1985; Heath, Burckle, et al, 1985) neatly define the source of the Northwest Pacific Ocean dropstones as the Sea of Okhotsk, or possibly the southern Kamchatka Peninsula, a fact first suspected by Conolly and Ewing (1970). Dropstones appear in the section at the time of the Matuyama/Gauss reversal boundary at 2.6 Ma and thus herald the onset of major glaciation in the Northern Hemisphere (Rea and Schrader, 1985). In contrast to more southerly locations, no dropstones older than late Pliocene were found in Site 883 or Site 884 sediments.

Ash layers are common to abundant in sediments younger than 2.6 Ma and occur again in the Eocene portion of the section. At 2.6 Ma, the deposition of volcanogenic material increases by more than an order of magnitude. This increase in ash deposition, beginning during the latest Pliocene in the North Pacific Ocean has been known for many years (Kennett and Thunell, 1975; Kennett et al., 1977), however, the Leg 145 sites provide much better dated sequences for determining timing of onset of the northwestern Pacific portion of this oceanwide volcanic episode than has been available previously. Examination of the individual ash layers should reveal geochemical trends in Kuril-Kamchatka volcanism. The lower occurrence of ash layers provides, along with Site 883, one of the first good definitions of a period of Eocene volcanism that has been suggested by various data from scattered locations such as Hess Rise (Vallier et al., 1983) and the Central Pacific Ocean basins (Rea and Thiede, 1981).

The presence of native copper as crystals and veinlets or streaks in the sediments of Site 884 is an unusual aspect of authigenic activity in this location. Copper in deep-sea sediments is very rare, but has been reported from the Pacific Ocean (Manihiki Plateau, Jenkyns, 1976), Atlantic Ocean (western Atlantic, Hollister, Ewing, et al., 1972; Angola Basin, Siesser, 1978) and the Caribbean Sea (Donelley and Nalli, 1973). Most occurrences have been related, without significant laboratory investigation, to percolation of hydrothermal fluids through a sedimentary section characterized by the proper geochemical host conditions (see Jenkyns, 1976). Enough copper exists in the sediments of Site 884 to provide a fruitful basis for a sophisticated geochemical study of this phenomenon.

The Meiji Drift

Deep thermohaline currents, confined to the Coriolis-correct side of a basin or deep-sea ridge, can be responsible for the long-term, long-distance transport of sediment. The resulting deposits are greatly elongated parallel to the flow-constraining bathymetry and may exceed 1 km in thickness. The sediments in these deposits are often some combination of biogenic-pelagic material and land-derived, fine-grained hemipelagic sediment. Drift sediments are almost always homogeneous and bioturbated and rarely display the sedimentary structures commonly associated with deep currents such as parallel laminae, sharp contacts, and scour marks or cross-bedding. Rates of deposition, often several tens of meters per million years, depend on supply and are noticeably higher in the drift deposit than in nearby deposits that have been accumulating under purely pelagic conditions (Kidd and Hill, 1987; Pickering et al., 1989).

During DSDP Legs 93 (van Hinte, Wise, et al., 1986) and 94 (Ruddiman, Kidd, et al., 1987), three of the major drift deposits in the North Atlantic Ocean were drilled. The Hatteras Outer Rise, drilled at Site 603, is a uniform silt and clay "muddy contourite," composed of silica and nannofossil-bearing clay. About 950 m of this deposit has accumulated at Site 603 since the middle Miocene, giving sedimentation rates of more than 90 m/m.y. for this time span (Wise and van Hinte, 1986). The Feni Drift, a deposit 600 km long, 100 km wide, and up to 1600 m thick, was drilled at Site 610 in the North Atlantic. This deposit is glacial-aged mud with ooze above 135 mbsf and nannofossil ooze and chalk with low clay content below that horizon. The deposit is early Miocene in age at a depth of 723 mbsf, giving a sedimentation rate of more than 40 m/m.y. (Ruddiman, Kidd, et al., 1987; Kidd and Hill, 1987). Drilling at Site 611 encountered the Gardar Drift, a deposit 1000 km long, 130 km wide, and 1450 m thick. The Gardar Drift is an alternating mud and carbonate ooze of late Pliocene and Quaternary age in the upper 105 mbsf and a structure-

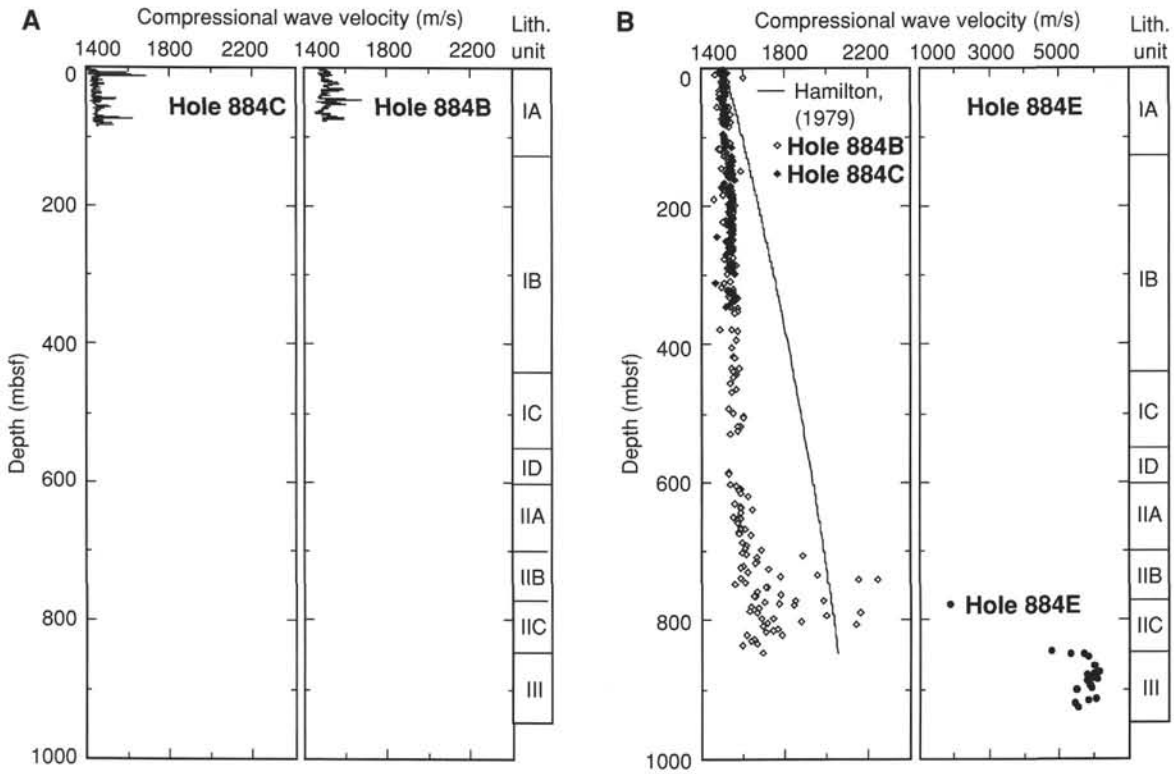

Figure 41. Compressional wave velocity data vs. depth. **A.** P-wave logger data from Holes 884B and 884C. Lithologic units are shown, as discussed in the text. **B.** Hamilton Frame and DSV data from Holes 884B, 884C, and 884E (the predicted velocity profile for diatomaceous silty clay is shown, after Hamilton [1979]). Lithologic units are shown as discussed in the text.

less, homogeneous, pure carbonate ooze and chalk below. The upper 571 m of this deposit was deposited at uniform rates of 60 m/m.y. in the Miocene and Pliocene to 100 m/m.y. in the Quaternary (Ruddiman, Kidd, et al., 1987; Kidd and Hill, 1987). The resulting overview of drift deposition provided by these and prior drilling legs shows that the deposits are fundamentally pelagic in bulk composition, consist of nannofossils and foraminifers, are without sedimentary structures indicative of current-controlled deposition, and have high and relatively uniform sedimentation rates. Tracing the reflector surfaces underlying the drift deposits to drill holes where they could be dated made it possible to determine that deposition of drift deposits in the North Atlantic began at the time of the Eocene/Oligocene boundary (Kidd and Hill, 1987).

The thick sediment deposit on the northeast side of the Obruchev Swell was first noted by Ewing et al. (1968) in their general review of Pacific Ocean sediment thicknesses. During DSDP Leg 19, one site (Site 192) was drilled on the upper portion of the swell, on Meiji Seamount, where thick pelagic and hemipelagic deposits were encountered (Creager, Scholl, et al., 1973). Scholl et al. (1977) provided the first detailed description of the Meiji Drift deposit, based upon seismic-reflection profiles and the Leg 19 findings at Meiji Seamount. The Meiji Drift in the Northwest Pacific Ocean is a sedimentary deposit on the northeastern side of the northernmost Emperor Seamount chain that is more than 800 km long and about 350 km wide, between 300-m isopachs. The deposit is up to 1800 m thick at its northwestern end at the Kamchatka Strait and thins to the southeast. Scholl et al. (1977) noted a clear link of the mineral component in the Miocene and younger deposits of Meiji Seamount to the same material at Site 191 in the Komandorski Basin and to Siberian source regions. They concluded that the Kamchatka Current that flows south through the deep Kamchatka Strait transports Siberian terrigenous materials to the northwestern Pacific Ocean, forming deposits both northeast of the northern Emperor Seamounts, the Meiji Drift, and along the base of the Kamchatka-Kuril continental margin.

Mammerickx (1985) presented information to suggest that the Meiji Drift deposit may be traceable as far south along the eastern flank of the Emperor Seamounts as 35°N, a distance of more than 2000 km from the Kamchatka Strait. She emphasized the strong similarity of the Meiji Drift to the North Atlantic Ocean drifts and presumed the same depositional process. In support of this hypothesis, she noted several reports of indications of sources of cold, deep water in the far Northwest Pacific (Mammerickx, 1985).

Site 884 was positioned on the Meiji Drift at a location where the deposit was expected to be thin enough (less than 800 m thick) so that it could be penetrated completely. The seismic reflection profile taken by the *Farnella* and processed at the U.S. Geological Survey by Scholl and Dadisman (pers. comm., 1992), along which Site 884 was chosen, shows clear evidence of ongoing sediment transport processes in the form of modern and buried channels (Fig. 60), demonstrating that this location has been one of active deep-water flow throughout the history of the deposit. Site 884 is on the southwestern side of the main sedimentary axis of the deposit; the site-survey profiles collected by the *JOIDES Resolution* show that the sedimentary horizons thicken to the northeast.

The information gathered as a result of drilling at Site 884 includes several important results. First, during Leg 145 we were able to define a sediment body that contains pelagic-biogenic materials, largely siliceous, and hemipelagic land-derived clays and quartz. Second, deposition of this feature has continued since the time of the Eocene/Oligocene boundary, with the possible exception of one or two brief lacunae in the Miocene. Third, the mineralogy of the terrigenous component has remained invariant throughout the time of deposition, with the exception of a modest increase in the relative abundance of the 7Å clay component, which is dominated by chlorite in the North

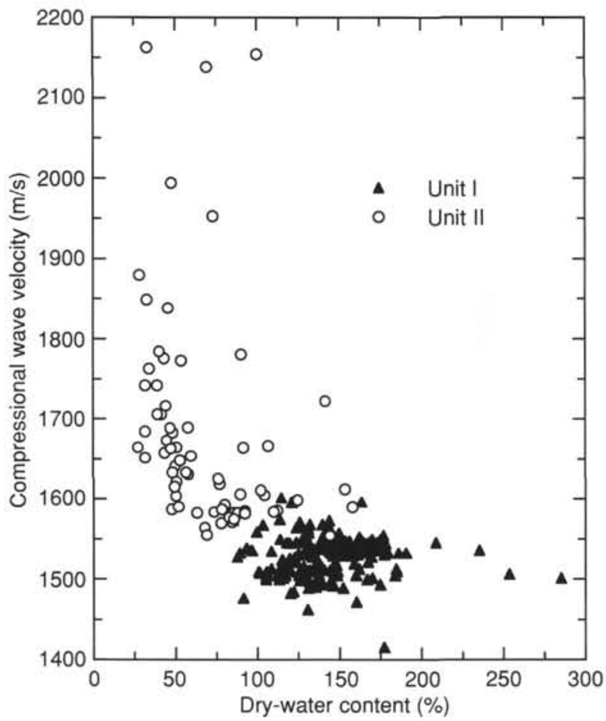

Figure 42. Compressional wave velocity vs. dry water content data for Hole 884B.

Pacific Ocean. Finally, northern-source diatoms occur throughout the deposit. All these indications suggest a constant depositional process supplied by sediment from the same northern or northwesterly source region. The MARs of the sediment components vary as plate motion carries the site toward the continental source, the importance of which varies with climatic regime, and as production of the biogenic component waxes and wanes.

Backtracking the site along the Hawaiian trend for the past 35 m.y. places it in the relative location of about 40°N and 165°W, in the middle of the Oligocene North Pacific Ocean (Rea and Duncan, 1986). Mineral fluxes in the Oligocene portion of the section are about 400 $g(cm^2 \cdot k.y.)^{-1}$, 20 to 40 times greater than mid-Cenozoic eolian fluxes to the ocean (Janecek and Rea, 1983; Janecek, 1985), and so are clearly hemipelagic. The problem is to discover how such long distance hemipelagic transport might be accomplished. One possibility is that the northwestward continuation of the Hawaii-Emperor Ridge acted as a flow guide for the North Pacific Ocean thermohaline circulation, diverting bottom-water flow coming south from the Bering Sea to the southeast along this proposed Meiji extension. If so, the history of the Hawaii-Emperor-Meiji extension ridge, hence the life of the Hawaiian hot spot, is extended by about 40 m.y.

The assembled data suggest that the deposition of the Meiji Drift was occurring by early Oligocene time. Northern-source minerals and diatoms have accumulated at moderate to high rates, generally increasing throughout the middle and late Cenozoic, in an elongate deposit on the northeast flank of the northwestern extension of the Emperor Ridge. The supply of terrigenous material increases markedly at times of known climate change during the middle Miocene and late Pliocene, and thus may be related to the enhanced physical erosion of the continents surrounding the North Pacific Ocean caused by deterioration of climate in those regions. The (presumably) early Oligocene onset and continuing deposition of the Meiji Drift entails important consequences to the physical oceanography of the North Pacific Ocean. Southerly flow of bottom waters from the Bering Sea into the North Pacific Basin has been occurring for as much as 35 m.y. Presumably, this flow has been controlled geographically by the location of one or two deep passages through the Aleutian Ridge. At present, and perhaps ever since the last important change in direction and rate of plate convergence in the region at about 43 Ma (Rea and Duncan, 1986), the deep passage is at the western end of the Aleutian chain, the Kamkchatka Strait. The basins of the Bering Sea have served as catchments for the voluminous clastics, mostly turbidites, that derive from Siberia and Alaska, allowing for bypassing of the finer, hemipelagic component to the North Pacific Ocean. Without such a large catchment basin, the clastics entering the Northeast Pacific directly from North America have formed the vast turbidite abyssal plains of the Gulf of Alaska.

In a broader sense, the onset of drift deposition in the North Pacific at generally the same time as in the North Atlantic suggests a similar oceanographic and probably climatic setting. The paleolatitude and paleodepth of the Bering Sea and the basins between the Iceland-Faeroes Ridge and the Charley-Gibbs Fracture Zone are similar. Pelagic sediments in the North Atlantic are more calcareous, but the mid-Tertiary supply of clastics appears to have been greater in the North Pacific. The response of the northern oceans to the onset of Southern Hemisphere glaciation during the earliest Oligocene time seems to have involved a fundamental change in deep circulation. It remains a fruitful area of research.

REFERENCES*

Akiba, F., 1985. Middle Miocene to Quaternary diatom biostratigraphy in the Nankai Trough and Japan Trench, and modified lower Miocene through Quaternary diatom zones for the middle- to high-latitudes of the North Pacific. *In* Kagami, H., Karig, D.E., Coulbourn, W.T., et al., *Init. Repts. DSDP,* 87:393–481.

Akiba, F., Hiramatsu, C., and Yanagisawa,Y., in press. A Cenozoic diatom genus *Cavitatus* Williams; an emended description and two new biostratigraphically useful species, *C. lanceolatus* and *C. rectus* from Japan. *Bull. Nat. Sci. Mus. (Tokyo).*

Archie, G.E., 1942. The electrical resistivity log as an aid in determining some reservoir characteristics. *Trans. Am. Inst. Min. Metall. Pet. Eng.,* 146:54–62.

Barron, J.A., 1980. Lower Miocene to Quaternary diatom biostratigraphy of Leg 57, off Northeastern Japan, Deep Sea Drilling Project. *In* von Huene, R., Nasu, N., et al., *Init. Repts. DSDP,* 56, 57 (Pt. 2): Washington (U.S. Govt. Printing Office), 641–686.

————, 1989. The late Cenozoic stratigraphic record and hiatuses of the northeast Pacific: results from the Deep Sea Drilling Project. *In* Winterer, E.L., Hussong, D.M., and Decker, R.W. (Eds.), *The Geology of North America* (Vol. N): *The Eastern Pacific Ocean and Hawaii.* Geol. Soc. Am., Geol. of North America Ser., 311–322.

————, 1992. Neogene diatom datum levels in the equatorial and North Pacific. *In* Saito, T., and Ishizaki, K. (Eds.), *The Centenary of Japanese Micropaleontology:* Tokyo (Tokyo Univ. Press), 413–425.

Barthes, V., 1990. Modelisation magnetique en forage. *Rap. CEA/LETI/DSYS/SETIA,* 90-59.

Basilian, A.E., Barinov, K.B., Oreshkina, T.V., and Trubikhin, V.N., 1991. Bering Sea transgressions in Pliocene. *Proc. 13th INQUA Congr. Pliocene Anthropogene Paleogeography and Biostratigraphy.* Moscow, 5–24. (in Russian)

Bodén, P., in press. Taxonomy and stratigraphic occurrence of *Thalassiosira tetraoestrupii* sp. nov. and related species in upper Miocene and lower Pliocene sediments from the Norwegian Sea, North Atlantic and northwest Pacific. *Terra Nova.*

Burckle, L.H., and Opdyke, N.D., 1977. Late Neogene diatom correlations in the circum-Pacific. *In* Saito, T., and Ujiié (Eds.), *Proc. 1st Int. Congr. Pacific Neogene Stratigr.,* Tokyo, 1976. Tokyo (Kaiyo Shupan), 255–284.

Cande, S.C., and Kent, D.V., 1992. A new geomagnetic polarity timescale for the Late Cretaceous and Cenozoic. *J. Geophys. Res.,* 97:13917–13951.

Conolly, J.R., and Ewing, M., 1970. Ice-rafted detritus in Northwest Pacific deep-sea sediments. *In* Hays, J.D. (Ed.), *Geological Investigations of the North Pacific.* Mem.—Geol. Soc. Am., 12:219–231.

* Abbreviations for names of organizations and publication titles in ODP reference lists follow the style given in *Chemical Abstracts Service Source Index* (published by American Chemical Society).

Cook, H.E., Jenkyns, H.C., and Kelts, K.R., 1976. Redeposited sediments along the Line Islands, equatorial Pacific. *In* Schlanger, S.O., Jackson, E.D., et al., *Init. Repts. DSDP,* 33: Washington (U.S. Govt. Printing Office), 837–847.

Creager, J.S., Scholl, D.W., et al., 1973. *Init. Repts. DSDP,* 19: Washington (U.S. Govt. Printing Office).

Damuth, J.E., Jacobi, R.D., and Hayes, D.E., 1983. Sedimentation processes in the northwest Pacific Basin revealed by the echo-character mapping studies. *Geol. Soc. Am. Bull.,* 94:381–395.

Deer, W.A., Howie, R.A., and Zussman, J., 1966. *An Introduction to the Rock-Forming Minerals:* London (Longman Group).

Donelley, T.W., and Nalli, G., 1973. Mineralogy and chemistry of Caribbean sediments. *In* Edgar, N.T., Saunders, J.B., et al., *Init. Repts. DSDP,* 15: Washington (U.S. Govt. Printing Office), 929–961.

Ewing, J., Ewing, M., Aitken, T., and Ludwig, W.J., 1968. North Pacific sediment layers measured by seismic profiling. *In* Knopoff, L., Drake, C.L., and Hart, P.J. (Eds.), *The Crust and Upper Mantle of the Pacific Area.* Am. Geophys. Union Monogr., 12:147–173.

Fertl, W.H., 1979. Gamma ray spectral data assists in complex formation evaluation. *Log Analyst,* 20:421–423.

Foreman, H.P., 1975. Radiolaria from the North Pacific, Deep Sea Drilling Project, Leg 32. *In* Larson, R.L., Moberly, R., et al., *Init. Repts. DSDP,* 32: Washington (U.S. Govt. Printing Office), 579–676.

Gieskes, J.M., 1981. Deep-sea drilling interstitial water studies: implications for chemical alteration of the oceanic crust, layers I and II. *In* Warme, J.E., Douglas, R.G., and Winterer, E.L. (Eds.), *The Deep Sea Drilling Project: A Decade of Progress.* Spec. Publ.—Soc. Econ. Paleontol. Mineral., 32:149–167.

Hamilton, E.L., 1979. Sound velocity gradients in marine sediments. *J. Acoust. Soc. Am.,* 65:909–922.

Hays, J.D., 1970. Stratigraphy and evolutionary trends of radiolaria in North Pacific deep sea sediments. *In* Hays, J.D. (Ed.), *Geological Investigations of the North Pacific.* Mem.—Geol. Soc. Am., 126:185–218.

Hays, J.D., and Shackleton, N.J., 1976. Globally synchronous extinction of radiolarian *Stylatractus universus. Geology,* 4:649–652.

Heath, G.R., Burckle, L.H., et al., 1985. *Init. Repts. DSDP,* 86: Washington (U.S. Govt. Printing Office).

Hollister, C.D., Ewing, J.I., et al., 1972. *Init. Repts. DSDP,* 11: Washington (U.S. Govt. Printing Office).

Janecek, T.R., 1985. Eolian sedimentation in the Northwest Pacific Ocean: a preliminary examination of the data from Deep Sea Drilling Project Sites 576 and 578. *In* Heath, G.R., Burckle, L.H., et al., *Init. Repts. DSDP,* 86: Washington (U.S. Govt. Printing Office), 589–603.

Janecek, T.R., and Rea, D.K., 1983. Eolian deposition in the northeast Pacific Ocean: Cenozoic history of atmospheric circulation. *Geol. Soc. Am. Bull.,* 94:730–738.

Jenkyns, H.C., 1976. Sediments and sedimentary history, Manihiki Plateau, South Pacific Ocean. *In* Schlanger, S.O., Jackson, E.D., et al., *Init. Repts. DSDP,* 33: Washington (U.S. Govt. Printing Office), 873–890.

Keigwin, L.D., Jones, G.A., and Froelich, N.P., 1992. A 15,000-year paleoenvironmental record from Meiji seamount, far northwestern Pacific. *Earth Planet Sci. Lett.,* 111:425–440.

Keller, G., and Barron, J.A., 1987. Paleodepth distribution of Neogene deep-sea hiatuses. *Paleoceanography,* 2:697–713.

Keller, G.V., 1982. Electrical properties of rocks. *In* Carmichael, R.S. (Ed.), *Handbook of Physical Properties of Rocks* (Vol. 1): Boca Raton, FL (CRC Press), 217–293.

Kennett, J.P., McBirney, A.R., and Thunell, R.C., 1977. Episodes of Cenozoic volcanism in the circum-Pacific region. *J. Volcanol. Geotherm. Res.,* 2:145–163.

Kennett, J.P., and Thunell, R.C., 1975. Global increase in Quaternary explosive volcanism. *Science,* 187:497–503.

Kidd, R.B., and Hill, P.R., 1987. Sedimentation on Feni and Gardar sediment drifts. *In* Ruddiman, W.F., Kidd, R.B., et al., *Init. Repts. DSDP,* 94 (Pt. 2): Washington (U.S. Govt. Printing Office), 1217–1244.

Koizumi, I., 1992. Diatom biostratigraphy of the Japan Sea: Leg 127. *In* Pisciotto, K.A., Ingle, J.C., Jr., von Breymann, M.T., Barron, J., et al., *Proc. ODP, Sci. Results,* 127/128 (Pt. 1): College Station, TX (Ocean Drilling Program), 249–289.

Koizumi, I., and Tanimura, Y., 1985. Neogene diatom biostratigraphy of the middle latitude western North Pacific, Deep Sea Drilling Project Leg 86. *In* Heath, G.R., Burckle, L.H., et al., *Init. Repts. DSDP,* 86: Washington (U.S. Govt. Printing Office), 269–300.

Krauskopf, K.B., 1979. *Introduction to Geochemistry* (2nd ed.): New York (McGraw-Hill).

Krissek, L.A., Morley, J.J., and Lofland, D.K., 1985. The occurrence, abundance, and composition of ice-rafted debris in sediments from Deep Sea Drilling Project Sites 579 and 580, northwest Pacific. *In* Heath, G.R., Burckle, L.H., et al., *Init. Repts. DSDP,* 86: Washington (U.S. Govt. Printing Office), 647–655.

Landing, W.M., and Bruland, K.W., 1980. Manganese in the North Pacific. *Earth Planet. Sci. Lett.,* 49:45–46.

Ling, H.Y., 1973. Radiolaria: Leg 19 of the Deep Sea Drilling Project. *In* Creager, J.S., Scholl, D.W., et al., *Init. Repts. DSDP,* 19: Washington (U.S. Govt. Printing Office), 777–797.

Mammerickx, J., 1985. A deep-sea thermohaline flow path in the northwest Pacific. *Mar. Geol.,* 65:1–19.

McDuff, R.E., 1985. The chemistry of interstitial waters, Deep Sea Drilling Project, Leg 86. *In* Heath, G.R., Burckle, L.H., et al., *Init. Repts. DSDP,* 86: Washington (U.S. Govt. Printing Office), 675–687.

Moberly, R., and Jenkyns, H.C., 1981. Cretaceous volcanogenic sediments of the Nauru Basin, Deep Sea Drilling Project Leg 61. *In* Larson, R.L., Schlanger, S.O., et al., *Init. Repts. DSDP,* 61: Washington (U.S. Govt. Printing Office), 533–548.

Morley, J.J., Hays, J.D., and Robertson, J.H., 1982. Stratigraphic framework for the late Pleistocene in the northwest Pacific ocean. *Deep-Sea Res. Part A,* 29:1485–1499.

Morley, J.J., and Shackleton, N.J., 1978. Extension of the radiolarian *Stylatractus universus* as a biostratigraphic datum to the Atlantic Ocean. *Geology,* 6:309–311.

Natland, J.H., 1973. Basal ferromanganoan sediments at DSDP Site 183, Aleutian Plain and Site 192, Meiji Guyot, Northwest Pacific, Leg 19. *In* Creager, J.S., Scholl, D.W., et al., *Init. Repts. DSDP,* 19: Washington (U.S. Govt. Printing Office), 629–641.

Pedersen, T.F., Vogel, J.S., and Southon, J.N., 1986. Copper and manganese in hemipelagic sediments at 21°N: diagenetic contrasts. *Geochim. Cosmochim. Acta,* 50:2019–2031.

Pickering, K.T., Hiscott, R.N., and Hein, F.J., 1989. *Deep Marine Environments: Clastic Sedimentation and Tectonics:* London (Unwin Hyman).

Rea, D.K., and Duncan, R.A., 1986. North Pacific Plate convergence: a quantitative record of the past 140 m.y. *Geology,* 14:373–376.

Rea, D.K., and Schrader, H., 1985. Late Pliocene onset of glaciation: ice rafting and diatom stratigraphy of North Pacific DSDP cores. *Palaeogeogr., Palaeoclimatol., Palaeoecol.,* 49:313–325.

Rea, D.K., and Thiede, J., 1981. Mesozoic and Cenozoic mass accumulation rates of the major sediment components in the Nauru Basin, Western Equatorial Pacific. *In* Larson, R.L., Schlanger, S.O., et al., *Init. Repts. DSDP,* 61: Washington (U.S. Govt. Printing Office), 549–555.

Riedel, W.R., and Sanfilippo, A., 1970. Radiolaria, Leg 4, Deep Sea Drilling Project. *In* Bader, R.G., Gerard, R.D., et al., *Init. Repts. DSDP,* 4: Washington (U.S. Govt. Printing Office), 503–575.

————, 1971. Cenozoic radiolaria from the western tropical Pacific, Leg 7. *In* Winterer, E.L., Riedel, W.R., et al., *Init. Repts. DSDP,* 7 (Pt. 2): Washington (U.S. Govt. Printing Office), 1529–1672.

————, 1978. Stratigraphy and evolution of tropical Cenozoic radiolarians. *Micropaleontology,* 24:61–96.

Ruddiman, W.F., Kidd, R.B., Thomas, E., et al., 1987. *Init. Repts. DSDP,* 94 (Pt. 1): Washington (U.S. Govt. Printing Office).

Sakai, T., 1980. Radiolarians from Sites 434, 435, and 436, Northwest Pacific, Leg 56, Deep Sea Drilling Project. *In* von Huene, R., Nasu, N., et al., *Init. Repts. DSDP,* 56, 57 (Pt. 2): Washington (U.S. Govt. Printing Office), 695–733.

Schlanger, S.O., Jackson, E.D., et al., 1976. *Init. Repts. DSDP,* 33: Washington (U.S. Govt. Printing Office).

Schlanger, S.O., and Premoli Silva, I., 1981. Tectonic, volcanic, and paleogeographic implications of redeposited reef faunas of Late Cretaceous and Tertiary age from the Nauru Basin and the Line Islands. *In* Larson, R.L., Schlanger, S.O., et al., *Init. Repts. DSDP,* 61: Washington (U.S. Govt. Printing Office), 817–827.

Scholl, D.V., Hein, J.R., Marlow, M., Buffington, E.C., 1977. Meiji sediment tongue: North Pacific evidence for limited movement between the Pacific and North American plates. *Geol. Soc. Am. Bull.,* 88:1567–1576.

Shackleton, N.J., Backman, J., Zimmerman, H., Kent, D.V., Hall, M.A., Roberts, D.G., Schnitker, D., Baldauf, J.G., Desprairies, A., Homrighausen, R., Huddlestun, P., Keene, J.B., Kaltenback, A.J., Krumsiek, K.A.O., Morton, A.C., Murray, J.W., and Westberg-Smith, J., 1984. Oxygen isotope calibration of the onset of ice-rafting and history of glaciation in the North Atlantic region. *Nature,* 307:620–623.

Siesser, W.G., 1978. Native copper in DSDP Leg 40 sediments. *In* Bolli, H.M., Ryan, W.B.F., et al., *Init. Repts. DSDP,* 40 (Suppl., Pt. 4): Washington (U.S. Govt. Printing Office), 761–765.

Thiede, J., and Rea, D.K., 1981. Mass accumulation rates of Barremian to Recent biogenic sediments from the Mid-Pacific Mountains (Deep Sea Drilling Project Site 463) and Hess Rise (Sites 464, 465, 466) central North Pacific Ocean. *In* Thiede, J., Vallier, T.L., et al., *Init. Repts. DSDP,* 62: Washington (U.S. Govt. Printing Office), 637–651.

Tjalsma, R.C., and Lohmann, G.P., 1983. Paleocene-Eocene bathyal and abyssal benthic foraminifera from the Atlantic Ocean. *Micropaleontol. Spec. Publ.,* 4.

Tucholke, B.E., Edgar, N.T., and Boyce, R.E., 1976. Physical properties and correlations with acoustic stratigraphy: Leg 35, Deep Sea Drilling Project. *In* Hollister, C.D., Craddock, C., et al., *Init. Repts. DSDP,* 35: Washington (U.S. Govt. Printing Office), 229–250.

Vallier, T.L., Dean, W.E., Rea, D.K., and Thiede, J., 1983. Geologic evolution of Hess Rise, central North Pacific Ocean. *Geol. Soc. Am. Bull.,* 94:1289–1307.

van Hinte, J.E., Wise, S.W., Jr., et al., 1987. *Init. Repts. DSDP,* 93: Washington (U.S. Govt. Printing Office).

van Morkhoven, F.P.C.M., Berggren, W.A., and Edwards, A.S., 1986. Cenozoic cosmopolitan deep-water benthic foraminifera. *Bull. Cent. Rech. Explor.-Prod. Elf-Aquitaine,* Mem. 11.

Wilkens, R.H., and Handyside, T., 1985. Physical properties of equatorial Pacific sediments. *In* Mayer, L., Theyer, F., Thomas, E., et al., *Init. Repts. DSDP,* 85: Washington (U.S. Govt. Printing Office), 839–847.

Wise, S.W., Jr., and van Hinte, J.E., 1987. Mesozoic-Cenozoic depositional environments revealed by Deep-Sea Drilling Project Leg 93 drilling on the continental rise off the Eastern United States: cruise summary. *In* van Hinte, J.E., Wise, S.W., Jr., et al., *Init. Repts. DSDP,* 93: Washington (U.S. Govt. Printing Office), 1367–1423.

Yanagisawa, Y., and Akiba, F., 1990. Taxonomy and phylogeny of three marine diatom genera, *Crucidenticula, Denticulopsis,* and *Neodenticula. Bull. Geol. Surv. Jpn.* [*Chishitsu Chosasho Geppo*], 41:197–301.

Ms 145IR-108

NOTE: For all sites drilled, core-description forms ("barrel sheets") and core photographs can be found in Section 3, beginning on page 395. Forms containing smear-slide data can be found in Section 4, beginning on page 985. Thin-section data are given in Section 5, beginning on page 1013. Conventional log, FMS, dipmeter, and geochemical log (element and oxide weight %) data can be found in CD-ROM form (back pocket).

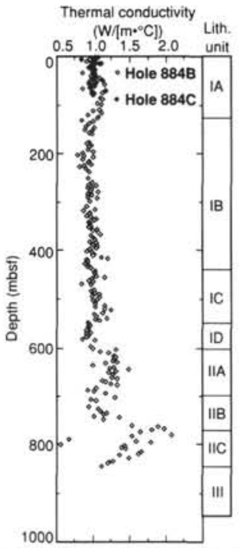

Figure 43. Thermal conductivity data vs. depth for Holes 884B and 884C. Lithologic units are shown at right, as discussed in the text.

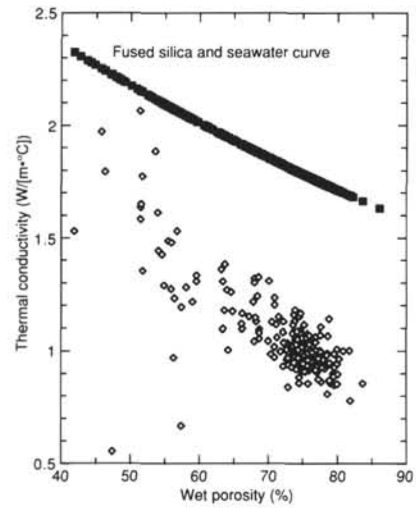

Figure 44. Thermal conductivity vs. wet porosity data for Hole 884B. The theoretical thermal conductivity of a mix of fused silica and seawater is shown in bold (after Wilkens and Handyside, 1985).

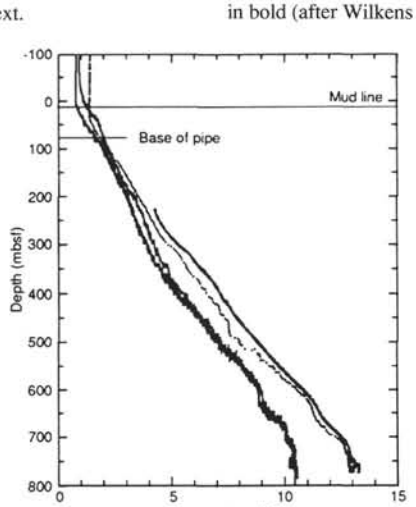

Figure 45. Temperature data recorded by the Lamont temperature logging tool on the quad combination and geochemical tool strings.

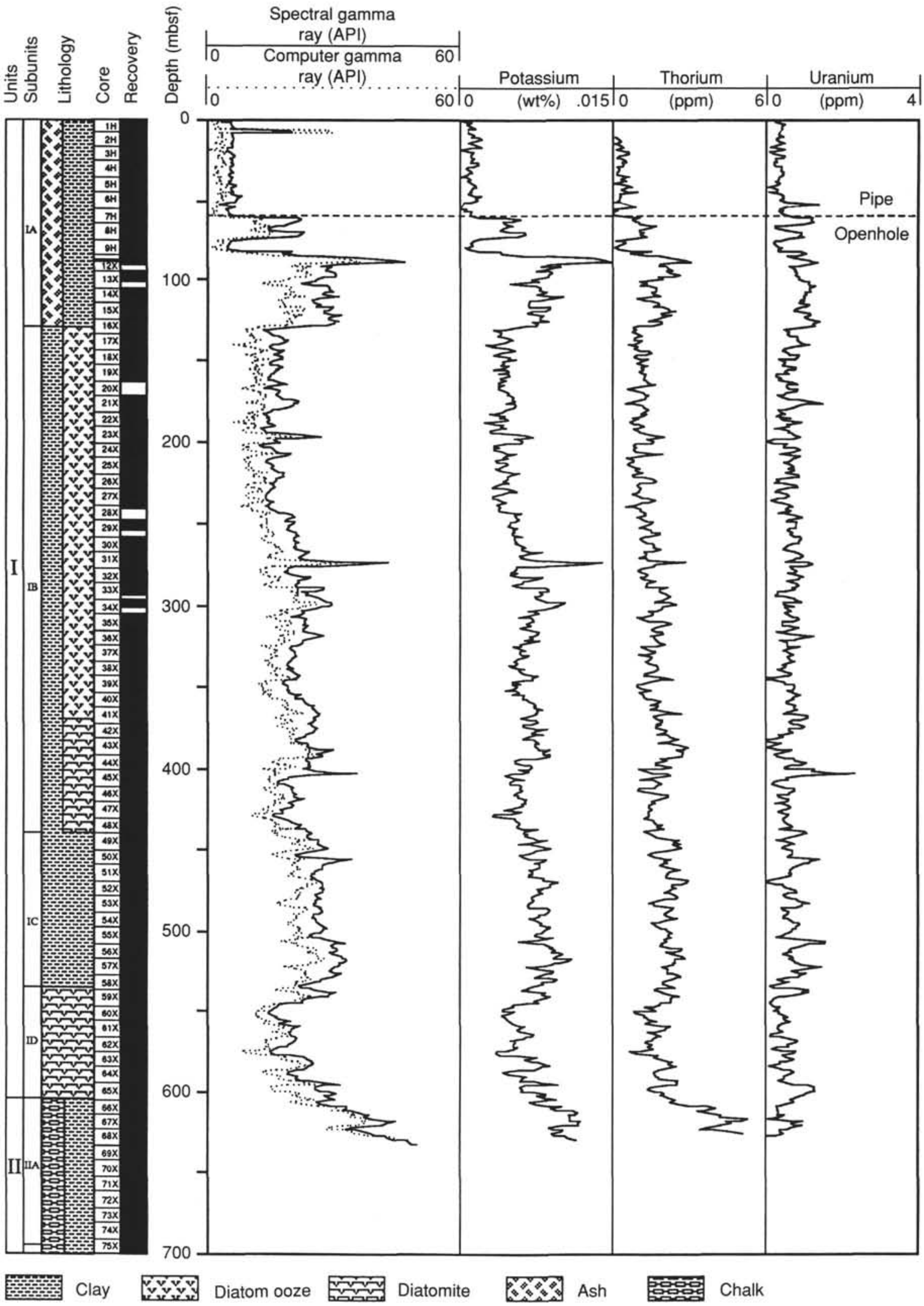

Figure 46. Data from the natural gamma-ray spectrometry tool (NGT) recorded on the geochemical tool string. The displayed data have been smoothed by a linear nine-point (1.37 m) moving average filter.

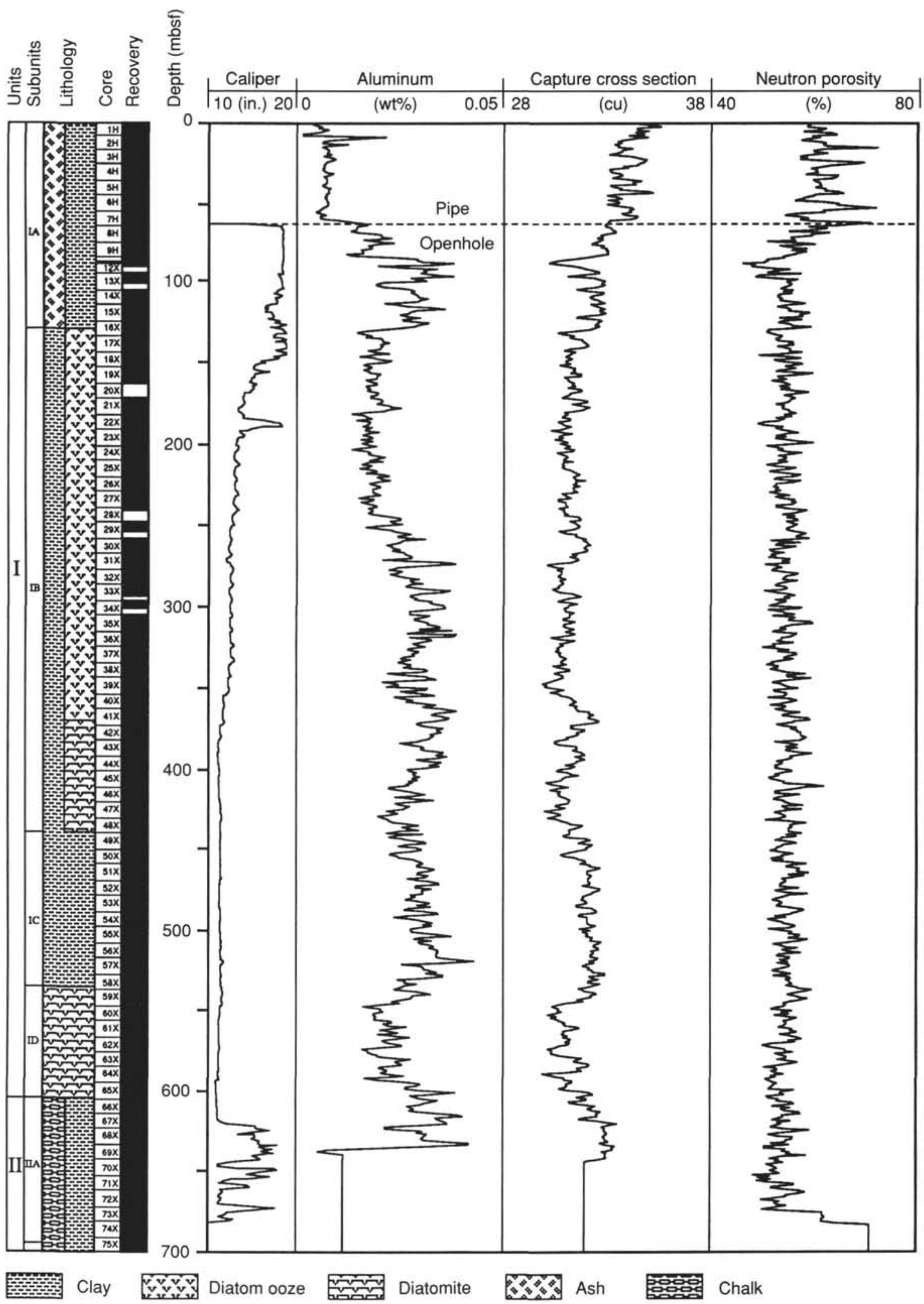

Figure 47. Caliper data from the high-temperature lithodensity tool (HLDT) and neutron porosity from the compensated neutron porosity tool (CNT); recorded on the Quad combination tool string. Aluminum concentration from the aluminum activation clay tool (AACT) and macroscopic thermal neutron capture cross section from the gamma-ray spectrometry tool (GST), recorded on the geochemical tool string. The displayed data have been smoothed by a linear nine-point (1.37 m) moving average filter.

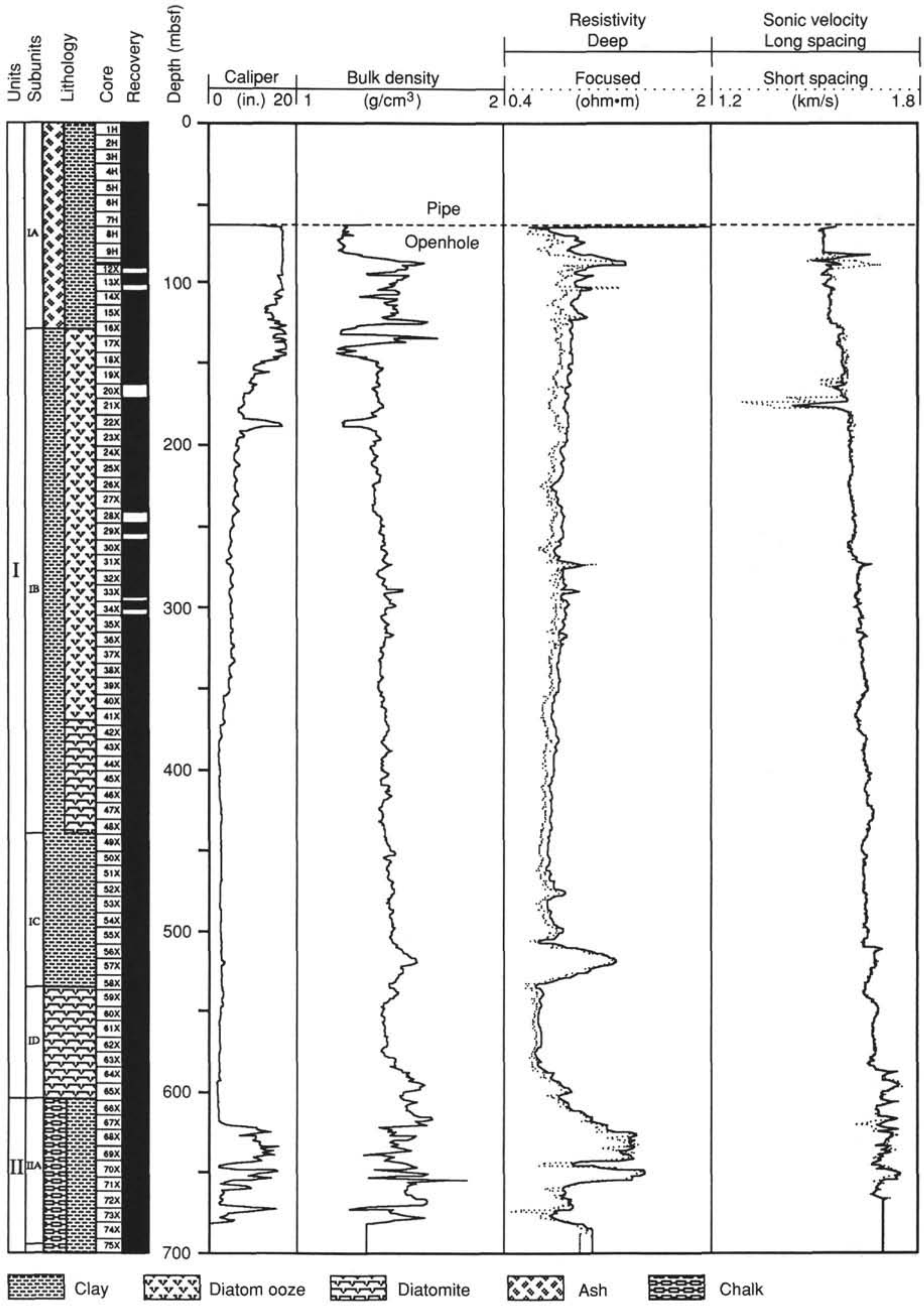

Figure 48. Logging data recorded with the Quad combination tool string; caliper and bulk density data from the HLDT; deep phasor induction and spherically focussed resistivity from the phasor dual induction tool (DIT); long- and short-spacing sonic velocity from the digital sonic tool (SDT). The displayed data have been smoothed by a linear nine-point (1.37 m) moving average filter.

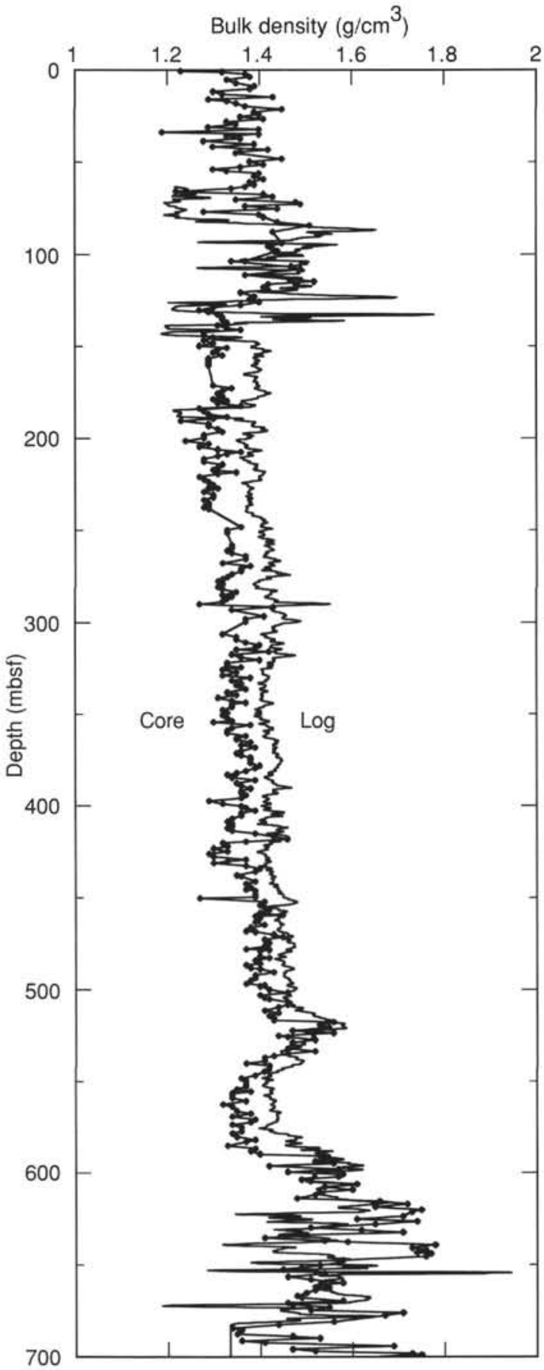

Figure 49. Comparison of log- and core-derived bulk density measurements. Logging data are from the HLDT and have been smoothed by a linear seven-point moving average filter.

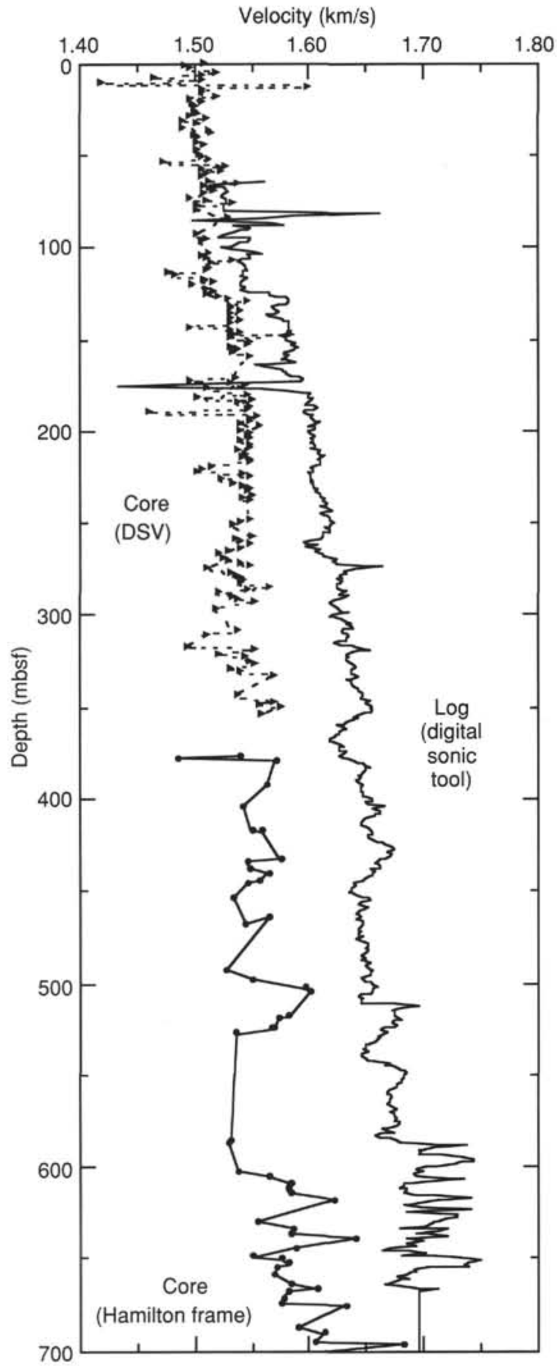

Figure 50. Comparison of log- and core-derived sonic velocity measurements. The logging data are from the digital sonic tool (SDT) and are an average of the long- and short-spacing measurements; these data have been smoothed by a linear nine-point moving average filter. The core measurements from discrete samples were performed using the digital sediment velocimeter (DSV) in the upper 350 m of the hole and using the Hamilton Frame apparatus in the lower section of the hole.

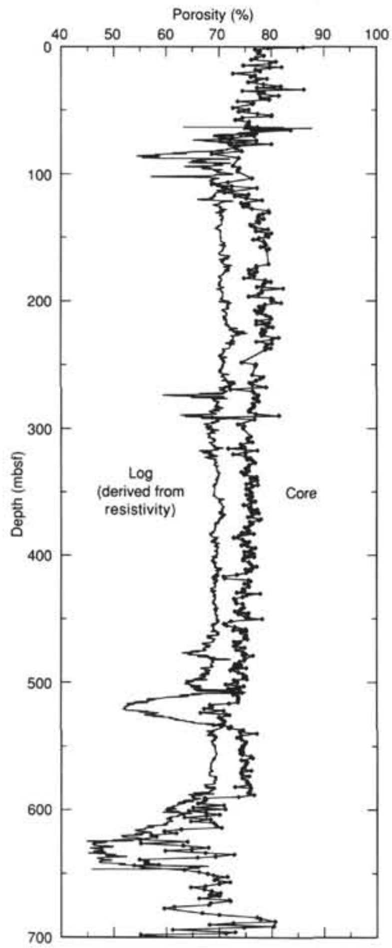

Figure 51. Porosity derived from the medium phasor induction log of the phasor dual induction tool (DIT) compared with core porosity measurements on discrete samples. The influx resistivity data and the final porosity log are unsmoothed.

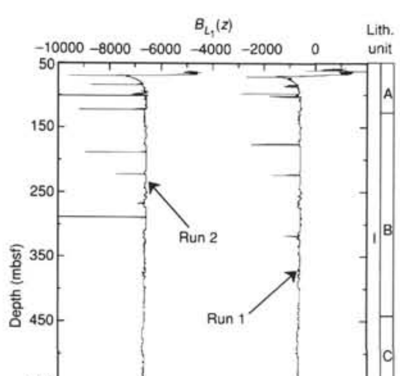

Figure 52. "Local" total induction B_L ("*B* field," see text) vs. depth in Hole 884E for the two successive runs. The boundaries between the main lithological units (as defined from Hole 884B) are shown on the right. The local part of the total induction has been obtained by correcting the total induction for the main dipolar field; scale shift between runs is 6000 nT.

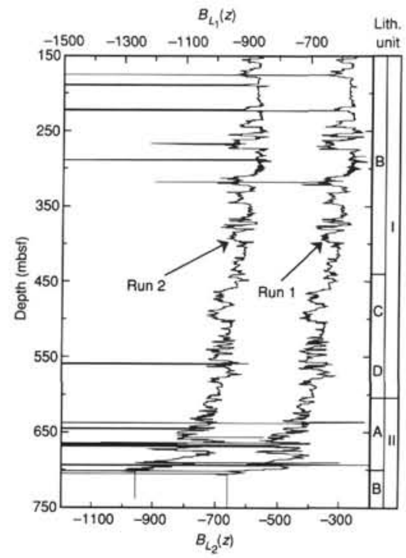

Figure 53. Detailed view of the "local" *B* field (B_L) between 150 and 750 mbsf in Hole 884E for the two successive logs; scale shift between runs is 300 nT. The boundaries between the main lithological units as defined from Hole 884B are shown on the right.

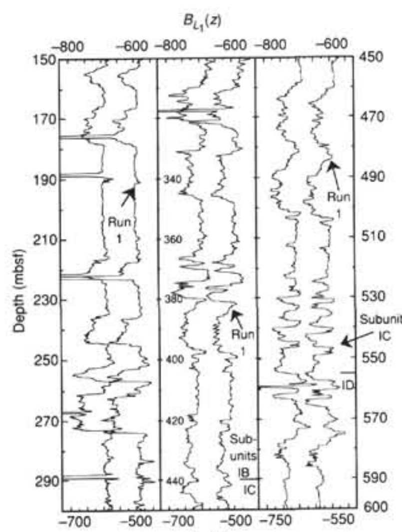

Figure 54. Close-up of the "local" *B* field (B_L) between 150 and 600 mbsf in Hole 884E for the two successive logs including location of the boundaries between the lithological subunits of Unit I as defined from Hole 884B; scale shift between runs is 100 nT.

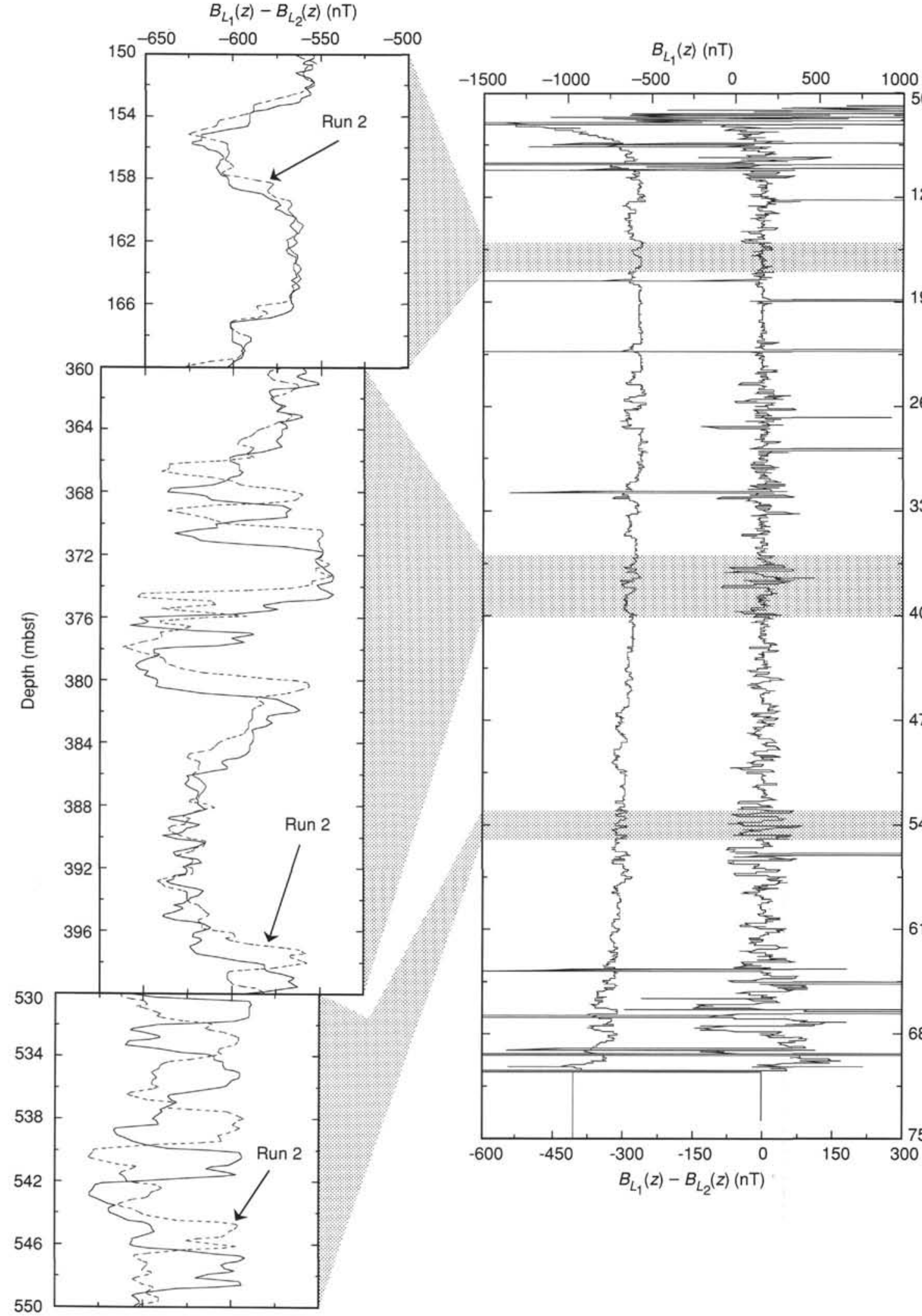

Figure 55. "Local" B field (B_L) between 50 and 750 mbsf in Hole 884E for the first run and difference ($B_{L2} - B_{L1}$) between the two runs. For three small depth intervals, a close-up of the two runs, B_{L1} and B_{L2} shows the depth shift between the two records and its evolution.

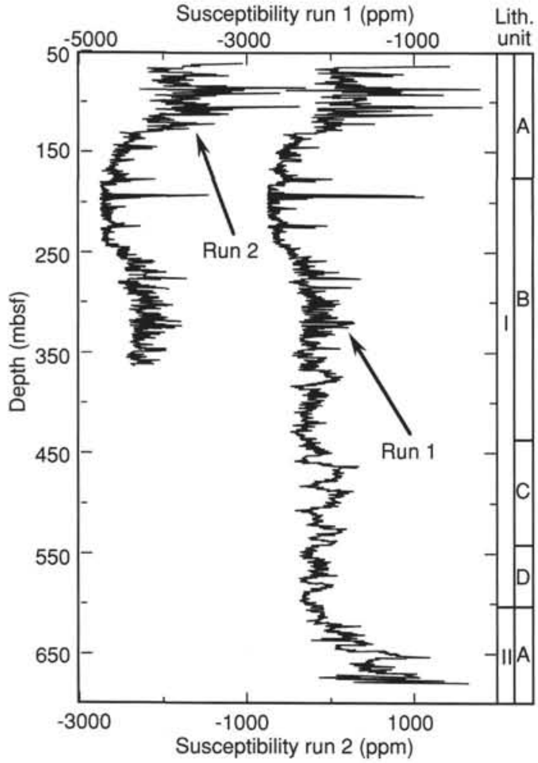

Figure 56. Susceptibility vs. depth in Hole 884E for the main log and the partial repeat section; scale shift between runs is 2000 ppm. The boundaries between the main lithological units, as defined from Hole 884B, are shown on the right.

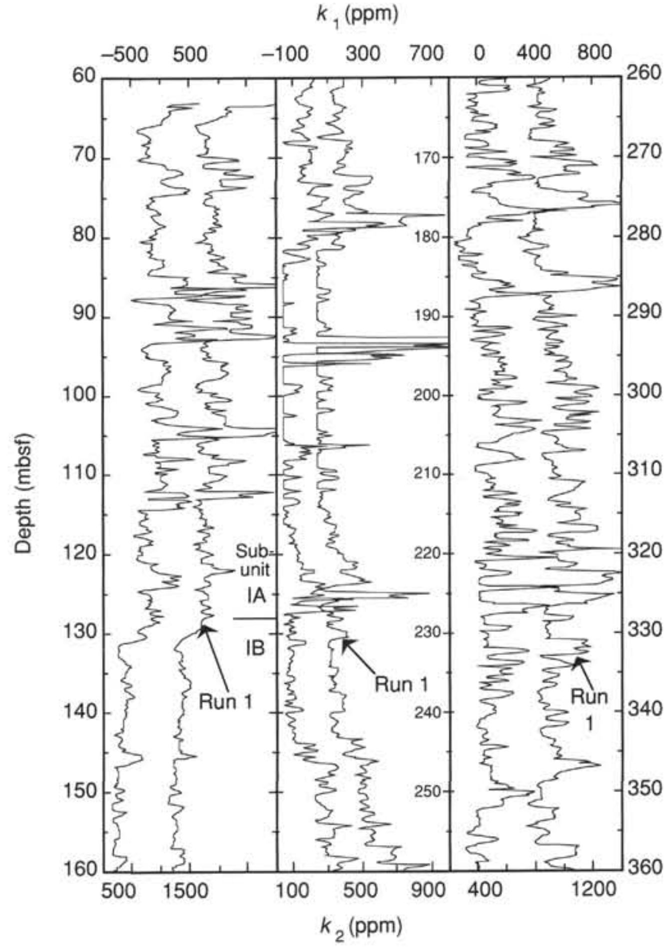

Figure 57. Detailed evolution between 60 and 360 mbsf of susceptibility for the main log and the partial repeat section (corrected for a –2750 ppm offset) in Hole 884E, including location of the boundaries between the main lithological units as defined from Hole 884B; scale shift between runs is 1000 (60–160 mbsf), 200 (160–260 mbsf), and 400 ppm (260–360 mbsf).

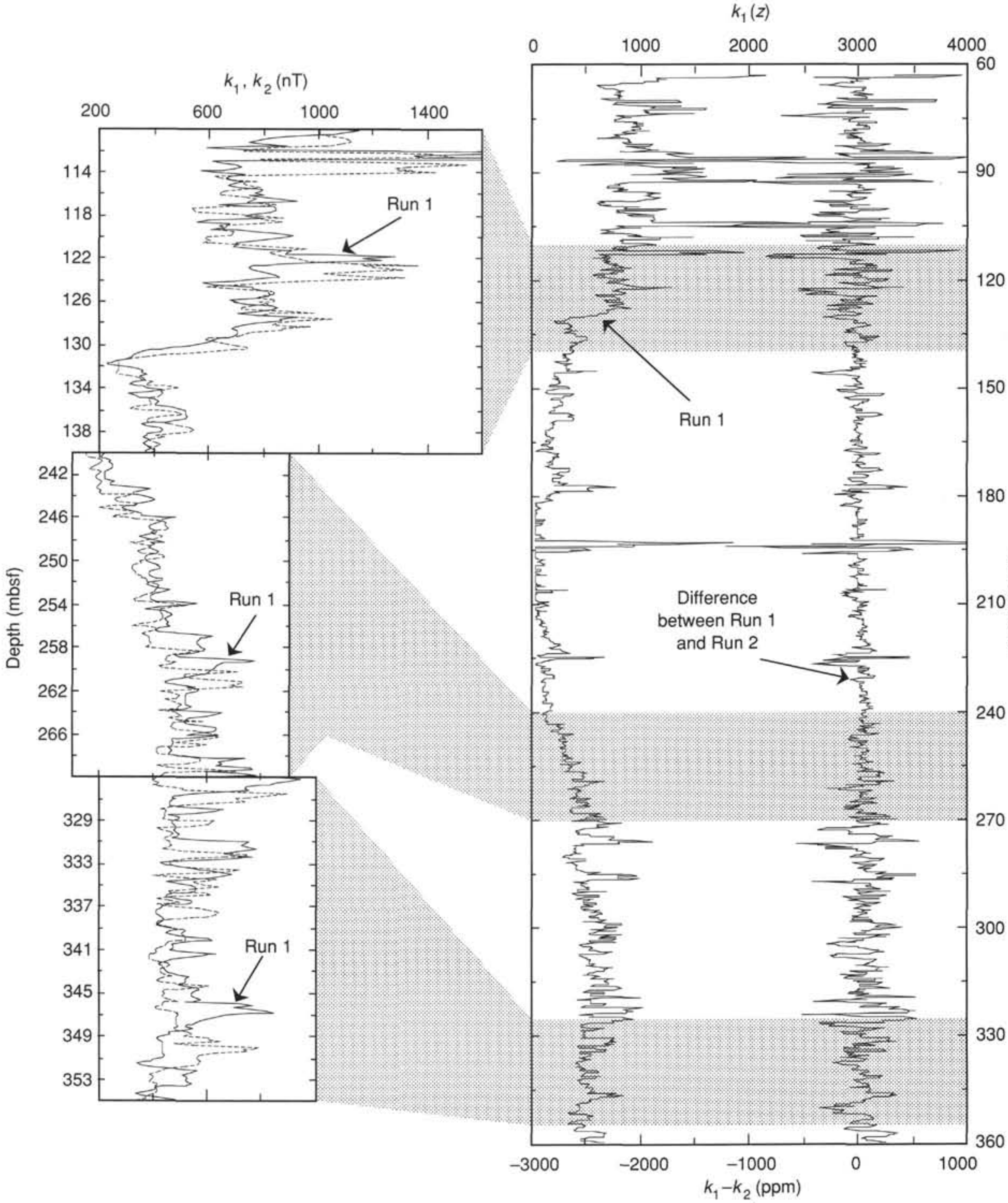

Figure 58. Detailed evolution in Hole 884E between 60 and 360 mbsf of susceptibility k_1 for the main log (corrected for a −2750 ppm offset) and difference $k_1 - k_2$ with the partial repeat section. For three small depth intervals, a close-up of the two runs, k_1 and k_2 shows the depth shift between the two records and its evolution.

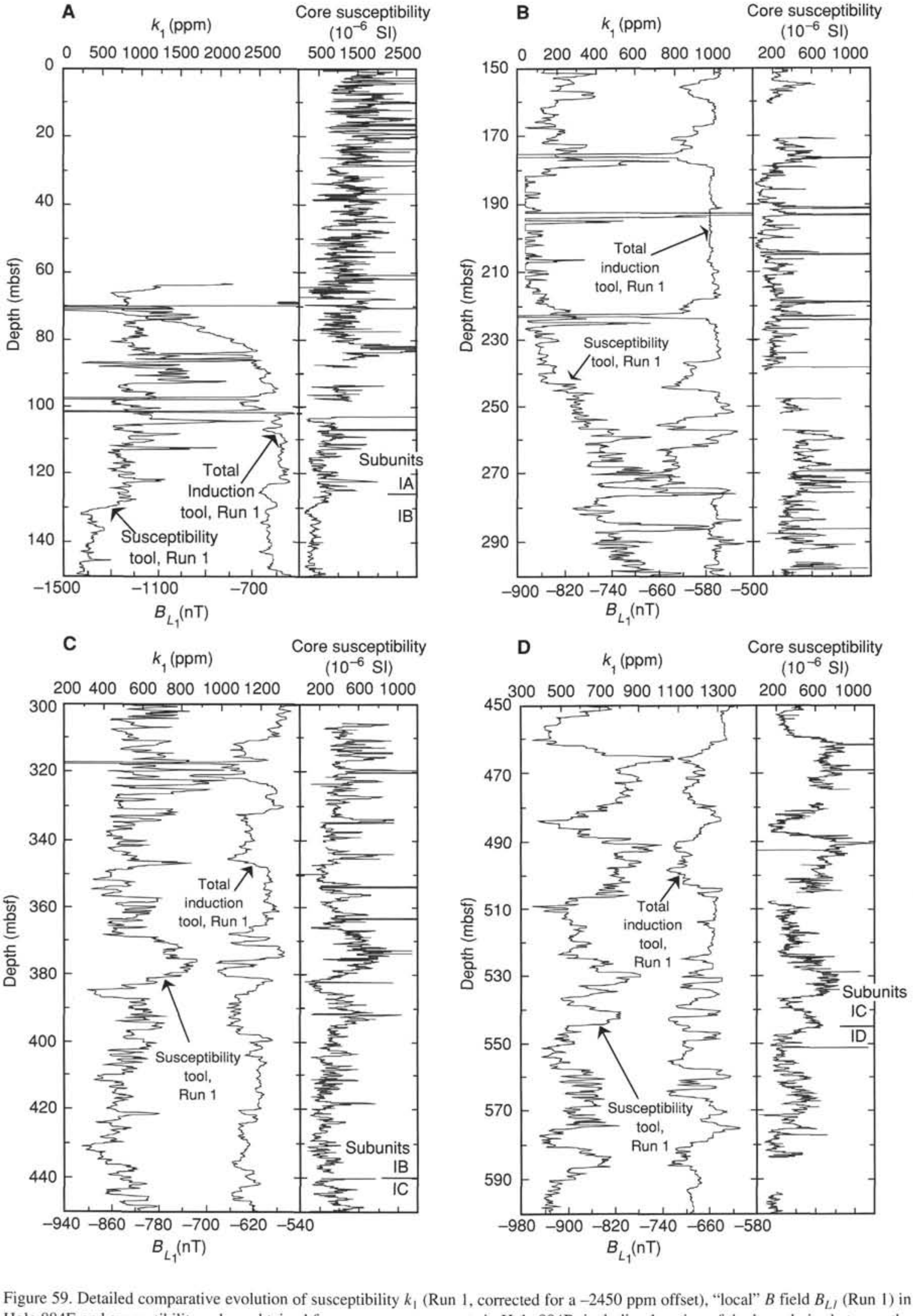

Figure 59. Detailed comparative evolution of susceptibility k_1 (Run 1, corrected for a –2450 ppm offset), "local" B field B_{L1} (Run 1) in Hole 884E and susceptibility values obtained from core measurements in Hole 884B, including location of the boundaries between the main lithological units as defined from Hole 884B. In all plots the relative full scales are preserved, whereas the width for log data full scale is double the one for core measurements. **A.** 0–150 mbsf, full-scale is 3000 ppm, 1000 nT, and 3000 10^{-6} SI. **B.** 150–300 mbsf, full-scale is 1200 ppm, 400 nT, and 1200 10^{-6} SI. **C.** 300–450 mbsf, full-scale is 1200 ppm, 400 nT, and 1200 10^{-6} SI. **D.** 450–600 mbsf, full-scale is 1200 ppm, 400 nT, and 1200 10^{-6} SI. **E.** 600–750 mbsf, full-scale is 3000 ppm, 1000 nT, and 3000 10^{-6} SI.

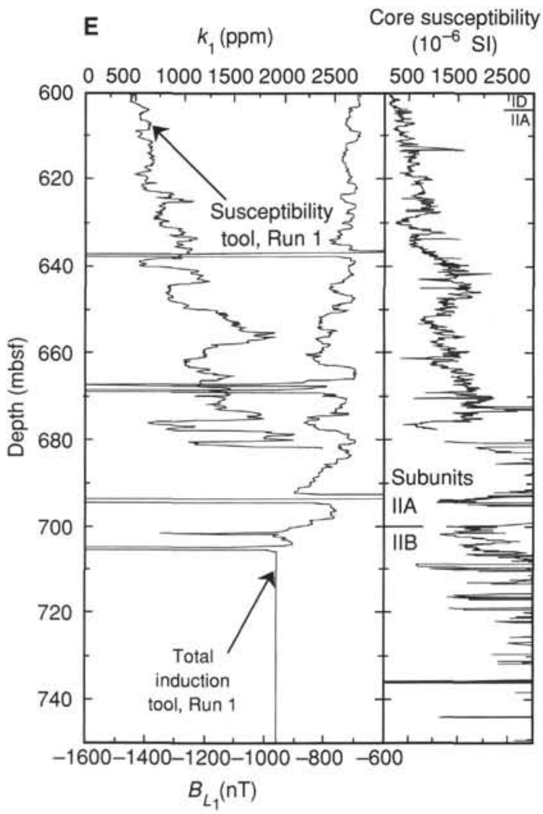

Figure 59 (continued).

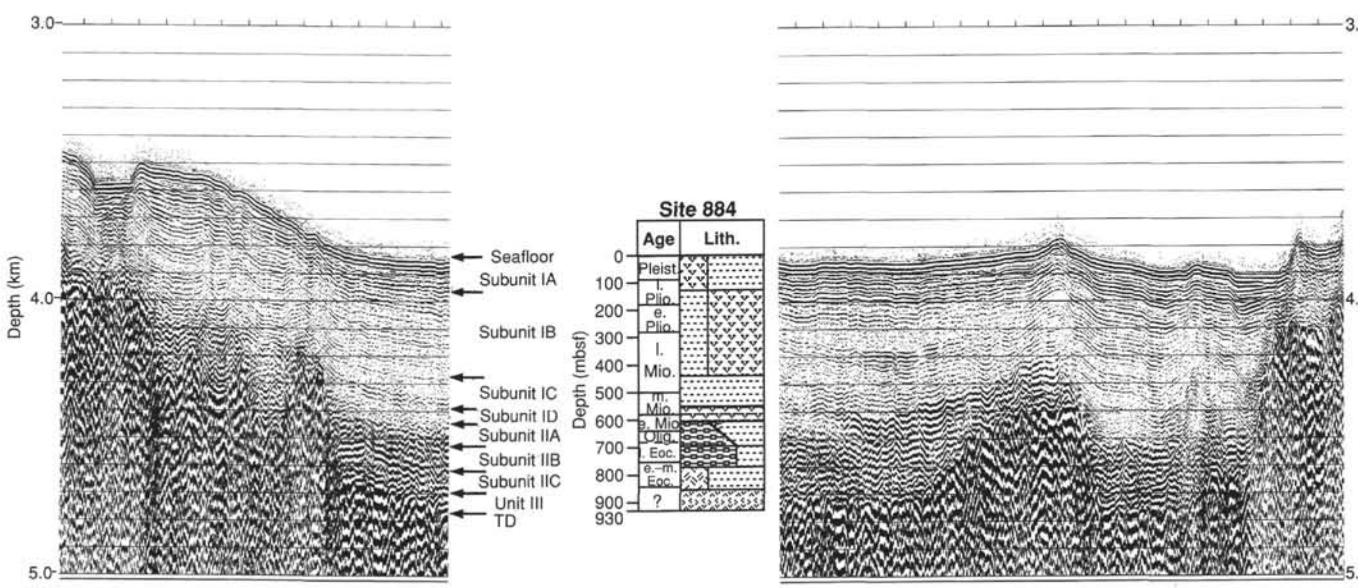

Figure 60. Seismic reflection profile of the Meiji Drift recorded by the *Farnella* in 1987. Profile crosses the Meiji Drift from southwest (left) to northeast (right). Note active channels at left and right and minor channels throughout the section. Profile processed and provided by Shawn Dadisman and David Scholl of the U.S. Geological Survey, Menlo Park, CA.

Hole 884E: Resistivity-Velocity-Natural Gamma Ray Log Summary

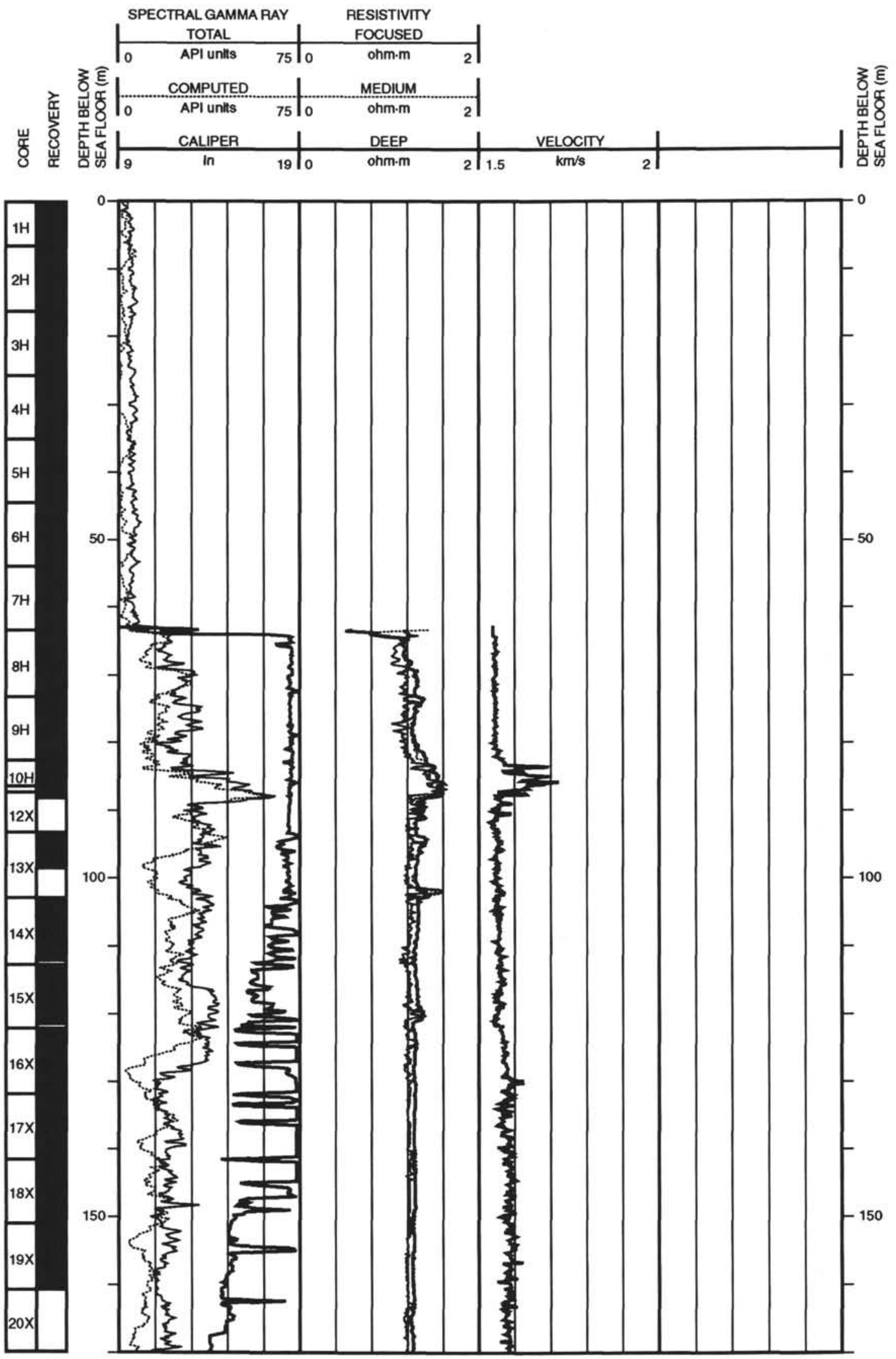

Hole 884E: Resistivity-Velocity-Natural Gamma Ray Log Summary (continued)

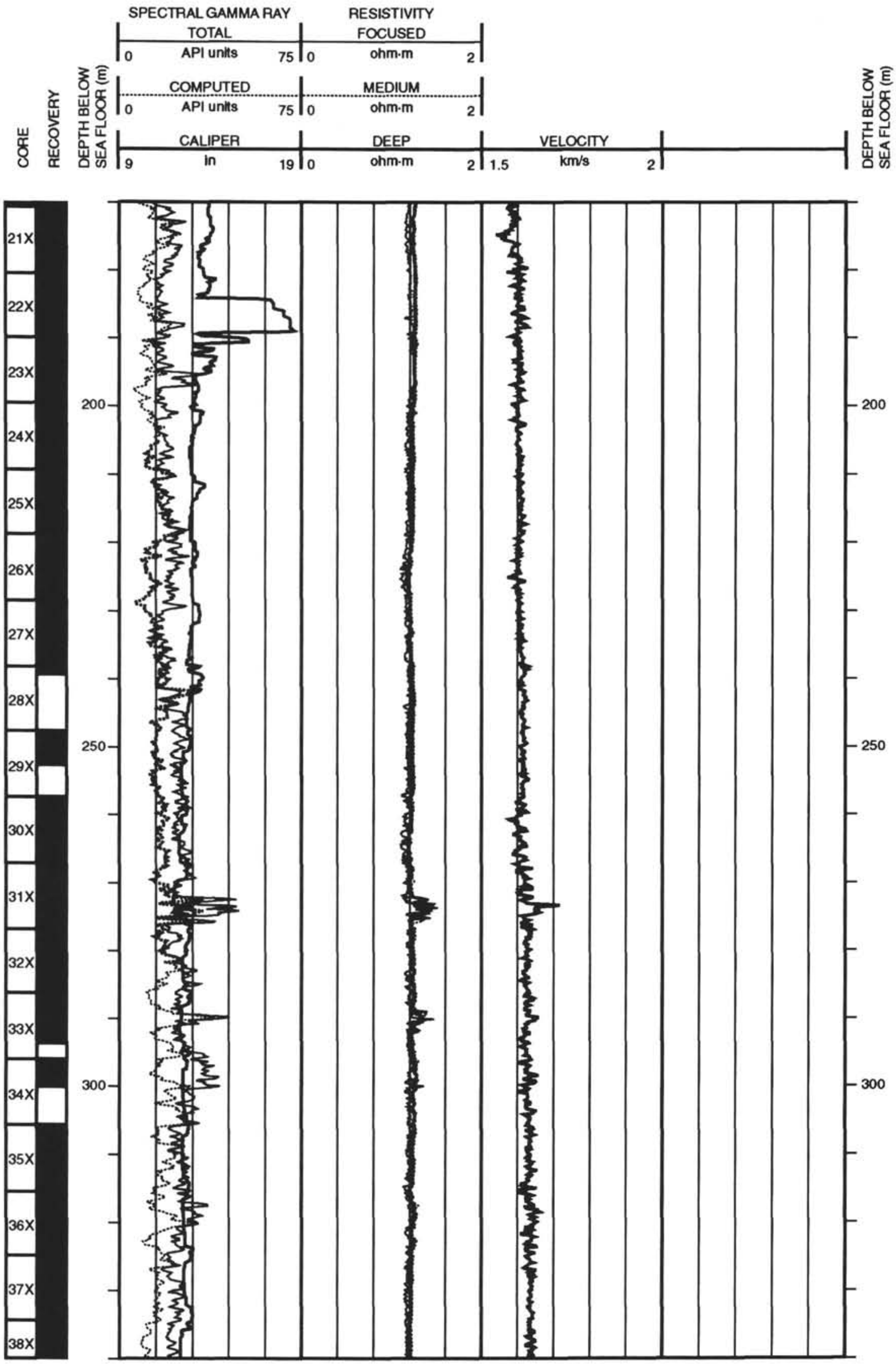

Hole 884E: Resistivity-Velocity-Natural Gamma Ray Log Summary (continued)

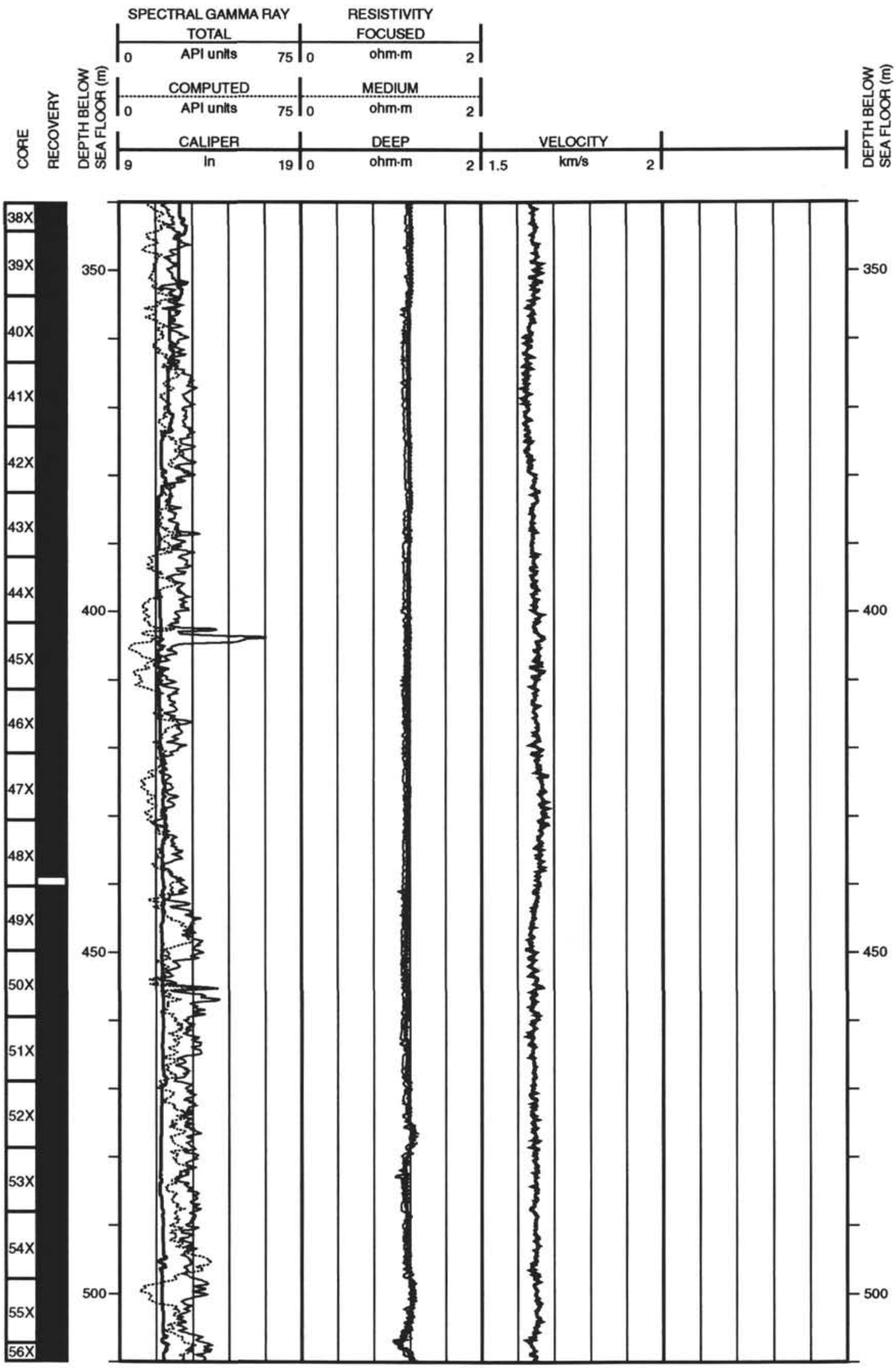

Hole 884E: Resistivity-Velocity-Natural Gamma Ray Log Summary (continued)

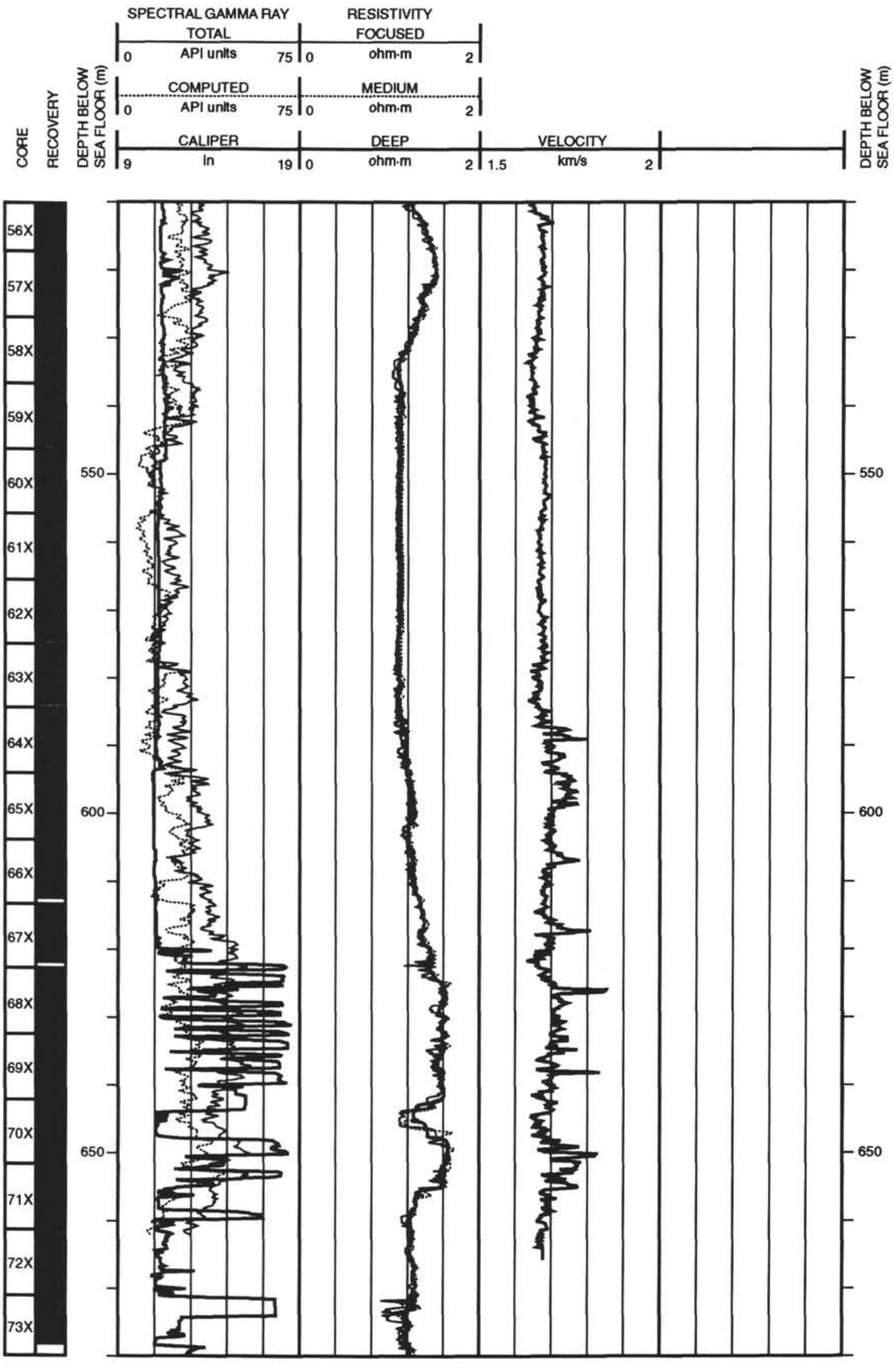

Hole 884E: Resistivity-Velocity-Natural Gamma Ray Log Summary (continued)

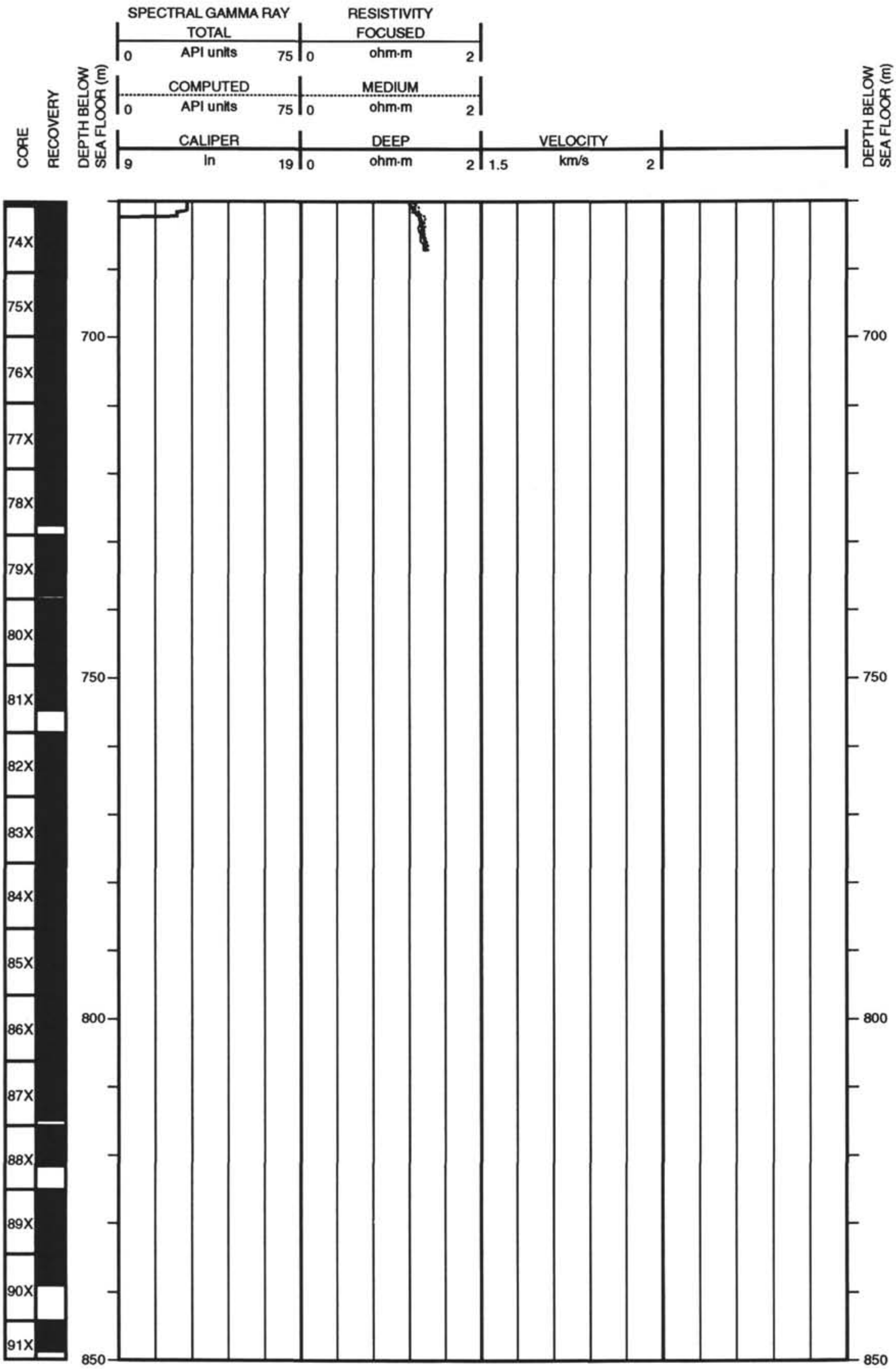

Hole 884E: Geochemical Log Summary

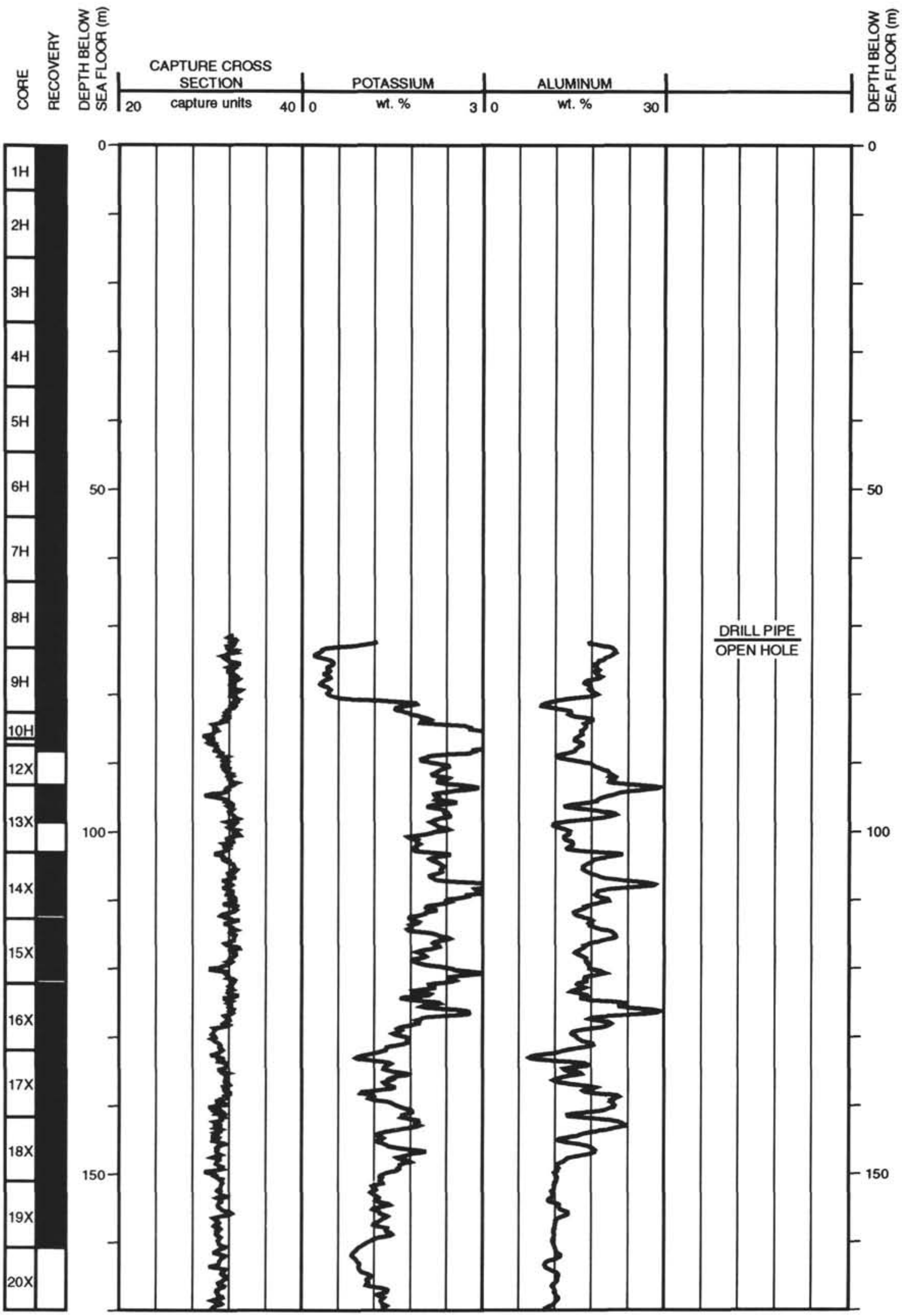

Hole 884E: Geochemical Log Summary (continued)

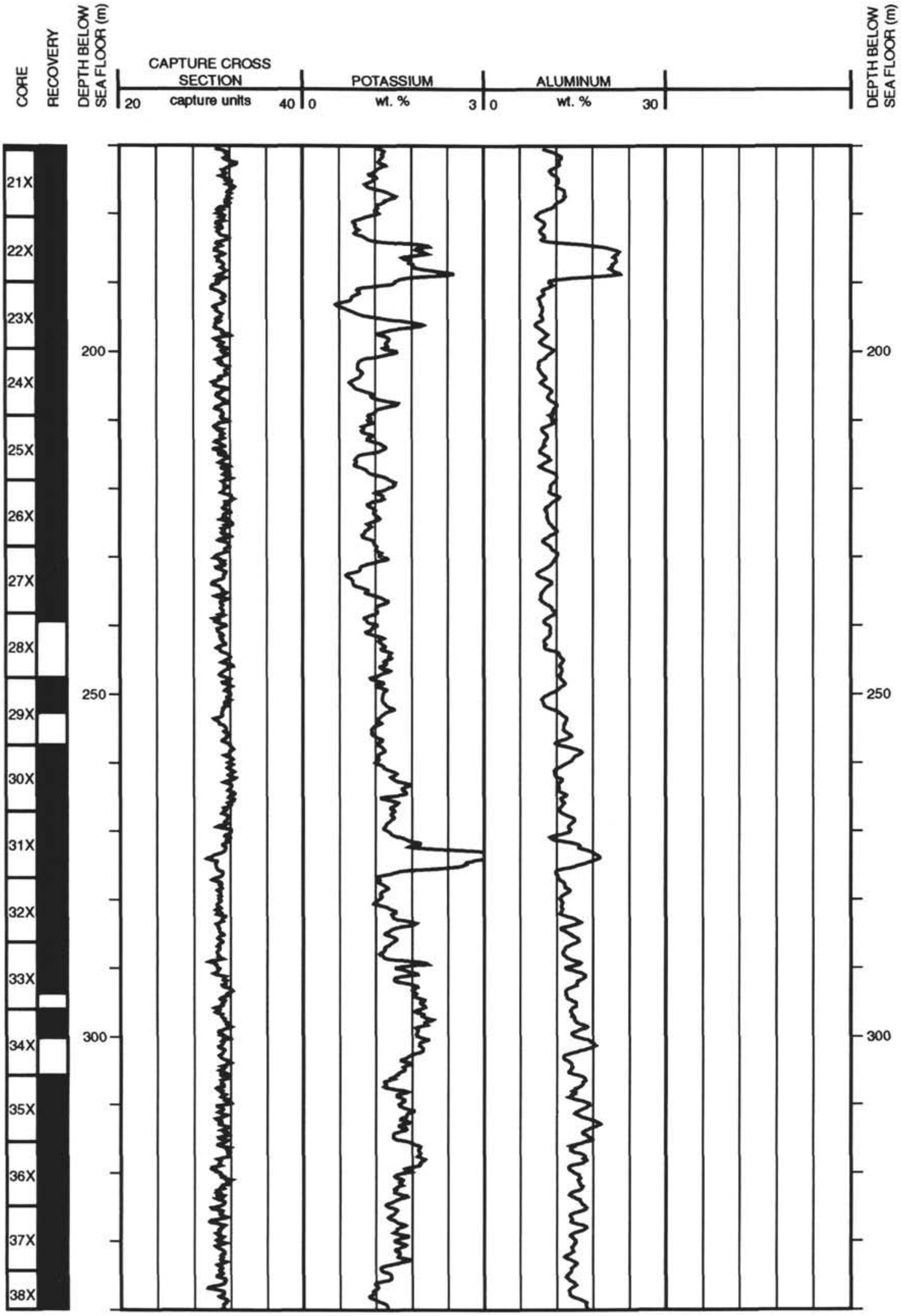

Hole 884E: Geochemical Log Summary (continued)

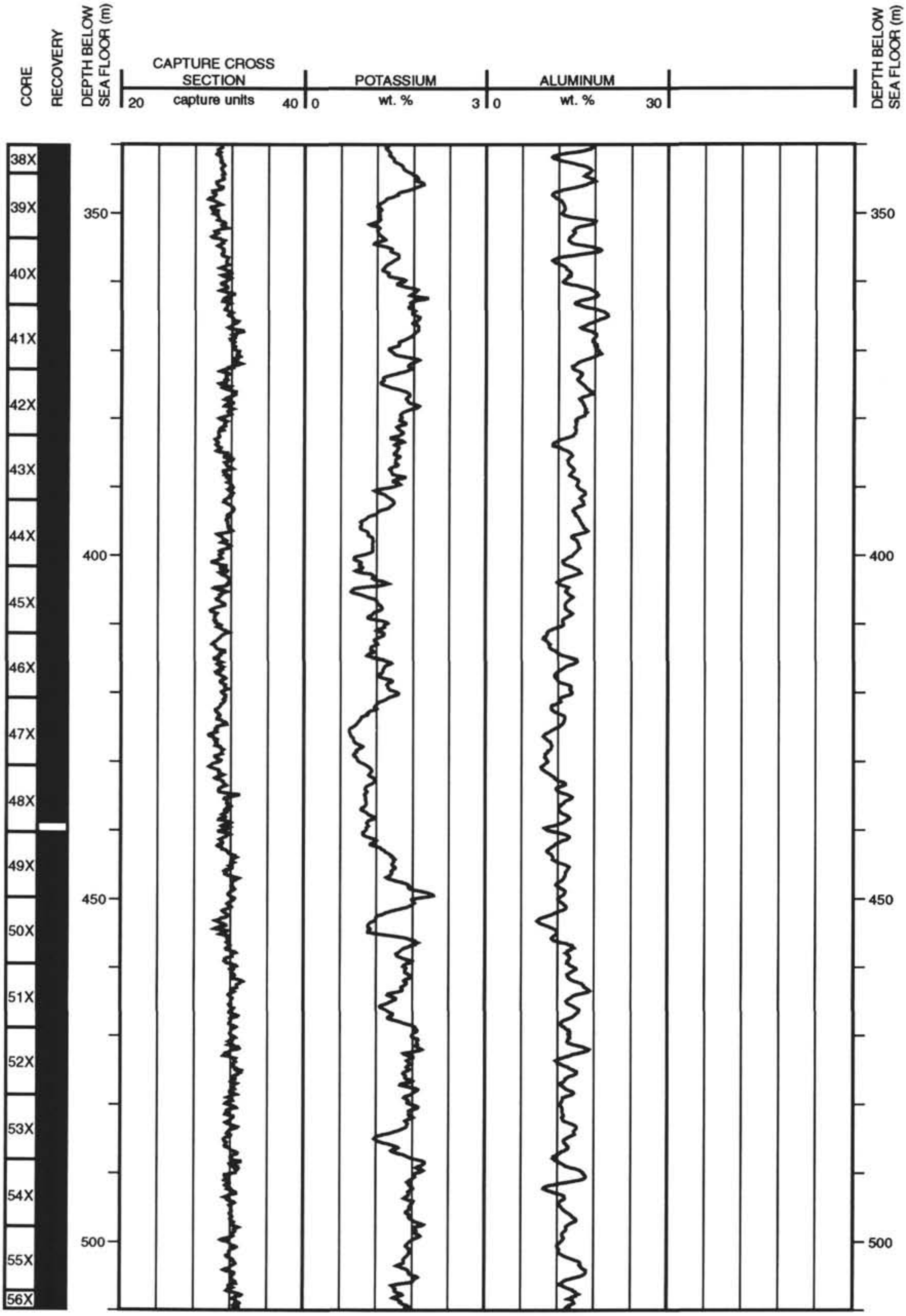

Hole 884E: Geochemical Log Summary (continued)

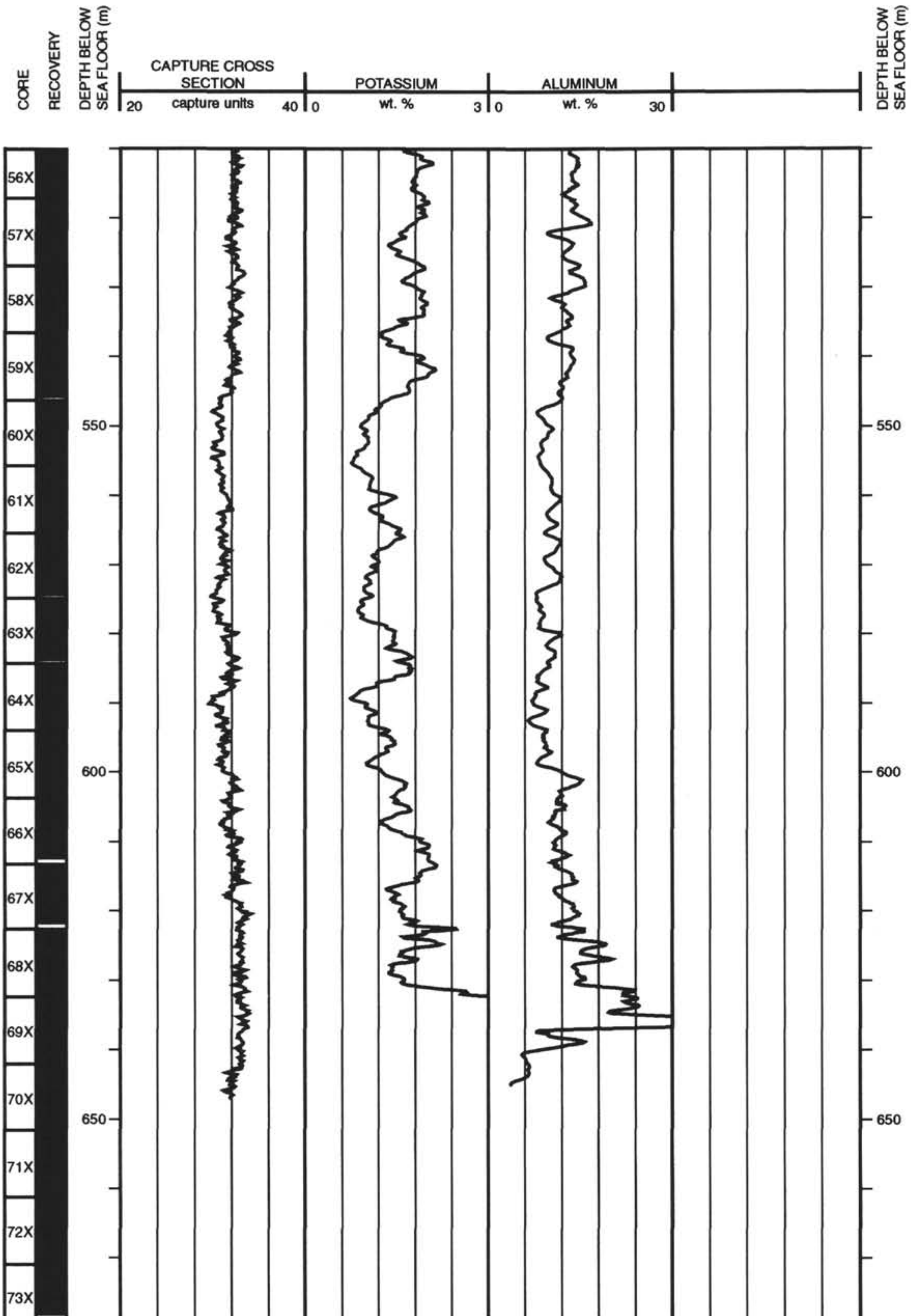

Hole 884E: Density-Porosity-Natural Gamma Ray Log Summary

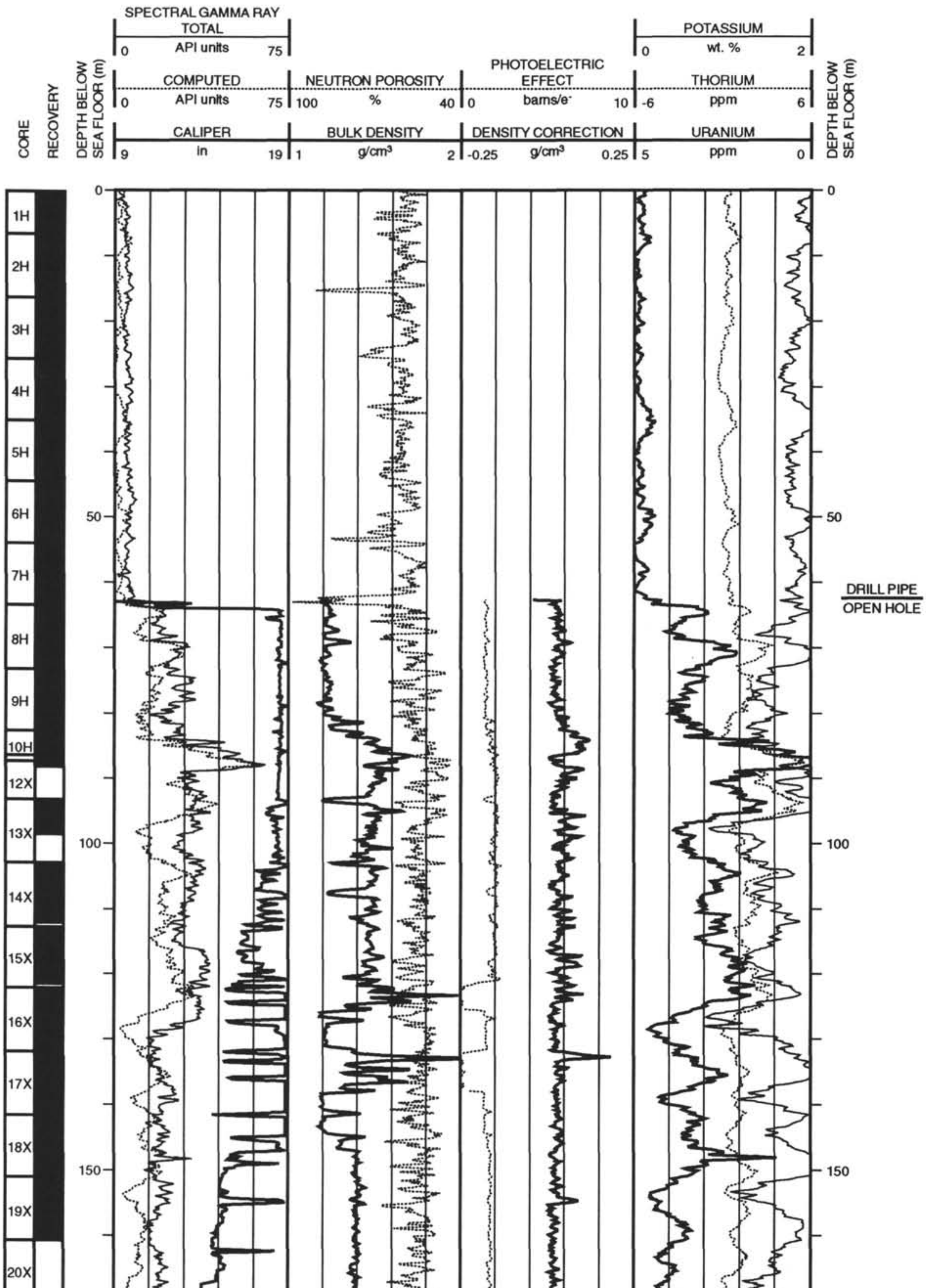

Hole 884E: Density-Porosity-Natural Gamma Ray Log Summary (continued)

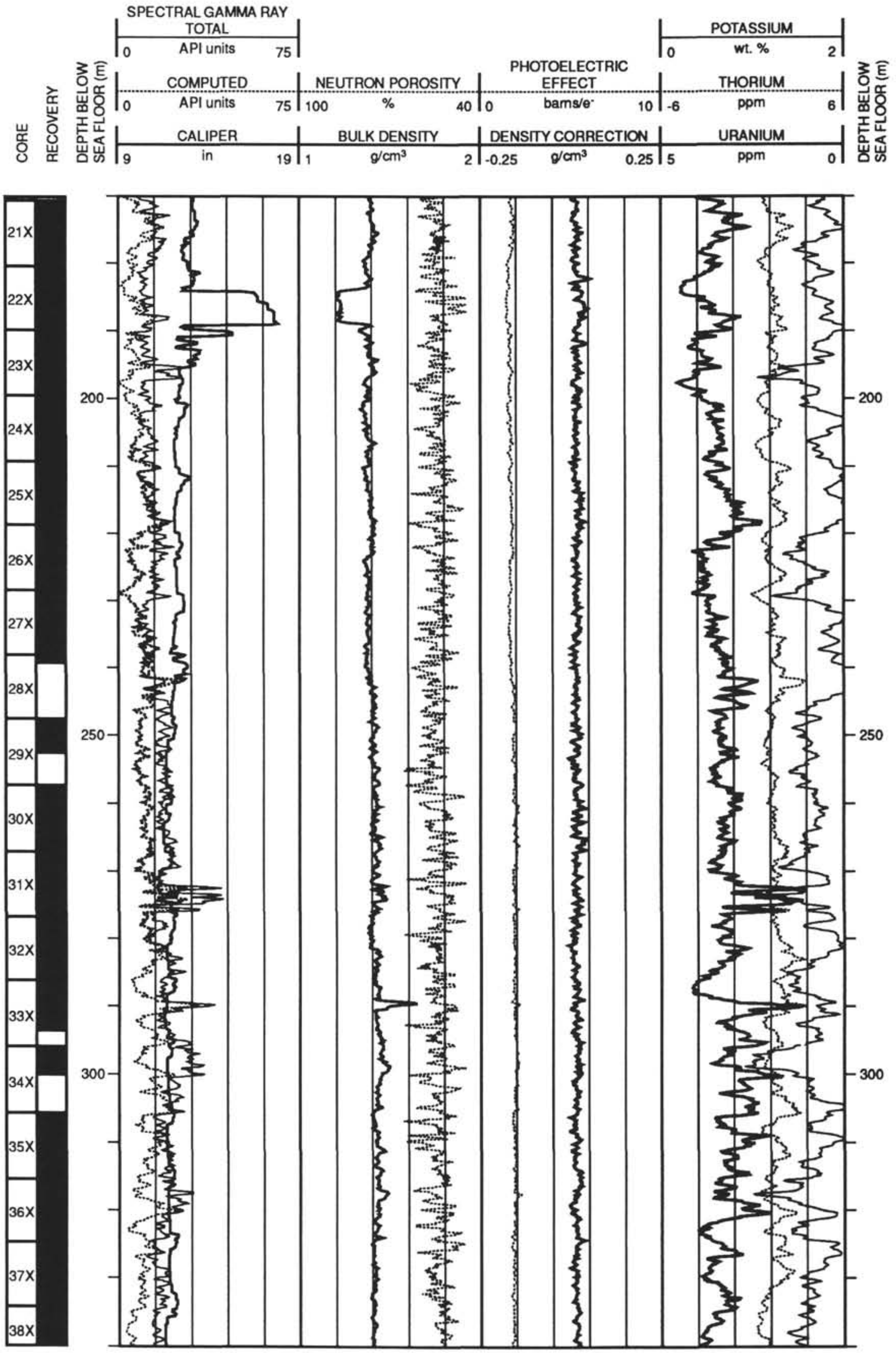

Hole 884E: Density-Porosity-Natural Gamma Ray Log Summary (continued)

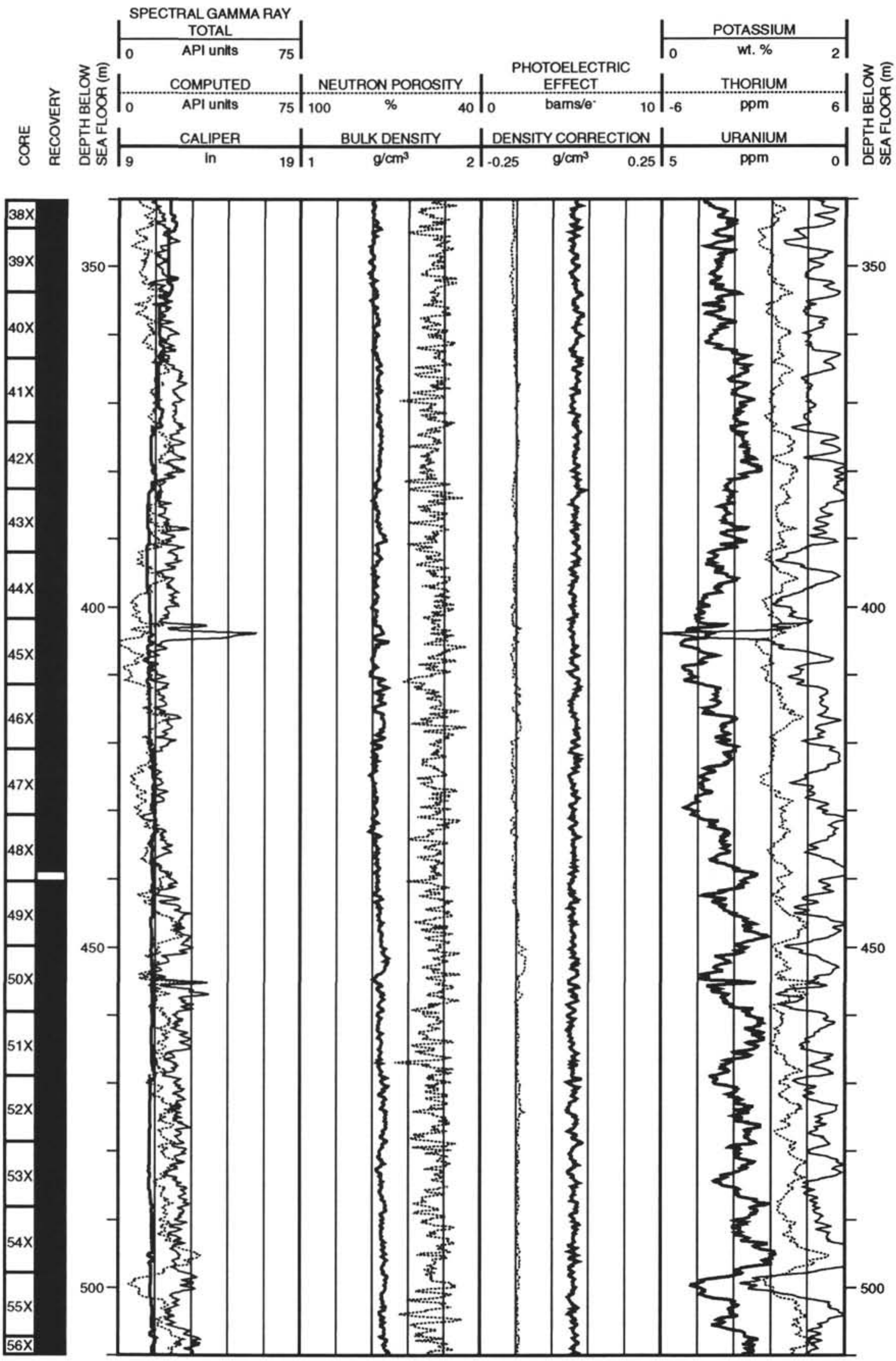

Hole 884E: Density-Porosity-Natural Gamma Ray Log Summary (continued)

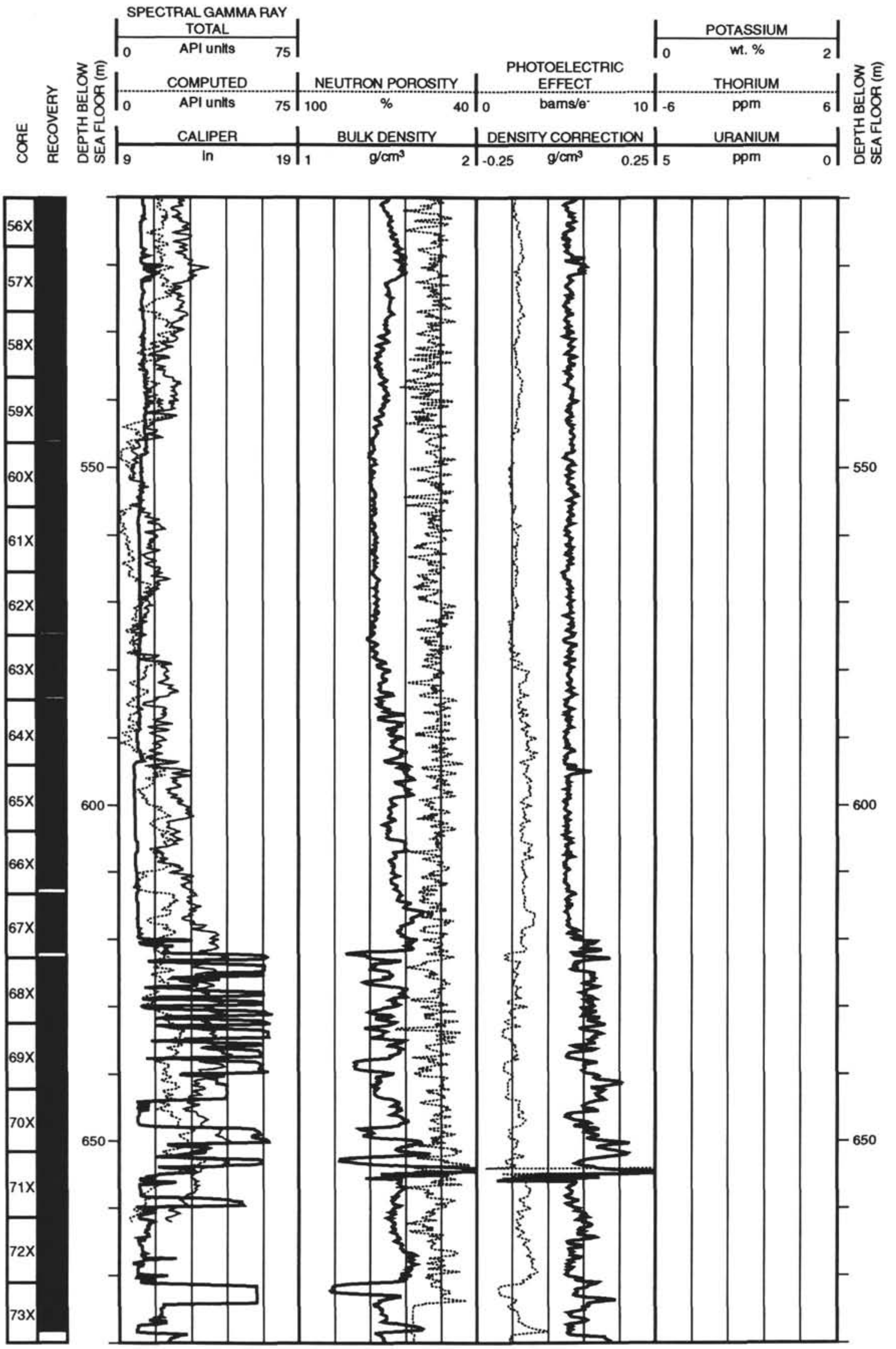

Hole 884E: Density-Porosity-Natural Gamma Ray Log Summary (continued)